Designing Nanoparticles for Self-Assembly of Novel Materials

by

Rose K. Cersonsky

A dissertation submitted in partial fulfillment
of the requirements for the degree of
Doctor of Philosophy
(Macromolecular Science and Engineering)
in The University of Michigan
2019

Doctoral Committee:

Professor Sharon C. Glotzer, Chair
Professor Jay Guo
Professor Nicholas A. Kotov
Assistant Professor Xiaoming Mao
Professor Greg van Anders, Queen's University

Rose K. Cersonsky

rosecers@umich.edu

ORCID iD: 0000-0003-4515-3441

Take as much care with words expressing your sentiments as you will crafting your doctoral dissertation.

– Marisha Pessl, *Special Topics in Calamity Physics*

I dedicate this work to my family: little, medium, big, and found, I love you all.

Dad, you are always with me.

ACKNOWLEDGEMENTS

I am not lucky. You know what I am? I am smart, I am talented, I take advantage of the opportunities that come my way and I work really, really hard. Don't call me lucky. Call me a badass.

– Shonda Rhimes, *Year of Yes*

First, I would like to thank my advisor Sharon Glotzer. Thank you for being an incredible role model and believing in my work and value as a scientist. Thank you for always knowing the exact question I needed to be asked and for pushing me outside of my comfort zone. Thank you for reminding me that I do not need to feel lucky to be in whichever room I'm in, that I have worked hard and earned my place there. You are *such* a badass.

Do your thing and don't care if they like it.

– Tina Fey, *Bossypants*

Thank you to the incredible people I have had the true honor to mentor in the past five years, including Sophie Barterian, Gabrielle Richmond, and Yuan Zhou. By letting me share my love for this amazing world of science, I got to fall in love with it over and over again. You are capable of whatever you put your mind to. You make me hopeful and excited for the next generation of scientists, and I am happy to have played even the smallest part in your journey.

"I like the cover," he said. "Don't Panic. It's the first helpful or intelligible thing anybody's said to me all day."

– Douglas Adams, *The Hitchhiker's Guide to the Galaxy*

Thank you to my friends who supported and distracted me throughout this process, including my wolf pack, Sophia, Brit, and my friends from UConn and home. Thank you to the colleagues who got me here and talked me through, including Jim Antonaglia, Chrisy Du, Bradley Dice, Alyssa Travitz, Ayse Muniz, Karen Coulter, Julia Dshemuchadse, the entire Glotzer group, and my little Macro cohort. Thank you for pushing me to think beyond myself, whether it be in the context of the scientific big picture or our roles in the world. You have taught me so much, answered so many questions, and listened to so many excited exclamations of "I found something really cool" or "what if we could do..." that this achievement belongs to you as well.

Some people care too much. I think it's called love.

– A. A. Milne, *Winnie the Pooh*

To my family – you have constantly been my biggest inspiration and my most welcome critics. Thank you for the lessons you have taught me about being curious, ambitious, honest, and above all, loving. Tess, thank you for celebrating with me the achievements big and small. James, thank you for reminding me the power and healing that comes through creativity. Emily, thank you for copy-editing everything (except this, so have fun reading!) and for constantly reminding me that I could do this. Mom, thank you for *everything*. You are a constant harbor from the storm. Dad, thank you for introducing me to one of my greatest loves: math.

I just want to make, like, crazy science with you. Totally crazy science.

– Cosima Niehaus, *Orphan Black*

I love you, and I like you.

– Leslie Knope and Ben Wyatt, *Parks and Recreation*

To my partner, Simon. We started this together and finished it together. I wouldn't have been the same person through and after this process without you by my side. You have challenged and championed me at every step, and helped me to define the type of scientist and person I want to be. You're my favorite person and my best friend.

TABLE OF CONTENTS

LIST OF FIGURES

Figure

LIST OF APPENDICES

Appendix

ABSTRACT

The design of new materials has often relied on crystal structure as a source for design complexity and innovation. This requires new crystal structures and new manners of constructing and synthesizing these structures. An ideal mechanism for synthesis is self-assembly, the spontaneous emergence of order due to particle interactions. For hard particles on the nanometer length scale, particle shape can drive or often dominate the self-assembly behavior of a system. Using Digital Alchemy (DA), a framework which provides theoretical thermodynamic interpretation of particle shape, we can obtain optimal particle shapes through simulation for assembling target structures, and use these results to understand the role of particle shape in stabilizing colloidal crystals. In Chapters III-V of this dissertation, I present multiple ways in which DA can (and cannot) be used to understand the self-assembly of hard polyhedral nanoparticles. First in Chapter III, I present how DA can be used to formally distinguish colloidal self-assembly from packing, which explains the contradictory behavior of certain hard polyhedral nanoparticles which self-assemble and pack into different crystal structures. Then in Chapter IV I present how phase transitions can occur in *shape space* and how this has implications on the properties exhibited by these colloidal crystals. Finally, in Chapter V, I give insight into the nuances of using DA as a tool for predicting particle shapes for self-assembly.

However, we are not limited to target only structures, but also materials properties, furthering the understanding of the interplay between materials synthesis, structure, and properties. Inspired by an open question in Chapter IV, I delve into the relationship between crystal structure and a particular materials property: photonic band gaps. A photonic

crystal is comprised of two materials with different interactions with light; a photonic band gap occurs in a photonic crystal when a range of light is not transmittable through the material, *i.e.* reflected. In Chapter VII, I explore which crystal structure properties will lead to a photonic band gap by computing more than 150,000 photonic band structures (a subset of which are given in Appendix C). In Chapter VIII, I use the knowledge gained in Chapter VII, apply modifications to known crystal structures, and compute the photonic band structures (which are included in Appendix D and Appendix E).

CHAPTER I

Introduction

There is geometry in the humming of the strings. There is music in the spacing of the spheres.

– Pythagoras

When we think of the eras of human civilization, such as the Stone Age, Bronze Age, the Information Age, technology is often the defining feature. However, this technology relies on the materials available to society, such that that new materials enable their advancement and become the driving feature to scientific discovery.

How do you design a new material? First, you must choose a length scale and therefore a building block. Are we designing materials on the atomic scale, on the order of Angstroms to nanometers, where atoms and molecules are our blocks? Are we designing on the macroscale, where our blocks can be larger, potentially *literal* blocks? Here I will discuss a length scale somewhere in between, the nanoscale.

Statistical physics is a powerful tool used to understand the self-assembly and stability of materials, including the crystalline order which can form due to entropy. Here entropy is not used in its traditional connotation as the amount of disorder within a system, but rather as it is defined in information theory. The information theory of entropy views entropy as the information yet to be learned for a system. Statistical physics states that a closed system will tend towards that which minimizes free energy and maximizes entropy; therefore, a system

will tend towards the state that leaves the most information unknown.

To better understand this, imagine a subway car. There are a variety of ways for people to sit, stand, hang from the subway rail, etc. Let's imagine there are four people sitting in a car with six seats – what does that tell us? From a quick probability calculation, we know that there are 360 ways for four people to sit in six seats. Therefore there are 360 snapshots, or "microstates" of what our car can look like. Now imagine two people get up and move to the one of six places it is comfortable to stand. Now we have 900 possible configurations. Therefore, we have more information about the configuration of people when everyone is sitting (there are only 360 choices) than when half are standing. According to the information theory of entropy, the latter has more entropy.

On a hot summer day – how are you more likely to find the subway car? Half standing and half sitting gives each person more room, and more possibility of switching seats, and will be more likely for people to adopt. The same goes for hard nanoparticles – they will adopt a state where the most microstates are accessible, and they have the most freedom to change their position or orientation. When a particle is non-spherical, such as in the case of hard polyhedral nanoparticles, there are more microstates if the faces of the nanoparticles are aligned, leading to order.[1, 2, 3, 4]

Additionally, when we look at this theory inversely, we can design novel materials; if we have a target structure in mind, we can we find the building blocks that will self-assemble and maximize entropy in the structure. This is the idea behind the *Digital Alchemy* (DA) framework, wherein some aspect of particle design, here particle shape, is optimized for entropic maximization for some target criterion.[4, 5, 6]

The first three projects within this dissertation will look closely into the DA framework, and how we can use it within three aspects of materials design: (Chapter III) What is the relationship between self-assembly and packing on the colloidal length scale? (Chapter IV) What kinds of structures and phase transitions can we observe by modifying the particle design? (Chapter V) How can the framework of DA be best realized to design nanoparticle

shapes for self-assembly?

In Chapter III, I will demonstrate that order formation at finite pressure and at infinite pressures, or self-assembly and packing, respectively, are distinct physical phenomena carrying their own characteristic signatures. [7]

In researching Chapter III, I came across a set of anomalous data points that serve as the basis for Chapter IV.[i] These data points suggest a phase transition that occurs from the well-studied diamond structure to a tetragonal derivative as a function of particle shape. In this chapter I will detail this phase transition and its parallels to the phase transitions that occur in atomic systems of Si, Ge, and Sn. I will also detail the impact of this structure change on the photonic properties of the system, which I will define later.[8]

Chapter V will look at the implementation of the DA framework across *shape space*, *i.e.* the variable space that defines nanoparticle shape. Chapter III and Chapter IV demonstrated the complexity of this space for design, large changes in physics or structure possible due to small displacements in shape space. Therefore, it is important to understand the influence of the underlying shape space on design for target structures. In this chapter I will report the ground state to shape space and the impact that structural constraints have on the results of DA and propose new methodologies for implementing DA for the purpose of materials design.[9]

The final two chapters, on the topic of photonic crystals, will feel somewhat disjoint from the first three, but comes from an open question in Chapter IV. Photonic crystals are systems of mixed dielectric media, *i.e.* where light moves at different speeds in different regions of the material, and are responsible for the brilliant color in some butterflies, birds, and in chameleons.[10, 11, 12, 13, 14, 15] Certain photonic crystals can exhibit a *photonic band gap*, or PBG, wherein a range of frequencies, commensurate with the length scale of the material, are not transmittable through the material, *i.e.* reflected. In Chapter. IV, we

[i]The quote from Lord Rayleigh, "One's instinct is at first to try and get rid of a discrepancy, but I believe that experience shows such an endeavour to be a mistake. What one ought to do is to magnify a small discrepancy with a view to finding out the explanation," comes to mind.

witnessed a phase transition from the popular photonic target, the diamond structure, to a tetragonal derivative. Based upon previous literature, this break in cubic symmetry should have destroyed the photonic band gap, but our system retained a sizable PBG. [16, 17] This led to an open question that I answer in Chapter VII: what crystal structures will result in a PBG? To answer this, I computed a database of photonic band structures of 2,714 crystal structures using MPB[18] and used crystallography and field analysis to understand the characteristics that lead to a PBG. We found that the design principles most commonly thought of as necessary or sufficient in producing a PBG are neither, and that for every general guideline there is an unexpected exception.[19]

In Chapter VIII, I use the insight gained from Chapter VII to modify structures and observe the response in their PBG. First, I apply a simple design principle to a set of 20 structures and show that this design principle, while successful in some cases, will not produce a PBG for all templates. [20] Lastly, I will show the effects of lattice distortion on some popular PBG target crystals.[21]

In my outlook and conclusions (Chapter IX) I will summarize the content of this dissertation and discuss some general insights and further questions for those pursuing similar research. I have also included appendices detailing the underlying theory of photonic crystals, some recipes for using the signac package, and containing photonic band structures from Chapters VII-VIII.

References

[1] Damasceno, P. F., Engel, M. & Glotzer, S. C. Predictive Self-Assembly of Polyhedra into Complex Structures. *Science* **337**, 453–457 (2012).

[2] Glotzer, S. C. Materials Science: Some Assembly Required. *Science* **306**, 419–420 (2004).

[3] Glotzer, S. C. & Solomon, M. J. Anisotropy of building blocks and their assembly into complex structures. *Nat Mater* **6**, 557–562 (2007).

[4] van Anders, G., Klotsa, D., Ahmed, N. K., Engel, M. & Glotzer, S. C. Understanding shape entropy through local dense packing. *Proceedings of the National Academy of Sciences* **11**, E4812–E4821 (2014).

[5] Dodd, P. M. Inverse Materials Design Employing Self-folding and Extended Ensembles. Dissertation.

[6] Geng, Y., van Anders, G., Dodd, P. M., Dshemuchadse, J. & Glotzer, S. C. Engineering entropy for design. *Submitted* `1712.02471`.

[7] Cersonsky, R. K., van Anders, G., Dodd, P. M. & Glotzer, S. C. Relevance of Packing to Colloidal Self-Assembly. *In Preparation* **115**, 1439–1444 (2018).

[8] Cersonsky, R. K., Dshemuchadse, J., Antonaglia, J., van Anders, G. & Glotzer, S. C. Pressure-Tunable Band Gaps in an Entropic Crystal. *Phys. Rev. Mat.* (2018).

[9] Cersonsky, R. K. *et al.* The Limits of Monoatomic Entropic Colloidal Self-Assembly. *In Preparation* .

[10] Michielsen, K. & Stavenga, D. Gyroid cuticular structures in butterfly wing scales: biological photonic crystals. *Journal of The Royal Society Interface* **5**, 85–94 (2008).

[11] Onslow, H. On a Periodic Structure in Many Insect Scales, and the Cause of Their Iridescent Colours. *Philosophical Transactions of the Royal Society B: Biological Sciences* **211**, 1–74 (1923).

[12] Vukusic, P. & Sambles, J. R. Photonic structures in biology. *Nature* **424**, 852–855 (2003).

[13] Galusha, J. W., Richey, L. R., Gardner, J. S., Cha, J. N. & Bartl, M. H. Discovery of a diamond-based photonic crystal structure in beetle scales. *Physical Review E* **77**, 050904 (2008).

[14] Yin, H. *et al.* Amorphous diamond-structured photonic crystal in the feather barbs of the scarlet macaw. *Proceedings of the National Academy of Sciences* **109**, 10798–10801 (2012).

[15] Teyssier, J., Saenko, S. V., van der Marel, D. & Milinkovitch, M. C. Photonic crystals cause active colour change in chameleons. *Nature Communications* **6**, 6368 (2015).

[16] Joannopoulos, J. *Photonic Crystals: Molding the Flow of Light, 2nd Edition* (Princeton University Press, 2008).

[17] Maldovan, M., Ullal, C. K., Carter, W. C. & Thomas, E. L. Exploring for 3D photonic bandgap structures in the 11 f.c.c. space groups. *Nature Materials* **2**, 664–667 (2003).

[18] Johnson, S. & Joannopoulos, J. Block-iterative frequency-domain methods for Maxwell's equations in a planewave basis. *Optics Express* **8**, 173 (2001).

[19] Cersonsky, R. K., Antonaglia, J. A., Dice, B. D. & Glotzer, S. C. Unexpected Diversity of Three-Dimensional Photonic Crystals. *Submitted* (2019).

[20] Cersonsky, R. K. & Glotzer, S. C. The Effect of Increasing Connectivity in Photonic Band Gap Crystals. *In Preparation* .

[21] Cersonsky, R. K. & Glotzer, S. C. The Effect of Lattice Distortion on Photonic Band Gap Crystals. *In Preparation* .

CHAPTER II

Digital Alchemy for Materials Design

Once I got home, I sulked for a while. All my brilliant plans foiled by thermodynamics. Damn you, Entropy!

– Andy Weir, *The Martian*

Imagine a box full of sugar cubes, which have a decidedly more defined shape than our subway riders in the introduction.[i] Often when you look into the box, they are arranged face to face in a "cubic" pattern. We can understand the origins of the phenomenon by using statistical mechanics. The box defines the volume of the system (V), the number of cubes remains constant (N), as does the temperature (T). The arrangements and orientations of the cubes define individual snapshots or "microstates" of the system. The face-to-face alignment is a feature of the system that we can observe, and can be quantified in the form of an order parameter. The set of microstates that have the given macroscopic properties of N, V, and T make up the macrostate.

The entropy S is defined as $S = k_B \ln(W)$, where k_B is the boltzmann factor and W is the number of microstates that fall under a specific description. In other words, the general configuration which corresponds to the greatest number of microstates will have the highest entropy.[1] Thermodynamics tells us that a system will adopt the configuration that has the

[i] we will ignore that sugar cubes can disintegrate, and a box of sugar cubes is not ergodic so it doesn't follow the laws of thermodynamics

lowest free energy, which in an NVT ensemble is given by $F = U - TS$, where F is the Helmholtz free energy, U is the internal energy, and T is the temperature.

When a system consists of anisotropic nanoparticles, entropic bonds will form due to the preferred alignments between particles.[2, 3, 4, 5, 6] Entropic bonds are effective attractions created by the increase of entropy based upon shape complement. We see this with our sugar cubes – there are more ways to arrange the cubes if the cube faces tend to line up, rather than meet at an angle, so systems of cubes will generally assemble favoring face-to-face arrangements and moving out of this configuration carries some free energy penalty.

We can extend our study of entropic self-assembly beyond the traditional variables of thermodynamics. In DA, the traditional partition function is extended to include particle design aspects, for example particle shape or interparticle interaction.[4]

$$Z = \sum_{\sigma} e^{-\beta\left(H - \sum_i \mu_i N \alpha_i\right)} \tag{2.1}$$

where β is $\frac{1}{k_B T}$, H is the classical hamiltonian, and conjugates μ and α are the *alchemical potential* and *alchemical design parameter*. The subscript i denotes the individual alchemical dimensions, *e.g.* two separate types of truncation.

One can optimize over these extended dimensions and determine the design parameters which will be entropically favorable for a given macrostate. In the following chapters, I will discuss the design parameter of particle shape, which can be sampled using an extended hard particle Monte Carlo (MC) algorithm.[7] In HPMC simulations, internal energy U is given by a piecewise function where $U = \infty$ when the particles are overlapping and $U = 0$ otherwise. In traditional HPMC, you can sample changes in particle position or orientation, accepting changes that do not cause overlaps and rejecting otherwise. With the addition of DA, you can also sample particle shape, either from a defined parameterization or by sampling small changes in vertex position for convex polyhedral particles. A thorough explanation of the algorithmic design and optimization is given in Refs. [4] and [8].

Digital Alchemy can be employed for a variety of applications. From a theoretical per-

spective, exploring these extended ensembles can give insight into the role of these design parameters on the stability and self-assembly of colloidal systems. In Ref. [9], DA was coupled with machine learning to determine the shape features that serve as the best predictors for self-assembly structure. I will employ Digital Alchemy in Chapter III to understand the role of particle packing arguments in predicting hard nanoparticle self-assembly and in Chapter IV to understand a phase transition that can occur across shape space.

From a design perspective, the implementation of Digital Alchemy has the potential to provide design rules to attain a target property or structure. In Ref. [10], DA was applied to multiple target systems to test the robustness of DA for determining particle shape for self-assembly. Furthermore, in Ref. [11], DA was employed to design particles to transition between two target structures at different pressures. The possibilities for DA for design are endless with the innumerable synthesis parameters yet to be explored.[12] However, there are considerations and limitations that must be taken into account when using DA for design of nanoparticle shapes for self-assembly, which I will discuss in Chapter V.

References

[1] Boltzmann, L. *Vorlesungen über Gastheorie* (Johann Ambrosius Barth, Leipzig, 1896).

[2] Frenkel, D. Order through entropy. *Nature Materials* **14**, 9–12 (2014).

[3] Damasceno, P. F., Engel, M. & Glotzer, S. C. Crystalline assemblies and densest packings of a family of truncated tetrahedra and the role of directional entropic forces. *ACS Nano* **6**, 609–614 (2012). 1109.1323.

[4] van Anders, G., Klotsa, D., Karas, A. S., Dodd, P. M. & Glotzer, S. C. Digital Alchemy for Materials Design: Colloids and Beyond. *ACS Nano* **9**, 9542–9553 (2015).

[5] Damasceno, P. F., Engel, M. & Glotzer, S. C. Predictive Self-Assembly of Polyhedra into Complex Structures. *Science* 453–457. 1202.2177.

[6] Agarwal, U. & Escobedo, F. A. Mesophase behaviour of polyhedral particles. *Nature Materials* **10**, 230–235 (2011).

[7] Anderson, J. A., Irrgang, M. E. & Glotzer, S. C. Scalable Metropolis Monte Carlo for simulation of hard shapes. *Computer Physics Communications* **204**, 21 – 30 (2016).

[8] Dodd, P. M. Inverse Materials Design Employing Self-folding and Extended Ensembles. Dissertation.

[9] Geng, Y., Van Anders, G. & Glotzer, S. C. Pre-

dicting colloidal crystals from shapes via inverse design and machine learning 1801.06219v1.

[10] Geng, Y., van Anders, G., Dodd, P. M., Dshemuchadse, J. & Glotzer, S. C. Engineering Entropy for Design. *Submitted* 1712.02471.

[11] Du, C. X., van Anders, G., Newman, R. S. & Glotzer, S. C. Shape-driven solidsolid transitions in colloids. *Proceedings of the National Academy of Sciences* **114**, E3892–E3899 (2017). 1603.00727.

[12] Glotzer, S. C. & Solomon, M. J. Anisotropy of building blocks and their assembly into complex structures. *Nat Mater* **6**, 557–562 (2007).

CHAPTER III

Relevance of Packing to Colloidal Self-Assembly

How wonderful that we have met with a paradox. Now we have some hope of making progress.

– Niels Bohr

The contents of this chapter are taken from "Relevance of Packing to Colloidal Self-Assembly," R. K. Cersonsky, G. van Anders, P. M. Dodd, and S. C. Glotzer. *Proceedings of the National Academy of Sciences* 115.7 (2018).[1]

3.1 Introduction

In this chapter, I will discuss how the use of an extended ensemble approach can be used to understand the distinction between assembly (*i.e.* where order forms at finite pressure) and packing (*i.e.* where order forms under infinite pressure). This question extends from the common correlation of structures formed at finite and infinite pressure. Take for example the rhombic dodecahedron, a nanoparticle shape which will both assemble into and fill space in the cubic close-packed (face-centered cubic, or fcc) structure. However, for other nanoparticle shapes, the finite and infinite pressure structures are not the same. Thus we ask: is packing a causal mechanism to self-assembly?

In 1929, Pauling proposed an answer to this question for atoms by demonstrating remarkable correlations between the sphere packing problem, the study of which dates back

to Sanskrit writings in 499CE [4], and the crystal structures of ionic solids [5]. The packing problem asks: given a set of hard, convex objects, such as spheres, what is the spatial arrangement of those objects that most densely fills space? Pauling argued that crystal structures could be explained by packings of spheres of appropriate atomic radii.

Variants of the packing problem have yielded solutions relevant not only to the rationalization of crystal structures [5], but also in optimal information transmission [6], DNA in cell nuclei [7, 8], blood clots [9], plant morphology [10], and the stacking of oranges in the produce section [11]. Packing rules were used by Frank and Kasper to rationalize complex crystal structures in intermetallic alloys [12, 13], and the molecular packing parameter, a popular geometric measure in surfactant self-assembly, is also based on packing principles [14].

More recently, Pauling's packing principles have been used to rationalize and predict colloidal crystals and nanoparticle superlattice structures by asserting packing as a causal mechanism. For example, packing rules explain many binary nanoparticle superlattice structures obtained from both spherical and nonspherical particle shapes [15, 16, 17]. Packing rules are also successfully used to design DNA-functionalized gold nanospheres [18, 19]. This raises the question: in instances where packing principles can describe observed crystal structures, does that necessarily imply that packing mechanisms are responsible?

For chemically bonded spherical particles, where, e.g. electrostatic forces between oppositely charged colloids or ligand-ligand attraction between functionalized nanoparticles may dominate, packing arguments seem plausible due to the tendency towards close-packed structures. However, when attractive interparticle forces are weak and particles are nonspherical, entropy arising from thermal motion can dominate and invalidate packing rules [20, 21, 22, 23, 24, 25, 26, 27, 28]. Nevertheless, there are examples in both situations where packing rules appear to explain self-assembled structures. Does that imply the crystal *formed* via a packing mechanism? Or is it simply the case that packing rules are useful to rationalize the structure retrospectively, as is the case for molecular packing rules in ordered surfactant

systems?

Statistical thermodynamics tells us that free-energy minimization dictates equilibrium structures. In the case of hard particles, free energy minimization is achieved by structures that self-assemble to maximize entropy except in the limit of very high pressures, where they maximize density [29, 30, 27, 31, 32, 33, 34]. It is these maximum density (or infinite pressure) structures that are invoked when packings are discussed. It is also this limiting case that offers an explanation of why systems of atoms, molecules, or nanoparticles might order through packing.

We can answer our questions by comparing for a given system the self-assembly density, η_{assembly}: the lowest density at which spontaneous self-assembly is observed, with the "packing onset density", η_{pack}: the lowest density at which the system exhibits packing behavior. We argue that packing behavior can occur in a finite pressure system if it follows the same asymptotic, infinite pressure behavior as idealized, mathematical packing. So the question of "when does matter pack?" reduces to searching for this asymptotic behavior. We test for the existence of this asymptotic behavior using generalized Maxwell relations derived in the alchemical ensemble first introduced in Ref. [35]. These generalized Maxwell relations are similar to the usual ones, but defined here in shape space, they can be used to define the packing onset density. One of these generalized relations directly relates the density of ordered structures to the "alchemical potential" μ, defined as the change in the alchemical free energy in response to a change in particle shape:

$$\left(\frac{\partial \mu_i}{\partial P}\right)_{N,T,\alpha_j} = \frac{1}{\eta^2}\left(\frac{\partial \eta}{\partial \alpha_i}\right)_{N,P,T,\alpha_{j\neq i}} \tag{3.1}$$

Here η denotes density, α represents the alchemical (here, shape) variable, P is pressure, N is the total number of particles, and T is temperature responsible for the thermal motion of the particles. The right-hand side of this equation can be computed analytically for systems at the limit of infinite pressure, i.e. densely packed systems, while the left-hand side can be computed via simulations in the isobaric alchemical ensemble [35]. We define η_{pack} as the

lowest density that satisfies this generalized Maxwell relation when the right-hand side is calculated at infinite pressure. To express this mathematically, we define

$$\varepsilon(P) = \left| \left(\frac{\partial \mu_i}{\partial P} \right)_{N,T,\alpha_j} - \lim_{P\to\infty} \frac{1}{\eta^2} \left(\frac{\partial \eta}{\partial \alpha_i} \right)_{N,P,T,\alpha_{j\neq i}} \right| , \tag{3.2}$$

and note that there must exist some P_{pack} such that $\varepsilon(P) \approx 0$ for all $P > P_{\text{pack}}$. The packing density $\eta_{\text{pack}} = \eta(P_{\text{pack}})$.

If we find for some system that $\eta_{\text{assembly}} \approx \eta_{\text{pack}}$, then this indicates that the onset of order is consistent with the existence of a global, dense packing mechanism. Conversely, if $\eta_{\text{assembly}} < \eta_{\text{pack}}$ this indicates that systems spontaneously order before they pack, and the mechanism that drives the order is not packing. However, in this case, it is possible that systems could be quenched to η_{pack} in a disordered state,[36] and then subsequently order by packing. To check for the existence of this possibility, we can compare η_{pack} to random close packing densities η_{rcp}. Random close packing has been defined in Ref. [37] as the density at which the metastable branch in the equation of state corresponding to a disordered system diverges, i.e. the maximum density at which it is possible for the system to be found in a disordered state. If $\eta_{\text{pack}} > \eta_{\text{rcp}}$ then we conclude that a given system cannot be ordered by a packing mechanism, as a system found at a density above $\eta > \eta_{\text{rcp}}$ must already be ordered. We will show below that in all systems we study $\eta_{\text{pack}} > \eta_{\text{rcp}} > \eta_{\text{assembly}}$, indicating that not only is the spontaneous order not driven by packing, but also the systems cannot be ordered by packing.

We also pose the following, related question: When can packing arguments be used for the inverse problem of predicting the thermodynamically optimal particle shape for a particular structure? In other words, when—if ever—is the space-filling shape of a target crystal structure thermodynamically optimal for self-assembling that crystal?

3.2 Methods

3.2.1 Shape Parameterization

Spheric triangle-group families are generated by the intersection of sets of symmetric planes [44]. They are parameterized by α_i parameters between 0 and 1, where α_i encodes the inverse distance of the i$^{\text{th}}$-fold symmetric planes from the particle center. Any α_i parameter can be more readily understood as the truncation of an i$^{\text{th}}$ fold axis of symmetry for the particle shape.

The shape family studied here is generated by intersections of planes perpendicular to the directions of the 4-fold, 2-fold, and 3-fold axes of rotational symmetry for a rhombic dodecahedron, shown in Fig. **3.1A** as red, blue, and grey, respectively, and is therefore named the 423 family of polyhedra (Δ_{423}). Δ_{423} is parameterized by three values, α_2, α_3 and α_4, in the manner described above. Planes perpendicular to the 2-fold direction remain fixed, as does α_2, so discussion is restricted to α_3 and α_4. We restrict our exploration to a shape space with restricted point group symmetry due to (i) geometric reasoning about shape features that lead to optimal thermodynamic behavior (ii) crystal growth processes that determine particle symmetries in nanoscale and synthesis protocols (e.g. [51, 52, 53]).

3.2.2 Simulation Methods

We simulate our shapes in the *alchemical ensemble* using the digital alchemy (DA) framework [35]. DA is a statistical mechanics simulation technique that employs thermodynamic ensembles extended into alchemical (here, particle shape) space by one or more dimensions, allowing fluctuations in the alchemical space or corresponding conjugate alchemical potential(s). This extended ("alchemical") ensemble has the partition function [35]

$$\mathcal{Z} = e^{-\beta F} = \sum_{\sigma} e^{-\beta(H - \sum_i \mu_i N \alpha_i - k\Lambda)} \,, \tag{3.3}$$

where σ labels microstates, H is the Hamiltonian, α_i are the alchemical parameters describing model-specific particle shape attributes (detailed above), μ_i are thermodynamically conjugate alchemical potentials, N is the number of particles, Λ is a structural design criterion that initially keeps the system in an FCC, SC, or BCC crystal structure, and k is the strength of the coupling to Λ.

We employed DA through the simulation method alchemical Monte Carlo (Alch–HPMC) [35]. In Alch–HPMC simulations, μ_i is held constant and particle position and orientation moves are accepted with standard acceptance criteria [54]. Unbiased shape moves (hereafter $\mu_i = 0$) are performed such that all particles in the system change simultaneously from a shape described by alchemical parameter α to a shape described by α', with probability

$$\pi = \min\left(1, \frac{(\det(I_\alpha))^{N/2}}{(\det(I_{\alpha'}))^{N/2}} e^{-\beta(U_\alpha - U_{\alpha'})}\right) \tag{3.4}$$

where U is the potential energy and I is the anisotropic particle moment of inertia tensor. See 3.6.2.1 and [35] for details. For the hard particle systems studied here the potential energy (and ΔU) vanishes for all valid, non-overlapping particle configurations so that $\pi = 0$ for a microstate in which any particles overlap.

We used DA and Alch–HPMC in two ways: (i) we computed the expectation value $\langle \alpha_i \rangle$ as a function of packing fraction in the $NVT\mu_i$ ensemble, and (ii) we performed Alch–HPMC within the $NPT\alpha_i$ ensemble, obtained by Legendre transforming the $NVT\mu_i$ ensemble twice, to calculate the alchemical potential μ_i. All simulations were run with systems of 500 or more particles. See 3.6.2.1 for numerical details and state points for $NVT\mu_i$ and $NPT\alpha_i$ simulations.

In (i), we initialized independent simulations with distinct shapes, taking Λ to be the potential energy function of an Einstein crystal for the target structure (FCC, SC or BCC at some density). We maintained non-zero k during initialization only to ensure the system did not transition out of the target structure. All data were collected on equilibrated systems

with $k = 0$; results were validated by directly computing the free energy [58] for selected state points in $NVT\mu_i$ simulations.

In (ii), simulations were used to evaluate alchemical potentials for space-filling shapes using the thermodynamic relation

$$\mu_i = -\frac{1}{N}\left(\frac{\partial F}{\partial \alpha_i}\right)_{N,\eta,T,\mu_{j\neq i}} \tag{3.5}$$

Our Alch–HPMC algorithm recorded the acceptance ratio for small trial moves from the space-filling shape, without performing such moves. We evaluated (3.5) numerically using the Bennett acceptance ratio method [56], which is described as it applies to the alchemical potential in Ref. [35] and employs a finite differencing method published in Ref. [57].

In this ensemble, we derive a Maxwell relation between alchemical potential μ and packing fraction η:

$$\left(\frac{\partial \mu_i}{\partial P}\right)_{N,T,\alpha_j} = \frac{1}{\eta^2}\left(\frac{\partial \eta}{\partial \alpha_i}\right)_{N,P,T,\alpha_{j\neq i}} \tag{3.6}$$

We used this expression to relate the high pressure asymptotic behavior of the alchemical potential to dense packing surfaces that have been computed in the literature [44].

Specifically, we consider systems to exhibit packing behavior when the slope of the alchemical potential approaches the infinite pressure asymptotic limit of the dense packing surface given by (3.1). Relevant data [44] has been recreated in 3.6.2.1 according to our variable notation.

All simulations were performed with a hard particle Monte Carlo (HPMC) [41] extension to HOOMD-Blue [62, 63], which we further extended to allow Alch–HPMC moves. Runs were partially performed on XSEDE computing resources [64]. The data management for this publication was supported by the signac data management framework [65, 66]. Details on statistical analyses can be found in 3.6.2.1.

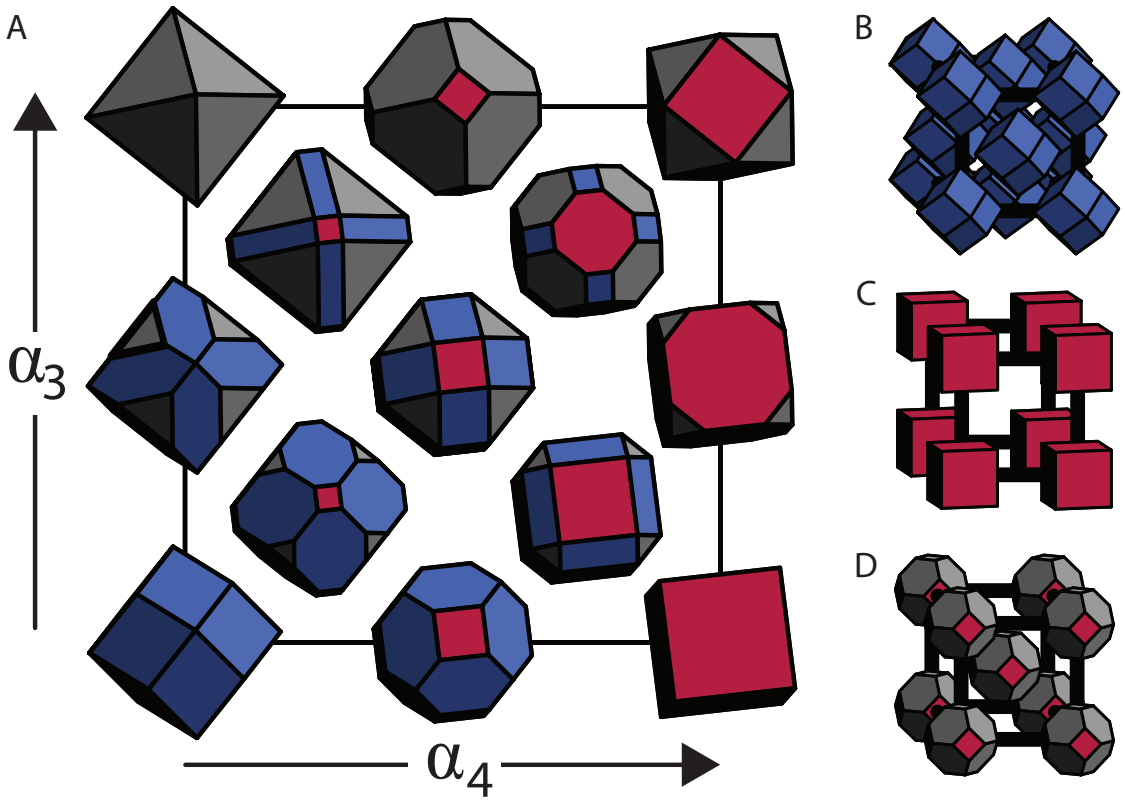

Figure 3.1: **Shape Family and Structures**. We rely on a previously defined parameterization **(A)** which continuously maps two values, α_3 and α_4, to convex polyhedra. This parameterization, here known as the Δ_{423} family, contains the space-filling shapes for **(B)** FCC, **(C)** SC and **(D)** BCC.

3.3 Models

To understand whether packing is driving self-assembly or fundamental to particle design, we study the most likely systems for this to be the case: idealized, perfectly hard, convex shapes. We consider three common structures: face-centered cubic (FCC), simple cubic (SC), and body-centered cubic (BCC) and their corresponding space-filling (Voronoi) shapes: rhombic dodecahedron, cube, and truncated octahedron, shown in Fig. **3.1(B–D)**. It is well known that, for each of these shapes, the corresponding structure is the only thermodynamic equilibrium assembly and the densest packing (at $\eta = 1$ by definition) [38, 39, 21, 20, 40, 30]. Yet, we show that, in each case, the onset of packing behavior occurs at a higher density than η_{rcp}, and therefore the observed structures cannot be ordering via a packing mechanism. Moreover, we show that the space-filling shape for all three structures is never thermodynamically optimal except at $\eta = 1$. From these two findings, we argue that there is only a correlation, not a causal relationship, between the observed thermodynamically assembled structures and those rationalized by packing arguments.

Hard Particle Monte Carlo (HPMC) simulations [41] of the self assembly of FCC, SC, and BCC crystals were carried out for a family of spheric triangle group invariant particle shapes, Δ_{423} (Fig. **3.1A**), which includes each crystal's space-filling particle, as shown in Fig. **3.1(B–D)**, but also, importantly, sets of truncated versions of those shapes that are nearby in shape space. This shape family maps two values, α_3 and α_4 to convex polyhedra, with $\alpha_3, \alpha_4 \in [0, 1]$. The space-filling shapes for FCC, SC, and BCC are defined at $(\alpha_4, \alpha_3) = (0, 0)$ (rhombic dodecahedron), $(\alpha_4, \alpha_3) = (1, 0)$ (cube), and $(\alpha_4, \alpha_3) = (\frac{2}{3}, 1)$ (Archimedean truncated octahedron), respectively.

To compute the packing onset density, we utilized analytical constructions of putative densest packings reported in Ref. [44] for the entire Δ_{423} shape family, giving η as a function of α, to evaluate the second term in (3.2) in the infinite pressure limit. We evaluated the first term in (3.2) at finite pressure using NPTα HPMC simulations at varying pressures. From this, we estimated the lower limit of η_{pack}. We also performed simulations in the NVTμ

ensemble to find the thermodynamically optimal shape for FCC, SC, and BCC as a function of density. Additional details and derivations for the parameterization of the Δ_{423} shape family, extended ensembles, free energy calculations, and the simulations conducted can be found in the 3.2 and in 3.6.2.1.

3.4 Results and Discussion

The computed alchemical potential as a function of pressure is plotted in Fig. **3.2** for **(A)** FCC, **(B)** SC, and **(C)** BCC. Particle shape is fixed to that of the space-filling particle in each case. Asymptotic behavior extracted from analytical results reported in Ref. [44] reveals that in all three cases, asymptotes have zero slope in the limit of infinite pressure and thus $\varepsilon \to 0$ as $\partial\mu_i/\partial P \to 0$, indicated with a horizontal line in each panel. We distinguish the onset of packing behavior in each panel, at $\eta_{\text{pack}} = 0.80$, 0.95, and 0.87 for FCC, SC, and BCC, respectively, as the densities that correspond to the lowest pressures for which $\partial\mu_i/\partial P \approx 0$. In Fig. **3.2**, results represent the first term in (3.2) and dotted lines represent the second term, adapted from analytical results reported in Ref. [44]. We also indicate both the assembly and random close packing densities for FCC, SC, and BCC: $\eta_{\text{assembly}} \approx 0.5$–$0.55$ [42, 21], and $\eta_{\text{rcp}} = 0.76 \pm 0.03$, 0.74 ± 0.03, 0.78 ± 0.03, respectively. We estimated upper limits on η_{rcp} using a procedure established in Ref. [37]. The procedure defined in Ref. [37] determines an upper bound for η_{rcp} from the divergence of the pressure on the metastable branch of the equation of state. The density at which this divergence occurs indicates the maximum density at which a system can be found in a disordered state, and indicates the maximum density to which a system of hard particles can be quenched without order. To estimate upper bounds for η_{rcp} we use generalized equations of state for anisotropic hard particles reported in Ref. [43], and identify the densities at which the equations of state diverge for each particle shape of interest. In every system, $\eta_{\text{pack}} > \eta_{\text{rcp}} > \eta_{\text{assembly}}$. Our results indicate that none of the systems investigated here order via a packing mechanism that occurs throughout space; rather, they indicate only that systems can self-assemble

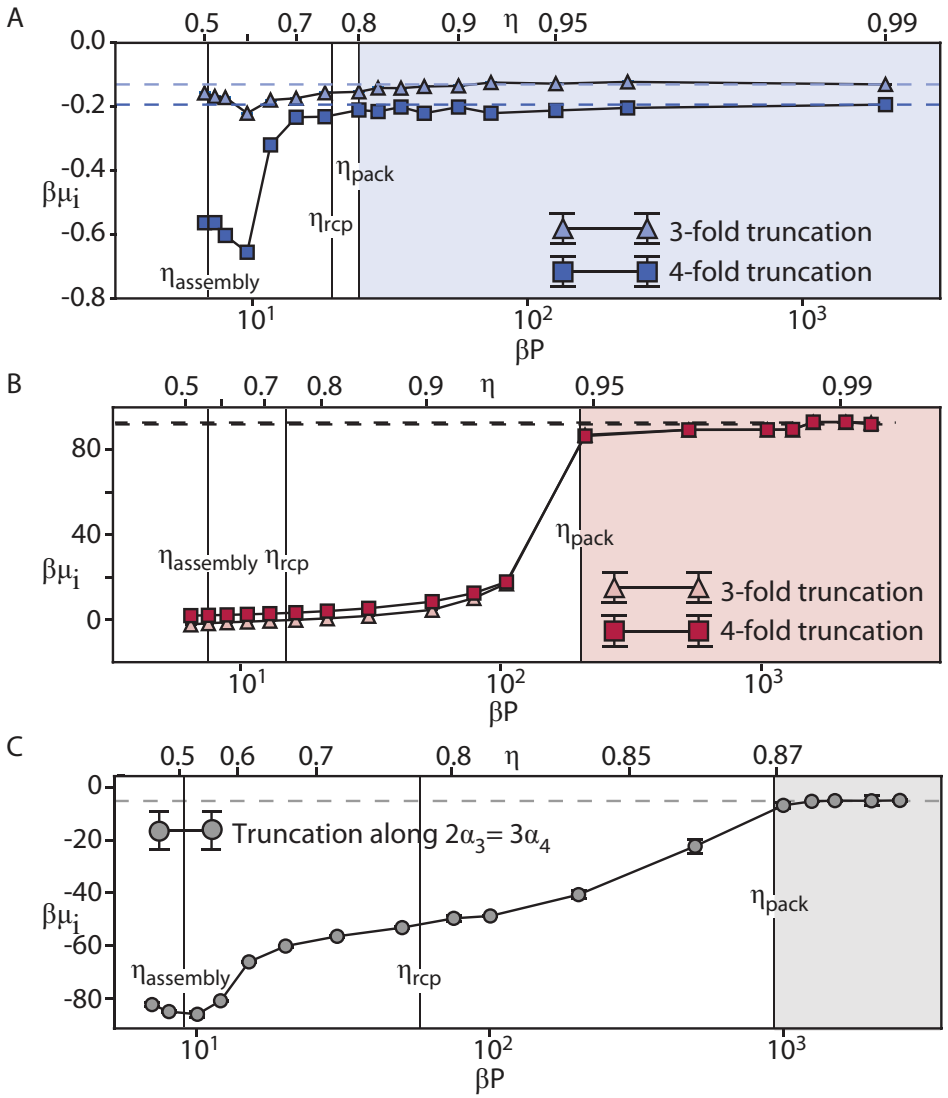

Figure 3.2: **Onset of Asymptotic Packing Behavior in (A) FCC, (B) SC, and (C) BCC.** We utilize the generalized Maxwell relation in (3.1) to extract the onset of asymptotic packing behavior for **(A)** FCC, **(B)** SC, and **(C)** BCC with respect to their space-filing particles. The shaded region in each figure denotes the density-pressure regime where the system is found to be "packing", i.e. where structure formation is driven by packing principles. By comparison, η_{pack} is much higher than either η_{assembly} and η_{rcp} shown for all three systems. For space-filling particles within FCC, SC, and BCC, $\eta_{\text{assembly}} \approx 0.5$–$0.55$ [42, 21], and $\eta_{\text{rcp}} \approx 0.76$, 0.74, and 0.78, respectively, calculated using methods from Refs. [37, 43].

into the same structures that correspond to packings. Note that this does not rule out the possibility that systems could order by packing layer-by-layer through sedimentation, but that mechanism would be fundamentally different from spontaneously packing globally

throughout space.

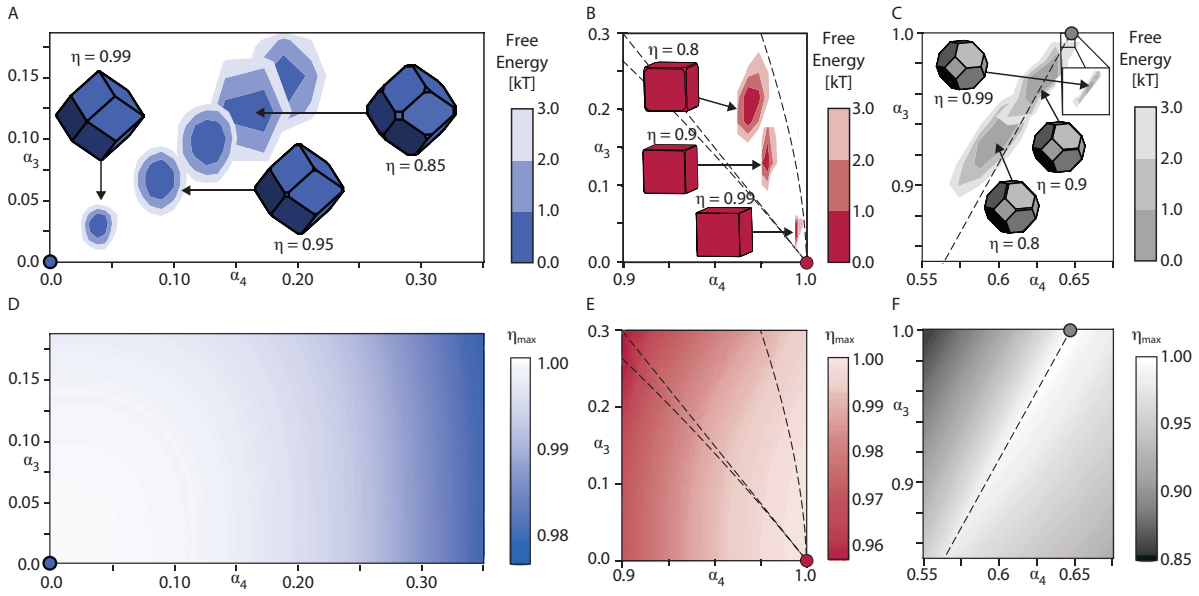

Figure 3.3: **Contour Maps of Free Energy for Δ_{323} in (A) FCC, (B) SC, and (C) BCC** The perfect space-filling (Voronoi) shape, indicated by a filled circle in each figure, is different from any of the optimal shapes determined from simulation, even up to densities of 0.99. **(D–F)** The densest packing surface reported in Ref. [44] in the regions closest to the space-filling shapes for **(D)** FCC, **(E)** SC, and **(F)** BCC The dotted lines in **(B–C), (E–F)** denote discontinuities in the derivative of the dense filling surface.

Moreover, results in Fig. **3.3(A–C)** indicate that packing cannot predict ideal particle shapes for self-assembly because the perfect space-filling shape is never thermodynamically preferred away from $\eta = 1$. Contours plotted in Fig. **3.3(A–C)** indicate the per particle free energy cost of modifying the shape of all colloidal particles while maintaining a fixed target structure. Even at $\eta = 0.99$, there is a tiny difference in shape that, in each case, produces a non-trivial difference in free energy (up to $> 3kT$) between identical crystals comprised of the thermodynamically optimal shape and those comprised of the space-filling shape. However, we do find that features in the global dense packing landscape do *generally* correlate with features found in the optimal particle shapes, as seen by comparing the optimal shape (Fig. **3.3(A–C)**) with the corresponding densest packing landscape from Ref. [44] (recreated in Fig. **3.3(D–F)**). Thus, while densest packing arguments do not predict the optimal shape for self-assembly, the densest packing landscape may provide qualitative guidance in

determining optimal particle shape.

3.5 Conclusions

Although packing arguments are often used successfully in nanoparticle and colloidal assembly, they often fail to explain experimental and computational observations. Our findings demonstrate that the use of packing arguments to rationalize observed structures or design particles to achieve target structures may not be well founded, even when the observed structure is the same as one would get from packing. Because one would expect packing principles—if they do hold—to hold for hard particles, our finding raises the question: is the apparent success of Pauling's packing principles for atomic systems also a spurious correlation? It could also be that the imperfect hardness of atoms and molecules makes them more amenable to dense packing as a mechanism. This counterintuitive possibility would beg for further understanding as the initial reasons for applying packing arguments were based on the existence of steep, sterically repulsive interaction potentials that are nearly hard. Combining the approach for studying sphere packings developed in Ref. [45] with the generalized Maxwell relation (3.1) could give additional insight into the behavior of putative sphere packings more generally. Indeed, for spherical nanoparticles recent work analyzing experiments reported in Ref. [15] has shown that the microscopic details of the particle organization are driven by a complex form of packing involving ligand topology.[46, 47, 48] In addition, in providing new, thermodynamic formulations with which to investigate the packing of hard shapes, we offer alternative approaches to the ubiquitous but notoriously difficult set of general packing problems [49].

Our results, combined with those reported in Ref. [50], indicate that in every case that has so far been investigated there is not a single instance in which a space filling shape is thermodynamically optimal for the self-assembly of its corresponding target structure, at least for hard colloidal particles, as entropic contributions cannot be ignored. Small, stabilizing entropic contributions one might have guessed to be irrelevant can arise from

nearly infinitesimal shape modifications, such as small truncations of vertices or edges of polyhedral nanoparticles. This means the space-filling shape is never thermodynamically optimal for self-assembling its corresponding structure, at least for hard colloidal particles. Our observations suggest that heroic efforts to synthesize perfectly shaped, space-filling particles to achieve the corresponding target structure are unnecessary, and that the entropy gained from slight imperfections may actually facilitate assembly.

3.6 Supplementary Information

3.6.1 Choice of Packing Criterion

If there exists a causal relationship between mathematical dense packing at infinite pressure and the behavior of a thermodynamic system at finite pressure, this implies that any thermodynamic quanity that is evaluated in the finite pressure system must saturate the infinite pressure asymptotic limit for that quantity. Hence, to show that a system's finite pressure behavior is not caused by the existence of the infinite pressure packing limit, it is sufficient to find a thermodynamic quantity that deviates from the infinite pressure asymptotic form. That means that our choice of criterion for distinguishing the onset of packing behavior is not unique nor does it preclude the existence of other thermodynamic quantities that show deviation from asymptotic packing behavior at even lower densities or pressures. Our results for η_{pack} should be interpreted as determining a set of upper bounds.

3.6.2 Detailed Methods

3.6.2.1 Using Trial Alch-MC in $NPT\mu$ to find the Alchemical Potential

The Maxwell relation from the alchemical-isothermal-isobaric ensemble ($NPT\mu$) is

$$\left(\frac{\partial \mu_i}{\partial P}\right)_{N,T,\alpha_j} = -\left(\frac{\partial V}{\partial \alpha_i}\right)_{N,P,T,\alpha_{j\neq i}} \tag{3.7}$$

We use the relationship $V = \frac{N}{\eta}$ to obtain the Maxwell relation reported in the main text.

We explicitly compute the alchemical potential of a system in $NPT\mu_i$ simulations by performing trial Alchemical Monte Carlo (Alch-MC) moves, using the Bennett acceptance ratio to estimate the partial derivative of free energy with respect to a given α [56, 35]:

$$\frac{\partial F}{\partial \alpha} \approx \frac{1}{h} \sum_{\nu} \gamma_\nu F(\alpha + \nu h) \; , \tag{3.8}$$

where h is a finite difference, ν is an index, and γ_v is an appropriate finite differencing coefficient from Ref. [57]. The alchemical potential is then given by:

$$\beta\mu \approx -\frac{1}{Nh} \sum_{\nu} \gamma_\nu \left(\log \frac{p(\alpha + \nu_0 h | \alpha + \nu h)}{p(\alpha + \nu h | \alpha + \nu_0 h)} \right) \; , \tag{3.9}$$

where $p(\alpha + \nu_0 h | \alpha + \nu h)$ and $p(\alpha + \nu h | \alpha + \nu_0 h)$ represent the acceptance ratio of moving from state $\alpha + \nu h$ to state $\alpha + \nu_0 h$, and from state $\alpha + \nu_0 h$ to state $\alpha + \nu h$, respectively [35]. For each simulation, particle shapes were either initialized at the space-filling shape for the crystal and sampled for each nearby $\alpha_\nu = \alpha + \nu h$ (calculating $p(\alpha + \nu h | \alpha + \nu_0 h)$) or initialized at a nearby $\alpha_\nu = \alpha + \nu h$ and sampled for the space-filling shape (calculating $p(\alpha + \nu_0 h | \alpha + \nu h)$).

For rhombic dodecahedra in FCC, we calculated the partial derivatives for three-fold and four-fold truncation with fixed $\alpha_4 = 0.0$ and $\alpha_3 = 0.0$, respectively. We simulated 500 particles with $h = 0.002$ at pressures corresponding to densities between 0.5 and 0.99 for 5×10^6 Monte Carlo sweeps after the target density was reached. For perfect cubes in SC, we calculated the partial derivatives for three-fold and four-fold truncation with fixed $\alpha_4 = 1.0$ and $\alpha_3 = 0.0$, respectively. We simulated 512 particles with h = 0.0002 at pressures corresponding to densities between 0.5 and 0.99 for a minimum of 3×10^7 Monte Carlo sweeps. For BCC, we computed the alchemical potential along $2\alpha_3 = 3\alpha_4$, the maximal ridge of the dense packing landscape surrounding the space-filling shape. At high pressures, truncation along other directions resulted in a sufficiently large free energy increase that then

caused a correspondingly large increase in numerical error. In all structures, five independent replicates with different random seeds were run for each state point. We simulated 686 particles with $h_{\alpha_3} = 0.003$ at pressures corresponding to densities between 0.5 and 0.90 for a minimum of 3×10^7 Monte Carlo sweeps.

3.6.2.2 Using Alch-MC in $NVT\mu$ to find $\langle \alpha_i \rangle$

Verifying Alch-MC with Frenkel-Ladd Integration We first compared the free energy results of these simulations with a modified Frenkel-Ladd free energy integration[59, 58], in which free energy is computed through the integration of the mean-squared displacement of particles tethered to Einstein crystal positions and orientations as the spring constant decreases. Each simulation ran for 2.2×10^7 MC sweeps, decreasing the spring constant by a factor of 10 every 1×10^5 MC sweeps.

We computed the modified Frenkel-Ladd free energy at 2601 evenly spaced shapes in Δ_{423} in FCC, varying α by $\Delta\alpha_{3,4} = 0.02$, with ten replica for each state point. We computed statistical error as the standard deviation over several replicates. Wherever the default orientation was geometrically forbidden, a random orientation was used. We compared Frenkel-Ladd integration and Alch-MC exploration for systems of 32, 256, and 500 particles.

Simulation Details We perform simulations in the alchemical ensemble through the incorporation of an "Alchemical Monte Carlo" (Alch-MC) shape move [35]. Similar to a rotational or translational Monte Carlo (MC) move, the system additionally samples the adjacent shape-states within a given search radius $r = \Delta\alpha_i$ using the Metropolis-Hastings algorithm and acceptance criterion to maintain detailed balance. A thorough discussion of detailed balance in Alch-MC can be found in Ref. [35].

We determine Helmholtz free energy in alchemical space by computing the microstate probabilities from the Monte Carlo results. We conduct Alch-MC simulations with $\mu_i = 0$, and then normalize free energies such that the lowest free energy state has zero free energy.

We compute $\langle \alpha_i \rangle$ via $NVT\mu_i$ simulations that are initialized in an Einstein crystal of the target structure with an external force field Λ tethering particles to their crystal site with springs of strength k = 10^{10} (measured in units of $k_{\mathrm{B}}T/l^2$). Every 5×10^5 Alch-MC sweeps, k is decreased by a factor of 10 until at 5×10^6 Alch-MC sweeps the spring constant was set to 0. This allows the particles to start in their target structure, while not binding them to strict positions or orientations throughout the simulation. Afterward, simulations are run for 12.5×10^6 Alch-MC sweeps to equilibrate, after which data (parameter(s) α_i) is retrieved for another 10×10^6 to 12.5×10^6 Alch-MC sweeps. For every simulation, data is collected after equilibration, at intervals of the autocorrelation time. Autocorrelation times were on the order of $10^3 - 10^5$ Alch-MC sweeps.

Alch-MC simulations were performed for FCC (with 500 particles), SC (with 512 particles) and BCC (with 686 particles) systems. All simulations were initialized with one of 36 evenly spaced shapes, varying by $\Delta\alpha_{3,4} = 0.2$ at densities between 0.5 and 0.99, varying by $\Delta\eta = 0.05$. Those initial simulations that were geometrically forbidden at the given density were discarded, and replicates were run such that a minimum of 10 independent replicates were run for each density and structure. In order to optimize the acceptance of these shape moves, replicates were run with Alch-MC search radius $r = \delta\alpha_i = 0.001 - 0.003$. Each system was run maintaining zero polydispersity, with one particle shape throughout. We visually and quantitatively (through the use of neighbor-averaged bond-order parameter $\bar{Q}_4$ [60, 61]) ensured that simulations did not transition from the target structure.

Additional Data for $\langle \alpha_i \rangle$ Here we provide an extended free energy landscape for FCC, SC, and BCC structures in Δ_{423} for densities from (0.7–0.99). Lower densities resulted in greater deviation from the space-filling shape, as seen in Fig. **3.4**.

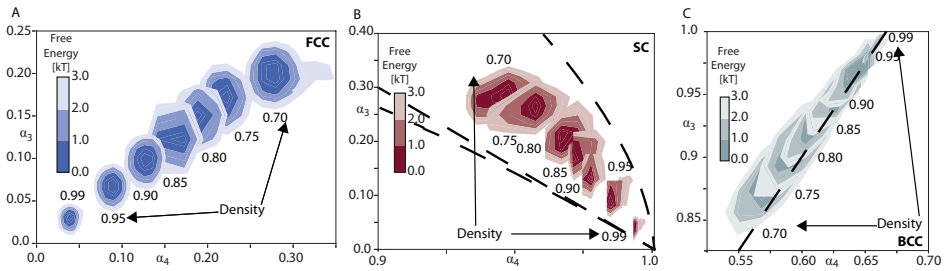

Figure 3.4: **Results from Alch-MC to determine the Optimal Particle Shape for (A) FCC, (B) SC, and (C) BCC.** The space-filling shape does not coincide with the shapes determined from simulation (contour lines), even up to densities of 0.99. In each case, there is non-trivial difference in free energy between the optimal shape and the space-filling shape (on the order of $> 3kT$).

3.6.3 Relevant Data for the Dense Packing Landscapes

Dense packing landscapes for Δ_{423} are reported in Supplemental Materials of Ref. [44]. We include here the relevant equations simplified and in our variable notation as reference for the analysis performed in the main text. In Δ_{423}, there are 17 distinct regions in the dense packing landscape. For each region, the maximum density is given by the ratio of the occupied volume (U) to the unit cell volume (V). The occupied volume is given by

$$U = \begin{cases} 16 - 8\alpha_4^3 - \frac{16}{3}\alpha_3^3 & \alpha_3 + \alpha_4 \leq 1 \\ 16 - 8\alpha_4^3 - \frac{16}{3}\alpha_3^3 + 4\left(\alpha_3 + \alpha_4 - 1\right)^3 & \alpha_3 + \alpha_4 > 1\ . \end{cases} \tag{3.10}$$

The unit cell volume is defined differently for the 17 subregions of Δ_{423}. For this study, the relevant regions are those that achieve perfect packing in any of the three target structures (FCC, SC, BCC). For for FCC the relevant region is 17 (surrounding the rhombic dodecahedron), SC they are 7, 9, 13, and 16 (surrounding perfect cube), and for BCC they are 11

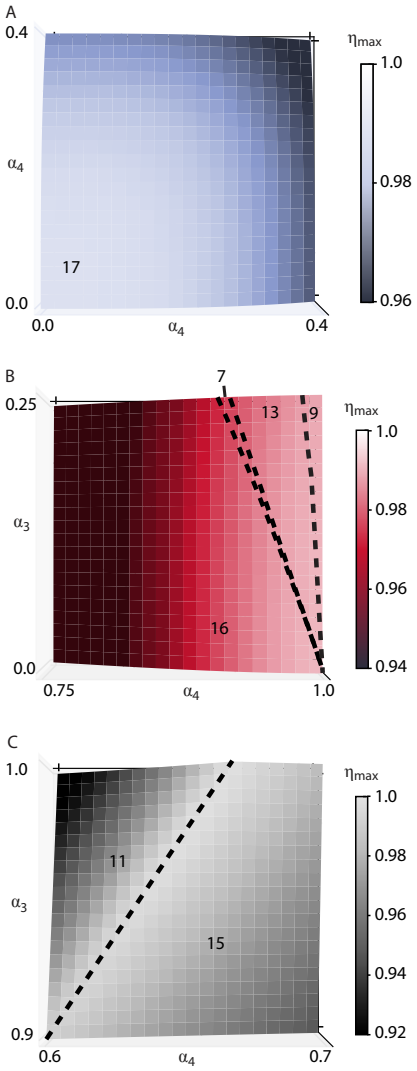

Figure 3.5: **Dense Packing Landscape near the Space-Filling Particles for (A) FCC, (B) SC, and (C) BCC**, generated from (3.12) from Ref. [44]. The dotted lines denote a discontinuity in the derivative of the surface, where two regions meet. Note that the axes are different for each plot. Numbers on each surface correspond to the numbered region of the dense packing landscape.

and 15 (surrounding the Archimedean truncated octahedron). The unit cell volumes are:

$$V_7 = 2\left(-\alpha_3+\alpha_4-3\right)\left(\alpha_4^2+3\alpha_4-\alpha_3\left(\alpha_4-2\right)-6\right) \tag{3.11a}$$

$$V_9 = \frac{8}{27}\left(3-\alpha_3\right)\left(27\alpha_4^2-9\alpha_4\alpha_3-81\alpha_4+\alpha_3^2+12\alpha_3+63\right) \tag{3.11b}$$

$$V_{11} = 2\left(\alpha_3-2\alpha_4+1\right)\left(-2\alpha_3+\alpha_4+4\right)^2 \tag{3.11c}$$

$$V_{13} = 8\alpha_4\left(2\alpha_4-3\right)^2 \tag{3.11d}$$

$$V_{15} = 8\left(\alpha_4-2\right)^2\left(-\alpha_3+\alpha_4+1\right) \tag{3.11e}$$

$$V_{16} = 32-24\alpha_4 \tag{3.11f}$$

$$V_{17} = 16 \tag{3.11g}$$

Combining (3.10) and Eqs. (3.11) gives the maximum densities:

$$\eta_{7,max} = \frac{8-\frac{8}{3}\alpha_3^3-4\alpha_4^3+2\left(\alpha_3+\alpha_4-1\right)^3}{\left(\alpha_4-\alpha_3-3\right)\left(\alpha_4^2+3\alpha_4-\alpha_4\alpha_3+2\alpha_3-6\right)} \tag{3.12a}$$

$$\eta_{9,max} = \frac{-27\left(-\frac{16\alpha_3^3}{3}-8\alpha_4^3+4\left(\alpha_3+\alpha_4-1\right)^3+16\right)}{8\left(\alpha_3-3\right)\left(\alpha_3^2+\left(12-9\alpha_4\right)\alpha_3+9\left(3\alpha_4^2-9\alpha_4+7\right)\right)} \tag{3.12b}$$

$$\eta_{11,max} = \frac{-\frac{8\alpha_3^3}{3}-4\alpha_4^3+2\left(\alpha_3+\alpha_4-1\right)^3+8}{\left(\alpha_3-2\alpha_4+1\right)\left(-2\alpha_3+\alpha_4+4\right)^2} \tag{3.12c}$$

$$\eta_{13,max} = \frac{2-\alpha_4^3-\frac{2}{3}\alpha_3^3-\frac{1}{2}\left(\alpha_3+\alpha_4-1\right)^3}{\alpha_4\left(2\alpha_4-3\right)^2} \tag{3.12d}$$

$$\eta_{15,max} = \frac{-\frac{2\alpha_3^3}{3}-\alpha_4^3+\frac{1}{2}\left(\alpha_3+\alpha_4-1\right)^3+2}{\left(\alpha_4-2\right)^2\left(-\alpha_3+\alpha_4+1\right)} \tag{3.12e}$$

$$\eta_{16,max} = \begin{cases} \frac{2-\alpha_4^3-\frac{2}{3}\alpha_3^3}{4-3\alpha_4} & \alpha_3+\alpha_4 \le 1 \\ \frac{2-\alpha_4^3-\frac{2}{3}\alpha_3^3-4\left(\alpha_3+\alpha_4-1\right)^3}{4-3\alpha_4} & \alpha_3+\alpha_4 > 1 \end{cases} \tag{3.12f}$$

$$\eta_{17,max} = \begin{cases} 1-\frac{1}{2}\alpha_4^3-\frac{1}{3}\alpha_3^3 & \alpha_3+\alpha_4 \le 1 \\ 1-\frac{1}{2}\alpha_4^3-\frac{1}{3}\alpha_3^3-\frac{1}{4}\left(\alpha_3+\alpha_4-1\right)^3 & \alpha_3+\alpha_4 > 1 \end{cases} \tag{3.12g}$$

These are plotted in Fig. **3.5** at $0.0 \leq \alpha_{3,4} \leq 0.4$ (Fig. **3.5A**), $0.0 \leq \alpha_3 \leq 0.25, 0.75 \leq \alpha_4 \leq 1.0$, (Fig. **3.5B**) and $0.9 \leq \alpha_3 \leq 1.0, 0.6 \leq \alpha_4 \leq 0.7$ (Fig. **3.5C**).

References

[1] Cersonsky, R. K., van Anders, G., Dodd, P. M. & Glotzer, S. C. Relevance of Packing to Colloidal Self-Assembly. *Proc. Nat. Acad. Sci.* **115**, 1439–1444 (2018).

[2] Travesset, A. Topological structure prediction in binary nanoparticle superlattices. *Soft Matter* **13**, 147–157 (2017).

[3] Travesset, A. Soft Skyrmions, Spontaneous Valence and Selection Rules in Nanoparticle Superlattices. *ACS Nano* **11**, 5375–5382 (2017).

[4] Thomas C. Hales. A Proof of the Kepler Conjecture. *Annals of Mathematics*, 162(3):1065–1185, 2005.

[5] Linus Pauling. The Principles Determing the Structure of Complex Ionic Crystals. *Journal of the American Chemical Society*, 51(4):1010–1026, 1929.

[6] S. Bischoff and L. Kobbelt. Ellipsoid Decomposition of 3D Models. *Proceedings of the First International Symposium on 3D Data Processing Visualization and Transmission*, pages 480–488., 2002.

[7] T. Cremer and C. Cremer. Chromosome territories, nuclear architecture and gene regulation in mammalian cells. *Nature Reviews Genetics*, 2(4): 292–301, 2001.

[8] D. Marenduzzo, C. Micheletti, and E. Orlandini. Biopolymer organization upon confinement. *Journal of Physics: Condensed Matter*, 22(28): 283102, 2010.

[9] Douglas B. Cines, Tatiana Lebedeva, Chandresekaran Nagaswami, Vincent Hayes, Walter Massefski, Rustem I. Litvinov, Lubica Rauova, Thomas J. Lowery, and John W. Weisel. Clot contraction: compression of erythrocytes into tightly packed polyhedra and redistribution of platelets and fibrin. *Blood*, 123(10):1596–1603, 2014.

[10] Philip Ball. *Shapes: Nature's Patterns: A Tapestry in Three Parts*. Oxford University Press, 2011. ISBN 978-0199604869.

[11] Thomas C. Hales. Historical Overview of the Kepler Conjecture. *Discrete & Computational Geometry*, 36(1):5–20, 2006.

[12] F. C. Frank and J. S. Kasper. Complex alloy structures regarded as sphere packings. I. Definitions and basic principles. *Acta Crystallographica*, 11(3):184–190, 1958.

[13] F. C. Frank and J. S. Kasper. Complex alloy structures regarded as sphere packings. II. Analysis and classification of representative structures. *Acta Crystallographica*, 12(7):483–499, 1959.

[14] Jacob N. Israelachvili, D. John Mitchell, and Barry W. Ninham. Theory of self-assembly of hydrocarbon amphiphiles into micelles and bilayers.

Journal of the Chemical Society, Faraday Transactions 2, 72(0):1525, 1976.

[15] Michael A. Boles and Dmitri V. Talapin. Self-Assembly of Tetrahedral CdSe Nanocrystals: Effective "Patchiness" via Anisotropic Steric Interaction. *Journal of the American Chemical Society*, 136(16):5868–5871, 2014.

[16] Kyung-Sang Cho, Dmitri V. Talapin, Wolfgang Gaschler, and Christopher B. Murray. Designing PbSe Nanowires and Nanorings through Oriented Attachment of Nanoparticles. *Journal of the American Chemical Society*, 127(19):7140–7147, 2005.

[17] Elena V. Shevchenko, Dmitri V. Talapin, Nicholas A. Kotov, Stephen O'Brien, and Christopher B. Murray. Structural diversity in binary nanoparticle superlattices. *Nature*, 439 (7072):55–59, 2006.

[18] Matthew R. Jones, Robert J. Macfarlane, Byeongdu Lee, Jian Zhang, Kaylie L. Young, Andrew J. Senesi, and Chad A. Mirkin. DNA-nanoparticle superlattices formed from anisotropic building blocks. *Nature Materials*, 9 (11):913–917, 2010.

[19] Robert J. Macfarlane, Matthew R. Jones, Andrew J. Senesi, Kaylie L. Young, Byeongdu Lee, Jinsong Wu, and Chad A. Mirkin. Establishing the Design Rules for DNA-Mediated Programmable Colloidal Crystallization. *Angewandte Chemie International Edition*, 49(27): 4589–4592, 2010.

[20] Pablo F. Damasceno, Michael Engel, and Sharon C. Glotzer. Predictive Self-Assembly of Polyhedra into Complex Structures. *Science*, 337 (6093):453–457, 2012.

[21] Frank Smallenburg, Laura Filion, Matthieu Marechal, and Marjolein Dijkstra. Vacancy-stabilized crystalline order in hard cubes. *Proceedings of the National Academy of Sciences*, 109 (44):17886–17890, 2012.

[22] Wiel H. Evers, Bart De Nijs, Laura Filion, Sonja Castillo, Marjolein Dijkstra, and Daniel Vanmaekelbergh. Entropy-Driven Formation of Binary Semiconductor-Nanocrystal Superlattices. *Nano Letters*, 10(10):4235–4241, 2010.

[23] Joost de Graaf, René van Roij, and Marjolein Dijkstra. Dense Regular Packings of Irregular Nonconvex Particles. *Physical Review Letters*, 107(15):155501, 2011.

[24] Laura Rossi, Vishal Soni, Douglas J. Ashton, David J. Pine, Albert P. Philipse, Paul M. Chaikin, Marjolein Dijkstra, Stefano Sacanna, and William T M. Irvine. Shape-sensitive crystallization in colloidal superball fluids. *Proceedings of the National Academy of Sciences*, 112 (17):5286–5290, 2015.

[25] Carlos Avendaño and Fernando A. Escobedo. Packing, entropic patchiness, and self-assembly of non-convex colloidal particles: A simulation perspective. *Current Opinion in Colloid & Interface Science*, 30:62–69, 2017.

[26] Carlos Avendaño and Fernando A. Escobedo. Phase behavior of rounded hard-squares. *Soft Matter*, 8(17):4675, 2012.

[27] Fernando A. Escobedo. Engineering entropy in soft matter: the bad, the ugly and the good. *Soft*

Matter, 10(42):8388–8400, 2014.

[28] G. Odriozola, F. Jiménez-Ángeles, and M. Lozada-Cassou. Entropy driven key-lock assembly. *The Journal of Chemical Physics*, 129 (11):111101, 2008.

[29] Greg van Anders, Daphne Klotsa, N. Khalid Ahmed, Michael Engel, and Sharon C. Glotzer. Understanding shape entropy through local dense packing. *Proceedings of the National Academy of Sciences*, 11(45):E4812–E4821, 2014.

[30] Greg van Anders, N. Khalid Ahmed, Ross Smith, Michael Engel, and Sharon C. Glotzer. Entropically Patchy Particles: Engineering Valence through Shape Entropy. *ACS Nano*, 8(1): 931–940, 2014.

[31] Daan Frenkel. Entropy-driven phase transitions. *Physica A: Statistical Mechanics and its Applications*, 263(1-4):26–38, 1999.

[32] Edward Barry and Zvonimir Dogic. Entropy driven self-assembly of nonamphiphilic colloidal membranes. *Proceedings of the National Academy of Sciences*, 107(23):10348–10353, 2010.

[33] Vinothan N. Manoharan. Colloidal matter: Packing, geometry, and entropy. *Science*, 349 (6251):1253751–1253751, 2015.

[34] Daan Frenkel. Order through entropy. *Nature Materials*, 14(1):9–12, 2014.

[35] Greg van Anders, Daphne Klotsa, Andrew S. Karas, Paul M. Dodd, and Sharon C. Glotzer. Digital Alchemy for Materials Design: Colloids and Beyond. *ACS Nano*, 9(10):9542–9553, 2015.

[36] Eric R. Weeks, J. C. Crocker, Andrew C. Levitt, Andrew Schofield, and D. A. Weitz. Three-dimensional direct imaging of structural relaxation near the colloidal glass transition. *Science*, 287(5453):627–631, 2000. ISSN 0036-8075.

[37] Randall D. Kamien and Andrea J. Liu. Why is Random Close Packing Reproducible? *Physical Review Letters*, 99(15):155501, 2007.

[38] Pablo F. Damasceno, Michael Engel, and Sharon C. Glotzer. Structural diversity and the role of particle shape and dense fluid behavior in assemblies of hard polyhedra. *arXiv*, 2012.

[39] Ran Ni, Anjan Prasad Gantapara, Joost de Graaf, René van Roij, and Marjolein Dijkstra. Phase diagram of colloidal hard superballs: from cubes via spheres to octahedra. *Soft Matter*, 8 (34):8826, 2012.

[40] Anjan P. Gantapara, Joost de Graaf, René van Roij, and Marjolein Dijkstra. Phase Diagram and Structural Diversity of a Family of Truncated Cubes: Degenerate Close-Packed Structures and Vacancy-Rich States. *Physical Review Letters*, 111(1):015501, 2013.

[41] Joshua A. Anderson, M. Eric Irrgang, and Sharon C. Glotzer. Scalable Metropolis Monte Carlo for simulation of hard shapes. *Computer Physics Communications*, 204:21 – 30, 2016.

[42] Umang Agarwal and Fernando A. Escobedo. Mesophase behaviour of polyhedral particles. *Nature Materials*, 10(3):230–235, 2011.

[43] Yuhua Song and E. A. Mason. Equation of state for a fluid of hard convex bodies in any number of dimensions. *Physical Review A*, 41(6):3121–3124, 1990.

[44] Elizabeth R. Chen, Daphne Klotsa, Michael En-

gel, Pablo F. Damasceno, and Sharon C. Glotzer. Complexity in surfaces of densest packings for families of polyhedra. *Phys. Rev. X*, 4:11024, 2014.

[45] Yoav Kallus. The 3-ball is a local pessimum for packing. *Advances in Mathematics*, 264:355–370, 2014.

[46] A. Travesset. Topological structure prediction in binary nanoparticle superlattices. *Soft Matter*, 13:147–157, 2017.

[47] Alex Travesset. Soft skyrmions, spontaneous valence and selection rules in nanoparticle superlattices. *ACS Nano*, 11(6):5375–5382, 2017.

[48] Curt Waltmann, Nathan Horst, and Alex Travesset. Capping ligand vortices as "atomic orbitals" in nanocrystal self-assembly. *ACS Nano*, 11(11):11273–11282, 2017.

[49] Jeffrey C. Lagarias and Chuanming Zong. Mysteries in Packing Regular Tetrahedra. *Notices of the American Mathematical Society*, 59(11):1392, 2012.

[50] Yina Geng, Greg van Anders, Paul M. Dodd, Julia Dshemuchadse, and Sharon C. Glotzer. Engineering entropy for the inverse design of colloidal crystals from hard shapes. *arXiv:1712.02471*, 2017.

[51] Yugang Sun and Younan Xia. Shape-Controlled Synthesis of Gold and Silver Nanoparticles. *Science*, 298(5601):2176–2179, 2002.

[52] Tapan K. Sau and Andrey L. Rogach. Nonspherical Noble Metal Nanoparticles: Colloid-Chemical Synthesis and Morphology Control. *Adv. Mater.*, 22(16):1781–1804, 2010.

[53] Younan Xia, Yujie Xiong, Byungkwon Lim, and Sara E. Skrabalak. Shape-Controlled Synthesis of Metal Nanocrystals: Simple Chemistry Meets Complex Physics? *Angewandte Chemie International Edition*, 48(1):60–103, 2009.

[54] Daan Frenkel and Berend Smit. *Understanding molecular simulation: from algorithms to applications*. Elsevier, 2002.

[58] Daan Frenkel and Anthony J C. Ladd. New Monte Carlo method to compute the free energy of arbitrary solids. Application to the fcc and hcp phases of hard spheres. *The Journal of Chemical Physics*, 81(7):3188–3193, 1984.

[56] Charles H. Bennett. Efficient Estimation of Free Energy Differences from Monte Carlo Data. *J. Comp. Phys.*, 22(2):245–268, 1976.

[57] Bengt Fornberg. Generation of finite difference formulas on arbitrarily spaced grids. *Mathematics of Computation*, 51(184):699–699, 1988.

[58] Daan Frenkel and Anthony J C. Ladd. New Monte Carlo method to compute the free energy of arbitrary solids. Application to the fcc and hcp phases of hard spheres. *The Journal of Chemical Physics*, 81(7):3188–3193, 1984.

[59] Amir Haji-Akbari, Michael Engel and Sharon C. Glotzer Phase diagram of hard tetrahedra. *AIP*, 2011(135):194101, 2011.

[60] Wolfgang Lechner and Christoph Dellago Accurate determination of crystal structures based on averaged local bond order parameters. *J. Chem. Phys.*, 129(11):11, 2008.

[61] Du, C. X., van Anders, G., Newman, R. S. & Glotzer, S. C. Shape-driven solidsolid tran-

sitions in colloids. *Proceedings of the National Academy of Sciences* **114**, E3892–E3899 (2017). 1603.00727.

[62] Joshua A. Anderson, Chris D. Lorenz, and A. Travesset. General purpose molecular dynamics simulations fully implemented on graphics processing units. *Journal of Computational Physics*, 227(10):5342–5359, 2008.

[63] Joshua A. Anderson and Sharon C. Glotzer. The development and expansion of HOOMD-blue through six years of GPU proliferation. *arXiv*, page 1308.5587, 2013.

[64] John Towns, Timothy Cockerill, Maytal Dahan, Ian Foster, Kelly Gaither, Andrew Grimshaw, Victor Hazlewood, Scott Lathrop, Dave Lifka, Gregory D. Peterson, Ralph Roskies, J. Ray Scott, and Nancy Wilkens-Diehr. XSEDE: Accelerating Scientific Discovery. *Computing in Science & Engineering*, 16(5):62–74, 2014.

[65] Carl S. Adorf, Paul M. Dodd, and Sharon C. Glotzer. signac - A Simple Data Management Framework. abs/1611.0, 2016. URL http://arxiv.org/abs/1611.03543.

[66] Carl S. Adorf and Paul M. Dodd. csadorf/signac: v0.7.0., 2016.

CHAPTER IV

Pressure-Tunable Photonic Band Gaps in an Entropic Colloidal Crystal

There is no cross-word puzzle that can compare in interest with the practical working out of a problem in Physics or Chemistry. You may say that to work at an amusing thing is not a very noble task. I can only answer that it makes a very happy life and I think that, if we can increase the number of human beings who find happiness in their work, we shall have gone some way towards creating a better state of things.

– William H. Bragg

The contents of this chapter are taken from "Pressure-Tunable Band Gaps in an Entropic Crystal.", R.K. Cersonsky, J. D. Dshemuchadse, J. Antonaglia, G. van Anders, and S. C. Glotzer, *Phys. Rev. Mat.* (2018).[1]

4.1 Introduction

In the century since it was first characterized in 1913 by W. H. and W. L. Bragg, the diamond structure has been a popular focus of materials research [2]. Diamond-type materials, including the diatomic equivalent, zincblende, exhibit extraordinary properties, such as high hardness, high thermal conductivity, and a high refractive index at room temperature. Also known for its opticalpress-properties, diamond was the first structure calculated to have a

photonic band gap, meaning it reflects all electromagnetic waves over a range of wavelengths that depends on the interparticle distance. Ho, *et al.* [3] showed that a diamond structure of overlapping silicon spheres arranged at a filling fraction of 34% reflects wavelengths a factor of roughly 2.4 times the crystal lattice parameter, at any length scale (e.g., a lattice parameter of 100 nm would result in the reflection of UV light). Crystals with photonic band gaps in the visible range can be achieved by using colloidal particles with sub-micron to micron diameters and are commonly a target for self-assembly within the colloids community [4, 5, 6, 7].

The unique properties of diamond-structured materials provide an interesting target for reconfigurable photonic materials; that is, a material designed to switch to and from a diamond-like structure with its concomitant properties. There is precedent for reconfigurable diamond-structured materials in elemental structures: Si, Ge, and Sn each form the diamond structure at ambient pressure and transition to a tetragonal metallic phase, β-Sn, at higher pressures [8, 9].

This inspires the question: can we design a photonic crystal that reflects wavelengths in the *visible* range of the electromagnetic spectrum, and whose structure and thus band gap are reconfigurable? Such target criteria lead us to consider colloidal crystals, where reconfigurability has been demonstrated [10, 11] and where the self-assembly of the diamond structure is possible [12, 13, 14, 15, 16, 17, 18]. Core-shell colloidal crystals offer the further possibility of operating on two separate length scales, that of the high dielectric core and that of the shell. Because the size and shape of the core is independent of the size and shape of the particle in which it is imbedded, the photonic properties are independently tunable from the length scale that is relevant for assembly.

Particle shape adds anisotropy dimensions ([19]) that allow one to assemble and transition between a diversity of crystal structures not easily achievable with spherical particles [20] and colloidal polyhedra have now been realized for a variety of materials [21, 22, 23, 24, 25, 26, 19]. Moreover, it has been demonstrated that directional entropic forces [27, 14] arising

from the statistical tendency for particle facets to align are more than sufficient to produce crystal structures of extraordinary complexity and diversity [28, 29, 30], including diamond [14]. Polyhedral nanoparticles have been synthesized with spherical and nonspherical cores [31, 32, 33, 34], comprised of materials such as silica, silver, gold, or palladium.

Here we report a reversible structural phase transition with photonic implications for a simulated system of hard core-shell polyhedra with tetrahedral symmetry ordering via directional entropic forces into a diamond structure. The transition is driven by pressure, and leads from the well-known cubic diamond structure to a tetragonal diamond derivative (TDD) distinct from the aforementioned β-Sn. The transition provides a reversible reconfiguration process for a new target for synthesis: a photonic colloidal material that can be switched among as many as four possible photonic states, each of which permits a different frequency range of light in the infrared or visible regimes. Additionally, by noting that all three phases — cubic diamond, TDD, and β-Sn — are related through scaling along a major axis, we gain insight into the mechanism driving high-pressure transitions between diamond and β-Sn in atomic systems.

4.2 Methods

We conduct our study in the alchemical thermodynamic ensemble, implemented through the Digital Alchemy framework [35]. This ensemble is an extension of the canonical ensemble that treats particle shape, parametrized by a set of values α_i, as a thermodynamic state variable. Each α_i parameter has an associated conjugate *alchemical potential* μ_i. The $NVT\mu$ ensemble, in which each α_i is allowed to fluctuate, is defined with the partition function

$$Z = \sum_{\sigma} e^{-\beta\left(H - \sum_i \mu_i N \alpha_i\right)}. \tag{4.1}$$

Here, $\sum_\sigma$ denotes a sum over all microstates σ and shape parameter values α_i. The variables α_i and μ_i are related to derivatives of F, the thermodynamic potential for the

ensemble:

$$\mu_i = \frac{1}{N}\left(\frac{\partial F}{\partial \alpha_i}\right)_{N,\phi,T,\alpha_{j\neq i}} \tag{4.2}$$

and

$$\alpha_i = \frac{1}{N}\left(\frac{\partial F}{\partial \mu_i}\right)_{N,\phi,T,\mu_{j\neq i}}, \tag{4.3}$$

where

$$F = -k_B T \log\left(Z\right). \tag{4.4}$$

For all simulations, we used the hard-particle Monte Carlo sampling method of the HOOMD-blue simulation toolkit [36, 37]. We conducted alchemical hard particle Monte Carlo (Alch-HPMC) simulations within the $NVT\alpha$, $NPT\alpha$, and $NVT\mu$ ensembles. Further details on Alch-HPMC can be found in Refs. [35, 38]. All simulations were run so that each particle's shape is specified by one α and every particle in the system changes identically and simultaneously as α changes.

4.2.1 Simulations in $NVT\alpha$

In the $NVT\alpha$ ensemble, we simulated systems of 1728 particles with unit volume, with state points from $\alpha \in [0.3, 0.5]$ with $\Delta\alpha = 0.01$ initialized in the diamond structure at $\phi = 0.55$, the known assembly structure for these shapes [14]. These simulations were then incrementally compressed to a target density of $\phi = 0.55$–0.95 with $\Delta\phi = 0.05$, allowing for the box aspect ratio to change as a separate MC move while maintaining constant box volume. For regions of interest, additional state points were run at $\Delta\phi = 0.025$. The box aspect ratio search radius was set to 0.01 per sweep. Simulations were then run for 1.1×10^7–2.4×10^7 MC sweeps, until equilibrated. A minimum of four replicas were run for each state point.

Similar simulations were run by initializing at the densest packing of the shape family

in both diamond and its tetragonal derivative. The box was expanded isotropically to a target density, then simulated using MC with box moves for 1.1×10^7–2.4×10^7 sweeps. These simulations were run with the same parameters as systems initialized in the diamond assembly phase.

4.2.1.1 Analysis

Each frame of a simulation was separated into crystal grains using in-house environment-matching algorithms (E. G. Teich, *private communication*) analyzing the bond angles of each particle with its nearest neighbors and then separating the particles into groups based upon these arrangements. For some simulations, compression and the reduction in symmetry caused the formation of multiple grains within the assembly, and these state points were removed from the results to avoid distorting the influence of these simulation data. We used in-house software *injavis* to determine the 8-particle unit cells of all simulation runs. We used the signac framework for all data management [39].

4.2.2 Simulations in $NPT\alpha$

We simulated systems of 512 particles with unit volume and constant shape in an $NPT\alpha$ ensemble to generate an equation of state for the given transformation at 35 unitless pressures ($= \frac{PV}{k_B T}$ with unit volume) between $\beta P = 5$–100 and $\alpha = 0.4$–0.5, with $\Delta\alpha = 0.01$. Additional state points were run for regions of interest and for $\alpha = 0.5$. Systems were initialized in the tetragonal diamond derivative ($c/a = \sqrt{0.4}$) at maximum density or in their assembled diamond phase at the assembly density, and held at target pressure to equilibrate over 1×10^7–4×10^7 MC sweeps. Simulations for shapes of interest ($\alpha = 0.5, P = 9.8$–10.0) were run with longer simulations and additional state points (up to 10). A minimum of three independent simulations were run for all other state points.

4.2.3 Simulations in $NVT\mu$

Alch-HPMC simulations were run in the $NVT\mu$ ensemble to find the thermodynamically preferred structure and particle shape. Systems of 512 particles were initialized with $\alpha = \frac{1}{3}$ and $\phi = 0.6$ and allowed to equilibrate in shape space. The particles were then compressed isotropically to a target $\phi \in [0.70, 0.95]$ with $\Delta\phi = 0.05$, and allowed to equilibrate using MC box moves and subsequently within shape space. This step was repeated until both structure and shape were at equilibrium. Systems were then decompressed to $\phi = 0.60$ and allowed once again to equilibrate to check for reversibility.

4.2.3.1 Potential of Mean Force and Torque (PMFT)

For the data shown, we averaged the PMFT values for 150 frames from earlier $NVT\mu$ simulations at a range of ϕ values. The PMFT results were visualized using the Python package *mayavi*.

4.2.4 Calculation of Photonic Band Structure

We computed the photonic band structure for different forms of tetragonal diamond using MIT Photonic Bands (MPB) [40]. This package computes the eigenmodes of Maxwell's equations through conjugate-gradient minimization of the block Rayleigh quotient in a plane-wave basis [40].

We computed the size and location of all photonic band gaps for all structures computed in $NVT\alpha$ simulations in Fig. 4.3**(b)**, including both c/a ratio and lattice vector magnitude (to reflect density). For radius we took the insphere of the respective polyhedra in Δ_{323} and for the dielectric constant we chose 11.56, that of a theoretical silicon-type material and assume the material to be lossless, as has been done in similar studies [41, 42, 43] Actual silicon would not make a good candidate material for photonic crystals in the visible range, as it has high absorbance in this range. We computed the irreducible Brillouin zone using the package *SeeK-path* [44], an open-source k-space path finder.

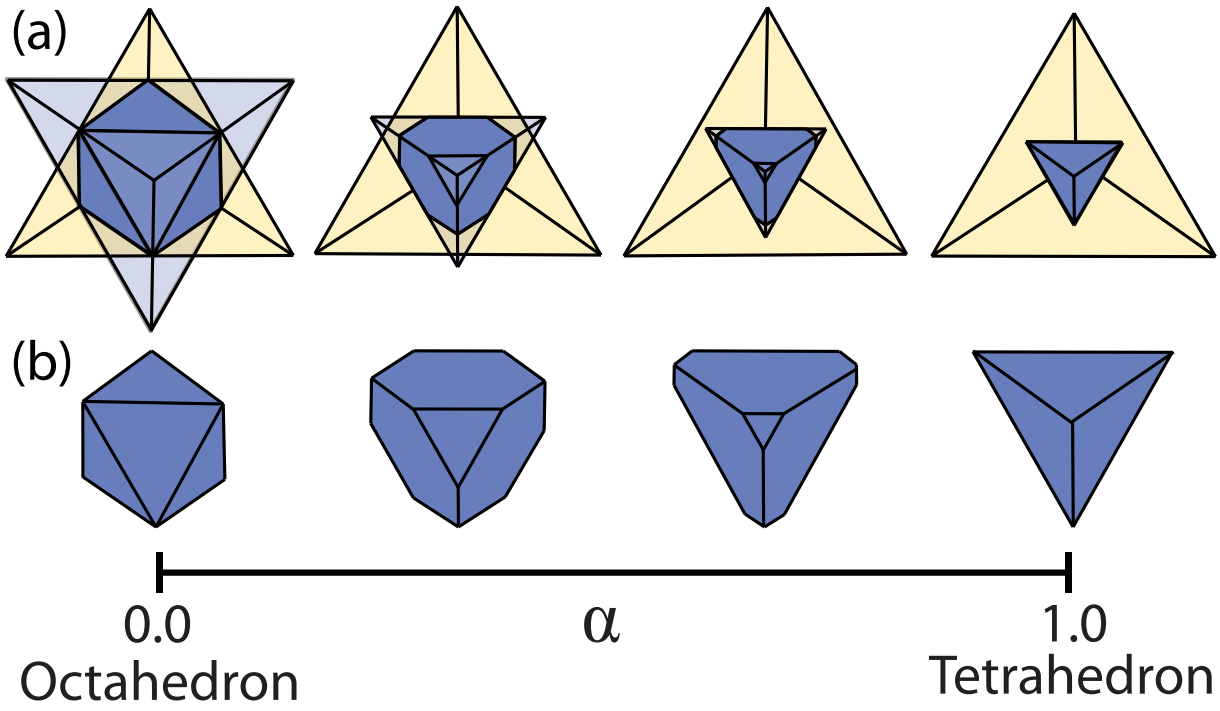

Figure 4.1: **The Δ_{323} Shape Parameterization. (a–b)** The Δ_{323} shape family, ranging from an octahedron ($\alpha = 0.0$) to a tetrahedron ($\alpha = 1.0$). The intersection of planes at parameterized distances shown in **(a)** generate the resulting shapes in **(b)**. All shapes are scaled to unit volume in simulations.

Resulting photonic band gaps were normalized by the mid-gap frequency, consistent with convention.

4.3 Model and Structural Comparison

To represent the particle shells, we simulated a family of convex shapes with tetrahedral symmetry (here denoted Δ_{323}) [45] using the Digital Alchemy (DA) framework [35]. In DA, a design parameter is introduced as a thermodynamic state variable, which defines an extended *alchemical ensemble* in which either the design parameter, the *alchemical variable*, or its conjugate, the *alchemical potential* can fluctuate while the other remains fixed.

The Δ_{323} family is constructed through the intersection of planes arranged tetrahedrally around the particle center, parametrized by α_3, which can be viewed as the truncation along

a set of three-fold axes, in the following called α for brevity. The shape family is shown in Fig. 4.1; all shapes are scaled to unit volume. Hard shapes with $\alpha = 0.3$–0.5 assemble into diamond at packing fraction (synonymous with filling fraction) $\phi = 0.5$–0.6 [14]. When these assembled crystals are compressed to higher packing fractions, we observe a transition to a tetragonal diamond derivative (TDD) structure. Because this transition occurs via local particle rearrangement only, it is easily achievable at higher densities, where self-assembly from a fluid may be thwarted by an intervening glass transition.

These two crystal structures, diamond and TDD, differ in two major respects: the aspect ratio of the unit cell and the particle orientations. The TDD structure is defined by lattice vectors $\vec{a}_1 = [a, 0, 0]$, $\vec{a}_2 = [0, a, 0]$, $\vec{c} = [0, 0, c]$, with particles situated at positions 0,0,0 and $\frac{1}{4}, \frac{1}{4}, \frac{1}{4}$ (in fractional coordinates) on a face-centered lattice (i.e., with centering vectors $[0, 0, 0]$, $[\frac{1}{2}, \frac{1}{2}, 0]$, $[\frac{1}{2}, 0, \frac{1}{2}]$, and $[0, \frac{1}{2}, \frac{1}{2}]$). For ease of comparison, tetragonal unit cells will be expressed in a non-standard face-centered setting $tF8$, such that all unit cells can be described in terms of c/a for a face-centered unit cell (containing 8 particles), where $c/a = 1$ for the face-centered cubic unit cell of diamond ($cF8$-C). Shapes from the Δ_{323} family densely pack into TDD with $c/a = \sqrt{0.4} \approx 0.6325$ (which is also $c/a_{\min}$ for Δ_{323}) and $\alpha = 0.5$.

The β-Sn structure (referred to by its Pearson symbol $tI4$-Sn) can be defined as a TDD structure at $c/a \approx 0.3859$ (given a $tF8$ unit cell). $tI4$-Sn and TDD structures in Δ_{323} both have space group $I4_1/amd$ and Wyckoff position $4c$ $0, 0, 0$, albeit at different ratios of c/a. TDD structures with $c/a \geq \sqrt{0.4}$ have tetrahedral coordination (coordination number 4), whereas $tI4$-Sn has two additional particles adjacent to the first neighbor shell, resulting in an octahedral coordination (coordination number 6). Other TDD phases have been found in studies of atomic structures although with aspect ratios near that of $tI4$-Sn or high-pressure $tI4$-Cs, which has $c/a > 1$ [46, 47].

Snapshots of the two structures observed in our simulations are shown in Fig. 5.2**(a–d)**, with their radial distribution function (RDF) peaks in Fig. 5.2**(e)** [i] .

[i] See Supplemental Material at [] for structure diagrams comparing diamond and TDD ($c/a = \sqrt{0.4}$) with $tI4$-Sn, a description of alchemical hard particle Monte Carlo (Alch-HPMC), plots of photonic band gap

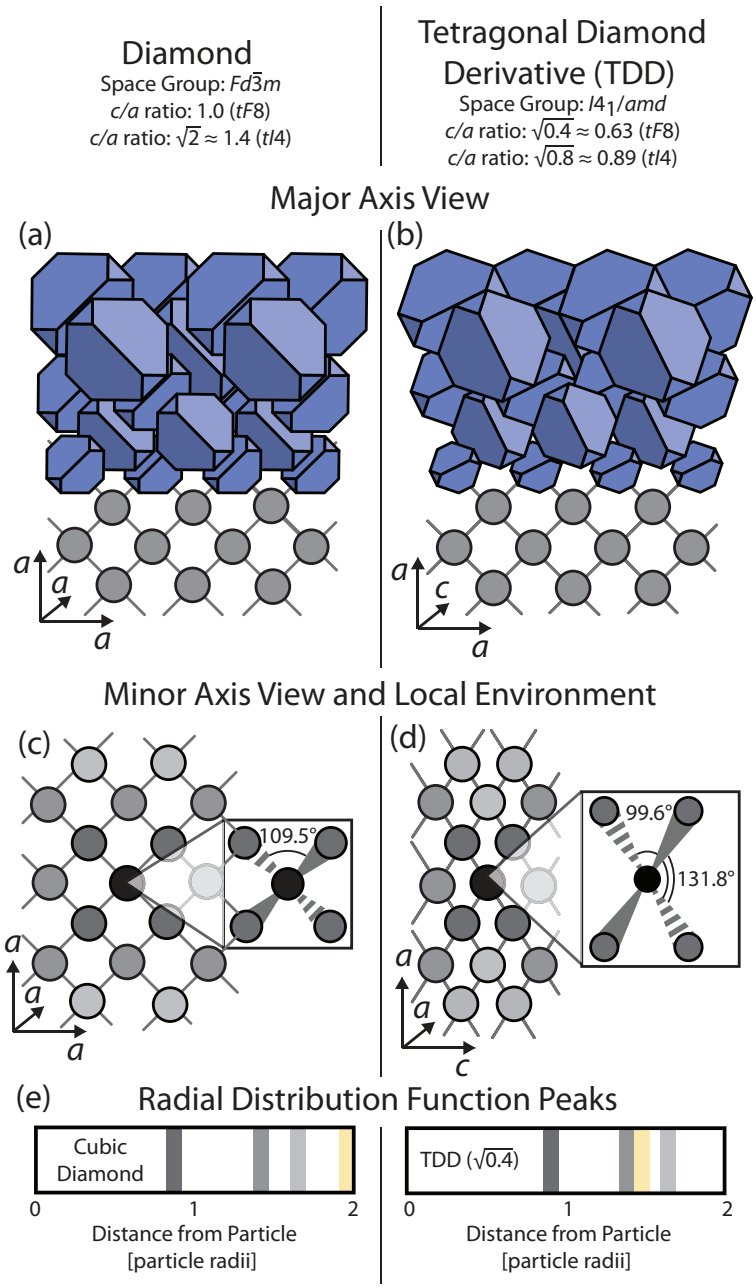

Figure 4.2: **Structural Diagrams for Diamond and its Tetragonal Derivative. (a–d)** Structural comparison between **(a, c)** diamond and **(b, d)** the tetragonal diamond derivative (TDD) with $c/a = \sqrt{0.4}$, both shown with shape at $\alpha = 0.5$. Here, we show projections along the major axis of cubic diamond and along two differing axes in the tetragonal derivative structure ($\vec{c}$ in **(b)** and one of the equivalent $\vec{a}$-axes in **(d)**). The particle positions appear unchanged when viewed along the $\vec{c}$-axis, but the particles rotate about the $\vec{c}$-direction. **(e)** The peaks in the radial distribution function (RDF), i.e., the distances of the nearest-neighbor shells. The fourth nearest neighbors (yellow) in the $\vec{c}$-direction in diamond are immediately outside the third neighbor shell in TDD at $c/a = \sqrt{0.4}$.

4.4 Results

4.4.1 Phase Diagram

We report phase diagrams comparing the c/a ratio of the $tF8$ unit cell for varying densities and shape parameter α. These phase diagrams reveal that, although all shapes with $0.3 \leq \alpha \leq 0.5$ assemble into diamond, they will transition to tetragonal unit cells at higher densities. The $NVT\alpha$ simulations generating this phase diagram and $NPT\alpha$ simulations for computing the equation of state were conducted by initializing both in the assembled and densely packed structures and equilibrating at the desired density or pressure.

In Fig. 4.3**(a)**, the contour lines map the c/a value of the unit cell of the equilibrium structure for systems of constant shape at varying densities. The shades of red represent the c/a ratio of the unit cell lattice vectors, with the lighter red region showing where cubic diamond is the configuration with the lowest free energy ($c/a = 1$), and darker reds indicating TDD structures, where $c/a < 1$ is lower in free energy. The region marked as geometrically forbidden (grey) shows the densities and α values at which particles would be forced to overlap.

In this study, shape and structure are intrinsically intertwined due to the shape-dependency of the transition from cubic diamond to its tetragonal derivative. Using Alchemical hard particle Monte Carlo (Alch-HPMC) (described in [38] and 4.6) with constant alchemical potential $\mu = 0$, we can find the shape that produces the lowest free energy structure at a given density or pressure, and determine where the crossover from the diamond to the TDD stability region occurs ($\langle\alpha\rangle$ shown in black on Fig. 4.3**(a)**). At low densities, the lowest free energy phase is diamond, but at densities $\gtrsim 0.75$ (or equivalently at unitless pressures $p^* \geq 10$–15) a TDD structure will have lower free energy in this shape space. Decompression of this high-density system showed full recovery of the diamond structure.

sizes at lower ε, and a diagram of the simulation protocol

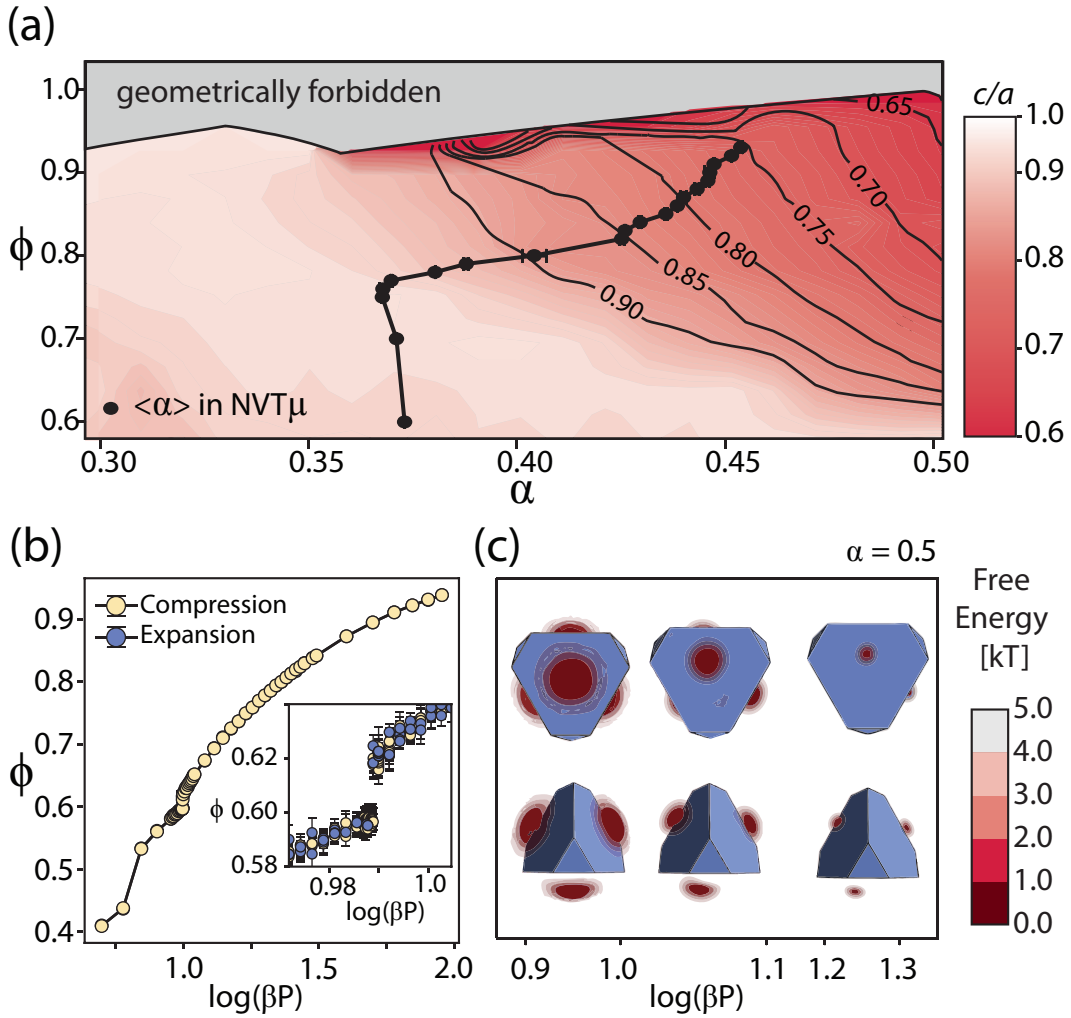

Figure 4.3: **Simulation Results for $NVT\alpha$, $NPT\alpha$, and $NVT\mu$. (a)** Composite "phase diagram" from all simulations. The putative densest packing in either diamond or TDD structure as a function of shape is the upper limit of the phase diagram, the geometrically forbidden region shown in grey. Shades of red represent the c/a ratio of the unit cell, with the lighter red region showing where diamond is the configuration with the lowest free energy ($c/a = 1$), and darker reds indicating TDD structures with lower c/a values. The black data set represents results from $NVT\mu$ simulations, denoting where the crossover from the diamond to the TDD stability region occurs as a function of density and shape. **(b)** Equation of state for $\alpha = 0.5$ evaluated in compression and expansion runs. The main plot shows the average values, with an inset showing the average and standard deviations around the transition pressure. **(c)** Potentials of mean force and torque for $\alpha = 0.5$ at varying pressures. The PMFT wells shift from the center of the large face of each particle toward one edge. This shows that the coordination remains tetrahedral, but becomes distorted with increasing pressure.

4.4.2 Equation of State and PMFT

We investigated the nature of the phase transition and behavior of potentials of mean force and torque (PMFTs) for the phase transition corresponding to the largest change in c/a, at $\alpha = 0.50$, in Fig. 4.3**(b, c)**. In Fig. 4.3**(b)**, the main plot represents the average for both initializations, with an inset representing the average and standard deviations around the transition pressure. The transition exhibits a small discontinuity in $\beta P(\phi)$ and no hysteresis, which implies that it is either a weak first-order or a second-order transition [48]. PMFTs, the calculation of which is detailed in [27], provide a statistical landscape for entropic particle bonding—i.e., they show the probable locations for the neighboring particles of a given reference particle in units of free energy. PMFTs show that after the transition occurs, the bonding remains four-fold, with the coordination being that of a distorted tetrahedron.

4.4.3 Photonic Band Structures

Diamond exhibits a complete photonic band gap when the lattice sites are populated with dielectric spheres [3]; thus the transition from the diamond structure to any form of TDD structure would result in a shift in the photonic properties due to the symmetry reduction of the lattice from cubic to tetragonal. We computed the photonic band structure of the equilibrated crystals found through simulation using MIT Photonic Bands (MPB) [40], replacing each polyhedral shell with its insphere core. Because the polyhedra are scaled to unit volume, there is a one-to-one mapping between shape parameter α and insphere radius.

We report the photonic band frequencies in units of (speed of light)$/a$, where a is the lattice constant. Each complete photonic band gap is reported in unitless dimensions, defined as the width of the band gap over the mid-gap frequency, ω^*. The conversion from ω^* to absolute wavelength is:

$$\lambda = \frac{a}{\omega^*}. \tag{4.5}$$

While we anticipated a change in photonic properties from an "on" to "off" state upon

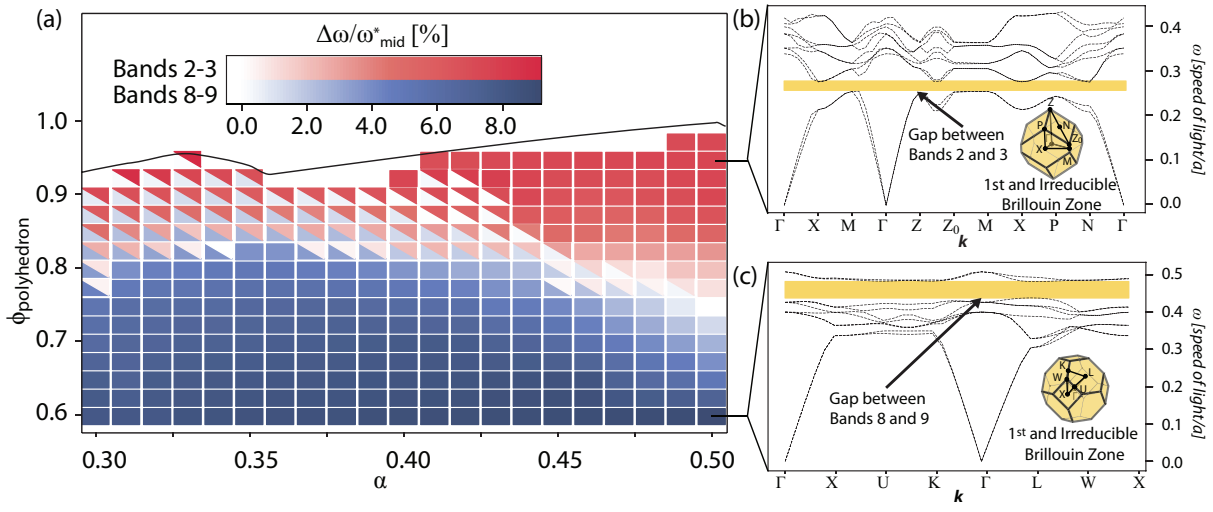

Figure 4.4: **Photonic Band Gap Structures and Sizes (a)** Size of photonic band gaps between bands 2 and 3 (red) and bands 8 and 9 (blue) for structures in Fig. 4.3**(a)**. All polyhedra have been replaced with spheres with radius equal to the polyhedral insphere radius, and with dielectric constant $\varepsilon = 11.56$. **(b–c)** Representative photonic band structures for $\alpha = 0.5$ at **(b)** $\phi = 0.6$, where it is in cubic diamond, and (c) $\phi = 0.95$, where it is in TDD at $\approx \sqrt{0.4}$. The insphere radius of $\Delta_{323}|_{\alpha=0.5}$ is 0.425.

converting the diamond structure to TDD, we were surprised to find that the results suggest a potential multistate material with one of four possibilities with regards to a complete photonic band gap: i) no gap, ii) a complete gap between bands 8 and 9, iii) a complete gap between bands 2 and 3, and (iv) complete gaps between both bands 2 and 3, and 8 and 9. Examples of (ii) and (iii) are shown in Fig. 4.4**(b)** and **(c)**, respectively. These findings suggest how to make a material that could switch between permitting all light and blocking one set of frequencies or another.

Taking the equilibrated structures (i.e., thermalized) from simulation and considering each core of the polyhedral particles as the high dielectric medium dielectric constant $\varepsilon = 11.56$, we computed the photonic band structure for structures with packing fractions $\phi = 0.6$–0.975 and shape parameters $\alpha = 0.3$–0.5. The maximum band gap width is 9.2% and all bands were centered around mid-gap frequencies of approximately 0.260–0.298 (between bands 2 and 3) or 0.384–0.459 (between bands 8 and 9). Unitless band gap widths are shown for the Δ_{323} family of shapes as a function of packing fraction in Fig. 4.4**(a)**.

In addition to computing the photonic band structure for $\varepsilon = 11.56$, we also considered lower dielectric constants (shown in Fig. 4.8). From these, we learn that complete photonic band gaps between bands 2 and 3 are possible with a minimum dielectric constant of 5.0, and between 8 and 9 with a minimum dielectric constant of 8.0. These values suggest that this type of photonic band structure would not be possible with crystals made of polymeric materials (which generally have $\varepsilon < 4.0$, such as poly(methyl methacrylate) particles), but would require materials of higher dielectric constant.

4.5 Discussion and Conclusions

We posit that this system could be synthesized via a variety of methods, including by assembling spherical core-polyhedral shell nanoparticles, as outlined earlier. The diamond structure has been stabilized with nanocages made of DNA that are functionalized to hybridize with coated nanoparticles [49]. This could potentially extend to the TDD structure

by changing the length of the strands at the binding sites or the cage geometry. The transition may also be achievable through DNA-programmable assembly [50], for which the lengths and bonding strength of DNA may be gleaned by examination of the PMFTs [51].

These results represent the theoretical behavior of an ideal system, and will be affected by imperfections introduced during synthesis. Previous studies have discussed the sensitivity of high band-number gaps to disorder [52], which may cause the gap between bands 8 and 9 to disappear in most real-world systems. In this case the system would only demonstrate a gap between bands 2 and 3, and the material would exhibit two states (e.g., "on" in the TDD state and "off" in the diamond state). This, in addition to the fact that the 8-9 band gap requires a much higher dielectric constant than the 2-3 gap, would make a two-state material a more robust target.

The phase transition we report at the colloidal length scale may also reveal insights about the atomic transition on which it is based. Although other TDD structures have not been observed as an intermediary between atomic diamond and β-Sn phases, such a consideration could provide new perspective into the mechanism underlying the phase transition. In our simulations, all effects other than shape entropy are excluded [27], and we restrict the particle geometry to symmetric truncations of tetrahedra, i.e., the Δ_{323} shape family. Thus we prove that entropy alone suffices to explain the transition in colloidal systems from diamond to a lower c/a tetragonal derivative. This correlation strengthens a supposition made by G. J. Ackland, who proposed that it was plausible that entropy is the driving force for diamond-to-β-Sn transitions, based on the absence of such a transition at 0 K [8].

Our colloidal system differs from atomic systems in several respects. At the higher c/a ratio (≈ 0.63 *vs.* ≈ 0.39), the coordination remains four-fold, while the neighboring particles form a distorted tetrahedron (as compared to a regular tetrahedron in perfect diamond). This retention of four-fold coordination may explain the reversibility in our system, compared to the irreversibility in atomic systems, which transition to octahedral coordination.

The same cannot be said for systems adopting the diatomic analog to diamond, zincblende,

as these systems do not adopt a β-Sn-equivalent structure upon pressurization: the transition geometry would result in the nearing of like-charged, mutually repulsive atoms [53]. Most III-V semiconducting zincblende-formers transition to wurtzite, a hexagonal diamond derivative under pressure. While β-Sn is topologically identical to diamond, wurtzite is to cubic diamond as cubic-close sphere packing is to its hexagonally-close packed relative: the local coordination is identical, but its network is topologically distinct, which would require a breaking of bonds and rearrangement of the constituent atoms in the transition.

We have predicted a new phase transition achievable in colloidal systems, induced by a slight change in pressure or in particle shape. This structural transition provides an exciting target for synthesis: a photonic material switchable between multiple photonic band gap states, either between two different gaps, or –perhaps more practically– between "on"/"off" states. Given the placement of the two possible gaps, complete photonic band gaps would be achievable in colloidal crystals in visible or infrared wavelengths, and could potentially toggle between two colors or separate regimes in the electromagnetic spectrum. For example, by using spheres made of a high-dielectric material with $\varepsilon \approx 8.0 - 9.0$ (such as titania [54]) that inscribe truncated tetrahedra with $\alpha = 0.5$ (see Fig. 4.4) and a lattice constant of $a = 200$ nm, a three-state material could be self-assembled with a violet (400 nm) band gap at low densities, no band gap at intermediate densities, and a red (685 nm) band gap at high densities. If a larger lattice constant of $a = 8.2$ μm is used, which is achievable for colloidal systems, the lower band gap occurs at 28 μm, or about 11 THz, suitable for sub-millimeter photonic applications. If a is a tunable design parameter, this system could exhibit bands gaps at target wavelengths whose ratios are approximately 5:3.

4.6 Supplementary Information

4.6.1 Comparison of Diamond, TDD, and β-Sn

Given a non-standard unit cell of $tF8$, these three structures have corresponding c/a ratios of 1.0, $\sqrt{0.4} \approx 0.6325$, and 0.3859, respectively. For unit cell $tI4$, the structures have corresponding c/a ratios of $\sqrt{2} \approx 1.4142$, $\sqrt{0.8} \approx 0.8944$, and 0.5515, respectively, as the standard body-centered setting $tI4$ differs in c/a ratio by a factor of $\sqrt{2}$ from $tF8$ systems. Both TDD and $tI4$-Sn exhibit symmetry of space group $I4_1/amd$ (no. 141), with diamond exhibiting higher symmetry, consistent with space group $Fd\bar{3}m$ (no. 227). Particles in TDD have four nearest neighbors as in diamond, but arranged in a distorted tetrahedral shape, while the coordination number of β-Sn-type structures is six, the coordination polyhedron being a distorted octahedron.

It should be noted that $tI4$-Sn is geometrically forbidden for shapes in Δ_{323}. Shapes in Δ_{323} pack into TDD at a maximum density of 1 and $c/a_{\text{min}} = \sqrt{0.4}$. The densest packing arrangement of shapes with $\alpha \leq 0.36$ corresponds to a different structure type, α-As ($hR6$-As) [14], which is not studied in this publication as the difference in topology suggests that it cannot be obtained by a non-reconstructive transition, *i.e.*, without a drastic change in topology.

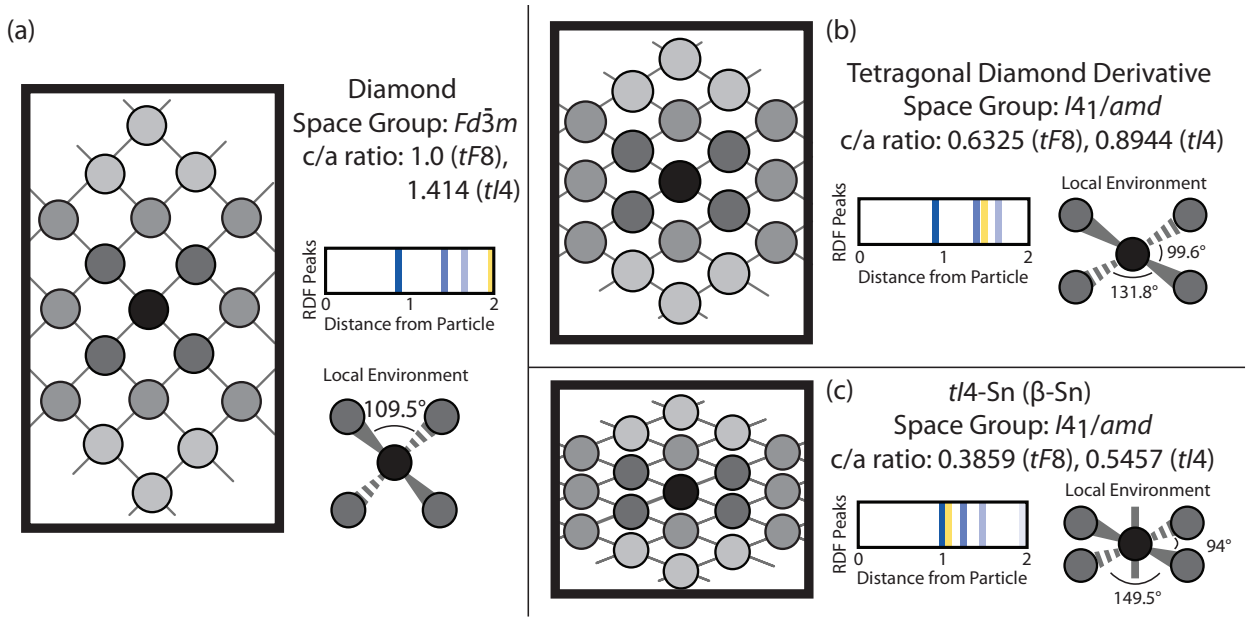

Figure 4.5: **Structure Diagrams for (a) diamond, (b) TDD at $c/a = \sqrt{0.4}$, and $tI4$-Sn** (β-Sn), including snapshots of nearest neighbor RDF peaks, and local environments. All three structures are related by a scaling along a major axis. Particles in TDD have four nearest neighbors as in diamond, but arranged in a distorted tetrahedral shape, while the coordination number of β-Sn-type structures is six, the coordination polyhedron being a distorted octahedron.

4.6.2 Equations of State

Here we present the equations of state (EOS) for $\alpha = 0.4, 0.45, 0.5$. Every EOS shows a kink in the density around the transition pressure, as seen in Fig. 4.6, implying a weak first-order or second-order phase transition. A kink in c/a ratio also occurs at the same pressure, as seen in blue in Fig. 4.6.

4.6.3 Protocol for $NVT\mu$ Simulations

Alchemical Monte Carlo simulations were run in the $NVT\mu$ ensemble to find the thermodynamically optimal shape and structure in Δ_{323}. Systems of 512 particles were initialized with $\alpha = \frac{1}{3}$ and $\phi = 0.6$ and equilibrated in shape space. The particles were then compressed isotropically to target $\phi = 0.7 - 0.9$ with $\Delta\phi = 0.05$, and equilibrated both with respect to

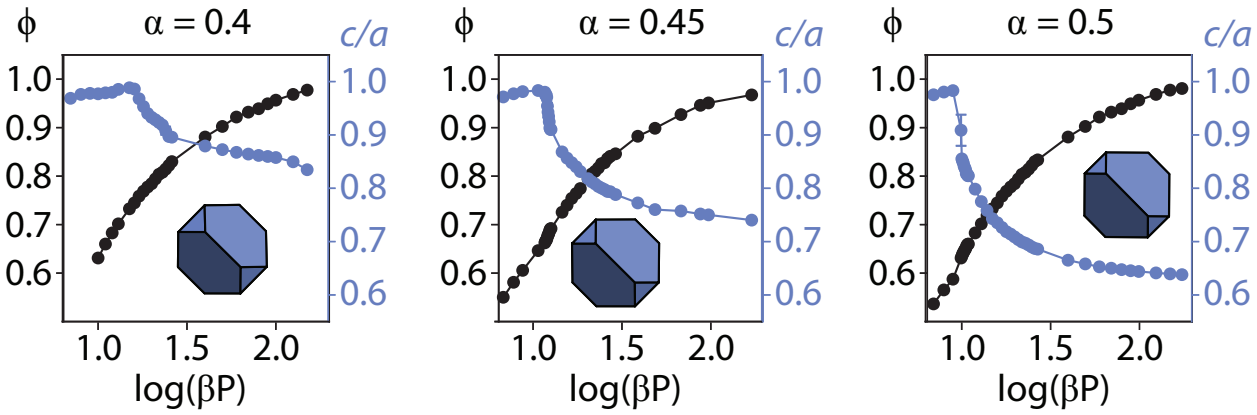

Figure 4.6: **Equations of state** for $\alpha = 0.4, 0.45, 0.5$. Density and c/a ratio with respect to pressure are shown in black and blue, respectively. Equations for all three shapes showed a small kink in density and c/a ratio with respect to pressure, implying a weak first-order or second-order transition. Error bars denote standard deviation across multiple independent simulations run at each statepoint, and are in most cases very small relative to the data points.

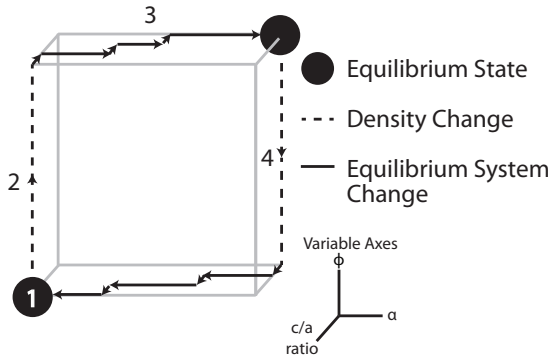

Figure 4.7: **Simulation Scheme for Alch-HPMC Simulations**, done in four separate steps: 1) Simulations were started by equilibrating a system with a diamond-type crystal structure at $\phi = 0.6$ to the previously reported low free energy shape $\alpha = 0.37$ [35]. 2) Systems were compressed to the target packing fraction, after which Monte Carlo moves with box aspect ratio change were enabled and equilibrated. 3) Alchemical Monte Carlo moves with box aspect ratio changes were run until both box and shape were equilibrated. 4) Systems were decompressed to $\phi = 0.6$, and allowed to equilibrate in box aspect ratio and shape, returning to step (1).

c/a and shape. This step was repeated until both structure and shape were at equilibrium. Systems were then decompressed to $\phi = 0.6$ and allowed once again to equilibrate with respect to α and the structure to check for reversibility.

4.6.4 Photonic Band Structure

In addition to computing the photonic band structure for the dielectric constant of silicon, we also computed the unitless width of any complete photonic band gaps for lower dielectric constants, included here. We sampled dielectric constants $\varepsilon \in [1.0, 12.0]$ and found complete band gaps in systems for dielectric constants as low as 5.0 (between bands 2 and 3) and 8.0 (between 8 and 9).

References

[1] Cersonsky, R. K., Dshemuchadse, J., Antonaglia, J., van Anders, G. & Glotzer, S. C. Pressure-Tunable Band Gaps in an Entropic Crystal. *Phys. Rev. Mat.* (2018).

[2] Bragg, W. H. & Bragg, W. L. The Structure of the Diamond. *Nature* **91**, 557–557 (1913).

[3] Ho, K. M., Chan, C. T. & Soukoulis, C. M. Existence of a photonic gap in periodic dielectric structures. *Physical Review Letters* **65**, 3152–3155 (1990).

[4] Xia, Y., Gates, B., Yin, Y. & Lu, Y. Monodispersed Colloidal Spheres: Old Materials with New Applications. *Advanced Materials* **12**, 693–713 (2000).

[5] Vlasov, Y. A., Bo, X.-Z., Sturm, J. C. & Norris, D. J. On-chip natural assembly of silicon photonic bandgap crystals. *Nature* **414**, 289–293 (2001).

[6] Arsenault, A. C., Puzzo, D. P., Manners, I. & Ozin, G. A. Photonic-crystal full-colour displays. *Nature Photonics* **1**, 468–472 (2007).

[7] Schroden, R. C., Al-Daous, M., Blanford, C. F. & Stein, A. Optical Properties of Inverse Opal Photonic Crystals. *Chemistry of Materials* **14**, 3305–3315 (2002).

[8] Ackland, G. J. High-pressure phases of group IV and III-V semiconductors. *Reports on Progress in Physics* **64**, 483–516 (2001).

[9] Clark, S. J., Ackland, G. J. & Crain, J. Theoretical study of high-density phases of covalent semiconductors. II. Empirical treatment. *Physical Review B* **49**, 5341–5352 (1994).

[10] Kohlstedt, K. L. & Glotzer, S. C. Self-assembly and tunable mechanics of reconfigurable colloidal crystals. *Physical Review E* **87**, 032305 (2013).

[11] Nguyen, T. D., Jankowski, E. & Glotzer, S. C. Self-Assembly and Reconfigurability of Shape-Shifting Particles. *ACS Nano* **5**, 8892–8903 (2011).

[12] Zhenli Zhang *et al.* Self-assembly of patchy particles into diamond structures through molecular mimicry. *Langmuir* **21**, 11547–11551 (2005). arXiv:1201.3425v1.

[13] Ducrot, É., He, M., Yi, G.-R. R. & Pine, D. J. Colloidal alloys with preassembled clusters and spheres. *Nature Materials* **16**, 652–657 (2017).

[14] Damasceno, P. F., Engel, M. & Glotzer, S. C. Crystalline assemblies and densest packings of a family of truncated tetrahedra and the role of directional entropic forces. *ACS Nano* **6**, 609–614 (2012). 1109.1323.

[15] Jain, A., Errington, J. R. & Truskett, T. M. Dimensionality and Design of Isotropic Interactions that Stabilize Honeycomb, Square, Simple Cubic, and Diamond Lattices. *Physical Review X* **4**, 31049 (2014).

[16] Wang, Y., Jenkins, I. C., McGinley, J. T., Sinno, T. & Crocker, J. C. Colloidal crystals with diamond symmetry at optical lengthscales. *Nature Communications* **8**, 14173 (2017).

[17] Romano, F., Sanz, E. & Sciortino, F. Phase diagram of a tetrahedral patchy particle model for different interaction ranges. *The Journal of Chemical Physics* **132**, 184501 (2010).

[18] Wang, Y. *et al.* Colloids with valence and specific directional bonding. *Nature* **491**, 51–55 (2012).

[19] Glotzer, S. C. & Solomon, M. J. Anisotropy of building blocks and their assembly into complex structures. *Nat Mater* **6**, 557–562 (2007).

[20] Du, C. X., van Anders, G., Newman, R. S. & Glotzer, S. C. Shape-driven solidsolid transitions in colloids. *Proceedings of the National Academy of Sciences* **114**, E3892–E3899 (2017). 1603.00727.

[21] .

[22] Sun, Y. & Xia, Y. Shape-Controlled Synthesis of Gold and Silver Nanoparticles. *Science* 2176–2179.

[23] Henglein, A. & Giersig, M. Reduction of Pt(II) by H 2 : Effects of Citrate and NaOH and Reaction Mechanism. *The Journal of Physical Chemistry B* **104**, 6767–6772 (2000).

[24] Licata, N. A. & Tkachenko, A. V. Self-assembling DNA-caged particles: Nanoblocks for hierarchical self-assembly. *Physical Review E* **79**, 011404 (2009).

[25] Kuo, C.-H. & Huang, M. H. Morphologically controlled synthesis of Cu2O nanocrystals and their properties. *Nano Today* **5**, 106–116 (2010).

[26] Personick, M. L., Langille, M. R., Zhang, J. & Mirkin, C. A. Shape Control of Gold Nanoparticles by Silver Underpotential Deposition. *Nano Letters* **11**, 3394–3398 (2011).

[27] van Anders, G., Klotsa, D., Ahmed, N. K., Engel, M. & Glotzer, S. C. Understanding shape entropy through local dense packing. *Proceedings of the National Academy of Sciences* **11**, E4812–E4821 (2014).

[28] Damasceno, P. F., Engel, M. & Glotzer, S. C. Predictive Self-Assembly of Polyhedra into

Complex Structures. *Science* 453–457. 1202.2177.

[29] Cargnello, M., Doan-Nguyen, V. V. T. & Murray, C. B. Engineering uniform nanocrystals: Mechanism of formation and self-assembly into bimetallic nanocrystal superlattices. *AIChE Journal* **62**, 392–398 (2016).

[30] O'Brien, M. N., Lin, H.-X., Girard, M., Olvera de la Cruz, M. & Mirkin, C. A. Programming Colloidal Crystal Habit with Anisotropic Nanoparticle Building Blocks and DNA Bonds. *Journal of the American Chemical Society* **138**, 14562–14565 (2016).

[31] Ma, Y. *et al.* Au@Ag Core-Shell Nanocubes with Finely Tuned and Well-Controlled Sizes, Shell Thicknesses, and Optical Properties. *ACS Nano* **4**, 6725–6734 (2010).

[32] Goia, D. V. & Matijević, E. Preparation of monodispersed metal particles. *New Journal of Chemistry* **22**, 1203–1215 (1998).

[33] Guo, S. & Wang, E. Noble metal nanomaterials: Controllable synthesis and application in fuel cells and analytical sensors. *Nano Today* **6**, 240–264 (2011).

[34] Lu, C.-L., Prasad, K. S., Wu, H.-L., Ho, J.-A. A. & Huang, M. H. Au Nanocube-Directed Fabrication of Au-Pd Core-Shell Nanocrystals with Tetrahexahedral, Concave Octahedral, and Octahedral Structures and Their Electrocatalytic Activity. *Journal of the American Chemical Society* **132**, 14546–14553 (2010).

[35] van Anders, G., Klotsa, D., Karas, A. S., Dodd, P. M. & Glotzer, S. C. Digital Alchemy for Materials Design: Colloids and Beyond. *ACS Nano* **9**, 9542–9553 (2015).

[36] Anderson, J. A., Lorenz, C. D. & Travesset, A. General purpose molecular dynamics simulations fully implemented on graphics processing units. *Journal of Computational Physics* **227**, 5342–5359 (2008).

[37] Anderson, J. A., Irrgang, M. E. & Glotzer, S. C. Scalable Metropolis Monte Carlo for simulation of hard shapes. *Computer Physics Communications* **204**, 21 – 30 (2016).

[38] Cersonsky, R. K., van Anders, G., Dodd, P. M. & Glotzer, S. C. Relevance of Packing to Colloidal Self-Assembly. *In Preparation* **115**, 1439–1444 (2018).

[39] Adorf, C. S., Dodd, P. M., Ramasubramani, V. & Glotzer, S. C. Simple data and workflow management with the signac framework. *Computational Materials Science* **146**, 220–229 (2018). 1611.03543.

[40] Johnson, S. & Joannopoulos, J. Block-iterative frequency-domain methods for Maxwell's equations in a planewave basis. *Optics Express* **8**, 173 (2001).

[41] Maldovan, M., Ullal, C. K., Carter, W. C. & Thomas, E. L. Exploring for 3D photonic bandgap structures in the 11 f.c.c. space groups. *Nature Materials* **2**, 664–667 (2003).

[42] Hynninen, A.-P., Thijssen, J. H. J., Vermolen, E. C. M., Dijkstra, M. & van Blaaderen, A. No Title **6** (2007).

[43] Pattabhiraman, H., Avvisati, G. & Dijkstra, M. Novel Pyrochlorelike Crystal with a Photonic

Band Gap Self-Assembled Using Colloids with a Simple Interaction Potential. *Physical Review Letters* **119**, 157401 (2017).

[44] Hinuma, Y., Pizzi, G., Kumagai, Y., Oba, F. & Tanaka, I. Band structure diagram paths based on crystallography. *Computational Materials Science* **128**, 140–184 (2017).

[45] Chen, E. R., Klotsa, D., Engel, M., Damasceno, P. F. & Glotzer, S. C. Complexity in surfaces of densest packings for families of polyhedra. *Phys. Rev. X* **4**, 11024 (2014).

[46] Bundy, F. P. *et al.* The pressure-temperature phase and transformation diagram for carbon; updated through 1994. *Carbon* **34**, 141–153 (1996).

[47] Jamieson, J. C. Crystal structures at high pressures of metallic modifications of silicon and germanium. *Science* **139**, 762–764 (1963).

[48] Ehrenfest, P. Phase transformations in the usual and extended sense, classified according to the corresponding singularities of the thermodynamic potential. *Proceedings of the Koninklijke Akademie Van Wetenschappen Te Amsterdam* **36**, 153–157 (1933).

[49] Liu, W. *et al.* Diamond family of nanoparticle superlattices. *Science* **351**, 582–586 (2016).

[50] Park, S. Y. *et al.* DNA-Programmable Nanoparticle Crystallization. *Nature* **451**, 553–556 (2008).

[51] Macfarlane, R. J. *et al.* Nanoparticle Superlattice Engineering with DNA. *Science* **334**, 204–208 (2011).

[52] Li, Z.-Y. Y. & Zhang, Z.-Q. Q. Fragility of photonic band gaps in inverse-opal photonic crystals. *Physical Review B* **62**, 1516–1519 (2000).

[53] Ackland, G. J. Theory of High Pressure Phases of Group-IV and III-V Semiconductors. *Physica Status Solidi (B) Basic Research* **223**, 361–368 (2001).

[54] DeVore, J. R. Refractive Indices of Rutile and Sphalerite. *Journal of the Optical Society of America* **41**, 416 (1951).

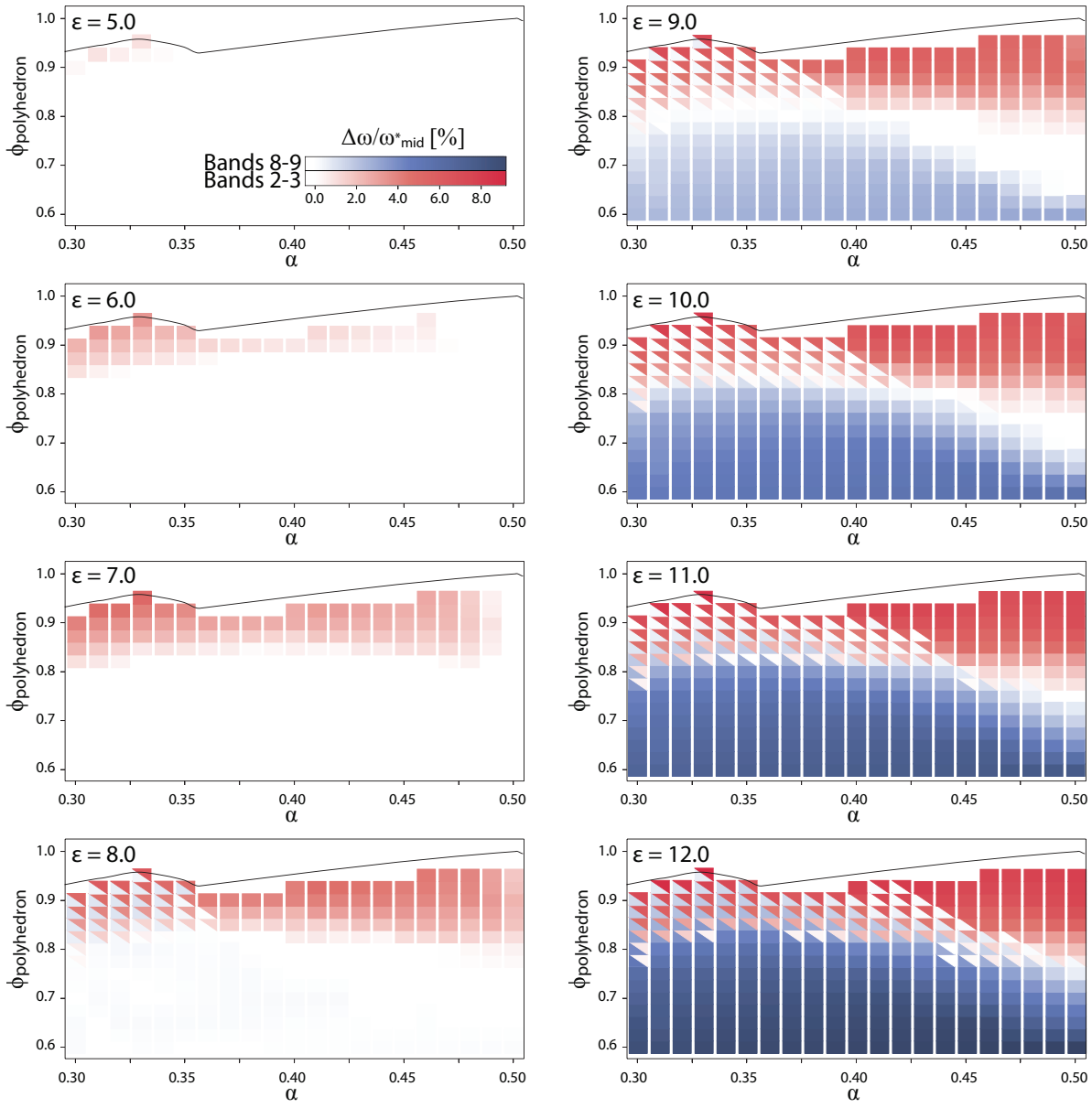

Figure 4.8: **Photonic band gap widths** measured between bands 2 and 3 (red) and between bands 8 and 9 (blue) for structures reported in the main text. All polyhedra have been replaced with spheres of radius equal to the polyhedral insphere radius, and with varying dielectric constants, $\varepsilon \in [5.0, 12.0]$. The legend in the upper left plot holds for all plots. The solid black line delineates allowed structures from geometrically forbidden structures.

CHAPTER V

Understanding Shape Space for Nanoparticle Design

The mathematical sciences particularly exhibit order symmetry and limitations; and these are the greatest forms of the beautiful.

– Aristotle

5.1 Introduction

In Chapter IV, we witnessed a system of nanoparticle shapes that transitioned between two structures within the $NVT\mu$ ensemble, even when constraints were imposed to maintain the target structure. This raises an alarming question: if the constraints are overpowered in DA simulation, what is driving the exploration of shape space? How will optimizing the free energy of nanoparticle shape for a target structure differ from designing the optimal nanoparticle for self-assembly?

To answer this lofty question would require a pre-emptive knowledge of the free energy landscape of highly dimensional space of all shapes, and the computation of this landscape would require untenable amount of compute time. Therefore, we must choose aspects of the free energy landscape to compute that provide the greatest amount of insight at smallest computational cost.

First, let's discuss some variable terminology. When discussing shape, I will use α to denote a particular shape space, whether through some parametrization or abstract reference.

To discuss a region of shape space, I will use $\boldsymbol{\alpha}$, and to discuss a region of shape space that assembles a structure, I will use $\boldsymbol{\alpha}_\Lambda$, where Λ is the structure assembled. To denote the shape corresponding to the global or local (to some region of shape space) free energy minimum, I will use $\langle\alpha\rangle$ and $\langle\alpha_\Lambda\rangle$, respectively.

In this chapter, I will focus on two such aspects: 1) the results of DA in an unconstrained system, and 2) the effect of varying the strength of spring-type constraints on the results of DA. The goal of (1) is to provide insight into the competing driving forces during shape space exploration. In other words, I aim to decipher which shape features are a result of the constraints provided for DA, and that are a result of the free energy landscape which DA is exploring. These simulations were designed by myself, C. X. Du, and S. C. Barterian. The goal of (2) is to report on the effects of constraints on the accessible shape space during simulation.

Finally, I will make suggestions as to implementations of DA aimed to provide ideal nanoparticle shapes for self-assembly. These methodologies will be implemented by T. C. Moore and R. A. LaCour as part of ongoing work.

5.2 The Ground State of Shape Space

5.2.1 Methods

DA can be implemented to explore a variety of "slices" of shape spaces, with the use of spheric triangle groups, truncation parameters, and rounding parameters as popular choices.[1, 2, 3, 4, 5] One may also implement shape space for all convex polyhedra with 3xN variables, where N is the number of vertices. The formulation of the partition function for this ensemble is:

$$Z = \sum_{\sigma} e^{-\beta\left(H - \sum_i N\alpha_i\mu_i\right)} \tag{5.1}$$

where β is the reciprocal to k_BT, H is the classical Hamiltonian, N are the number of

particles, α_i and μ_i are the alchemical parameter and its conjugate, the alchemical potential. For each independently optimized vertex, there are three α and μ parameters, one for each coordinate of the vertex.

We choose the initial shapes by randomly placing N vertices on a unit sphere, where $N \in [4-12, 14-20, 24, 28, 32, 40, 50]$, with 5-10 unique shapes for each N. For $N = 4, 6, 8, 12, 20$, we also initialized shapes corresponding to the Platonic solids. All shapes are scaled such that $V = 1$ throughout simulation.

For each shape, I simulated independently-seeded systems of 512 particles initialized in a periodic structure at sub-assembly packing fractions ($\phi \approx 0.1$). Systems were compressed isotropically without change in particle shape to the target packing fraction ϕ with the hard-particle Monte Carlo (HPMC) functionality of HOOMD-Blue [6, 7] and then ran until equilibration over $1.0E7 - 2.0E8$ Monte Carlo sweeps implementing the alchemical ensemble extension to HPMC (Alch-HPMC). Simulations were run for $\phi = 0.5$, 0.51, 0.52, 0.53, 0.54, 0.55, 0.57, 0.59, 0.61, 0.63, 0.65.

The resulting shapes were analyzed using the isoperimetric quotient (IQ) as a scalar representation of the shape.[i,ii,iii] IQ is not a unique value – many distinct shapes share similar IQ values, therefore I qualitatively analyzed the resulting shapes to ensure that all shapes corresponding to a single IQ value were of the same type. Autocorrelation times of the IQ were on the order of $1.0E3 - 8.0E5$ Monte Carlo sweeps.To determine structure of the system throughout simulation, I analyzed the structures using in-house software Injavis and with the Steinhardt order parameters.[9]

5.2.2 Results

Here I report two representations of the phase diagram for unconstrained systems: 1) equilibrium shape, 2) equilibrium structure.

[i]Isoperimetric quotient is defined as $IQ = 36\pi * V^2/S^3$. The trace of the moment of inertia could also be used as a scalar representation.

[ii]The method for finding the isoperimetric quotient are reported in Ref. [8].

[iii]The values of IQ for a sphere is by definition 1.0

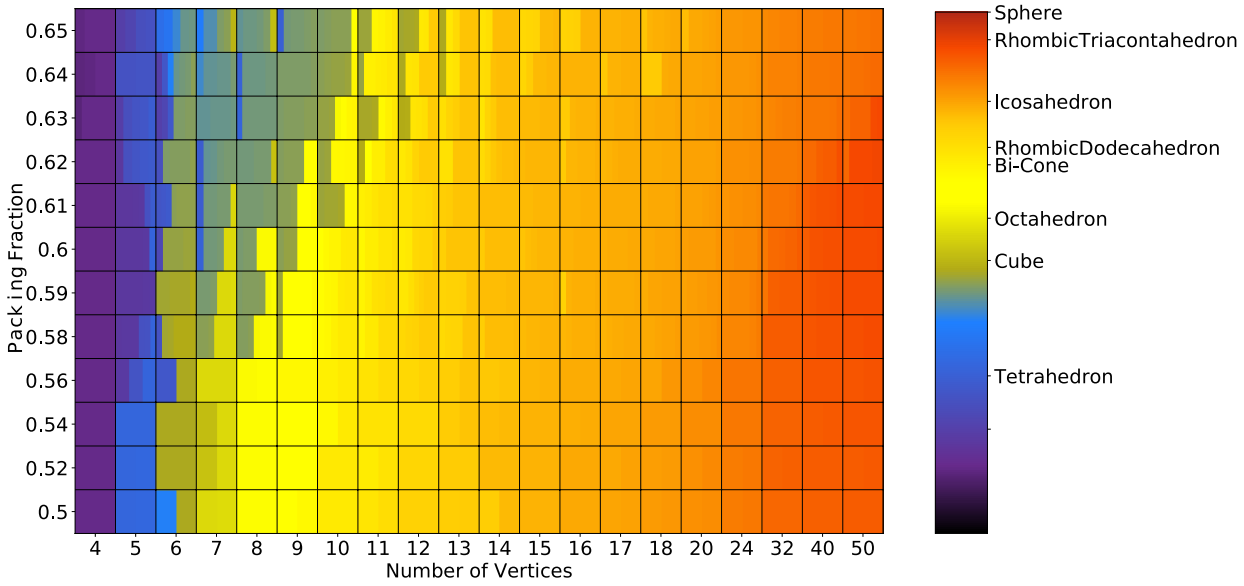

Figure 5.1: **Results of Simulation Across Unconstrained Shape Space: Resulting Polyhedra.** The color of the phase diagram corresponds to values of isoperimetric quotient (IQ). Examples of common polyhedra are listed on the colorbar at the appropriate IQ value to give reference for the shapes found in simulation. Shapes with IQ values similar to the sphere and bi-cone, which are both non-polyhedral, were approximates; *i.e.* highly spherical shapes with many vertices or n-gonal bipyramids, respectively. Multiple colors within the same pixel correspond to multiple replicas yielding varying shapes.

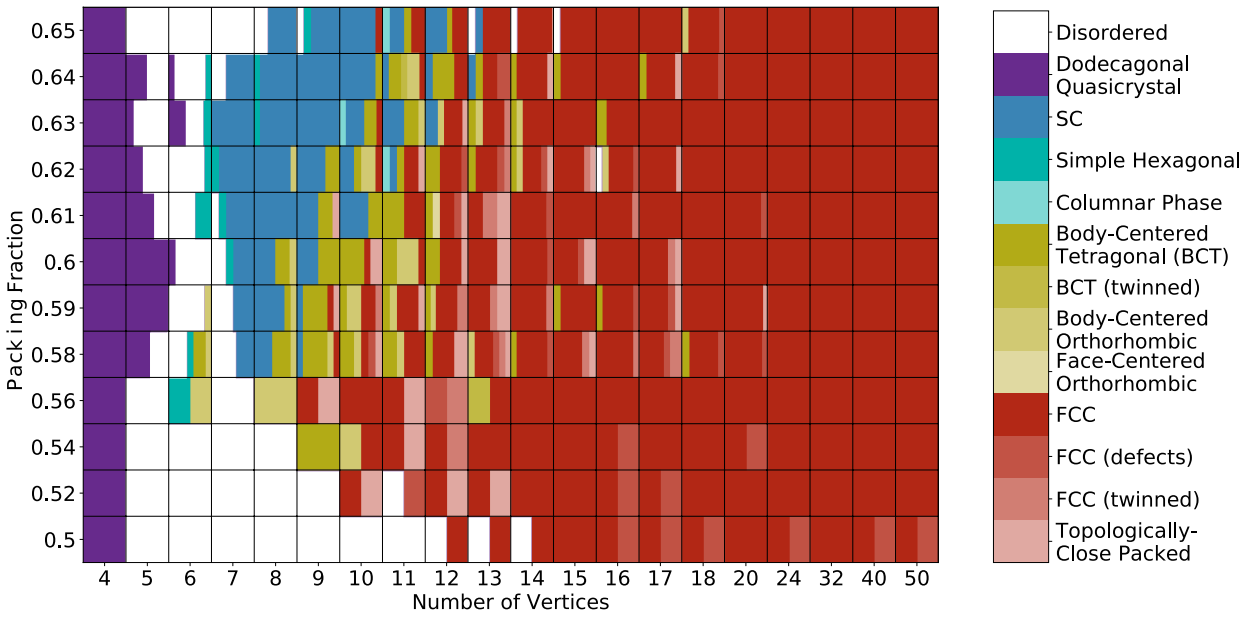

Figure 5.2: **Results of Simulation Across Unconstrained Shape Space: Resulting Structures.** The color of the phase diagram correspond to self-assembled structures from simulation. Six distinct categories of structures emerged (1) FCC and FCC-like (red), (2) BCT and BCT-like green), (3) SC (blue), (4) Simple hexagonal or Columnar hexagonal (teal), (5) Dodecagonal Quasicrystal (violet), and (6) Disordered (white). Multiple colors within the same pixel correspond to multiple replicas yielding varying structures.

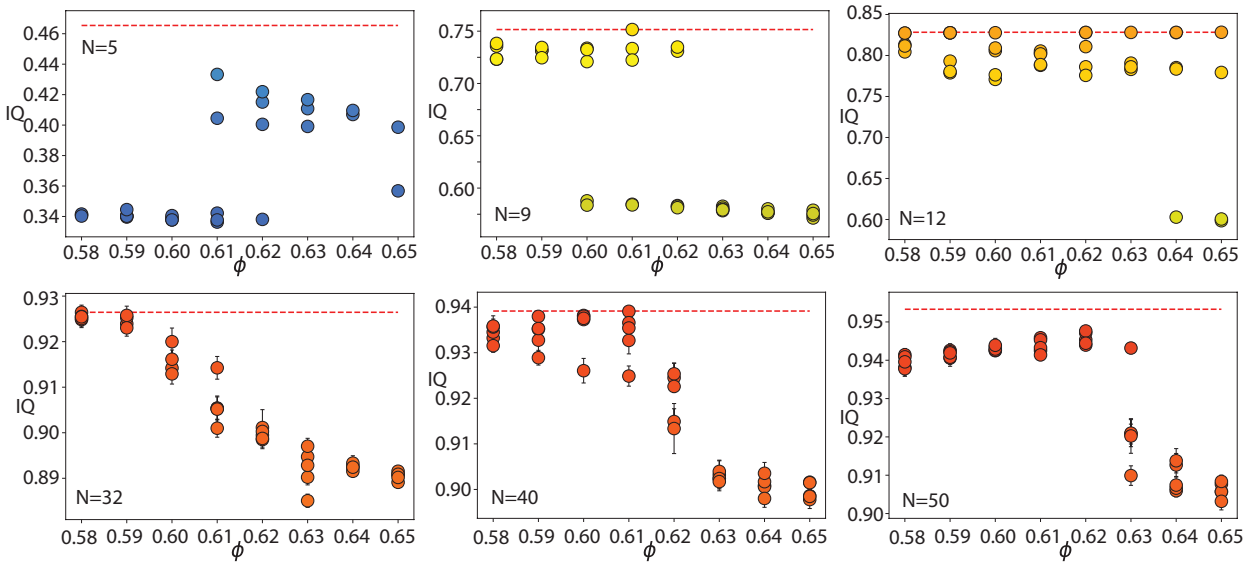

Figure 5.3: **Examples of Large Change in $\langle\alpha\rangle$ across ϕ for N = 5, 9, 12, 32, 40, and 50** The colors of the data points correspond to values of isoperimetric quotient (IQ) with the same color scheme as Fig. 5.1. Each plot is marked with a red dotted line corresponding to the most spherical shape accessible in the given shape space of N vertices. Data points shown are for independent simulations, with error bars marking the standard deviation.

For shapes with four vertices, the system adopted a regular tetrahedral shape in a dodecagonal quasicrystal for all ϕ. For shapes with five or six vertices, the ground state corresponds to an asymmetric polyhedron in a disordered phase (rather than converging to the more symmetric tetrahedron in the dodecagonal quasicrystal phase).

For shape spaces containing shapes with 12 or more vertices, FCC is the dominant ground state. At low packing fractions, a sphere-like shape is thermodynamically preferred, whereas at higher packing fractions ($\phi \approx 0.63$) a less spherical rhombictricontahedron is the preferred shape. This is potentially due to the onset of jamming which occurs for spheres at $\phi = 0.63$, below which spheres can spontaneously assemble from a disordered fluid.

I have highlighted cases of N with a large change in $\langle\alpha\rangle$ across packing fractions in Fig. 5.3.

5.2.3 Discussion

The results from this section demonstrate that, in the absence of any structural constraints, there is a large free energy well within shape space, as shown in Fig. 5.1 and 5.2. This implies that the results of DA simulation are heavily influenced by the underlying free energy landscape, which must be taken into account when performing DA for design. Practically, this suggests that the particle shapes found by exploring shape space using DA may be more spherical than necessary to assemble the target structure – if shape space has a large free energy well corresponding to sphere-like particles, then the entropy gained by increasing the sphericity of a particle in simulation may be on the same scale as the entropy gained due to the specific shape characteristics that lead to higher entropy in the target structure. In such a case, suppressing the effects of the free energy landscape of shape space may lead to particle shapes that are more likely to assemble the target structure.

5.3 The Effects of Structural Constraints

Given that the free energy well within shape space can contribute to the entropy of the lowest free energy shape for a given structure, it becomes more important to inspect the constraints that bias a solution away from this global minimum. Previous implementations of DA have used translation and rotational restraints quantified with spring constants to restrict the space of shapes within which DA may sample and transform the free energy landscape through energetic penalties applied to environments not found in the target crystal.

Let me pose a few scenarios. Imagine structures Λ_1 and Λ_2 such that $\boldsymbol{\alpha}_{\Lambda_1}$ and $\boldsymbol{\alpha}_{\Lambda_2}$ lie near each other in shape space and $\min F_{\Lambda_1} >> \min F_{\Lambda_2}$ (*e.g.* imagine that Λ_1 and Λ_2 are BCC and FCC, respectively). Λ_1 and Λ_2 are topologically similar but distinct, such that the boundary between $\boldsymbol{\alpha}_{\Lambda_1}$ and $\boldsymbol{\alpha}_{\Lambda_2}$ is not well defined, and many α's between $\boldsymbol{\alpha}_{\Lambda_1}$ and $\boldsymbol{\alpha}_{\Lambda_2}$ form distortions or mixtures of Λ_1 and Λ_2. When using DA to sample this shape space, designing for structure Λ_1, the entropy gained by small distortions along the path to Λ_2

may be larger than the entropy gained by finding a shape that assembles perfectly into Λ_1. Applying constraints may apply an energy penalty to these distortions, but may also restrict the entropy enough such that a flat, asymmetric shape is preferable based upon rotational entropy maximization in a highly constrained system.

Consider also a structure Λ_3 where $\boldsymbol{\alpha}_{\Lambda_3}$ fully bounds another region $\boldsymbol{\alpha}_{\Lambda_4}$. This may happen where Λ_3 will form for shapes only where Λ_4 is not geometrically possible at assembly packing fractions. This "interrupting" phase may have one of many effects. If $\langle\alpha_{\Lambda_3}\rangle \in \boldsymbol{\alpha}_{\Lambda_4}$, the optimization of free energy for Λ_3 becomes ill-defined, as there is no free energy minimum shape which assembles Λ_3. Where do we go next? $\langle\alpha_{\Lambda_3}\rangle$ s.t. $\langle\alpha_{\Lambda_3}\rangle \notin \boldsymbol{\alpha}_{\Lambda_4}$? This shape may, if F_{Λ_3} is smooth, be at the boundary of $\boldsymbol{\alpha}_{\Lambda_3}$ and $\boldsymbol{\alpha}_{\Lambda_4}$ and may not easily form Λ_3.

5.3.1 Methods and Models

To test the sensitivities of free energy minimization to the structural constraints, I computed $\alpha_{\min F_\Lambda}$ for different Λ across various translational and rotational spring constants k and q, respectively. I chose Λ to be structures which were either (1) well-studied and thereby comparable across past literature, (2) topologically similar to a structure in (1), or (3) contained multiple rotations of the same particle environments. For this, our set of structures studied is (1) FCC, BCC, SC, diamond, (2) $oF8$-Am, and simple hexagonal (3) $cI12$-Ga, $tI32$-K.

The simulation protocol consisted of three parts, denoted (A), (B), and (C). All simulations used HOOMD-Blue, including volume-constrained box MC moves.[10] (A) Each of these structures were simulated at $\phi = 0.6$ with $256-734$ particles and $q, k \in \{0, 10, 100, 1000, 10000\}$. All shapes were intialized with 50 vertices (to avoid the vertex-dependent effects found in Sec. 5.2) and run with DA for a total of $1E7-1E8$ MC sweeps. Autocorrelation times of the isoperimetric quotient were on the order of $1E3-3.5E6$ MC sweeps. IQ was used as the order parameter to assess when the simulation had reached equilibrium. Simulations that quickly converged to $IQ \approx 0$ were interrupted, as computational complexity grows exponentially

as $L/D \to \infty$, and this signified that the system was over-constrained and would continue to flatten with further simulation. (B) The resulting particle shapes were initialized in the target structure and run for up to $1E7$ MC sweeps without constraints to see if the structure melted, recording the pressure. (C) Those systems which did not melt after this timeframe were re-initialized in a fluid at $\phi \approx 0.1$ and compressed to $\phi = 0.6$ and run for $1E7 - 5E7$ MC sweeps to see if the target structure would assemble. Pressure was used as the order parameter to assess when the simulation had reach equilibrium. Structures were classified as having (1) assembled the target, (2) assembled a lower F phase, or (3) assembled a higher F phase. (2) and (3) were assessed by comparing the pressure of the system to that of step (B), as lower F phases, through the thermodynamic relationship, will have lower pressure.

5.3.2 Results

Here I report $\langle \alpha_\Lambda \rangle$ for each of our structures, and note which particle shapes were (1) unstable in the target structure, (2) stable in the target structure but self-assemble a lower pressure structure, (3) stable in the target structure but failed to self-assemble, and (4) stable and self-assembled into the target structure.

For all previously studied targets, I was able to find shapes using digital alchemy that would assemble the target structure, consistent with previous literature.[11] Additionally, I found a few new shapes capable of assembling these targets: the golden rhombohedron in simple cubic in (c) and the squashed gyrobifastigium in diamond in (d), which were found at $k = 10 - 100, q = 1000 - 10000$ and $k = 0, q = 10000$, respectively. I was unable to find a shape that would self-assemble into any of the complex phases in Fig. 5.5.

5.3.3 Discussion

From Fig. 5.4-5.5, we can see a few universal effects of structural constraints for DA simulations. For example, for all systems under strong structural constraints (*i.e.* $q > 1000$ and $k > 1000$) $\langle \alpha_\Lambda \rangle$ approached flat, disc-like shapes and under weak constraints

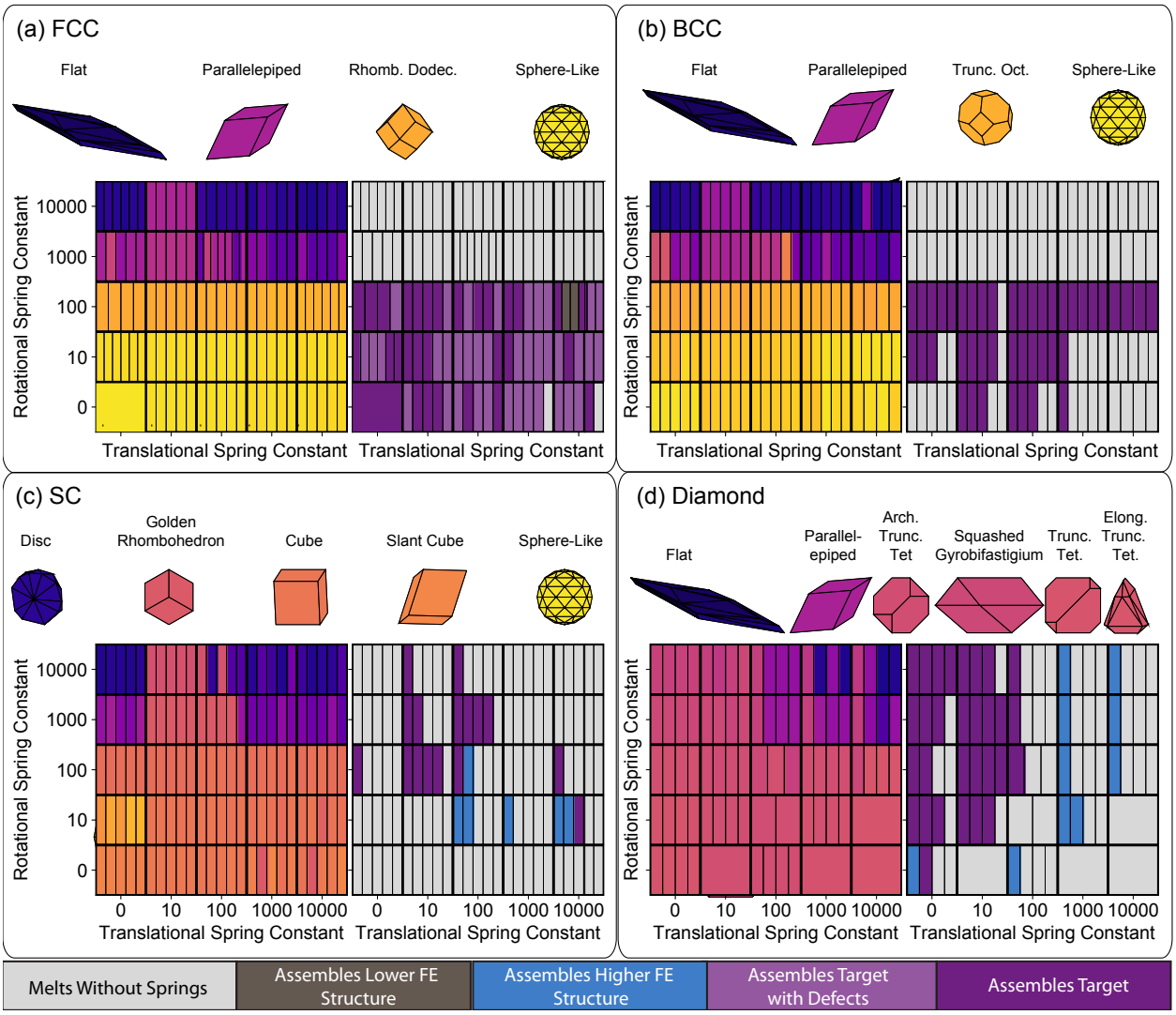

Figure 5.4: **Effect of Spring Constraints on $\langle \alpha_\Lambda \rangle$ and target structure stability for (a) FCC, (b) BCC, (c) SC, and (d) Diamond.** In each subfigure, the left panel corresponds to equilibrium particle shape obtained using digital alchemy for the indicated target structure with the indicated constraints. The colors used in the left panel refer to the shapes above the panel. The right panel denotes the stability of the shape in the target structure upon release of the constraints, where grey, brown, purple, and blue denote that the system melts upon release of the springs, does not melt but assembles a different crystal, assembles a crystal with higher F than the target, and assembles the target (with lighter purple denoting that the shape assembles the target structure with defects), respectively.

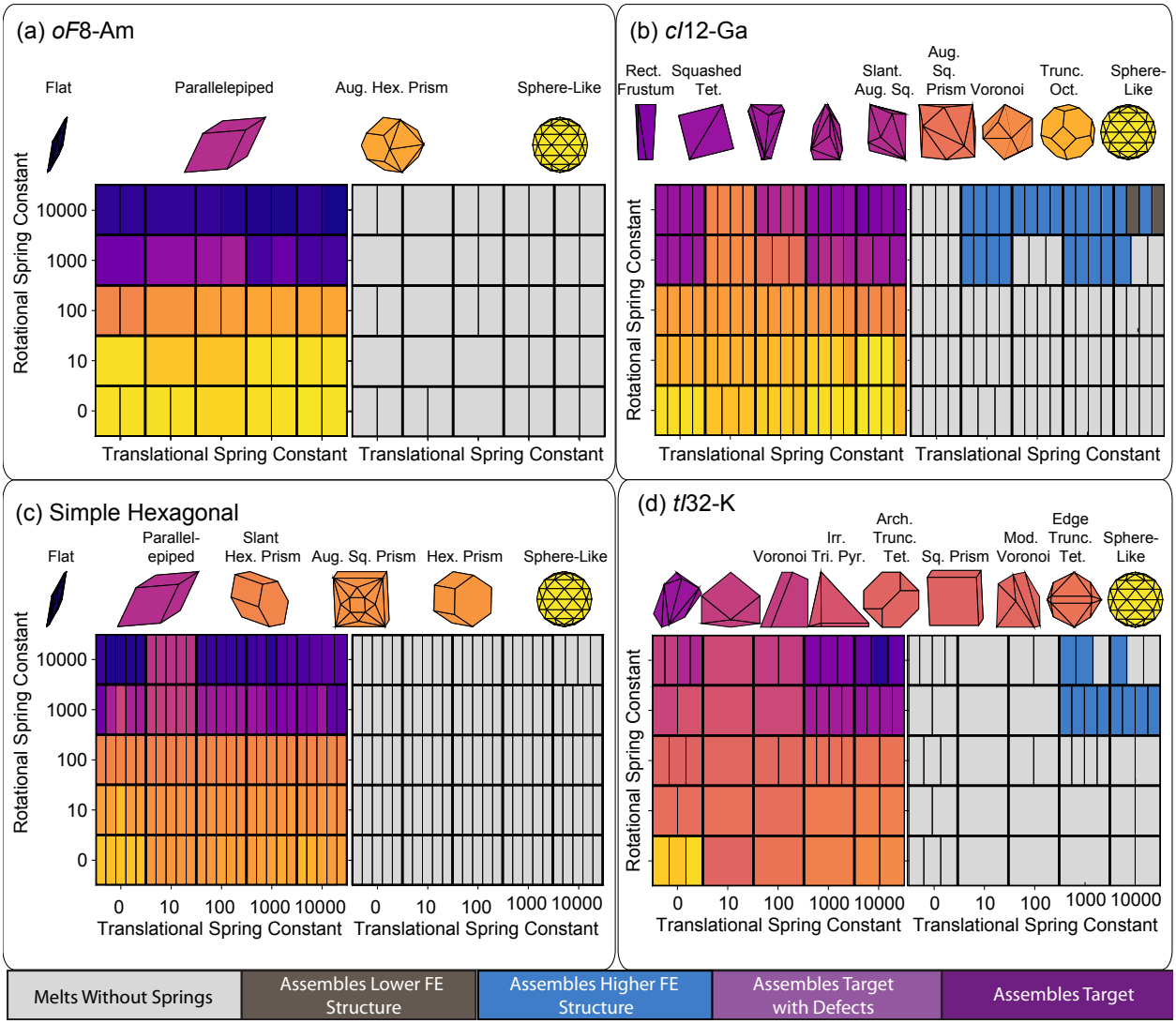

Figure 5.5: **Effect of Spring Constraints on $\langle \alpha_\Lambda \rangle$ and Target Structure Stability for More Complex Phases: (a) $oF8$-Am, (b) $cI12$-Ga, (c) Simple Hexagonal and (d) $tI32$-K.** In each subfigure, the left panel corresponds to equilibrium particle shape obtained using digital alchemy for the indicated target structure with the indicated constraints. The colors used in the left panel refer to the shapes above the panel. The right panel denotes the stability of the shape in the target structure upon release of the constraints, where grey, brown, purple, and blue denote that the system melts upon release of the springs, does not melt but assembles a different crystal, assembles a crystal with higher F than the target, and assembles the target (with lighter purple denoting that the shape assembles the target structure with defects), respectively.

went towards the global free energy well (sphere-like shapes in FCC), with the exception of diamond. [iv]

Another general feature is the large effect of rotational spring constant q – for every structure, there are greater similarities across the range of translational spring constant k, however the equilibrium shape drastically changes for different q.

We were unable to find shapes that self-assemble the target structures for most systems. In $oF8$-Am, which is topologically similar to FCC, the lowest free energy shapes transitioned to FCC or HCP. In simple hexagonal (Fig. 5.5(c)), the columns would shear alongside each other, forming a hexagonal columnar phase, with little order in the xy plane. $cI12$-Ga and $tI32$-K had similar phenomena – the only $\langle \alpha_\Lambda \rangle$ that did not melt once the springs were cut was often a long shape found in simulations with large k and q values. However, the shapes did not self-assemble the target structure, rather assembling a structure with a *larger* free energy than the target, alluding to some kinetic barrier for self-assembly. These sorts of systems may be a rich area for further inquiry using advanced sampling methods, such as umbrella sampling or forward flux sampling.

5.4 Conclusions

From the data presented in Chapter V it is clear that using DA in shape space requires further investigation as to its implementation. I have identified a few concerns within this chapter regarding the current implementation:

- **Resulting Shapes from DA may be Rounder than Necessary.** Given that there is a large free energy well in shape space surrounding sphere-like shapes in the FCC structure, it may be possible that DA is driven by two design principles in simulation: the overall free energy minimum and the constraints. The balance of these two motivations is crucial and non-trivial.

[iv] As diamond is topologically distinct from FCC, and may have been confined to a local free energy well.

- **Constraining Particles to the Target with Springs Leads to a Wide Array of Results.** As seen in Figs. 5.4-5.5, the values of spring constant k and q can change the resulting $\langle \alpha_\Lambda \rangle$ from a DA simulation. Furthermore, the effects of k and q are not universal, and different targets may require different magnitudes of k and q to properly search shape space.

- **Spring Constraints are Not Always Sufficient to Find a Suitable Shape for Self-Assembly.** For the structures shown in Fig. 5.5, DA was unable to find a suitable shape to self-assemble any of the target structures, either because of strongly competing structures (5.5(a,c)) or potential kinetic obstacles (5.5(b,d))

So knowing all this, how do we more generally implement DA in shape space? With T. C. Moore and R. A. LaCour, I have developed a few potential methodologies, to be tested in continued work. These methodologies, in addition to the pros and cons of each, are shown in Fig. 5.6.

Using a Distribution of Constraint Strengths An under-constrained system will transition to FCC during an alchemical simulation. An over-constrained system will result in a flat $\langle \alpha_\Lambda \rangle$, which will always form a variety of liquid crystal. Where is the *just right* amount of constraint? Because this can vary greatly based upon the target structure, we propose that using a distribution of k and q values assigned randomly to particles in the simulation might be sufficient to avoid the effects of an over- or under-constrained system, while sampling a variety of microstates.

The main benefit of this implementation is little anticipated increase in computational complexity and it would not require much new code within HOOMD-Blue. However, it may not address the global free energy well surrounding sphere-like shapes or other competing phases. Furthermore, it is unknown whether it addresses the universal effects of over- and under-constrained systems, as the strongest constraint may serve as a limiting case to the other particles.

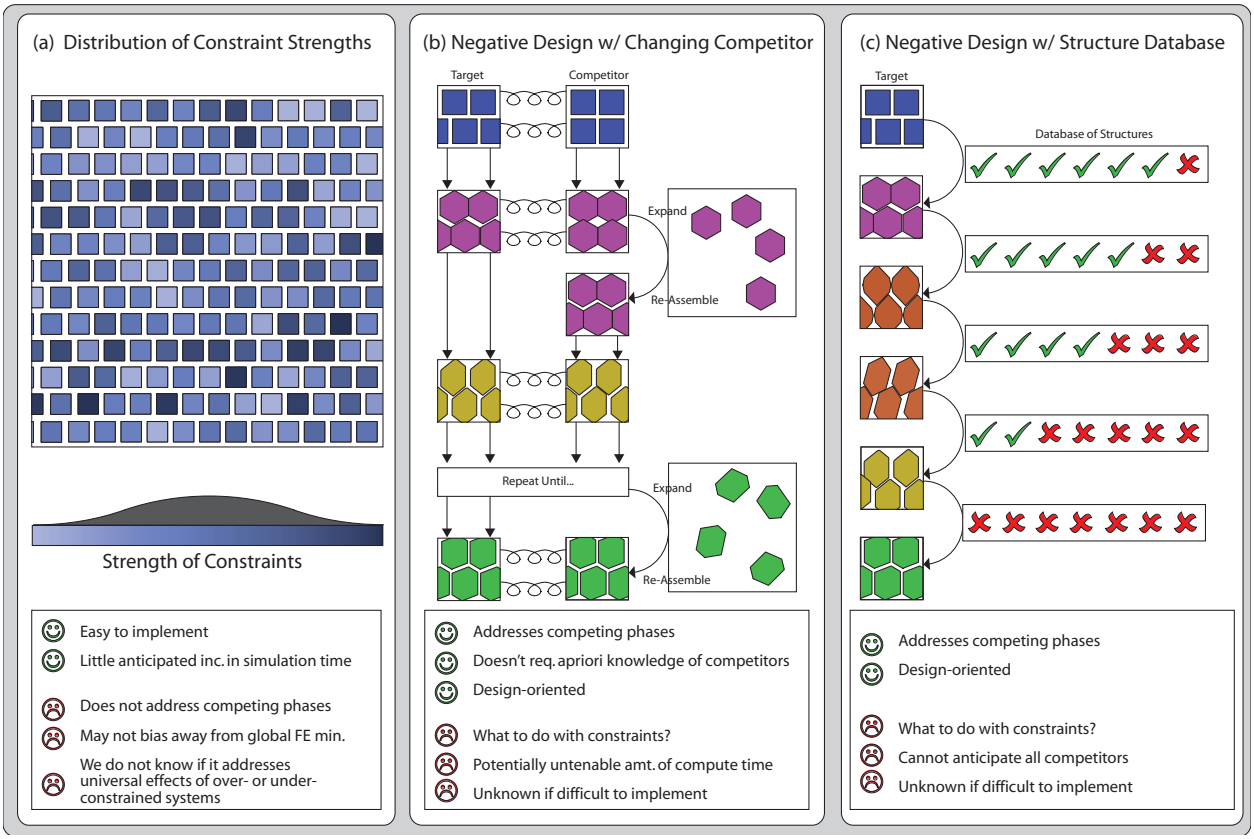

Figure 5.6: **Proposed Implementations of Digital Alchemy.** (a) Distribution of Constraint Strengths. Instead of a constant or changing constraint strength, each simulation is initialized with a normal distribution of strengths. The distribution should be centered at a strength where the crystal structure is maintained, but the distribution may go as low as 0. (b) Negative Design with Changing Competitor. Here, two systems are initialized within the same ensemble and with the same "Alchemostat" (*i.e.* their shapes change simultaneously). The shape is sampled positively with the target and negatively with the competitor. When the shape becomes geometrically forbidden in the competitor, the competitor system is expanded and re-assembled into a new competing phase. This is repeated until the competitor assembles the target phase. (c) Negative Design with a Structure Database. Here, a single system is initialized and run with an advanced sampling method, such as umbrella sampling.[12] The sampling method queries a database of structures, and shapes are accepted/rejected based upon their ability to fit geometrically in the competing phases. The simulation minimizes the FE and the number of competing phases that the shape may fit into.

Negative Design with Changing Competitor. Here, two systems are initialized within the same ensemble and with the same "Alchemostat" (*i.e.* their shapes change identically) but in two different crystal structures. The shape is sampled positively with the target and negatively with the competitor. When the shape becomes geometrically forbidden in the competitor, the competitor system is expanded and re-assembled into a new competing phase. This is repeated until the competitor assembles the target phase.

This implementation holds true to the mission of DA for design – find a shape that will self-assemble a target phase and avoid assembling other competing phases. However, expanding and re-assembling a system may drastically increase the length of the simulation to an unknown extent, and the implementation of this may be difficult. Furthermore, this case does not address the issue of structural constraints.

Negative Design with a Structure Database. Here, a single system is initialized and run with an advanced sampling method, such as umbrella sampling.[12] The sampling method queries a database of structures, and shapes are accepted/rejected based upon the free energy difference of the shape within the target and within the competing phases.

This implementation may be the most advisable given the problem and our current computation tools, as it does address competing phases and we anticipate it being less computationally costly than option (1). However, this implementation requires a preemptive knowledge of the competing phases, and the exclusion of any competing phase may result in shapes which do not successfully assemble the target phase. Furthermore, the choice of assessment for the competitor phases is crucial – we propose using a method such as phase switch Monte Carlo[13] which can estimate the difference in free energies between two phases.

Outlook It is unknown if these methods will find shapes capable of assembling *any* phase, and further design dimensions may be necessary, including multiple particles types, inter-particle interactions, or polydispersity.

References

[1] Chen, E. R., Klotsa, D., Engel, M., Damasceno, P. F. & Glotzer, S. C. Complexity in surfaces of densest packings for families of polyhedra. *Phys. Rev. X* **4**, 11024 (2014).

[2] Cersonsky, R. K., van Anders, G., Dodd, P. M. & Glotzer, S. C. Distinguishing Packing and Assembly Behavior via Phase Transitions in Shape Space. *In Preparation* (2017).

[3] Cersonsky, R. K., Dshemuchadse, J., Antonaglia, J., van Anders, G. & Glotzer, S. C. Pressure-Tunable Band Gaps in an Entropic Crystal. *Phys. Rev. Mat.* (2018).

[4] Du, C. X., van Anders, G., Newman, R. S. & Glotzer, S. C. Shape-driven solidsolid transitions in colloids. *Proceedings of the National Academy of Sciences* **114**, E3892–E3899 (2017). `1603.00727`.

[5] Ni, R., Gantapara, A. P., de Graaf, J., van Roij, R. & Dijkstra, M. Phase diagram of colloidal hard superballs: from cubes via spheres to octahedra. *Soft Matter* **8**, 8826 (2012).

[6] Anderson, J. A., Irrgang, M. E. & Glotzer, S. C. Scalable Metropolis Monte Carlo for simulation of hard shapes. *Computer Physics Communications* **204**, 21 – 30 (2016).

[7] Anderson, J. A., Lorenz, C. D. & Travesset, A. General purpose molecular dynamics simulations fully implemented on graphics processing units. *Journal of Computational Physics* **227**, 5342–5359 (2008).

[8] Damasceno, P. F., Engel, M. & Glotzer, S. C. Predictive Self-Assembly of Polyhedra into Complex Structures. *Science* 453–457. `1202.2177`.

[9] Steinhardt, P. J., Nelson, D. R. & Ronchetti, M. Bond-orientational order in liquids and glasses. *Physical Review B* 784–805.

[10] Anderson, J. A., Lorenz, C. D. & Travesset, A. General purpose molecular dynamics simulations fully implemented on graphics processing units. *Journal of Computational Physics* **227**, 5342–5359 (2008).

[11] Geng, Y., van Anders, G., Dodd, P. M., Dshemuchadse, J. & Glotzer, S. C. Engineering entropy for design. *Submitted* `1712.02471`.

[12] Torrie, G. M., Valleau, J. P Nonphysical sampling distributions in Monte Carlo free-energy estimation: Umbrella sampling. *Journal of Computational Physics* **23**, 187-199 (1977).

[13] Bruce, A. D., Jackson, A. N., Ackland, G. J. & Wilding, N. B. Lattice-switch monte carlo method. *Phys. Rev. E* **61**, 906–919 (2000).

CHAPTER VI

Photonic Crystals

Color is my day-long obsession, joy, and torment.

– Claude Monet

Many butterflies, birds, and chameleons owe their spectacular colors to the microscopic patterns within their wings, feathers, or skin.[1, 2, 3, 4, 5, 6] These microscropic patterns, known as *photonic crystals*, affect the transmission, and reflection of light. This can lead to a phenomenon known as a photonic band gap (PBG) resulting in the total reflection of light with wavelengths commensurate with the length scale of the pattern, *i.e.* for photonic crystals on the nanoscale, where the particles or lattice parameters are on the length scale of nanometers to microns, light with wavelengths of nanometers or microns will be reflected. It follows then that the colloidal self-assembly community, photonic properties are very often used as motivation for crystal design. [3, 4, 7, 8, 9, 10, 11, 12, 13, 14, 15]

A Brief History. The existence of structural color was first noted in 1888 by Lord Rayleigh[16] , when he observed that the color of his crystalline specimen changed with rotation (similar to the phenomenon of "iridescence"). Further observations were made over the following century about structurally dependent color, often inspired by the brilliant blue and green hues found in nature that did not originate in any sort of pigmentation or exhibited similar iridescence as Lord Rayleigh's sample.[2] About 100 years after Lord Rayleigh's first

observation, Eli Yablonovitch published Ref. [17], which postulated the existence of crystals that would reflect certain wavelengths of lights from all directions, naming them "photonic crystals". Within that year, Sajeev John made the same observation independently.[18] Yablonovitch had theorized that the cubic-close packed structure, more commonly known as fcc, would possess a complete photonic band gap when spheres with a high dielectric constant (hereon called "dielectric medium" or "dielectric"). However this was later disproved, as fcc exhibits a "pseudo-gap", where the reflection of light is dependent on the incidence of the light wave, much like the crystal in Rayleigh's observation. It wasn't until 1990 that a crystal structure with a complete photonic band gap was found – Chan, Ho, and Soukolis [19] discovered that the diamond structure, when either the lattice sites were occupied by spheres of the low or high dielectric medium, would exhibit a large photonic band gap between bands 2 and 3. A few years later, Yablonovitch responded with a modified FCC structure, known as "Yablonovite", which exhibited a complete photonic band gap.[20] With this, analytical and experimental study of photonic crystals exploded, with many potential photonic crystal structures reported.

Known 3D Photonic Crystals These photonic crystal structures spanned different topologies and were derived from natural analog or geometric arguments. Chan, Ho, and Soukolis found that adding dielectric rods between the lattice sites of the diamond structure, as opposed to spheres on the lattice sites, greatly increased the PBG and was more readily experimentally realizable.[21] They also reported PBGs found in the A7 family of structures [22] and worked with experimental collaborators to develop a wide array of layer-by-layer structures, including the woodpile family of structures.[21, 23] Layer-by-layer structures, or structures formed by the stacking of 2D structures into 3D, became popular due to the synthesis possibilities, with a variety of 2D topologies for PBG crystals reported.[24, 25, 26]

Sözüer and Haus showed that the FCC structure would have a complete PBG, however it only occurred when the lattice sites were occupied by the low dielectric medium, the reverse

of computations completed by Yablonovitch in 1987.[27] Sözüer and Haus also reported a complete photonic band gap in the simple cubic structure, with either rods connecting neighboring lattice sites or with spheres of the low dielectric constant on the lattice sites,[28] which was later expanded upon by Maldovan, *et al.* [29] In addition to simple cubic systems, Maldovan also expanded upon the investigations of the gyroid (first theorized by Martin-Moreno in 1999), diamond, and face-centered photonic crystals, showing that 1) many large band gap structures resembled diamond and 2) there were many FCC space groups in which a photonic band gap can occur.[30, 31, 32]

Known Design Principles. The general design principles for photonic crystals have largely stemmed from the more computationally straightforward 2D case. In 2D, the two polarizations of photonic band structure, the transverse electric (TE) modes and the transverse magnetic (TM) modes, can be computed separately, leading to simpler analysis of the underlying field configurations. In 1993, Meade *et al.* showed that producing a photonic band gap between either set of modes came with different topological requirements. In 2D, a gap will occur when there is a large change in concentration factor f, or the proportion of electric energy density found in the high dielectric medium, between two consecutive modes. This leads to the classification of the mode below a PBG as the "dielectric band", where the electric energy is found in the high dielectric medium, and the mode below the PBG as the "air band", where the electric energy is found in the low dielectric medium. These monikers were quickly adopted to describe the modes delineating a PBG in 1-, 2-, and 3D. The difference in concentration factor between consecutive modes can be optimized in systems where the high dielectric medium is connected (for TE modes) or where the high dielectric medium is sufficiently isolated (for TM modes). The two dimensional triangular lattice optimizes both effects, and thereby has a gap between both TE and TM modes.[33] Due to this observation about TE modes in 2D crystals, network structures have been a focus of PBG materials design in 3D.[24, 25, 26, 34, 35]

Many publications have pointed to certain symmetry elements as conducive to producing a PBG. The symmetry elements of a crystal directly relate to the degeneracies within the PBG structure and the BZ over which the PBG is calculated. Understanding the degeneracies inherent to particular symmetry groups is a focus of group theory, and can be used to predict which space groups are prohibited from having a PBG between specific eigenmodes of their photonic band structure.[36] However, group theory cannot be used to predict where a PBG *will* occur. Due to the relationship between symmetry and the BZ, the set of structures with FCC lattices have been the focus of much literature,[17, 32] based upon the assumption that the frequency ω roughly scales with $|\vec{k}|$ at which it is computed. Given that a more spherical BZ would lead to a more uniform $|\vec{k}|$, it would follow that the bands would be relatively flat, less likely to intersect. Therefore, the lattice with the most spherical BZ, FCC, would be most likely to exhibit a band gap.[37]

Computing the Photonic Band Structure. There has also been great progress in approaches to computing photonic band gaps. The photonic band structure corresponds to the eigenvalues of the eigenproblem:

$$\nabla \times \frac{1}{\varepsilon(\boldsymbol{r})} \left(\nabla \times \boldsymbol{H}(\boldsymbol{r})\right) = \frac{\omega^2}{c^2} \boldsymbol{H}(\boldsymbol{r}) \tag{6.1}$$

calculated across reciprocal space. Practically, this can be computed in O(n) as any other eigenproblem of the form $A\boldsymbol{v} = \lambda \boldsymbol{v}$, however, the treatment of the $\varepsilon(\boldsymbol{r})$ term has a large effect on the convergence and therefore computational complexity of the problem. In 1990, Sözüer and Haus identified this convergence problem, wherein the truncation of basis functions within the approximation of the matrix components of 6.1 would lead to incorrect values for PBG size, and corrected errors in [19] due to this issue.[27] Instead, Sözüer and Haus suggested a smoothed representation of $\varepsilon(\boldsymbol{r})$, or effective dielectric function, which was implemented and explained well in [38] .

This method of solving 6.1 has been implemented in MPB, an open-source code which

uses an iterative eigensolver on a planewave basis. MPB is a frequency-domain calculation software, such that degenerate modes of the photonic band structure can be easily identified, wherein the time-domain software MEEP degenerate modes would be indistinguishable.[38]

References

[1] Michielsen, K. & Stavenga, D. Gyroid cuticular structures in butterfly wing scales: biological photonic crystals. *Journal of The Royal Society Interface* **5**, 85–94 (2008).

[2] Onslow, H. On a Periodic Structure in Many Insect Scales, and the Cause of Their Iridescent Colours. *Philosophical Transactions of the Royal Society B: Biological Sciences* **211**, 1–74 (1923).

[3] Vukusic, P. & Sambles, J. R. Photonic structures in biology. *Nature* **424**, 852–855 (2003).

[4] Galusha, J. W., Richey, L. R., Gardner, J. S., Cha, J. N. & Bartl, M. H. Discovery of a diamond-based photonic crystal structure in beetle scales. *Physical Review E* **77**, 050904 (2008).

[5] Yin, H. *et al.* Amorphous diamond-structured photonic crystal in the feather barbs of the scarlet macaw. *Proceedings of the National Academy of Sciences* **109**, 10798–10801 (2012).

[6] Teyssier, J., Saenko, S. V., van der Marel, D. & Milinkovitch, M. C. Photonic crystals cause active colour change in chameleons. *Nature Communications* **6**, 6368 (2015).

[7] Biswas, R., Sigalas, M. M., Subramania, G. & Ho, K.-M. Photonic band gaps in colloidal systems. *Physical Review B* **57**, 3701–3705 (1998).

[8] Li, Z.-Y. & Zhang, Z.-Q. Fragility of photonic band gaps in inverse-opal photonic crystals. *Physical Review B* **62**, 1516–1519 (2000).

[9] Xia, Y., Gates, B. & Li, Z.-Y. Self-Assembly Approaches to Three-Dimensional Photonic Crystals. *Advanced Materials* **13**, 409–413 (2001).

[10] Ducrot, É., He, M., Yi, G.-R. R. & Pine, D. J. Colloidal alloys with preassembled clusters and spheres. *Nature Materials* **16**, 652–657 (2017).

[11] Aguirre, C. I., Reguera, E. & Stein, A. Tunable Colors in Opals and Inverse Opal Photonic Crystals. *Advanced Functional Materials* **20**, 2565–2578 (2010).

[12] Galisteo-López, J. F. *et al.* Self-Assembled Photonic Structures. *Advanced Materials* **23**, 30–69 (2011).

[13] Vigneron, J. P. & Simonis, P. Natural photonic crystals. *Physica B: Condensed Matter* **407**, 4032–4036 (2012).

[14] Rauh, A., Carl, N., Schweins, R. & Karg, M. Role of Absorbing Nanocrystal Cores in Soft Photonic Crystals: A Spectroscopy and SANS Study. *Langmuir* **34**, 854–867 (2018).

[15] Cersonsky, R. K., Dshemuchadse, J., Antonaglia, J., van Anders, G. & Glotzer, S. C. Pressure-Tunable Band Gaps in an Entropic

Crystal. *Phys. Rev. Mat.* (2018).

[16] Rayleigh, L. XXVI. On the remarkable phenomenon of crystalline reflexion described by Prof. Stokes. *The London, Edinburgh, and Dublin Philosophical Magazine and Journal of Science* **26**, 256–265 (1888).

[17] Yablonovitch, E. Inhibited spontaneous emission in solid-state physics and electronics. *Physical Review Letters* **58**, 2059–2062 (1987).

[18] John, S. Strong localization of photons in certain disordered dielectric superlattices. *Physical Review Letters* **58**, 2486–2489 (1987).

[19] Ho, K. M., Chan, C. T. & Soukoulis, C. M. Existence of a photonic gap in periodic dielectric structures. *Physical Review Letters* **65**, 3152–3155 (1990).

[20] Yablonovitch, E., Gmitter, T. & Leung, K. Photonic band structure: The face-centered-cubic case employing nonspherical atoms. *Physical Review Letters* **67**, 2295–2298 (1991).

[21] Ho, K., Chan, C., Soukoulis, C., Biswas, R. & Sigalas, M. Photonic band gaps in three dimensions: New layer-by-layer periodic structures. *Solid State Communications* **89**, 413–416 (1994).

[22] Chan, C., Datta, S., Ho, K. & Soukoulis, C. A 7 structure: A family of photonic crystals. *Physical Review B* **50**, 1988–1991 (1994).

[23] Sözüer, H. & Dowling, J. P. Photonic Band Calculations for Woodpile Structures. *Journal of Modern Optics* **41**, 231–239 (1994).

[24] Johnson, S. G. & Joannopoulos, J. D. Three-dimensionally periodic dielectric layered structure with omnidirectional photonic band gap. *Applied Physics Letters* **77**, 3490–3492 (2000).

[25] Leung, K. M. Diamondlike photonic band-gap crystal with a sizable band gap. *Physical Review B* **56**, 3517–3519 (1997).

[26] Roundy, D. & Joannopoulos, J. Photonic crystal structure with square symmetry within each layer and a three-dimensional band gap. *Applied Physics Letters* **82**, 3835–3837 (2003).

[27] Sözüer, H. S., Haus, J. W. & Inguva, R. Photonic bands: Convergence problems with the plane-wave method. *Physical Review B* **45**, 13962–13972 (1992).

[28] Sözüer, H. S. & Haus, J. W. Photonic bands: simple-cubic lattice. *Journal of the Optical Society of America B* **10**, 296 (1993).

[29] Maldovan, M. & Thomas, E. L. Photonic crystals: six connected dielectric networks with simple cubic symmetry. *Journal of the Optical Society of America B* **22**, 466 (2005).

[30] Maldovan, M., Ullal, C. K., Carter, W. C. & Thomas, E. L. Exploring for 3D photonic bandgap structures in the 11 f.c.c. space groups. *Nature Materials* **2**, 664–667 (2003).

[31] Maldovan, M. & Thomas, E. L. Diamond-structured photonic crystals. *Nature materials* **3**, 593–600 (2004).

[32] Maldovan, M., Ullal, C. K., Carter, W. C. & Thomas, E. L. Exploring for 3D photonic bandgap structures in the 11 f.c.c. space groups. *Nature Materials* **2**, 664–667 (2003).

[33] Meade, R. D., Rappe, A. M., Brommer, K. D. & Joannopoulos, J. D. Nature of the photonic

band gap: some insights from a field analysis. *Journal of the Optical Society of America B* **10**, 328 (1993).

[34] Maldovan, M. Layer-by-layer photonic crystal with a repeating two-layer sequence. *Applied Physics Letters* **85**, 911–913 (2004).

[35] Men, H., Lee, K. Y. K., Freund, R. M., Peraire, J. & Johnson, S. G. Robust topology optimization of three-dimensional photonic-crystal band-gap structures. *Optics Express* **22**, 22632 (2014).

[36] Watanabe, H. & Lu, L. Space Group Theory of Photonic Bands. *Physical Review Letters* **121**, 263903 (2018). 1805.10103.

[37] Joannopoulos, J. *Photonic Crystals: Molding the Flow of Light, 2nd Edition* (Princeton University Press, 2008).

[38] Johnson, S. & Joannopoulos, J. J. Block-iterative frequency-domain methods for Maxwell's equations in a planewave basis. *Optics Express* **8**, 173 (2001).

CHAPTER VII

The Unexpected Diversity of 3D Photonic Crystals

I was from the first inclined to attribute the colours to a periodic structure.

– Lord Rayleigh

The contents of this chapter are taken from "Unexpected Diversity of Three-Dimensional Photonic Crystals". R. K. Cersonsky, J. A. Antonaglia, B. D. Dice, and S. C. Glotzer. *Submitted.*

7.1 Introduction

Which 3D crystals will possess an omnidirectional photonic band gap (PBG)? The current understanding within the scientific community is: this question has been largely answered.

Much of what is assumed for 3D PBGs comes from our experiences with 2D PBGs. Meade, *et al.* explain the origins of PBGs in 2D crystals by looking at the modes of the photonic band structure defining the PBG.[i] They showed that PBGs occur when there is a large shift in where the electric energy density is localized. In the band below the PBG, the electric energy density primarily resides in the medium with the higher dielectric constant (hereon "dielectric"); this band is known as the "dielectric band" where dielectric constant ε

[i]The photonic band structure is given by solving, in reciprocal space, the eigenproblem $\nabla \times \frac{1}{\varepsilon(\vec{r})} \nabla \times \vec{H}(\vec{r}) = \left(\frac{\omega}{c}\right)^2 \vec{H}(\vec{r})$, where $\varepsilon(\vec{r})$ is the spatially-dependent dielectric function, c is the speed of light, and $\vec{H}(\vec{r})$ is the magnetic field.

is the square of the index of refraction n. Above the PBG, the electric energy density is in the medium with the lower dielectric constant (typically called "air"); this band is known as the "air band." Meade, *et al.* suggest one must aim to decrease the energy of the dielectric band in order to increase the size of the PBG. For a PBG between the transverse electric (TE) modes,[ii] this requires that regions of dielectric be connected.[6] Likewise, the importance of energy localization suggests that the greater the difference in ε of the two regions, the larger the PBG, as this will decrease the similarity between the dielectric and air band. These 2D principles are used to understand and design 3D photonic crystals; even the terminology of dielectric and air band has become convention in 3D PBG crystals.[7]

Additionally, Yablonovitch,[8] John,[9] and Ho, *et al.* [10] pointed to the sphericity of the Brillouin Zone (BZ), which is the reciprocal space analog to the real space primitive unit cell, as an important feature for predicting which photonic crystals have a PBG. Their reasoning suggests that cubic face-centered (cF) and body-centered (cI) lattices are the most likely targets for PBGs, as they have the most spherical BZs. These have been realized, but are highly sensitive to thermal disorder.

These heuristics – connectivity of the dielectric, increasing gap size with increasing ε, and spherical BZ – have proved useful, but have inadvertently restricted the design search space to structures near diamond and inverse opal, both of which are face-centered cubic structures that exhibit PBGs when the dielectric forms a continuous network.[10, 11, 12, 13, 14, 7, 15, 16, 17, 18, 19] Here we assess the fitness of these design rules using a large dataset of PBG crystals, and demonstrate that the space of PBG crystals is much richer than previously thought, going well beyond these heuristics.

[ii] One of the two polarizations of light in 2D, the other being transverse magnetic, or TM.

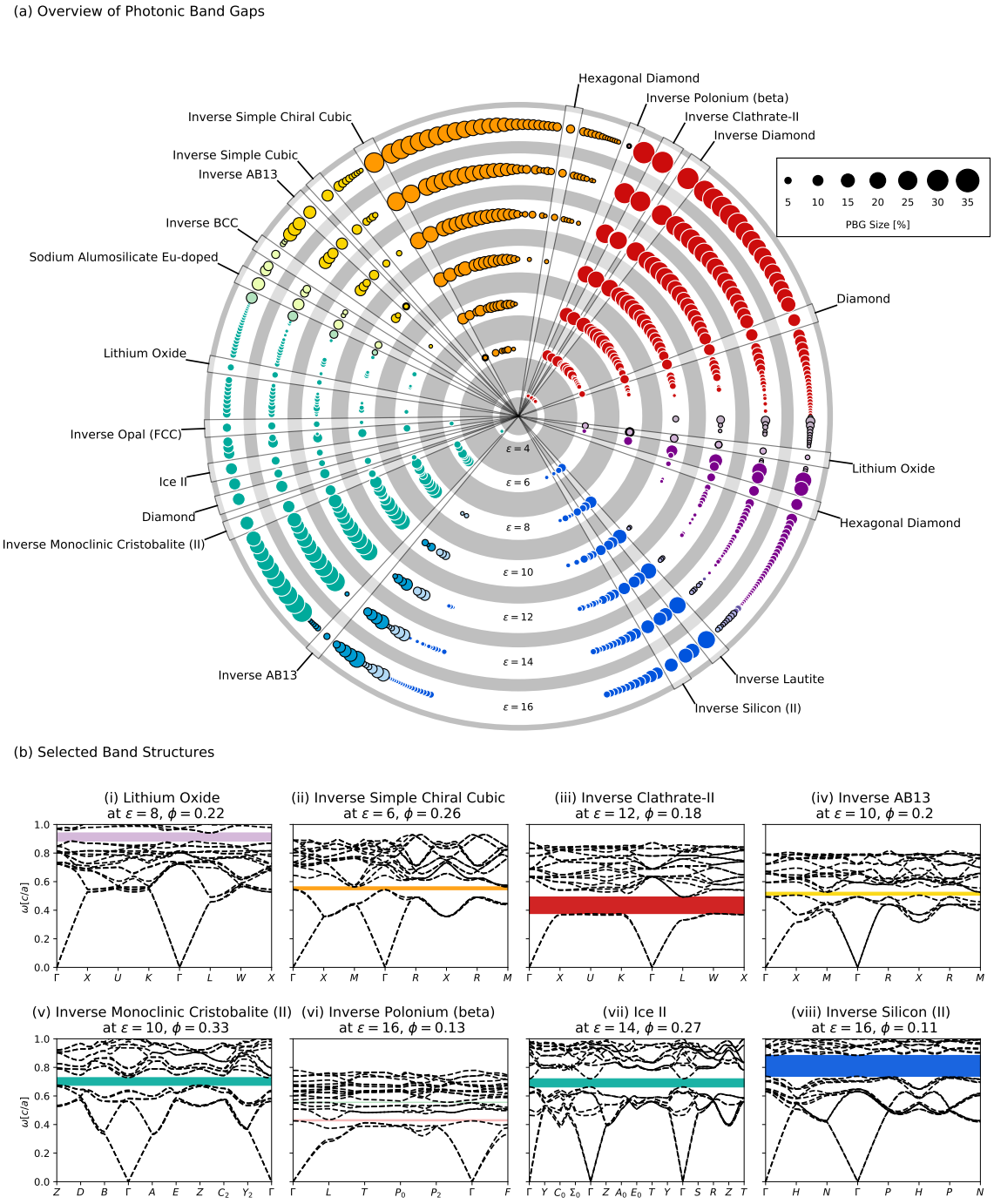

Figure 7.1: **PBG Properties of Nature-Inspired Structural Templates.** (a) The largest PBGs in each PBG location found for each structure computed for $\varepsilon = 4$–16. Circle areas are proportional to the PBG size; colors correspond to the location of the PBG. Some structures are shown more than once, since some structures were found to exhibit PBGs in different locations at different filling fractions. Structures that have been previously studied or noted elsewhere in the text have been labeled. (b) Selected band structures, plotted for the first 20 bands across reciprocal space. (i) Lithium Oxide, (ii) Inverse Simple Chiral Cubic, (iii) Inverse Clathrate II, (iv) Inverse AB_{13}, (v) Monoclinic Tridymite, (vi) Inverse β-Polonium (the only template found to have a PBG between Bands 3-4) , (vii) Ice II, and (viii) Inverse Silicon II.

7.2 Results

Our data set consists of 2,714 crystal structures from multiple sources.[20, 21] Each structure is used as a template, with identical dielectric or air spheres on every lattice site for the "direct" or "inverse" versions, respectively. We screened each structure for PBGs between the first 20 bands across the structural parameters of volume filling fraction ϕ (from 0-1) and dielectric constant ε (from 4-16 in reduced units), resulting in 151,593 band structure calculations via MIT Photonic Bands (MPB)[22] and managed with the *signac* data framework.[23] PBGs are reported as dimensionless percentages, *i.e.* , the range of frequencies within the PBG ($\Delta\omega$) divided by the mid-gap frequency (ω^*).[22] Of the photonic band structures studied, 12,778 contain PBGs of size 0.1% or larger for $0.022 \leq \phi \leq 0.711$. The lowest ε resulting in a PBG is $\varepsilon = 4$ (agreeing with literature)[10] and many structures have PBGs with values of ε as low as 6. In total, we find 471 unique PBGs ¿ 0.1% in 351 structures (some structures exhibit PBGs at more than one band location at different filling fractions). A summary of the PBGs is shown in Fig. 7.1, with the maximum gap size for each location (above band 2 and higher) indicated by the size and color of the circles.[iii,iv] Photonic band structures for templates that are of special interest or mentioned later in the text are shown in Fig. 7.1(b). Results were validated where possible against previous literature. [24, 25, 22, 10, 14, 12],[v]

7.2.1 Correlations with Crystal Symmetry

Of the 14 types of Bravais lattices, we find PBGs for all of them, including monoclinic and triclinic lattices whose asymmetry should preclude a PBG based on current assumptions. In Fig. 7.2(a), we find that PBGs most often exist not only in cF and cI lattices, but also in rhombohedral (hR) and cubic primitive (cP) lattices, despite their aspherical BZs. As

[iii]PBGs under the first band or between bands 1 and 2 are physically impossible, as the first two bands will approach zero frequency at the center of the BZ.

[iv]The gap atlas, selected photonic band structures, and isosurface representations of structures mentioned in the main text can be found in the Additional Data.

[v]Validation data sets can be found in the Additional Data.

expected, large PBGs (¿25%) tend to occur in structures with diamond or gyroid-like topologies, but surprisingly, they also occur in tI lattices, which can have highly aspherical BZs (Fig. 7.2(b)(i)).[vi] Thus a nearly spherical BZ is neither necessary nor sufficient to produce a PBG.[vii] Additionally, we find that a large fraction of PBGs between bands 2 and 3 are in cF and tI structures, and PBGs between bands 5 and 6 are primarily found in cP structures, as shown in Fig. 7.2(b)(ii and iii). The former corroborates earlier correlations suggesting a strong link between symmetry elements of cF space groups and PBG location.[13, 26]

7.2.2 Connectivity of the High Dielectric Medium

Next, we look at the 2D heuristic of connectivity of the dielectric.[6] For any structure realized with monoatomic spheres on every lattice site, there are two connectivity thresholds defined by the geometry. The first, which we denote ϕ_N, is $\min(\phi)$ such that the dielectric forms a continuous network, for direct and inverse structures. The second, which we denote ϕ_T, is $\min(\phi)$ such that the dielectric spheres on any two lattice sites overlap, and can only be defined for direct structures. For some direct structures, $\phi_N = \phi_T$. As shown in Fig. 7.2(b), we find that many PBGs, including large PBGs, occur for $\phi < \phi_N$ and for $\phi < \phi_T$, especially in PBGs at high frequencies, as these modes can more easily travel between disconnected regions of dielectric.

7.2.3 Dielectric Constant

Finally, in our dataset we find 41 of 471 cases where the PBG size is non-monotonic with ε, as seen in Fig. 7.2(d)(iii). The most dramatic non-monotonicity occurs for lithium oxide (also known as the fluorite or the C1 structure), whose PBG between bands 17 and 18 increases for $6 \leq \varepsilon \leq 9$ but then decreases to half its maximum size for $9 \leq \varepsilon \leq 16$, as seen

[vi] We can compare the sphericity of the BZs using the isoperimetric quotient, defined as $\frac{36\pi V^2}{A^3}$, where IQ=1 for perfect spheres. The IQ of hR, cP, and tI lattices are at most $\pi/6 \approx 0.523$, whereas the IQ of cF and cI lattices are 0.7533 and 0.7404, respectively.

[vii] Discussions of the point group symmetry of the structures and Wyckoff sites, sphericity of the BZ, space group, and angles between nearest neighbor vectors can be found in the Additional Data.

in Fig. 7.2(d)(ii). The 8-9 PBG of space group 225 with tetrahedral sites was previously theorized in Maldovan *et al.* [13] and is monotonic with ε.

7.2.4 Field Analysis

To understand the failure of 2D heuristics extrapolated to 3D, we analyzed the configurations of electromagnetic modes delineating PBGs. In contrast to 2D, the 3D Maxwell eigenproblem is fully vectorial and conformations of field lines do not easily decompose into separate TE and TM polarizations. For select structures found to have a PBG, we calculated the electric displacement field $\vec{D}$ above and below the gap and constructed a flow diagram. Several general motifs of displacement field localization appear, as shown in Fig. 7.3(a)(i–viii).[viii] We quantify the fraction of electric energy found in the dielectric with the concentration factor f, as per convention.[6] For each PBG, we highlight four properties of the eigenmodes delineating the PBG: (1) band number, (2) Γ representation of the bands, (3) f, and (4) the motif that most closely resembles the displacement field lines. All of these properties are computed for the filling fraction that maximizes the PBG of a given structure and for the wavevectors $\vec{k}$ corresponding to the maxima and minima of the bands below and above the PBG, respectively. The dotted line signifies ϕ_N (for the structures shown, $\phi_N = \phi_T$).[ix]

In 2D the dielectric band typically has 50% or more of the electric energy density localized in the dielectric compared to the air band.[6] For example, from band 2 to 3 in diamond (Fig. 7.3(b)), the concentration factor f decreases by 0.1, *i.e.* 10% more of the electric energy is in the dielectric in band 2 as compared to band 3. There is no change in concentration factor between bands 8 and 9, and the concentration factor of band 15 is *higher* than that of band 14. Thus band 15 is more of a "dielectric band" than band 14, which implies that the concept of "dielectric" and "air" bands is not sufficient to describe the electric energy localization of the bands surrounding a gap in 3D.

[viii] More details on the reduction from vector fields to flow diagrams can be found in the Additional Data.

[ix] Field analysis for additional structures can be found in the Additional Data.

Indeed, 2D design rules aimed at lowering the energy of the dielectric band do not always optimize PBGs in 3D. There are more ways of localizing electric energy in 3D than in 2D, and these motifs do not fall neatly into the categories of "dielectric" and "air" band. In 3D, we find several motifs, in two broad categories: those that travel between adjacent unit cells (Fig. 7.3(a)(i–iii)) and those that remain confined to a single region of dielectric (Fig. 7.3(a)(iv–viii)). For modes with field conformations similar to Fig. 7.3(a)(i–iii), increasing the connectivity of the dielectric reduces the mode frequency. Therefore if this motif is found in the band below a gap (but not above the gap), increasing connectivity will enlarge the PBG, as seen in the PBG between bands 2-3 in Fig. 7.3(b)). However, if both modes or the mode above the gap exhibit this type of motif, increasing the connectivity will reduce or close the PBG, such as the 8-9 and 14-15 PBG in Fig. 7.3(b)).

We can use a similar analysis to explain the surprising relationship between ε and PBG size in the lithium oxide crystal structure shown in Fig. 7.2(b). The heuristic of monotonicity of gap size with ε assumes a mode configuration where the PBG is enlarged by higher localization in the dielectric, *e.g.* , when there is a distinct air band and dielectric band. However, as the PBG in lithium oxide decreases as the filling fraction approaches the connectivity threshold, this assumption is invalid, and the relationship of $\Delta\omega/\omega^*$ and ε is understandably more complex.

7.3 Conclusions

Although our data-driven exploration of the possible space of photonic band gap crystal structures calls into question many of the assumptions from 2D PBGs as they have been applied to 3D, it is clear that no single design rule applies to all PBGs. Further inquiry is needed to understand the PBGs in 3D, especially at higher frequencies, where these design rules most typically fail.

The 293 new PBG structures reported here should make for interesting targets, in particular for colloidal systems where the focus on diamond has been fraught with synthe-

sis obstacles. Several of the structures shown to have PBGs are known to assemble on colloidal length scales: lithium oxide (6% in direct form) and simple chiral cubic (3.4% PBG in direct form, 27% PBG in inverse form) can be self-assembled using polyhedral nanoparticles,[27, 28] the Clathrate II structure (33% PBG in inverse form) was recently found using DNA-programmed self-assembly,[29] and the AB_13 structure (13.3% PBG in inverse form) is easily achievable with binary mixtures of hard spheres. [30, 31] Furthermore there are structures, previously unstudied, that can be new targets for colloidal self-assembly, such as $tI8$[32] (6.0% PBG in direct form, 25% PBG in inverse form) or $cI16$[33] (6.4% PBG in direct form, 18.4% PBG in inverse form).

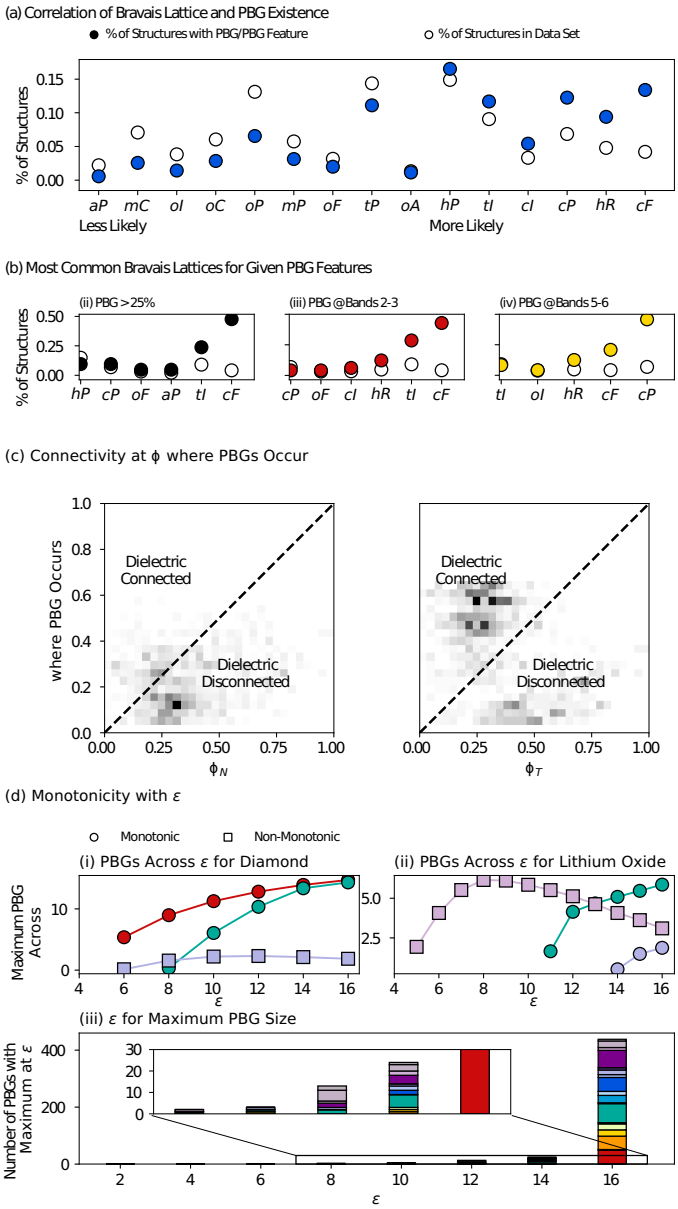

Figure 7.2: **Correlation of PBG Existence, Size, and Location with Structural Features.** (a) Bravais Lattice (BL) having a (i) PBG, (ii) PBG¿20%, (iii) PBG between bands 2-3, and (iv) PBG between bands 5-6. For each plot, unfilled and filled circles correspond to the fraction of structures with the given BL across the data set of 2,714 structure and that have the given PBG property, respectively. For (ii-iv), figures have been truncated to only show those BL which are likely to have the given PBG property. (b) Comparison of ϕ where PBGs Occur with ϕ_T and ϕ_N. Data above and below the dotted lines denote PBGs which occur when the dielectric is connected or disconnected, respectively, based upon the given threshold. (c) Monotonicity with ε. (i and ii) Size of PBGS in Diamond (i) and Lithium Oxide (ii) across ε. PBGs which are monotonic and non-monotonic with ε are denoted with circles and squares, respectively. (iii) ε where the maximum PBG size occurs, which an inset showing the PBGs with maxima at lower ε.

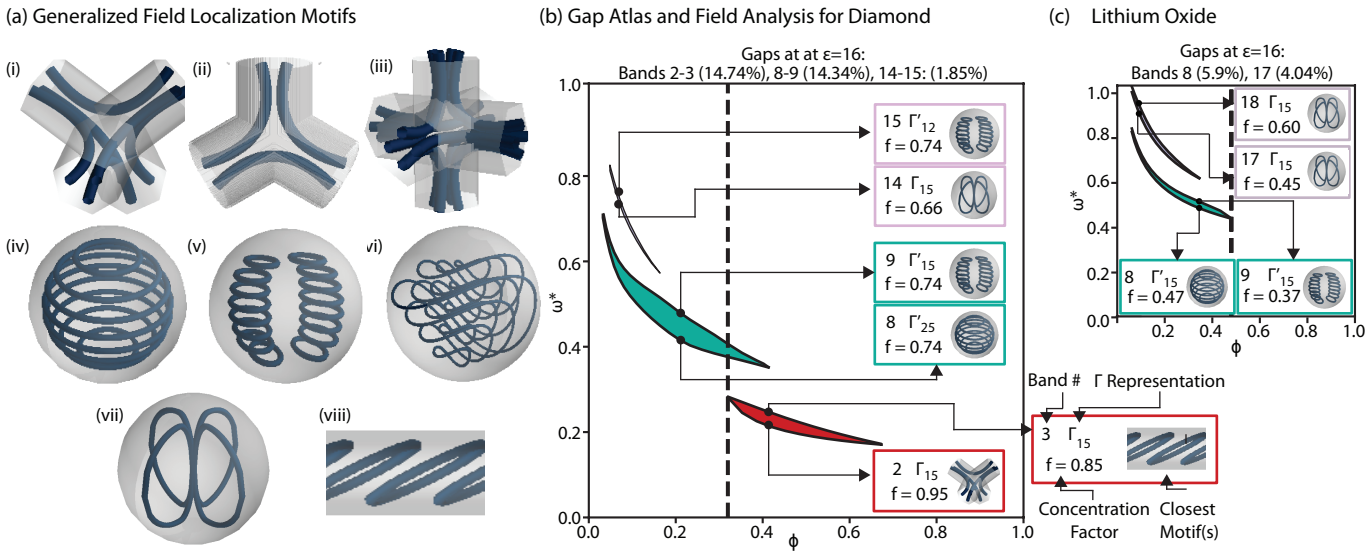

Figure 7.3: **(a–c) Mode Configurations and Motifs for PBG Photonic Crystals** (a) Common Motifs in the Mode Conformations of PBG Photonic Crystals. Motifs (i–iii) exhibit regions of high electric energy density between adjacent unit cells, while the electric energy density for modes (iv–viii) is confined to an isolated region of dielectric material. (b) Gap atlas and field analysis of diamond, which has two large PBGs at different regions of filling fraction, either between bands 2-3 or 8-9, and a small PBG between bands 14-15. The dotted line denotes the filling fraction at which the dielectric has formed a continuous network. (c) Gap atlas and field analysis of lithium oxide, which has two PBGs at different regions of filling fraction, either between bands 8-9 or 17-18. The dotted line denotes the filling fraction at which the dielectric has formed a continuous network.

7.4 Methods

7.4.1 Data Management and Archival

The data for this project was managed using signac and the workflow was managed by signac-flow [23] in a multi-level project. The top level of the project consists of statepoints associated with the structural data. Inside each structure statepoint was an additional project managing the statepoints containing radii and dielectric constant.

Data for all PBG structures has been made available in conjunction with University of Michigan's Deep Blue data storage, and is publicly available at `https://glotzerlab.engin.umich.edu/photonics/index.html`.

7.4.2 Structure Retrieval and Conversion

Crystallographic Information Files (".cif" format) were downloaded from the Crystallographic Open Database (COD) and the Inorganic Crystallographic Structure Database (ICSD). Information regarding atomic constituents and structure name were taken directly from the *.cif* files, regardless of the correctness or conditions of the original authors' publication or data. Additionally, we included structures found in unrelated simulations in the Glotzer group, some of which have no natural analogue. These position files were then converted to a set of lattice vectors and a fractional basis, with the first lattice vector normalized to unit length.

7.4.3 Input parameters for MPB

All PBG calculations were conducted using MPB, a Scheme-based eigenmode solver developed at MIT [22]. MPB calculates the photonic band structure through iterative planewave eigenmode searching. In MPB, the input parameters required are: 1) lattice vectors and fractional basis, 2) particle radius and dielectric constant, 3) fractional k-point path in reciprocal space, 4) k-point interpolation, 5) resolution, 6) mesh size, and 7) number

of bands to calculate.

(1) and (2) define the statepoints for this study. (3) was generated using the procedure below. (4) was set to 16 in initial screening, and set to 32 in complex structures or during the second round of screening. (5) was set to 1 in initial screening, and 6 during the second round of screening. (6) was set to 5. (7) was set to 20. Only those statepoints with PBGs during initial screening were included in the second round of screening, as those structures found to not have a PBG with minimal k-points would not have a PBG with additional k-points, which would only reduce or close the calculated PBG.

7.4.4 Radius Screening

For each structure, particle radii were initialized to $r \in (0.0, 1.5)$ and $\Delta r = 0.01$ and calculations run. MPB outputs were then queried, and radii with filling fractions outside of $[0.0, 1.0]$ for a structure were removed. For each structure radii were added uniformly at smaller intervals where necessary, such that each structure was screened with at least 20 radii for both dielectric spheres and air spheres.

7.4.5 Dielectric Constants

For each structure, we initially assumed a dielectric constant $\varepsilon = 16$, the highest theorized dielectric constant for solid, translucent media [34]. It has been postulated that any crystal will exhibit a PBG in the limit of infinite dielectric constant [7], thus we tested a wide variety of crystals, even if difficult to realize in experiment. After the initial computations at $\varepsilon = 16$, we performed computations for structures and statepoints found to have PBGs at lower ε, down to $\varepsilon = 2$ or such that $\Delta\omega = 0$.

7.4.6 k-Point Path Generation

The first Brillouin zone was computed by finding the Voronoi tessellation of the reciprocal lattice for each structure using the Voronoi functionality of SciPy [35]. The path through

the BZ was taken to be a highly redundant traversal along the edges of each face of the surface of the BZ, including to and from the face center and the Γ-point. This path, though redundant, is guaranteed to exhaustively sample the high symmetry points at which band extrema occur. An example of a highly redundant k-point path is given in the Extended Data.

For field analysis, the irreducible BZ was calculated to ensure correct k-point labels in the calculation of Γ representation.

7.4.7 Structural Analysis

In order to calculate the connectivity thresholds (included in Extended Data) and bond angles, we used the Python package pymatgen [36], an open-source materials analysis package.

For every structure, we computed the radius r and filling fraction ϕ for up to two different thresholds, (1) corresponding to the first peak in the radial distribution function (RDF), denoted ϕ_T, and (2) corresponding to the radius at which the spheres on the lattice sites are connected in a continuous network, denoted ϕ_N. ϕ_T is ill-defined for inverse structures. (2) was found for direct structures using pymatgen, and by analyzing the voxelizations of inverse structures using the *skimage* package[35]. For some direct structures, these thresholds are the same.

Space groups and symmetry information were found using the open-source package spglib [37] and 3D visualization was done with the open-source package *mayavi*[38].

7.4.8 Field Analysis

For MPB, there is an option to output field files for a given computation at every $\vec{k}$ and band. We took the electric fields in these files and visualized them using *mayavi*[38]. The flow reduction was done on 1-2 unit cells of the structure with a resolution of 24-40 grid points. Motifs were drawn based upon analysis of these flow diagrams. A schematic of this

process is provided in the Extended Data.

Concentration factor was computed using:

$$f = \frac{\int_{V_\varepsilon} (\boldsymbol{E}^*(\boldsymbol{r})) \cdot (\boldsymbol{D}(\boldsymbol{r}))\ dr}{\int (\boldsymbol{E}^*(\boldsymbol{r})) \cdot (\boldsymbol{D}(\boldsymbol{r}))\ dr} \tag{7.1}$$

as described in Meade, *et al.* [6]

Γ classification was done using character tables found in the Bilbao Crystal Database[39] and Dresselhaus, *et al.* .[40]

7.5 Supplementary Information

In addition to the information shown in this section, there is a large glossary of photonic band structures for the majority of the crystal structures included in this study in Appendix C.

7.5.1 Summaries of Data

Another way of viewing Fig. 1 from the main text is to organize in terms of PBG size and ε, as shown in 7.4.

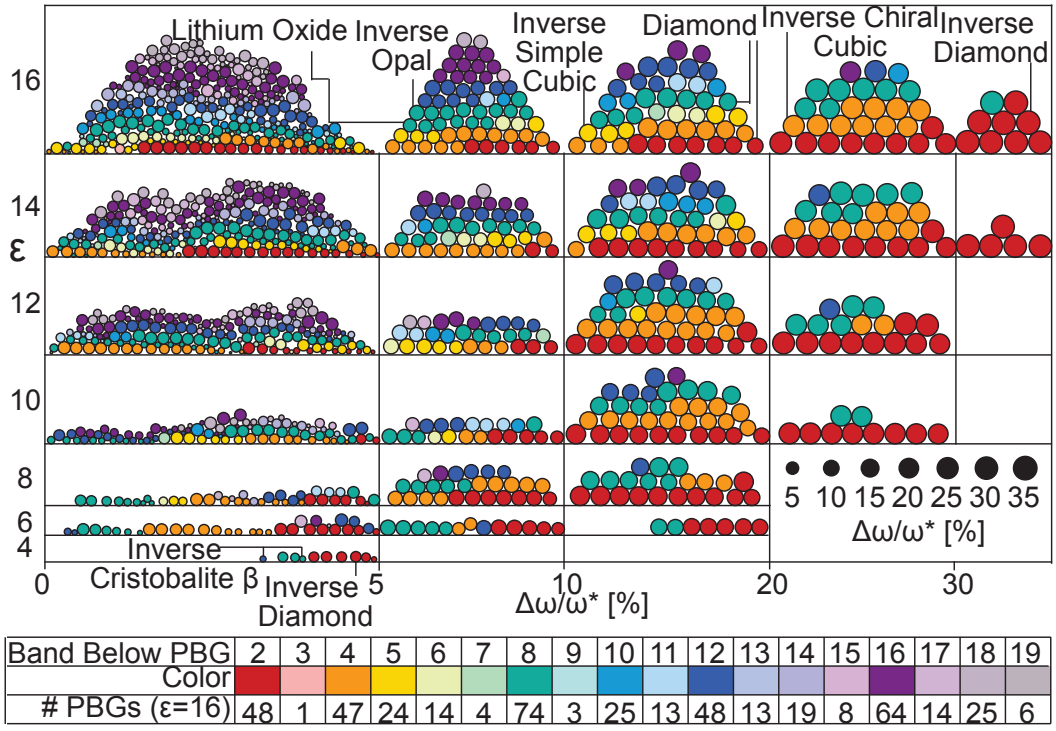

Figure 7.4: **PBGs Properties of Nature-Inspired Structural Templates**. Largest PBGs found for each structure generated among $\varepsilon = 4$–16. Circle areas are proportional to the PBG size; colors correspond to the location of the PBG. Some structures are shown more than once, as some structures were found to exhibit PBGs in two different locations at different filling fractions. Structures that have been previously studied or noted in the main text have been labeled.

7.5.2 Method Figures

Comparison with Previously Published Data In Fig. 7.5, we compare the PBG sizes computed using our methodology and previously published in literature within references [10, 12, 25, 22, 14, 24].[x]

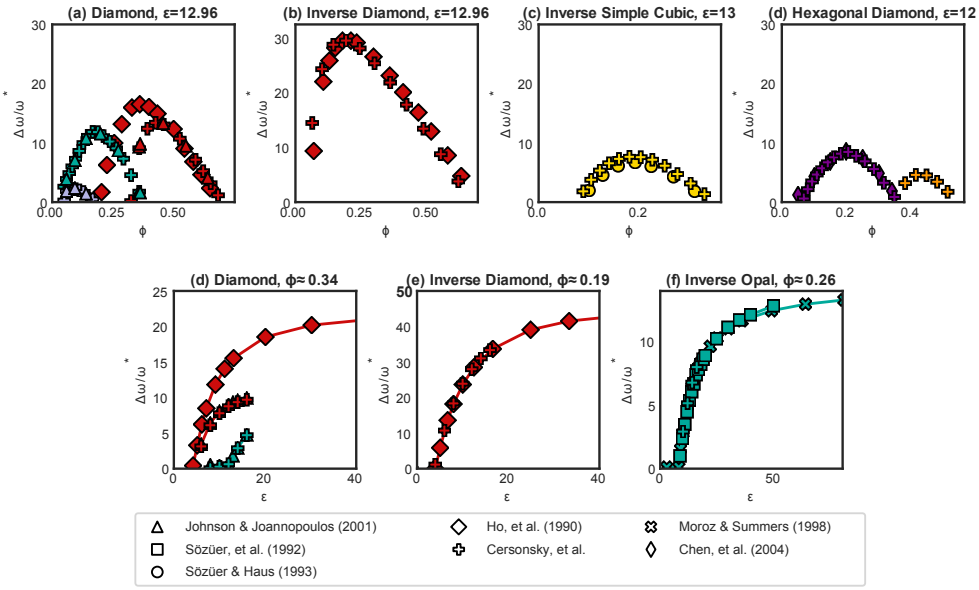

Figure 7.5: **Comparison of Reported and Previously Published Data for Fixed ε and ϕ.** Color indicates bands between which the PBG occurs, with plotting marker corresponding to data source. (a) PBG between bands 2-3 (red), 8-9 (teal) and 14-15 (lavender) for Diamond at $\varepsilon = 12.96$, as reported by [10] and generated by the example code given by [22]. PBG sizes reported in Ref. [10] were found to be overestimated in [14], therefore a better benchmark for diamond is provided by [22]. (b) PBG between bands 2 and 3 in Inverse Diamond at $\varepsilon = 12.96$, as reported by [10]. (c) PBG between bands 5 and 6 in Inverse Simple Cubic at $\varepsilon = 13$, as reported by [12]. (d) PBG between bands 16 and 17 in Hexagonal Diamond at $\varepsilon = 12$, as reported by [25]. PBG between bands 4 and 5 (orange) were unreported in [25], with no indication if calculations for corresponding ϕ were run. (e) PBG between bands 2-3 (red) and 8-9 (teal) for Diamond at $\phi \approx 0.34$, as reported by [10] and generated by the example code given by [22]. PBG sizes reported in Ref. [10] were found to be overestimated in [14], therefore a better benchmark for diamond is provided by [22]. (f) PBG between bands 2 and 3 in Inverse Diamond at $\phi \approx 0.19$, as reported by [10]. (g) PBG between bands 8 and 9 in Inverse Opal at $\phi \approx 0.26$, as reported by [14, 24].

[x]Any discrepancies between the computations reported and previous literature can be due to differing smoothing functions of ε space, using a more exhaustive IBZ, and small errors in transcribing previous literature, which were available in figure, and not table, form.

Data Management with Signac The data for this project was managed using signac and the workflow managed by signac-flow in a multi-level project.[23] The top level of the project consisted of statepoints consisting of structural data. Inside each structure statepoint was an additional project managing the statepoints containing radii and dielectric constant.

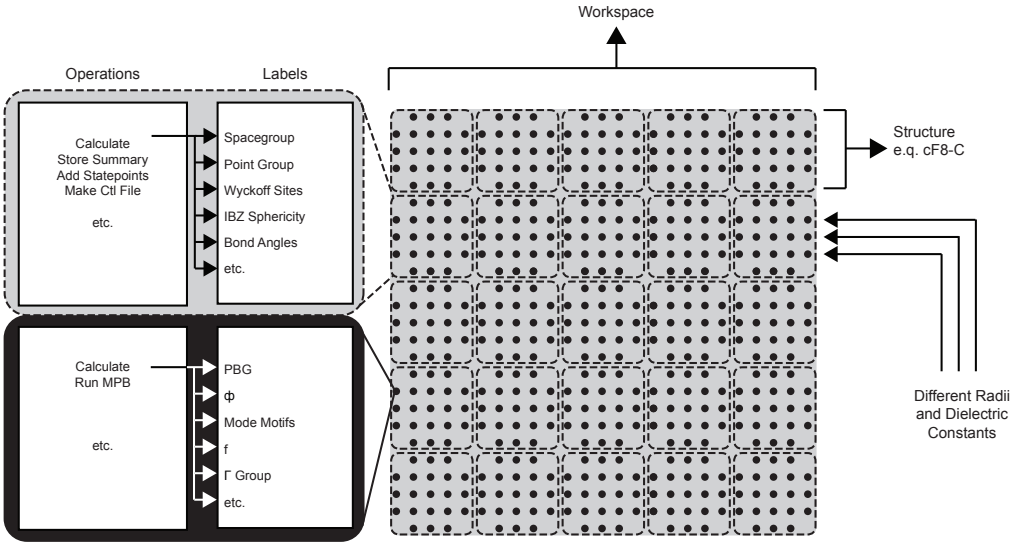

Figure 7.6: **Organization of Project Using *signac* and *signac-flow***. Operations and labels were stored individually for the structure at large and independent radii and dielectric constants, as was appropriate. Typical structure-level operations included symmetry calculations, PBG atlas generation, and summarizing lower level data. Typical lower level operations include running and analyzing MPB, computing fill fraction, and field analysis.

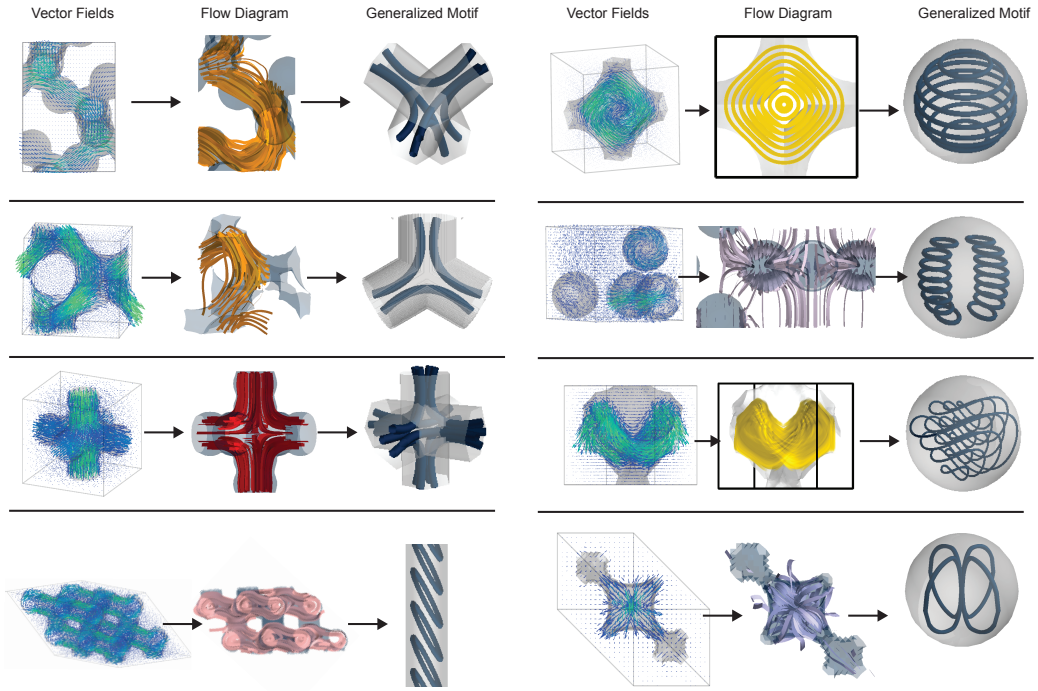

Figure 7.7: **Schematic of Complexity Reduction from Vector Fields to Mode Motifs**. For each mode motif in the main text, we show the reduction in visual complexity from the vector fields to a flow diagram to a mode motif. For each motif we attempted to provide a visual that best represents the motif, with many structures exhibiting variations on these motifs or mixed motif behavior.

7.5.3 Extended Analysis

7.5.3.1 Structural Features and PBGs

For this section, we will report percentages of structures that have a particular structural fingerprint across all structures studied and the 351 that have PBGs. We will also report relative probabilities, *i.e.* the probability a given fingerprint is found in structures with PBGs divided by its probability of being found in all structures.[xi]

Bravais Lattice and Gap Location

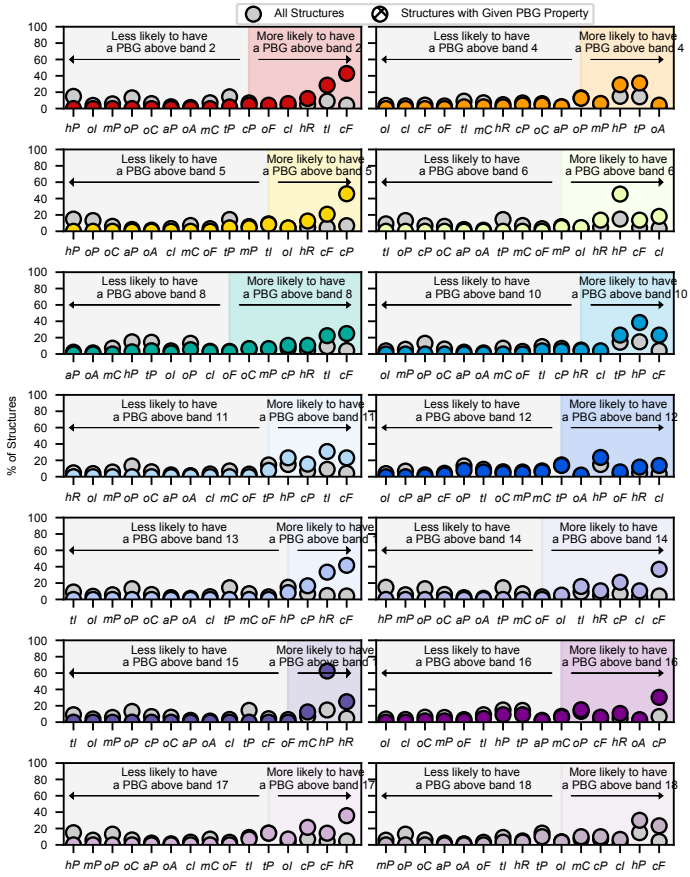

Figure 7.8: **Correlation between PBG Location and Bravais Lattice**. Here we show an extension of Fig. 2(a)(iii-iv) from the main text, including PBG locations where there was less clear correlation between Bravais Lattice and PBG location.

[xi] We compared the sample of structures used in this project with a rough estimate of the data space available through ICSD and COD to show that our sample set can represent a general distribution.

Correlation with PBG Existence

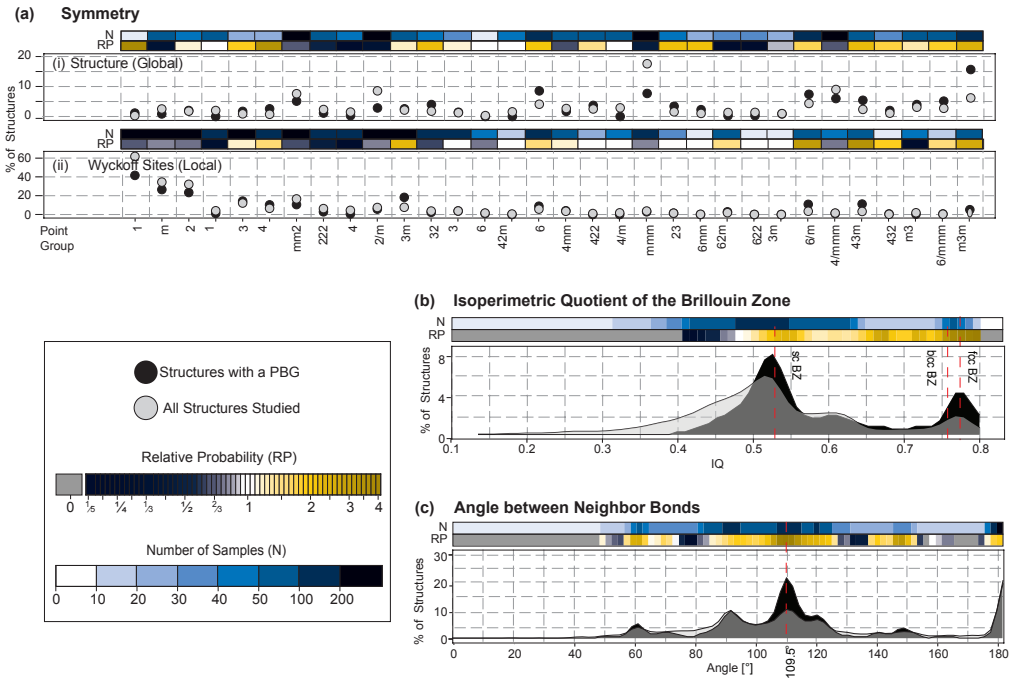

Figure 7.9: **Comparison of Structural Features for PBG Structures and All Structures**. For each subfigure, the grey and black markers/area denote values for all structures and those with PBGs, respectively. (a) Point group symmetry of the (i) structure and (ii) Wyckoff sites, increasing in symmetry order to the right. (b) Isoperimetric quotient of the first Brillouin zone (BZ). Isoperimetric quotient is a measure of sphericity, close to 0 for highly non-spherical shapes and 1 for spheres. The values for cubic structures, which are constant for all structures of a given centering, are denoted with red dotted lines. (c) Measure of the angle between neighboring "bonding" sites. For each lattice site, we computed this value by considering the first shell of nearest neighbor sites.

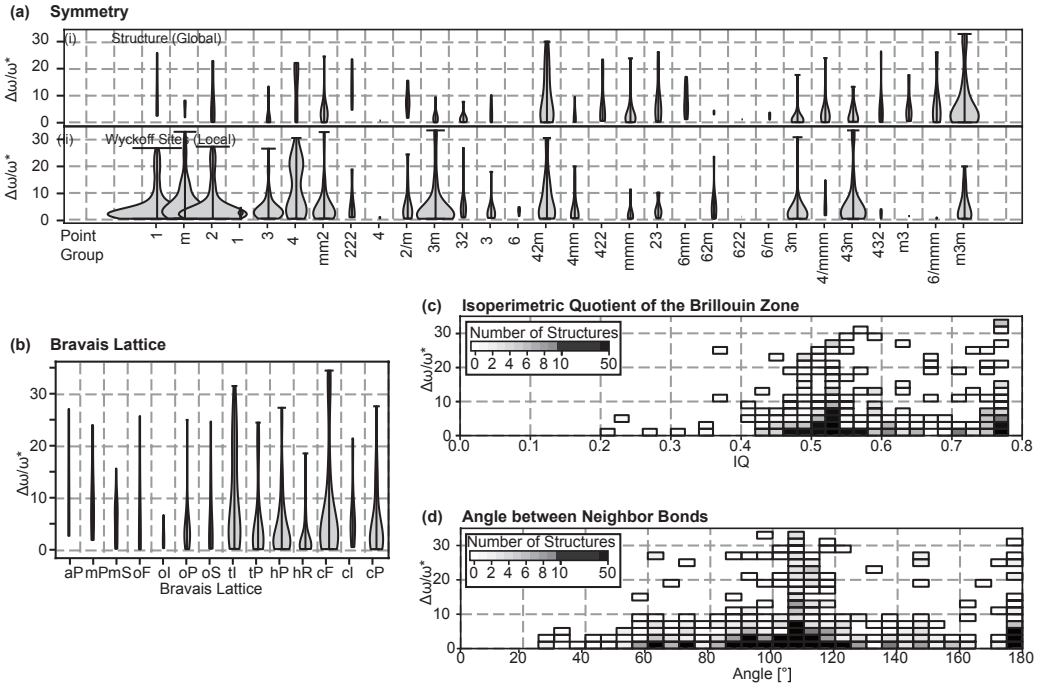

Figure 7.10: **The Correlation of Structural Features with Large PBGs**. (a) The distribution of PBGs with respect to lattice setting and PBG size, with the Bravais lattices increasing in symmetry order to the right. (a) Distribution of PBGs with respect to (i) point group of the structure or (ii) point group of individual Wyckoff sites and PBG size, with the point groups increasing in symmetry order to the right. (b) Heat map of sphericity of the BZ and PBG size. (c) Heat map of bond angles and PBG size.

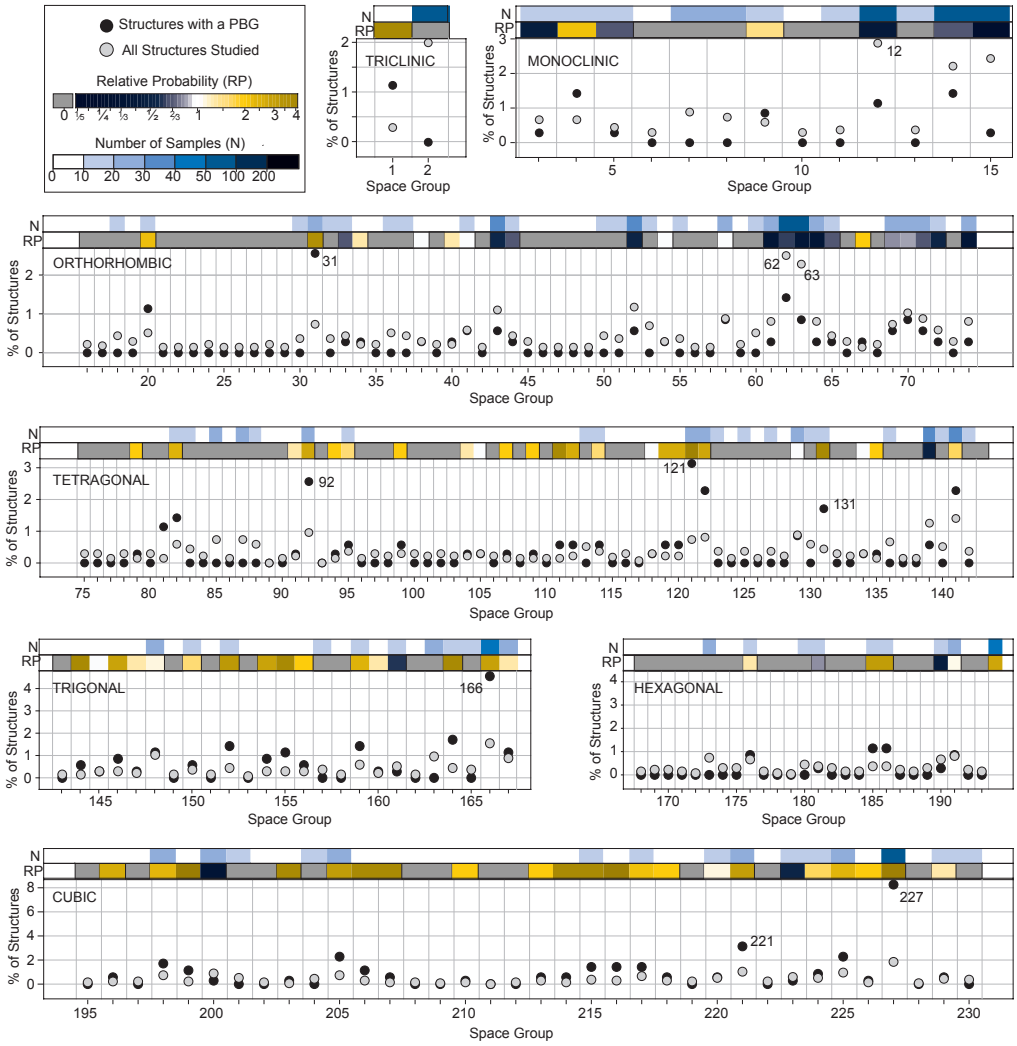

Figure 7.11: **Relative Probabilities for Space Group Numbers**. Of the 230 total space groups, structures were calculated in the available 227 space groups. Space groups are separated by lattice group, with blue and yellow colormaps denoting the sample size and relative probabilities, respectively. Grey and black circles correspond to percentages of structures across the entire dataset and those with PBGs, respectively. Space group numbers with high or low relative probability are individually labelled.

Effects of ϕ and ε

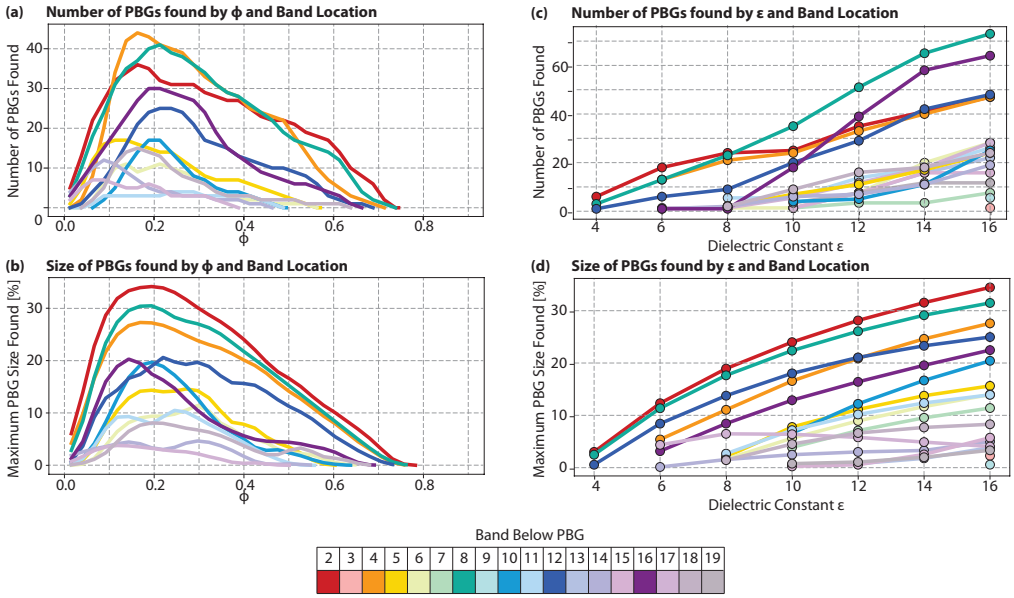

Figure 7.12: **Summary of PBGs across Different Filling Fractions and Dielectric Constants**. (a) Number of PBGs found across filling fractions from 0 to 1. (b) Largest PBGs found at each filling fraction. (c) Number of PBGs found across dielectric constants, from 4–16. (d) Largest PBGs found at each dielectric constant. Each plot is separated by band number indicated by the color guide.

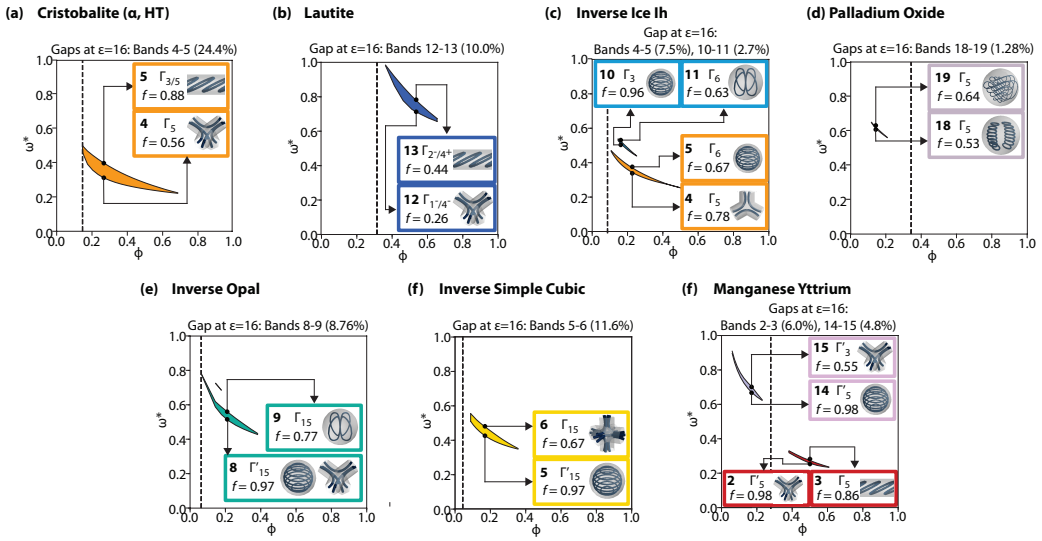

Figure 7.13: **Additional Field Analyses Computed**. (a) α-Cristobalite, which has a 24.4% PBG above band 4 above $\phi_T = \phi_N$. Mode analysis appears similar to the 2-3 PBG in Diamond. (b) Lautite, an orthorhombic crystal which has a 10.0% PBG above band 12 above ϕ_N. Mode analysis appears similar to the 2-3 PBG in Diamond. (c) Inverse Ice Ih, which has two PBGs above bands 4 and 10 above $\phi_T = \phi_N$. The mode of band 4 has a trigonal motif, whereas above the PBG is a confined motif. The 10-11 occurs between two confined-motif modes. (d) Palladium Oxide, which has a PBG below $\phi_T = \phi_N$ between bands 18 and 19 due to two confined motifs surrounding the PBG. (e) Inverse Opal, which has a mixed motif within band 8 and a confined motif in band 9. (f) Inverse Simple Cubic, which has a reverse case to the 2-3 PBG of diamond: a confined motif below the PBG and a traveling motif above, however with a much lower concentration factor. (g) Pseudo-Manganese Yttrium, due to its topological similarity to diamond, this structure has similar PBGs and motifs to diamond, with the exception of the 8-9 PBG.

References

[1] Michielsen, K. & Stavenga, D. Gyroid cuticular structures in butterfly wing scales: biological photonic crystals. *Journal of The Royal Society Interface* **5**, 85–94 (2008).

[2] Onslow, H. On a Periodic Structure in Many Insect Scales, and the Cause of Their Iridescent Colours. *Philosophical Transactions of the Royal Society B: Biological Sciences* **211**, 1–74 (1923).

[3] Galusha, J. W., Richey, L. R., Gardner, J. S., Cha, J. N. & Bartl, M. H. Discovery of a diamond-based photonic crystal structure in beetle scales. *Physical Review E* **77**, 050904 (2008).

[4] Yin, H. *et al.* Amorphous diamond-structured photonic crystal in the feather barbs of the scarlet macaw. *Proceedings of the National Academy of Sciences* **109**, 10798–10801 (2012).

[5] Teyssier, J., Saenko, S. V., van der Marel, D. & Milinkovitch, M. C. Photonic crystals cause active colour change in chameleons. *Nature Communications* **6**, 6368 (2015).

[6] Meade, R. D., Rappe, A. M., Brommer, K. D. & Joannopoulos, J. D. Nature of the photonic band gap: some insights from a field analysis. *Journal of the Optical Society of America B* 328.

[7] Joannopoulos, J. *Photonic Crystals: Molding the Flow of Light, 2nd Edition* (Princeton University Press, 2008).

[8] Yablonovitch, E. Inhibited spontaneous emission in solid-state physics and electronics. *Physical Review Letters* **58**, 2059–2062 (1987).

[9] John, S. Strong localization of photons in certain disordered dielectric superlattices. *Physical review letters* **58**, 2486–2489 (1987).

[10] Ho, K. M., Chan, C. T. & Soukoulis, C. M. Existence of a photonic gap in periodic dielectric structures. *Physical Review Letters* **65**, 3152–3155 (1990).

[11] Chan, C. T., Ho, K. M. & Soukoulis, C. M. Photonic Band Gaps in Experimentally Realizable Periodic Dielectric Structures. *Europhysics Letters (EPL)* **16**, 563–568 (1991).

[12] Sözüer, H. S. & Haus, J. W. Photonic bands: simple-cubic lattice. *Journal of the Optical Society of America B* 296.

[13] Maldovan, M., Ullal, C. K., Carter, W. C. & Thomas, E. L. Exploring for 3D photonic bandgap structures in the 11 f.c.c. space groups. *Nature Materials* **2**, 664–667 (2003).

[14] Sözüer, H. S., Haus, J. W. & Inguva, R. Photonic bands: Convergence problems with the plane-wave method. *Physical Review B* **45**, 13962–13972 (1992).

[15] Men, H., Lee, K. Y. K., Freund, R. M., Peraire, J. & Johnson, S. G. Robust topology optimization of three-dimensional photonic-crystal band-gap structures. *Optics Express* 22632.

[16] Cersonsky, R. K., Dshemuchadse, J., Antonaglia, J., van Anders, G. & Glotzer, S. C. Pressure-Tunable Band Gaps in an Entropic Crystal. *Phys. Rev. Mat.* (2018).

[17] Ducrot, É., He, M., Yi, G.-R. R. & Pine, D. J.

Colloidal alloys with preassembled clusters and spheres. *Nature Materials* **16**, 652–657 (2017).

[18] Leung, K. M. Diamondlike photonic band-gap crystal with a sizable band gap. *Physical Review B* **56**, 3517–3519 (1997).

[19] Maldovan, M. & Thomas, E. L. Diamond-structured photonic crystals. *Nature Materials* **3**, 593–600 (2004).

[20] Graulis, S. *et al.* Crystallography Open Database - An open-access collection of crystal structures. *Journal of Applied Crystallography* **42**, 726–729 (2009).

[21] G Bergerhoff, ID Brown, F. A. Crystallographic Databases. *nternational Union of Crystallography* (1987).

[22] Johnson, S. & Joannopoulos, J. Block-iterative frequency-domain methods for Maxwell's equations in a planewave basis. *Optics Express* **8**, 173 (2001).

[23] Adorf, C. S., Dodd, P. M., Ramasubramani, V. & Glotzer, S. C. Simple data and workflow management with the signac framework. *Computational Materials Science* **146**, 220–229 (2018). 1611.03543.

[24] Moroz, A. Three-Dimensional Complete Photonic-Band-gap Structures in the Visible. *Physical Review Letters* **83**, 5274–5277 (1999).

[25] Chen, H., Zhang, W. & Wang, Z. Comparative studies on photonic band structures of diamond and hexagonal diamond using the multiple scattering method. *Journal of Physics: Condensed Matter* **16**, 741–748 (2004).

[26] Watanabe, H. & Lu, L. Space Group Theory of Photonic Bands. *Physical Review Letters* **121**, 263903 (2018). 1805.10103.

[27] Cadotte, A. T., Dshemuchadse, J., Damasceno, P. F., Newman, R. S. & Glotzer, S. C. Self-assembly of a space-tessellating structure in the binary system of hard tetrahedra and octahedra. *Soft Matter* **12**, 7073–7078 (2016).

[28] Damasceno, P. F., Karas, A. S., Schultz, B. A., Engel, M. & Glotzer, S. C. Controlling Chirality of Entropic Crystals. *Physical Review Letters* **115**, 158303 (2015).

[29] Lin, H. *et al.* Clathrate Colloidal Crystals. *Science* **355**, 931–935 (2017).

[30] Hachisu, S. & Yoshimura, S. Optical demonstration of crystalline superstructures in binary mixtures of latex globules. *Nature* **283**, 188–189 (1980).

[31] Bartlett, P., Ottewill & Pusey. Superlattice formation in binary mixtures of hard-sphere colloids. *Physical review letters* **68**, 3801–3804 (1992).

[32] Cywinski, R., Kilcoyne, S. H. & Scott, C. A. Magnetic order and moment stability in YMn2. *Journal of Physics: Condensed Matter* **3**, 6473–6488 (1991).

[33] Frank, F. C. & Kasper, J. S. Complex alloy structures regarded as sphere packings. I. Definitions and basic principles. *Acta Crystallographica* **11**, 184–190 (1958).

[34] Li, H. H. Refractive index of silicon and germanium and its wavelength and temperature derivatives. *Journal of Physical and Chemical Reference Data* **9**, 561–658 (1980).

[35] Jones, E., Oliphant, T., Peterson, P. & Others. {SciPy}: Open source scientific tools for {Python} (2001).

[36] Ong, S. P. *et al.* Python Materials Genomics (pymatgen): A robust, open-source python library for materials analysis. *Computational Materials Science* **68**, 314–319 (2013).

[37] Togo, A. & Tanaka, I. Spglib: a software library for crystal symmetry search (2018). 1808.01590.

[38] Ramachandran, P. & Varoquaux, G. Mayavi: 3D Visualization of Scientific Data. *Computing in Science & Engineering* **13**, 40–51 (2011).

[39] Aroyo, M. I., Kirov, A., Capillas, C., Perez-Mato, J. M. & Wondratschek, H. Bilbao Crystallographic Server. II. Representations of crystallographic point groups and space groups. In *Acta Crystallographica Section A: Foundations of Crystallography*, vol. 62, 115–128 (2006).

[40] Dresselhaus, M. S., Dresselhaus, G. & Jorio, A. A. *Group theory : application to the physics of condensed matter* (Springer-Verlag, 2008).

CHAPTER VIII

The Effects of Structural Modifications on Photonic Band Gaps

The important thing is not to stop questioning. Curiosity has its own reason for existence.

– Albert Einstein

8.1 Introduction

In Chapter VII, we showed that the breadth of crystal structures are capable of producing a photonic band gap is larger than previously expected, and a large variety of photonic crystals are available. In this chapter, I will discuss the effects of some modifications to the structures studied in Chapter VII, primarily the results from 1) manipulating the connectivity of the structure and 2) distorting large PBG structures.

The connectivity of the high dielectric medium, hereon referred to simply as "connectivity", was shown to be neither necessary nor sufficient to create a PBG, primarily for those at high frequencies. That being said, connectivity can be important at low frequencies, as the smooth dielectric channel will lower the energy required for confinement within the high dielectric medium. For a particular crystal structure with spheres on each of the lattice sites, the filling fraction range over which it is connected is fixed, as determined by the structure's

interparticle distances. However, what if we could modify the structure such that the symmetry is maintained, but we lower the minimum filling fraction necessary to yields a network structure? Will decreasing this lower limit always lead to a larger PBG?

One way to decrease the interparticle distances is to introduce additional lattice sites between neighboring sites, creating effective "rods" connecting the neighboring lattice sites. This idea has been introduced previously, with rod-connected diamond, FCC, and simple cubic all having been studied.[1, 2, 3] In each case the "rod-connected" version of the crystal improved upon the PBG size from the sphere-instantiated version. This approach would open up fabrication possibilities, as network structures can be fabricated using 3D printing. Thus, it is important to understand if this design rule can be universally applied to crystal templates.

A previous publication has attempted to define a universal design rule for photonic crystals. In [4], the authors constructed a spiral pattern on various crystal lattices, improving the PBG size in every case. Based upon this finding, the authors claimed the macrostructure (*i.e.* bravais lattice) was less important than the microstructure (the topology).[i] Here I will construct a similar rule and apply it to a range of crystal templates and report whether a similar universal effect exists.

I will also report the effects of tetragonal and orthorhombic distortion on the gaps in a few photonic structures that have a PBG in their undistorted form.

8.2 The Effect of Network Connectivity on PBGs

8.2.1 Methods and Models

I chose a space of crystal templates for which the effects of connectivity were previously studied (such as diamond, FCC, and SC), or those that had well-defined nearest neighbor shells with uniform nearest neighbor distances. I instantiated each structure with 0-9 addi-

[i]This study, while insightful, overlooked that each of the instantiations described in the study roughly approximated a 2D photonic crystal, for which the structural requirements are well known and less stringent.

tional lattice sites between nearest neighbor pair (we will denote this with the variable I in the upcoming results and discussion), with 0 corresponding to the original structure and 9 corresponding to an effective "rod-connected" structure. I sampled the PBG properties for $\phi \in [0, 1]$ by varying the sphere radius and $\varepsilon \in [4, 16]$ using the MPB software. Photonic band structures for this chapter are given in Appendix D.

I will report with the structures the coordination of the nearest neighbor "bonds", which will inform our later analysis. The structures investigated are shown in Fig.8.1, arranged by the aforementioned coordination.

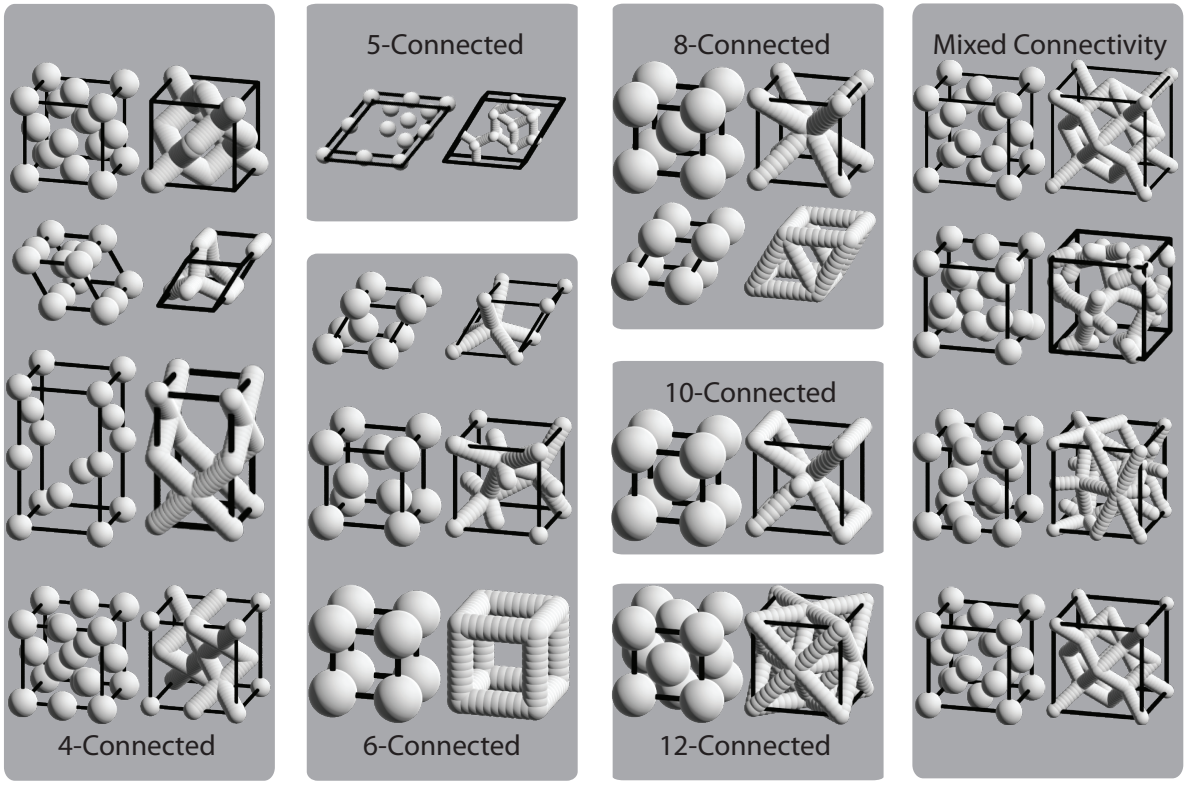

Figure 8.1: **Snapshots of Templates, Original and "Rod-Connected".** I computed the photonic band structure for multiple templates with different types of "connectivity" between neighboring lattice sites. In each panel, the original structure is shown to the left, with the "rod-connected" version on the right.

8.2.2 Results

As a single crystal template may exhibit gaps at multiple frequencies, the remainder of the results and discussion will focus on the structures and each gap separately, *e.g.* the gap between bands 8 and 9 in diamond will be discussed independently from that between bands 2 and 3.

For each gap, we computed the photonic band structure for $0 <= \phi <= 1$ for up to 9 additional lattice sites between nearest neighbors. In Fig. 8.2, the gap size across ϕ is shown as a function of additional lattice sites for $\varepsilon = 16$, with the color corresponding to the location of the gap and the opacity corresponding to the size, as reflected in the color bar.

Figure 8.2: **Examples of the Effects of Connectivity on Photonic Band Gap Size.** The peaks of these plots, with respect to gap size across ϕ, are plotted in Fig. 8.4.

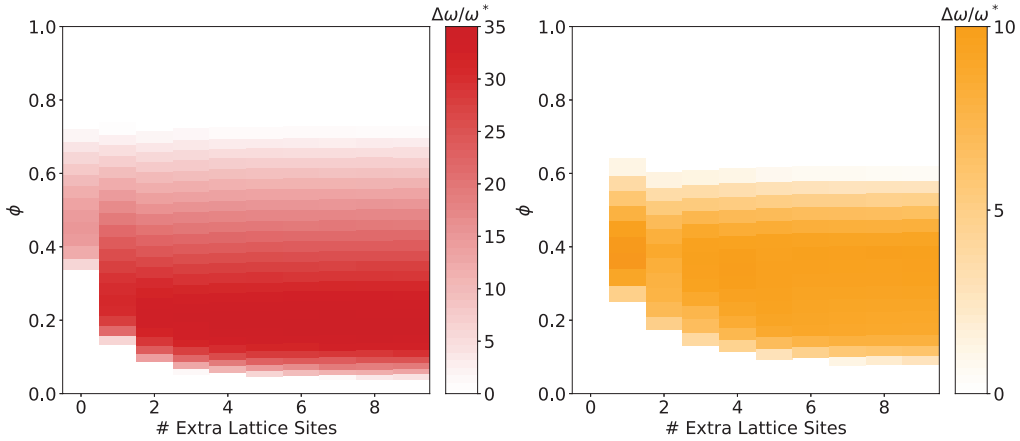

Diamond (Bands 2-3) and Simple Chiral Cubic (Bands 4-5). With the additional lattice sites, the PBG increases due to the lowering of the filling fraction threshold ϕ at which the structure is connected. The upper limit of ϕ where PBGs occur remains unchanged.

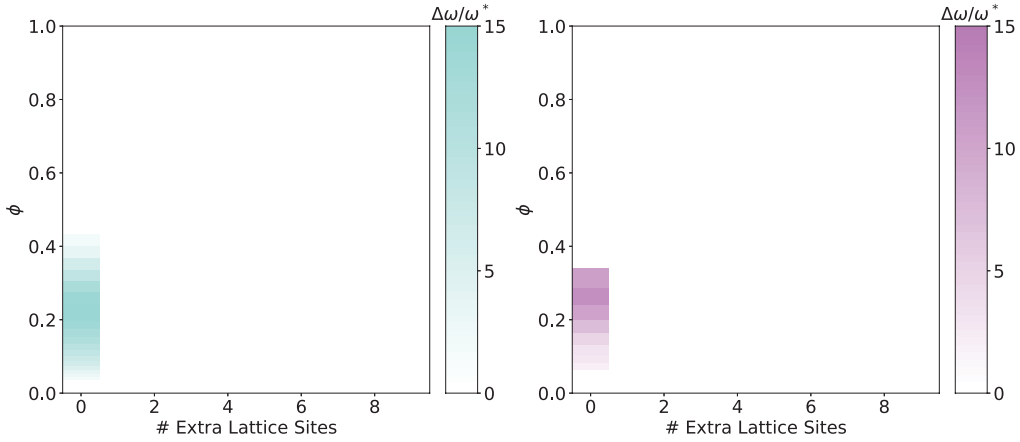

Diamond (Bands 8-9) and Lonsdaleite or Hexagonal Diamond (Bands 16-17). With the additional lattice sites, the PBG disappears.

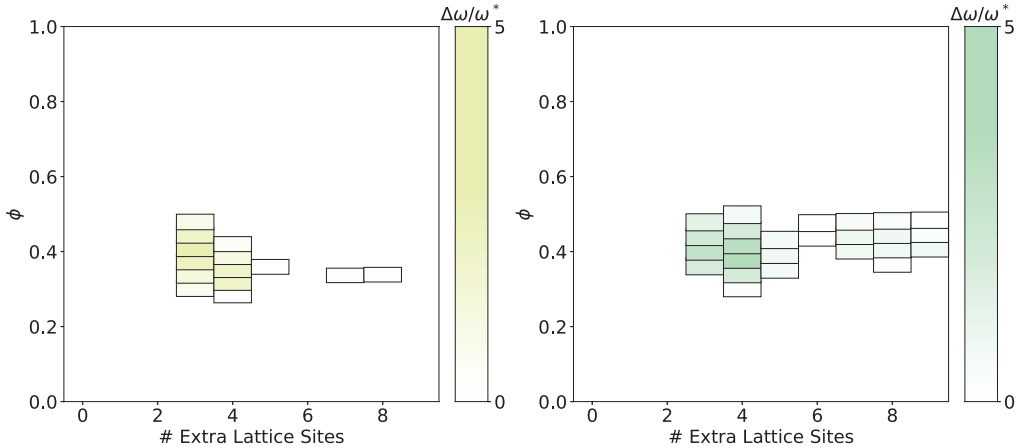

BCC (Bands 6-7) and CN=10 (Bands 7-8). A PBG occurs for a small number of lattice sites, but disappears as the structure becomes more rod-like. Outlines have been added for visual clarity.

For the majority of structures tested, 1) a gap opened where one had previously not existed or 2) a PBG that occurred in the original template grew with additional extra lattice sites. These PBGs of these structures are shown in Fig. 8.4(a) as a function of number of additional lattice sites.

Figure 8.4: **PBGs that Increased and Decreased with Connectivity.**

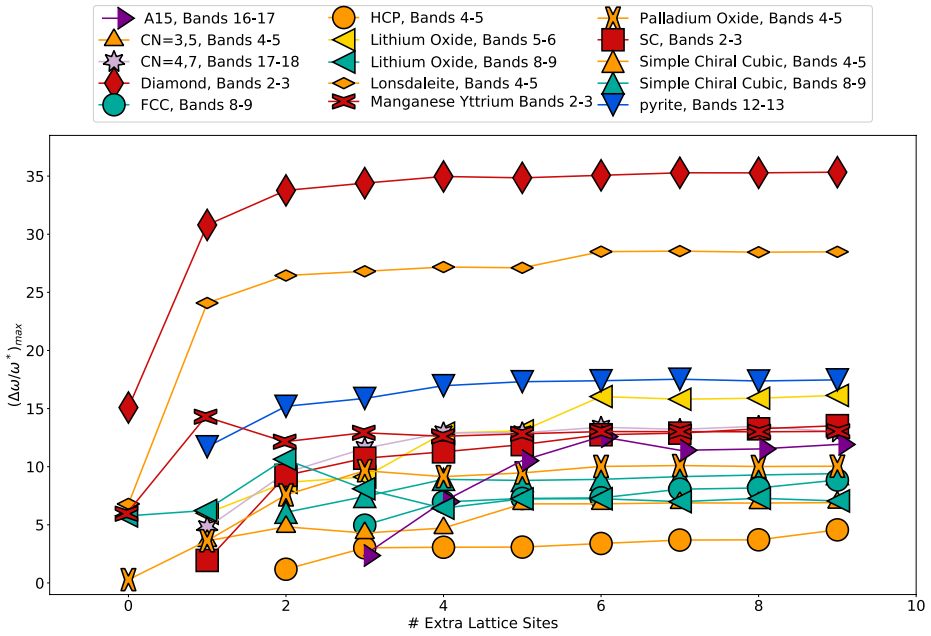

PBGs that Increased. Most structures have a gap that increases in size with the introduction of even a few additional sites, and plateaus when the topology of the high dielectric medium approaches a rod.

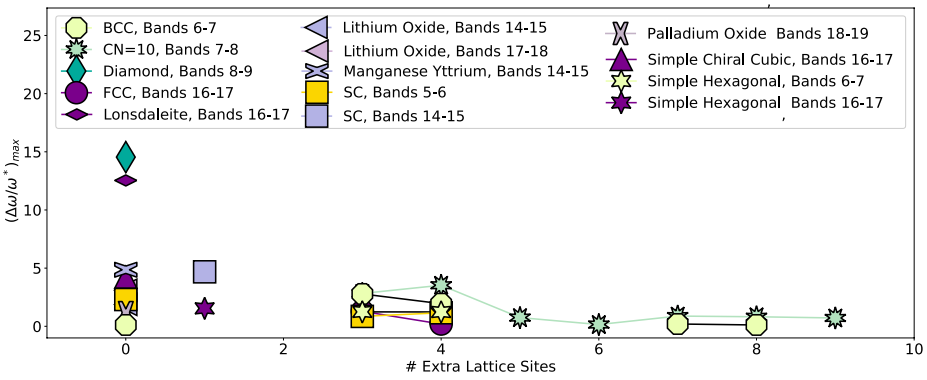

PBGs that Decreased. For many PBGs, one of two decreasing effects occurred: (1) a PBG that occurred at I=0 disappeared with the introduction of additional lattice sites (*e.g.* Diamond, Bands 8-9 or Londaleite, Bands 16-17) or a PBG occurred for intermediate values of I and disappeared as I grew larger (*e.g.* BCC, Bands 6-7 or CN=10, Bands 7-8).

Unexpectedly, several structures show gaps that decrease with increased connectivity. These structures and PBGs are shown in Fig. 8.4(b). For many of these systems, a gap that occurs in the original structure disappears for all $I > 0$. However, some systems that had little to no PBG in the original structure exhibit a gap at $0 < I < 9$, yet the gap disappeared as $I \to 9$ (*e.g.* BCC and CN=10).

8.2.3 Discussion

To understand the cases in which connectivity is not sufficient to produce a PBG, I will look at the effect of connectivity on the bands surrounding the potential PBGs. For a given structure, there are a finite number of locations at which a PBG may occur, governed by the symmetry of the crystal and computed using group theory[5, 6]. For each of our templates, the symmetry class of the crystal does not change with the introduction of extra lattice sites, so the potential locations for PBGs stay the same.

For this section, I will use $max(\omega_i)$ and $min(\omega_{i+1})$ to denote the frequencies that delineate a PBG between the i^{th} and $(i+1)^{th}$ bands.

For diamond or simple cubic, for which the PBG between bands 2 and 3 increases with increased connectivity, the addition of extra lattices sites greatly decreases $max(\omega_2)$, opening or widening the gap, as seen in Fig. 8.6(a-b). For BCC, the increased connectivity lowers both $max(\omega_6)$ and $min(\omega_7)$, but at different rates. The PBG appears at $I = 3$ because the $min(\omega_7)$ decreases less rapidly than $max(\omega_6)$. When the system approaches a rod-like morphology, as seen in Fig. 8.6(c), the frequencies are comparable, with the $min(\omega_7)$¡$max(\omega_6)$, thus the PBG disappears. A similar effect also happens for the 8-9 PBG in diamond (Fig. 8.6(d)).[ii]

It is most likely that connectivity will have a beneficial effect on the PBG size of a structure when the modes delineating the PBG differ in concentration factor f,[iii], as the connectivity will affect the frequency of the two modes differently.

[ii] This does not preclude a PBG opening at a higher band location, but as seen in Chapter 3, for PBGs at high frequencies typically do not rely on connectivity, meaning this is an unlikely, albeit not impossible, scenario.

[iii] defined in Chapter VII)

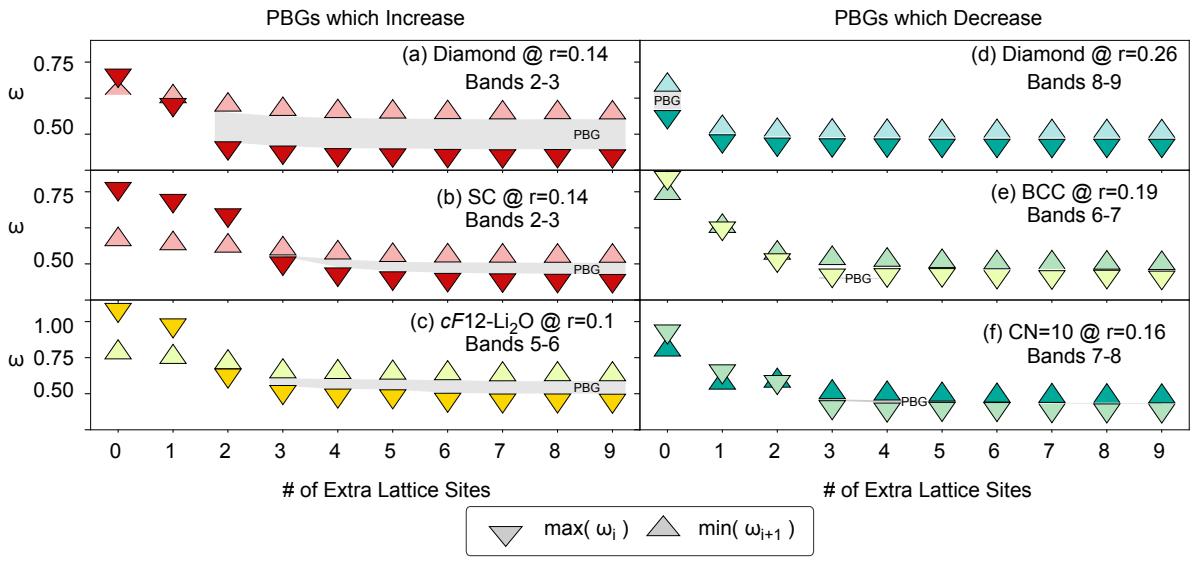

Figure 8.6: **Effect of Connectivity on Bands Surrounding a PBG**. Frequency of the bands surrounding a PBG for (a) diamond, bands 2-3, (b), SC, bands 2-3, (c) lithium oxide, bands 5-6, (d) diamond, bands 8-9, (e) BCC, bands 6-7, and (f) CN=10, bands 7-8. Arrow direction corresponds to whether it is the maximum of the lower band (down) or minimum of the upper band (up), and color denotes band number. A grey box and "PBG" indicate where a PBG occurs.

8.2.4 Conclusions

I have shown that network connectivity morphology is not a sufficient condition for creating a PBG, as increased connectivity may lower the frequencies of both bands delineating a PBG. I have also identified several new systems that have increased PBGs with increased network connectivity and may be ideal candidates for fabrication in future work.

8.3 Effect of Lattice Distortion on PBG Structures

I looked at the effect of lattice distortion on several well studied photonic crystals to understand the resilience of the PBGs. Photonic band structures for this section can be found in Appendix E. For each of the structures, we looked at the effect of orthorhombic scaling, wherein $|a_2|, |a_3|$ change and the original angles are preserved. For each structure we report based upon the standard setting, but compute with the primitive cell. For example,

diamond is reported with its cubic lattice setting, as opposed to its rhombohedral primitive cell.

First we looked at the photonic crystal staple: diamond, summarized in Fig. 8.7.[iv] Both the PBGs found between Bands 2-3 and 8-9 decrease most with orthorhombic settings, however the 8-9 PBG persists to higher asymmetry, as seen by the width of the region where the 8-9 PBG is greater than 0 in Fig. 8.7. Both PBGs disappear for $|a_2|, |a_3| > 2.0$. At $|a_2|$ or $|a_3| >= 2$, the topology resembles 2D sheets, leading to the PBG found between bands 10-11. The PBG between bands 14-15 *increased* marginally upon scaling to $|a_2|, |a_3| = 1.25$, yet was only found for small lattice distortions.

Fig. 8.8 shows the effect of orthorhombic scaling on (a) Inverse Opal, (b) Inverse Simple Cubic, (c) Inverse Simple Chiral Cubic, and (d) Simple Chiral Cubic. Surprisingly, the PBGs for (a) and (b) decreased greatly with small changes in $|a_2|$ and $|a_3|$, whereas the decrease in PBG size for (c) and (d) was much smaller. For (d), the PBG between bands 4-5 and 16-17 increased with small scaling along one axis.

8.3.1 Discussion

It is clear from the figures in this section that orthorhombic scaling greatly affects the PBGs of a crystal structure. However, the reason is unknown and must be an area for further investigation. Possible causes are a loss of connectivity of the high dielectric medium (for those band gaps where connectivity is required) the energy changes in the electromagnetic modes due to the distortion. I think that this study would be well coupled with a self-assembly study where these structures were analyzed for the distortion that may occur due to particle polydispersity or non-uniaxial pressure.

References

[iv] I took this structure in the direct instantiation, as there exist 3 potential PBGs to study, as opposed to the single PBG in inverse diamond.

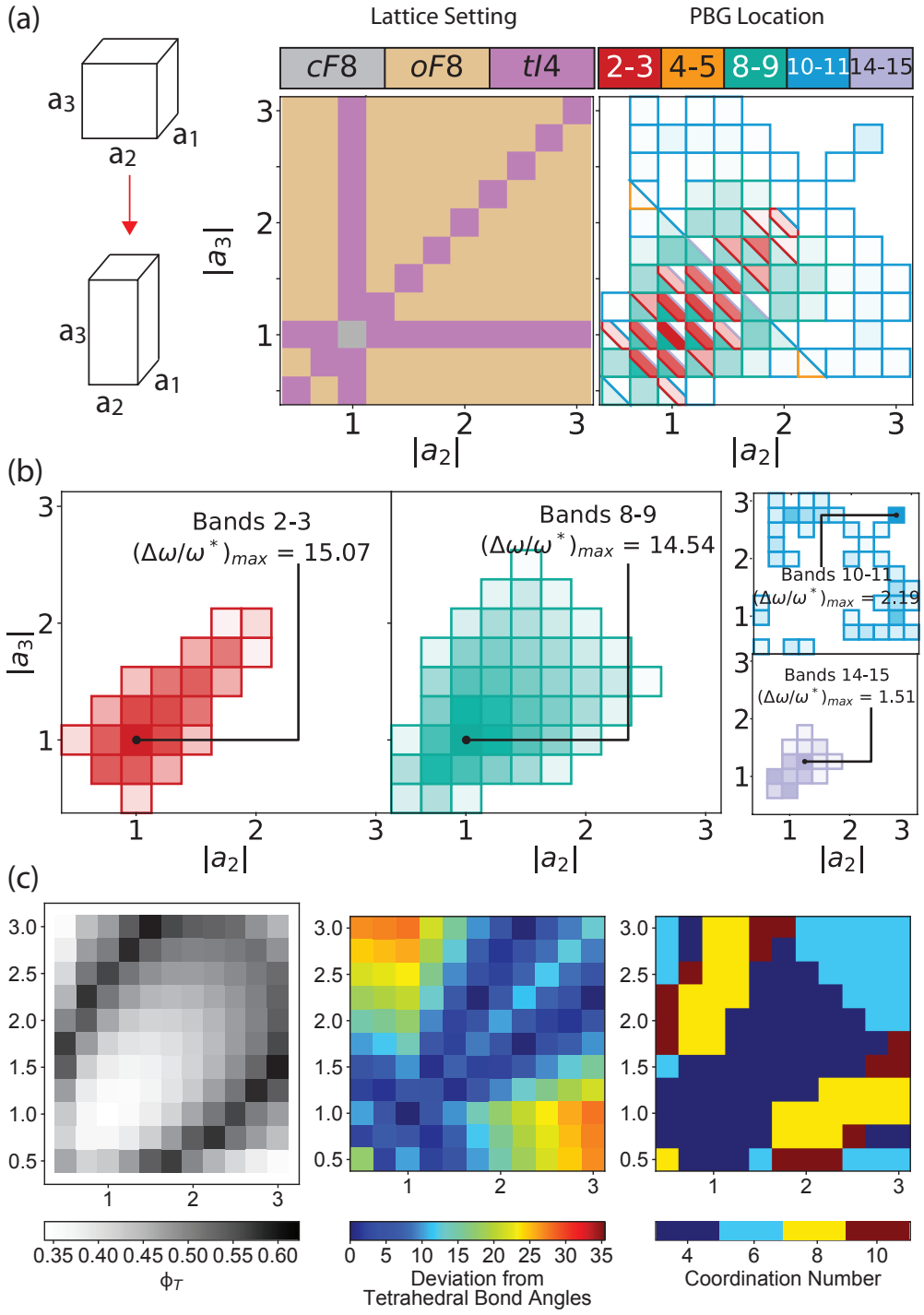

Figure 8.7: **The Effects of Orthorhombic Scaling on the PBGs in Diamond** (a) Effect of Orthorhombic Scaling on Lattice Setting and Photonic Band Gaps. (b) Effect on PBGs found between bands 2-3, 8-9, 10-11, and 14-15. (c) Effects on Connectivity Threshold ϕ_T, Bond Angles, and Coordination Number

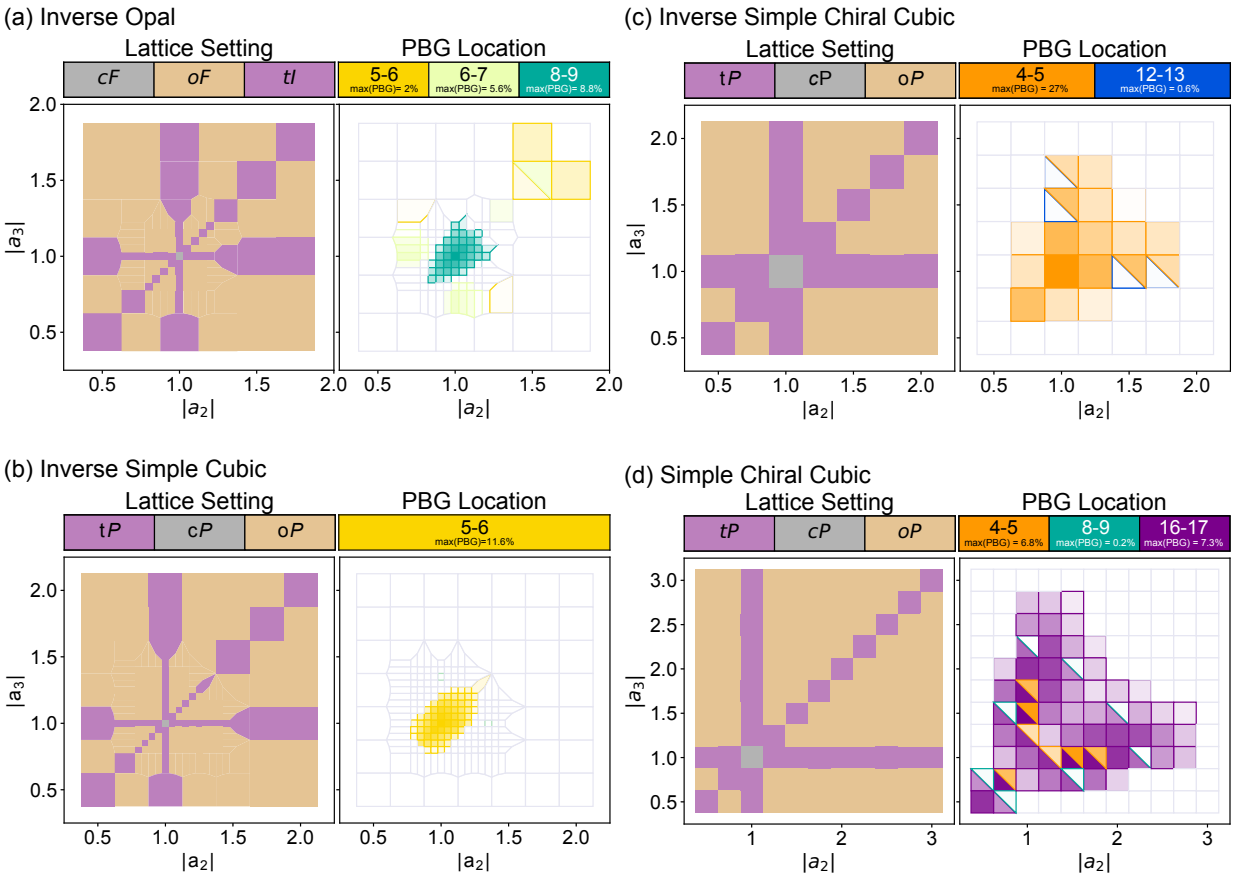

Figure 8.8: **The Effects of Orthorhombic Scaling on Other PBGs** (a) Inverse Opal, (b) Inverse Simple Cubic, (c) Inverse Simple Chiral Cubic, and (d) Simple Chiral Cubic.

[1] Photonic Band Gaps in Experientally Realizable Periodic Dielectric Structures. *Europhysics Letters* **16**, 563-568(1991).

[2] Robust topology optimization of three-dimensional photonic-crystal band-gap structures.. *Optics Express* **22**, 22632(2014).

[3] Sözüer, H. S. & Haus, J. W. Photonic bands: simple cubic lattice. *Journal of the Optical Society of America B* **10**, 296(1993).

[4] Chutinan, A. & Noda, S. Spiral three-dimensional photonic-band-gap structure. *Physical Review B* **57**, R2006–R2008 (1998).

[5] Dresselhaus, M. S., Dresselhaus, G. & Jorio, A. A. *Group theory : application to the physics of condensed matter* (Springer-Verlag, 2008).

[6] Watanabe, H. & Lu, L. Space Group Theory of Photonic Bands. *Physical Review Letters* **121**, 263903 (2018). 1805.10103.

CHAPTER IX

Conclusions

I once asked a young dissertation writer whether her suddenly grayed hair was due to ill health or personal tragedy; she answered: "It was the footnotes".

– Joanna Russ, *How to Suppress Women's Writing*

In this dissertation I have presented work as it relates to the self-assembly and design of novel colloidal and photonic systems. I have done so by performing computations to understand the role of shape in colloidal self-assembly and to understand the relationship between structure and photonic band gaps.

Here I highlight the scope and main conclusions from each of the five main chapters forming this dissertation. The first of these chapters[1] investigated the role that packing plays in colloidal self-assembly of hard polyhedra. We examined the three systems, BCC, FCC, and SC in the alchemical ensemble and demonstrated that the onset of packing occurs at densities higher than spontaneous self-assembly. We also showed that packing rules were not necessarily predictive of the ideal shapes for self-assembly.

The second study[2] focused on a shape-induced phase transition in a system of diamond-assembling hard polyhedral nanoparticles. We quantified the transition using the box ratio c/a as an order parameter, and demonstrated that it was a continuous transition by examining the equation of state and potential of mean force and torque (PMFT). We computed the effects of this transition on the photonic properties of the corresponding structures, and

found that this system could potentially toggle between 4 photonic states.

The third of the works included in this thesis focused on the implementation of Digital Alchemy for design across shape space. In this section, I demonstrated two features of shape space that may influence the results through exploration in the extended ensemble. First, there exists a global free energy well towards which simulations will drive under no structural constraints. Secondly, the structural constraints impart a non-trivial bias on the results of DA simulations and may not ensure the identification of a the optimized design parameter.

The second part of the dissertation, spanning Chapters VII-VIII, focused on the properties underlying a popular motivator for nanoparticle self-assembly: photonic band gaps. In Chapter VII[3], we computed over 150,000 photonic band structures and showed that the range of photonic crystal targets is far broader and more complex than previously thought, calling for a more exhaustive theory of photonic band gap materials. The final chapter looked at some structural modifications possible on photonic crystals, both in attempt to increase the photonic band gaps or understand the robustness of these gaps.

9.1 Additional Work

There are also a few supplementary works are briefly mentioned below.

1. **Digital Alchemy for Novel Photonic Crystals.** In continued work with Yuan Zhou, I am looking to design the self-assembly of photonic nanocrystals. Together, we are exploring the use of Digital Alchemy and interparticle interactions to design PBG colloidal crystals capable of self-assembly and reconfigurability. Currently, she has started investigating $cI16$-Li, and I have looked into $tI8$-YMn and Simple Chiral Cubic (previously studied in [4, 5]).

2. **Binary Mixtures that form the Lithium Oxide Structure.** A colleague, Andrew Cadotte, previously found a binary system capable of assembling the lithium oxide structure (which exhibited many interesting photonic properties, as seen in Chapter

VII)[6]. I ran simulations to test the conditions where this binary mixture would self-assemble, across size ratio and truncation parameters, and determined the range of these parameters that self-assemble Lithium Oxide.

9.2 Outlook

9.3 Open Questions

1. **Does shape entropy play a role in the stability of atomic phases?** The phase transition witnessed in Chapter IV parallels one that occurs at the atomic length scale in systems of Si, Ge, and Sn. We have shown that tetrahedral coordination and pressure alone can induce a phase transition to tetragonal derivatives. It is plausible that the shape of the electron orbitals for the lower pressure atomic structures (tetrahedral in diamond) may drive the transition to β-Sn at higher pressures. It follows to ask: are there other atomic systems that form or transition based upon the shape entropy of their orbitals? What can we infer from understanding shape entropy at colloidal length scales?

2. **Can we make reconfigurable photonic crystals from the expanded list of PBG crystals?** One of the most exciting implications of Chapter VII is the inspiration we can gain from the structural templates. Given that many templates are polymorphs of one another in their natural forms, it is possible that a single system can transition between these two states.

3. **What design spaces of photonic crystals have yet to be explored?** In Chapter VII, we only scratched the surface with designing photonic crystals. There are so many other spaces to explore: multicomponent systems, polyhedral regions of dielectric medium, and design with specific synthesis or fabrication methods in mind.

The work presented has applications across many fields; colloidal systems have been used

in photonic crystals, data storage, and drug delivery. [7, 8, 9, 10, 11] The ability to design for the self-assembly of these systems is a large part of this, as it will enable the development and use of novel materials. Photonic crystals, given the dependence of their properties on the scale on which the crystal is made, can be used across the electromagnetic spectrum. The work covered in Chapters VII - VIII pushed the understanding of the phenomenon and opened a wide new space of photonic crystal targets for fabrication.

9.4 Concluding Remarks

It feels surreal to be concluding five years of hard work and inquiry. My best advice, for those who should ever look here for it, is to follow a question. It is very easy to define research in terms of "I have done X. Let me try X on A, B, and C", but without a guiding question it's hard to see the big picture. I've not always succeeded at this, the purpose of a PhD is to learn how to learn through *both* failures and triumphs. Yet, if you have a question, if you have a concrete purpose to the research you're conducting, it's much easier to push through these obstacles to seek understanding.

One never notices what has been done; one can only see what remains to be done.

– Marie Curie

References

[1] Cersonsky, R. K., Dshemuchadse, J., Antonaglia, J., van Anders, G. & Glotzer, S. C. Pressure-Tunable Band Gaps in an Entropic Crystal. *Phys. Rev. Mat.* (2018).

[2] Cersonsky, R. K., Antonaglia, J. A., Dice, B. D. & Glotzer, S. C. Unexpected Diversity of Three-Dimensional Photonic Crystals. *Submitted* (2019).

[3] Cersonsky, R. K., Antonaglia, J. A., Dice, B. D. & Glotzer, S. C. Unexpected Diversity of Three-Dimensional Photonic Crystals. *Submitted* (2019).

[4] Damasceno, P. F., Karas, A. S., Schultz, B. A., Engel, M. & Glotzer, S. C. Controlling Chirality of Entropic Crystals. *Physical Review Letters* **115**, 158303 (2015).

[5] Geng, Y., van Anders, G., Dodd, P. M., Dshemuchadse, J. & Glotzer, S. C. Engineering Entropy for Design. *Submitted* `1712.02471`.

[6] Cadotte, A. T., Dshemuchadse, J., Damasceno, P. F., Newman, R. S. & Glotzer, S. C. Self-assembly of a space-tessellating structure in the binary system of hard tetrahedra and octahedra. *Soft Matter* **12**, 7073–7078 (2016).

[7] Glotzer, S. C. & Solomon, M. J. Anisotropy of building blocks and their assembly into complex structures. *Nat Mater* **6**, 557–562 (2007).

[8] Aguirre, C. I., Reguera, E. & Stein, A. Tunable Colors in Opals and Inverse Opal Photonic Crystals. *Advanced Functional Materials* **20**, 2565–2578 (2010).

[9] Zhang, J., Sun, Z. & Yang, B. Self-assembly of photonic crystals from polymer colloids (2009).

[10] Phillips, C. L. *et al.* Digital Colloids: Reconfigurable Clusters as High Information Density Elements. *Soft Matter* **10**, 7468–7479 (2014).

[11] Nguyen, T. D., Jankowski, E. & Glotzer, S. C. Self-Assembly and Reconfigurability of Shape-Shifting Particles. *ACS Nano* **5**, 8892–8903 (2011).

APPENDICES

APPENDIX A

An Explanation of Photonic Crystals, Starting with Maxwell's Equations

A1. Useful Equations

1. Mathematic Equivalences and Definitions

Here, A is a general field or equation, depending on the definition.

1. Curl: $\nabla \times \mathbf{A}(x,y,z) = \det \begin{bmatrix} \hat{x} & \hat{y} & \hat{z} \\ \frac{\partial}{\partial x} & \frac{\partial}{\partial y} & \frac{\partial}{\partial z} \\ A_x & A_y & A_z \end{bmatrix}$

2. Divergence: $\nabla \cdot \mathbf{A}(x_1, x_2, ..., x_n) = \frac{\partial A_1}{\partial x_1} + \frac{\partial A_2}{\partial x_2} + ... + \frac{\partial A_n}{\partial x_n}$

3. Laplace Operator: $\nabla^2 \mathbf{A} = \nabla(\nabla \cdot \mathbf{A}) - \nabla \times (\nabla \times \mathbf{A})$

4. Stoke's Theorem: $\oint \mathbf{A} \cdot d\mathbf{l} = \iint_{\mathbf{S}} \nabla \times \mathbf{A} \cdot d\mathbf{S}$

5. $\nabla \cdot (\nabla \times \mathbf{A}) = 0$ (This is a feature of all continuous vector fields)

2. Physical Relations

Here, **D**, **E**, **H**, and **B** are the divergence, electric, magnetic, and magnetic flux fields, respectively. μ, ε, and χ represent the magnetic permeability, dielectric constant, and electric susceptibility, respectively.

1. $\mathbf{D} \equiv \varepsilon \mathbf{E}$

2. $\mu \mathbf{H} \equiv \mathbf{B}$

3. $\varepsilon \equiv \varepsilon_0(1 + \chi_e)$

4. $\varepsilon \equiv \varepsilon_0 \varepsilon_r$

A2. The Maxwell Equations

The Maxwell Equations are four equations that apply to describe electromagnetic behavior. The four equations can be used to derive all other equations in electromagnetism.

1. Gauss's Law

   $\nabla \cdot \mathbf{E} = \frac{1}{\varepsilon_0}\rho$

2. Gauss's Law for Magnetism

   $\nabla \cdot \mathbf{B} = 0$

3. Faraday's Law

   $\nabla \times \mathbf{E} = -\frac{\partial \mathbf{B}}{\partial t}$

4. Ampère's Law with Maxwell's Correction

   $\nabla \times \mathbf{B} = \mu_0 \mathbf{J} + \mu_0 \varepsilon_0 \frac{\partial \mathbf{E}}{\partial t}$

1. Gauss's Law

Origins The history of Gauss's Law is a point of debate, as four scientists have discovered it independently, Carl Friedrich Gauss in 1813, [1]Joseph-Louis Lagrange in 1760,[2] George Green in 1823 in his *Essay on the Mathematical Theory of Electricity and Magnetism*[3] and Mikhail Ostrogradsky in 1826.[4]

Whether it be Lagrange's Theorem, Gauss's Theorem, Green's Theorem, or Ostrogradsky's Theorem, it states that for a closed surface:

$$\nabla \cdot \mathbf{E} = \frac{1}{\varepsilon_0}\rho \tag{A.1}$$

where $\nabla \cdot \mathbf{E}$ is the electric flux, ε_0 is the dielectric constant, and ρ is the electric charge density per unit volume for both free and bound charge ($\rho = \rho_f + \rho_b$). Now we can write this in terms of the free charge and polarization density:

$$\begin{aligned} \rho &= \rho_f + \rho_b \\ \rho &= \rho_f - \nabla \cdot \mathbf{P} \\ \nabla \cdot \mathbf{E} &= \frac{1}{\varepsilon_0}\left(\rho_f - \nabla \cdot \mathbf{P}\right) \\ \rho_f &= \nabla \cdot (\varepsilon_0 \mathbf{E} + \mathbf{P}) \end{aligned} \tag{A.2}$$

This equation can be transformed to detail the electric displacement field $\mathbf{D}$,

$$\begin{aligned} \mathbf{D} &\equiv \varepsilon_0 \mathbf{E} + \mathbf{P} \\ \nabla \cdot \mathbf{D} &= \rho_f \end{aligned} \tag{A.3}$$

where ρ_f is the free surface charge density.

Practical Interpretations Essentially, this means that without an electric charge on the surface, it is impossible to have a divergent electric field on a closed surface. In a pure Faraday field, where any electric field is based upon a changing **B** field and no surface charge is present, the electric field is non-divergent.

$$\nabla \cdot \mathbf{E} = 0 \tag{A.4}$$

2. Gauss's Law for Magnetism

Origins Whereas for electric fields there can exist free charges, the same cannot be said for magnetic fields. This idea, the nonexistence of magnetic monopoles (magnetic fields originate from magnetic dipoles) dates back to 1269 with Petrus Peregrinus Maricourt.[5] Over the next 600 years, the idea was expanded to its current form:

$$\nabla \cdot \mathbf{B} = 0 \tag{A.5}$$

If a magnetic monopole were to be found to exist, this law would take the form:

$$\nabla \cdot \mathbf{B} = \rho_m \tag{A.6}$$

where ρ_m would be the magnetic charge density.

Practical Interpretations Consider a bar magnet. If you were to split it into two along the division between the (-) and (+) poles, would you create two separate (-) and (+) magnets? In fact, you would create two smaller magnets, each with their own (-) and (+) poles. This is due to the many currents within the magnets, which would not fail to flow if the magnet were made smaller, but would oscillate within the new shape, again creating the two separate poles.

3. Faraday's Law

Origins In 1831, Michael Faraday conducted a series of experiments that led to the formulation of Faraday's law. In each experiment, he placed a loop of wire within a magnetic field and performed three actions: (1) he pulled the loop to the right through the magnetic field, (2) he moved the magnet to the left and held the loop still, and (3) he left both the magnet and the loop in place and changed the strength of the magnetic field. In each case, a current flowed through the loop, which led him to the conclusion that there must be a relationship between magnetic and electric fields. He deduced that *A changing magnetic field induces an electric field.* [6]

He then formulated an equation to describe their relationship. He was able to measure the emf ($\mathcal{E}$ electromotive force or electromotance, which is the integration of the electric field with respect to a distance), and found that it was equal to the rate of change in the flux of the magnetic field Φ, i.e. the flux rule:

$$\mathcal{E} = \oint \mathbf{E} \cdot d\mathbf{l} = -\frac{d\Phi}{dt} \tag{A.7}$$

where we know that:

$$\begin{aligned} \Phi &= \iint_S \mathbf{B} \cdot d\mathbf{S} \\ \frac{d\Phi}{dt} &= \iint_S \frac{\partial \mathbf{B}}{\partial t} \cdot d\mathbf{S} \end{aligned} \tag{A.8}$$

therefore, using Stoke's Theorem,

$$\begin{aligned} \oint \mathbf{E} \cdot d\mathbf{l} &= -\iint_S \frac{\partial \mathbf{B}}{\partial t} \cdot d\mathbf{S} \\ \iint_{\mathbf{S}} \nabla \times \mathbf{E} \cdot d\mathbf{S} &= -\iint_S \frac{\partial \mathbf{B}}{\partial t} \cdot d\mathbf{S} \\ \nabla \times \mathbf{E} &= -\frac{\partial \mathbf{B}}{\partial t} \end{aligned} \tag{A.9}$$

Practical Interpretations The best way to think of this law is as nature's response to unbalance. Nature does not like a change in magnetic flux, so it induces a current to maintain balance. Griffiths points out that based upon this definition, we really should not consider (1) an example of Faraday's law: (2) and (3) were cases of static electrons being mobilized by a change in the magnetic field, whereas in (1) the electrons were being dragged by the moving electric field.

4. Ampère's Law with Maxwell's Correction

Origins Ampère was conducting experiments with forces on wires in the 1820s, looking at the magnetic effects of a current running through a wire. He found that for a wire or conductor containing an electric current I, there would be a magnetic field B created. This magnetic field would encircle the wire, and the integral of the magnetic field along a given path would be equal to the current it encloses. In other words:

$$\mu_0 \oint \mathbf{B} \cdot d\mathbf{l} = I_{enc}\mu_0 \tag{A.10}$$

Note that this integration is agnostic to the line chosen (this will be important later). Again, using Stoke's theorem,

$$\oint \mathbf{B} \cdot d\mathbf{L} = \int_{\mathbf{S}} \nabla \times \mathbf{B} \cdot d\mathbf{S} \tag{A.11}$$

The enclosed current can be written as the surface integral of the current density J:

$$I_{enc} = \int_S \mathbf{J} \cdot d\mathbf{S} \tag{A.12}$$

therefore,

$$\begin{aligned} \int_{\mathbf{S}} \nabla \times \mathbf{B} \cdot d\mathbf{S} &= \mu_0 \int_{\mathbf{S}} \mathbf{J} \cdot d\mathbf{S} \\ \nabla \times \mathbf{B} &= \mu_0 \mathbf{J} \end{aligned} \tag{A.13}$$

Because the choice of surface and line are arbitrary, we can set the integrands of these two equations to be equal. This final result was thought to be the relationship between the magnetic field and current density from the 1820s up through the 1860s, at which point it was corrected by this identity:

$$\nabla \cdot (\nabla \times \mathbf{A}) = 0 \tag{A.14}$$

which is true for any vector field. Given this equation, $\nabla \cdot (\nabla \times \mathbf{B}) = \nabla \cdot \mathbf{J} = 0$, which implies that all current densities are without divergence. However, for a length of conductor, there are many cases in which the density in does not equal the density out (equalling divergence), such as when the conductor is interrupted by a capacitor. In reality:

$$\nabla \cdot \mathbf{J} = -\frac{\partial \rho}{\partial t} \tag{A.15}$$

James Clerk Maxwell conceived of displacement current as a polarization current in the dielectric vortex sea, which he used to model the magnetic field hydrodynamically and mechanically. He added this displacement current to Ampère's circuital law at equation 112 in his 1861 paper *On Physical Lines of Force*,[7] creating what we now know as the fourth

Maxwell equation:

$$\nabla \times \mathbf{B} = \mu_0 \mathbf{J} + \mu_0 \varepsilon_0 \frac{\partial \mathbf{E}}{\partial t} \tag{A.16}$$

which was found experimentally in systems of $\mathbf{J} = 0$.

Practical Interpretations A flowing electric current gives rise to a magnetic field that circles that current, as will a changing **E** or corresponding **D** flux.

A3. Simple Formulation of EM Waves

Consider a force F on a taut string:

$$\Delta F = T sin\theta' - T sin\theta \tag{A.17}$$

where T is the tension in the string and θ' and θ are the angles that the string makes with the z-axis at distance z and $z + \Delta z$, respectively. When θ is small we can approximate:

$$\begin{aligned} \Delta F &\approx T tan\theta' - T tan\theta \\ \Delta F &= T\left(\left(\frac{\partial f}{\partial z}\right)_{z+\Delta z} - \left(\frac{\partial f}{\partial z}\right)_{z}\right) \\ \Delta F &= T\left(\frac{\partial^2 f}{\partial z^2}\right)\Delta z \end{aligned} \tag{A.18}$$

Newton's law can be understood as $\Delta F = m\Delta a$, therefore:

$$\begin{aligned} \Delta F &= m\left(\frac{\partial^2 f}{\partial t^2}\right) \\ \Delta F &= \mu\left(\frac{\partial^2 f}{\partial t^2}\right)\Delta z \\ T\left(\frac{\partial^2 f}{\partial z^2}\right)\Delta z &= \mu\left(\frac{\partial^2 f}{\partial t^2}\right)\Delta z \\ T\left(\frac{\partial^2 f}{\partial z^2}\right) &= \mu\left(\frac{\partial^2 f}{\partial t^2}\right) \end{aligned} \tag{A.19}$$

Given $v = \sqrt{\frac{T}{\mu}}$, we get the classical wave equation:

$$\frac{\partial^2 f}{\partial z^2} = \frac{1}{v^2}\frac{\partial^2 f}{\partial t^2} \tag{A.20}$$

for a given displacement f along the z axis. This gives us the form of a wave:

$$f(z,t) = g(z - vt) + h(z + vt) \tag{A.21}$$

which for sinusoidal waves takes the form:

$$f(z,t) = f_0 cos[k(z - vt)] = f_0 cos[kz - \omega t] \tag{A.22}$$

Alas, this is only the real component of the wave. Considering the complex components and Euler's formula, the wave will then take the form:

$$\begin{aligned} \tilde{f}(z,t) = f_0\left[cos[kz - \omega t] + isin[kz - \omega t]\right] \\ \tilde{f}(z,t) = f_0 e^{i(kz - \omega t)} \end{aligned} \tag{A.23}$$

We can decouple the spatial and time dependence:

$$\tilde{f}(z,t) = f_0 e^{i(kz)} e^{-i(\omega t)} \tag{A.24}$$

A4. Extension to Photonic Crystals

Let's take the Maxwell equations and transform them into the *macroscopic* Maxwell equations, for which the formulations of Gauss's law and Ampere's law take into account two new fields, the displacement field **D** and the magnetizing field **H**, defined in homogenous

materials as

$$\begin{aligned} \mathbf{D} &\equiv \varepsilon \mathbf{E} \\ \mu \mathbf{H} &\equiv \mathbf{B} \\ \varepsilon = \varepsilon_0 \varepsilon_R &= \varepsilon_0 \left(1 + \chi_e\right) \mu = \mu_0 \mu_R \end{aligned} \tag{A.25}$$

where ε_0 and μ_0 are the material permittivity and permeability, respectively. This takes into account the macroscopic properties of the bulk material where appropriate. We are also going to arrange the equations to reflect the "fields" and "sources" on the left and right, respectively. Now we have:

1. $\nabla \cdot \mathbf{D} = \rho$
2. $\nabla \cdot \mathbf{B} = 0$
3. $\nabla \times \mathbf{E} + \frac{\partial \mathbf{B}}{\partial t} = 0$
4. $\nabla \times \mathbf{H} - \frac{\partial \mathbf{D}}{\partial t} = \mathbf{J}$

Now we will consider a material of mixed but homogenous material in which light propagates but no light is necessarily introduced (that is, $\rho = 0$ and $\mathbf{J} = 0$). Given that the material consists of regions of differing dielectric strength, we consider ε to be a real, positive function of $\mathbf{r}$, ignoring any frequency dependence (more on this later). We'll also assume that each region of material is isotropic and macroscopic, such that higher order terms in the relationship between the $\mathbf{D}$ field and $\mathbf{E}$ field can be ignored (for mixed dielectric media, the displacement field of region i is defined $D_i/\varepsilon_0 = \sum_j \varepsilon_{ij} E_j + \sum_{j,k} \chi_{ijk} E_j E_k + O(E^3)$, we disregard all but the first term). Given the hetergeneity of the materials, we define $\varepsilon = \varepsilon_0 \varepsilon(\mathbf{r})$

and $\mu = \mu_0\mu(\mathbf{r})$ to give us:

$$\begin{aligned} \mathbf{D}(\mathbf{r}) &\equiv \varepsilon_0\varepsilon(r)\mathbf{E}(\mathbf{r}) \\ \mathbf{H}(\mathbf{r}) &\equiv \mu_0\mu(r)\mathbf{B}(\mathbf{r}) \end{aligned} \tag{A.26}$$

Therefore, let's include our assumptions and get our Maxwell equations into only two field variables:

1. $\nabla \cdot [\varepsilon(\mathbf{r})\mathbf{E}(\mathbf{r},t)] = 0$
2. $\nabla \cdot \mathbf{H}(\mathbf{r},t) = 0$
3. $\nabla \times \mathbf{E}(\mathbf{r},t) + \mu_0 \frac{\partial \mathbf{H}(\mathbf{r},t)}{\partial t} = 0$
4. $\nabla \times \mathbf{H}(\mathbf{r},t) - \varepsilon_0\varepsilon(\mathbf{r}) \frac{\partial \mathbf{E}(\mathbf{r},t)}{\partial t} = 0$

Given that our fields can be expanded into as harmonic modes, we can now separate our fields into their spatial ($\mathbf{r}$) and time (t) dependent components (see section A3):

$$\begin{aligned} \mathbf{H}(\mathbf{r},t) &= \mathbf{H}(\mathbf{r})e^{(-i\omega t)} \\ \mathbf{E}(\mathbf{r},t) &= \mathbf{E}(\mathbf{r})e^{(-i\omega t)} \end{aligned} \tag{A.27}$$

If we take a look at our constraints given by Gauss's law of magnetism and we define $\mathbf{H}(\mathbf{r}) = \mathbf{H}_0 e^{i\mathbf{k}\cdot\mathbf{r}-\omega t}$, as is customary for electromagnetic waves, we must constrain $\mathbf{H}_0$ and $\mathbf{k}$ such that $\mathbf{H}_0 \cdot \mathbf{k} = 0$.

Now let's apply our formulations to Faraday's and Ampere's laws:

$$\begin{aligned} \nabla \times \mathbf{E}(\mathbf{r}) - i\omega\mu_0\mathbf{H}(\mathbf{r}) &= 0 \\ \nabla \times \mathbf{H}(\mathbf{r}) + i\omega\varepsilon_0\varepsilon(\mathbf{r})\mathbf{E}(\mathbf{r}) &= 0 \end{aligned} \tag{A.28}$$

Focusing on the **H** field (although this choice is arbitrary), we can simplify to our master equation by (1) dividing by $\varepsilon(\mathbf{r})$, (2) taking the curl, and (3) using the previous **E** equation to eliminate **E** in the final equation in four steps:

$$\begin{aligned} \frac{1}{\varepsilon(\mathbf{r})}\nabla \times \mathbf{H}(\mathbf{r}) &= -i\omega\varepsilon_0 \mathbf{E}(\mathbf{r}) \\ \nabla \times \left(\frac{1}{\varepsilon(\mathbf{r})}\nabla \times \mathbf{H}(\mathbf{r})\right) &= -i\omega\varepsilon_0 \left(\nabla \times \mathbf{E}(\mathbf{r})\right) \\ \nabla \times \left(\frac{1}{\varepsilon(\mathbf{r})}\nabla \times \mathbf{H}(\mathbf{r})\right) &= -i\omega\varepsilon_0 \left(i\omega\mu_0 \mathbf{H}(\mathbf{r})\right) \\ \nabla \times \left(\frac{1}{\varepsilon(\mathbf{r})}\nabla \times \mathbf{H}(\mathbf{r})\right) &= \omega^2\varepsilon_0\mu_0 \mathbf{H}(\mathbf{r}) \end{aligned} \tag{A.29}$$

and thus:

$$\nabla \times \left(\frac{1}{\varepsilon(\mathbf{r})}\nabla \times \mathbf{H}(\mathbf{r})\right) = \left(\frac{\omega}{c}\right)^2 \mathbf{H}(\mathbf{r}) \tag{A.30}$$

Tada! This is the **master equation**, from which we can calculate ω, the frequencies that serve as solutions to the eigenproblem, given a periodic dielectric function ε. From now on, for brevity, we will formulate this equation:

$$\Theta\mathbf{H}(\mathbf{r}) = \left(\frac{\omega}{c}\right)^2 \mathbf{H}(\mathbf{r}) \tag{A.31}$$

where $\Theta\mathbf{H}(\mathbf{r})$ represents $\nabla \times \left(\frac{1}{\varepsilon(\mathbf{r})}\nabla \times \mathbf{H}(\mathbf{r})\right)$. Θ is both linear (i.e. if $\mathbf{H}_1(\mathbf{r})$ and $\mathbf{H}_2(\mathbf{r})$ are both solutions, so is $\alpha\mathbf{H}_1(\mathbf{r}) + \beta\mathbf{H}_2(\mathbf{r})$, where α and β are constants) and Hermitian.[i]

A5. Computing the Photonic Band Structure

Practically, the eigenvalues of the master equation in A.31 can be computed as any other eigenproblem of the form $A\boldsymbol{v} = \lambda\boldsymbol{v}$, so the main source of computational complexity lies in solving for the matrix components.

[i] A hermitian matrix is one which is unchanged by the conjugate transpose operation. Because Eq. A.31 is Hermitian, it follows that the square of the eigenvalues will be real. A full derivation of this property is given in [8], pages 11-13.

Johnson and Joannopoulos showed that A.31 could be simplified by rewriting the magnetic field H into a sum of basis functions, given in Dirac notation as:

$$\hat{A}_{\vec{k}}\big|H_{\vec{k}}\big\rangle = \frac{\omega^2}{c^2}\big|H_{\vec{k}}\big\rangle \tag{A.32}$$

$$\big|H_{\vec{k}}\big\rangle = \sum_{m=1}^{N} h_m|b_m\rangle \tag{A.33}$$

this gives $Ah = \frac{\omega^2}{c^2}Bh$, where:

$$A_{lm} = \langle b_l|\hat{A}_{\vec{k}}|b_m\rangle \tag{A.34}$$

$$B_{lm} = \langle b_l b_m|\rangle \tag{A.35}$$

here B_{lm} will reduce to the identity matrix, and A_{lm} can be computed in O(n log(n)) using[9]:

$$A_{lm} = -(\vec{k}+\vec{G}_l)...IFFT...\tilde{\varepsilon^{-1}}...FFT...(\vec{k}+\vec{G_m}) \tag{A.36}$$

where "FFT" and "IFFT" represent a fast Fourier transform and the inverse operation.

A6. The Caveats

1. Length-Scale Covariance

In the master equation, it is interesting to note that there are no constants with dimensions of length - alluding to the fact that the results found are scale-invariant. Let's test this theory.

Say that our dielectric function is scaled by some parameter s, such that $\mathbf{r}' = s\mathbf{r}$. Changing the variables, we get $\nabla' = \nabla/s$ and replace all remaining $\mathbf{r}$ in our master equation by

$\mathbf{r}'/s$:

$$s\nabla' \times \left(\frac{1}{\varepsilon\left(\mathbf{r}'/s\right)} s\nabla' \times \mathbf{H}(\mathbf{r}'/s) \right) = \left(\frac{\omega}{c}\right)^2 \mathbf{H}(\mathbf{r}'/s) \tag{A.37}$$

By extracting the s's from the left side of the equation, we create:

$$\nabla' \times \left(\frac{1}{\varepsilon\left(\mathbf{r}'/s\right)} \nabla' \times \mathbf{H}(\mathbf{r}'/s) \right) = \left(\frac{\omega}{sc}\right)^2 \mathbf{H}(\mathbf{r}'/s) \tag{A.38}$$

Which shows that for a scaling by a factor of s, our eigenvalues will scale by $1/s$, such that $\omega' = \omega/s$. Our mode profile for $\mathbf{r}$ ($\mathbf{H}(\mathbf{r})$) similarly scales, i.e. the solution of the problem at one length scale determines the solutions at other length scales.

However, the practical applications of photonic properties requires a scale-covariance, i.e. that there needs to be a determined length scale in order to find the corresponding gap frequencies. The returned eigenvalues will be in units c/a, where c is the speed of light and a is the lattice parameter. The unit-bearing frequencies are then given by:

$$\lambda = \frac{a}{\omega} \tag{A.39}$$

2. Frequency Dependence of Permittivity

The permittivity, or dielectric constant ε, is not a constant, but rather a function of the wavelength λ. This frequency-dependence is called dispersion, and materials exhibiting it are known as dispersive media. We can actually consider the electrons in the dielectric under multiple forces:

$$\begin{aligned} F_{binding} &= -k_{spring}x = -m\omega_0^2 x \\ F_{damping} &= -m\gamma\frac{dx}{dt} \\ F_{driving} &= qE = qE_0 cos[\omega t] \\ m\frac{d^2x}{dt^2} &= F_{tot} = F_{binding} + F_{damping} + F_{driving} \end{aligned} \tag{A.40}$$

where x is our displacement coordinate, m is the mass, q is change of an electron, and γ is the damping constant.

Assuming a complex equation $\tilde{x}$, this becomes:

$$\begin{aligned} m\frac{d^2\tilde{x}}{dt^2} + m\gamma\frac{d\tilde{x}}{dt} + m\omega_0^2\tilde{x} &= qE_0e^{(i\omega t)} \\ \frac{d^2\tilde{x}}{dt^2} + \gamma\frac{d\tilde{x}}{dt} + \omega_0^2\tilde{x} &= qE_0/me^{(i\omega t)} \end{aligned} \tag{A.41}$$

which at steady state gives:

$$\begin{aligned} \tilde{x}(t) &= \tilde{x_0}e^{(i\omega t)} \\ -\omega^2\tilde{x_0} + i\omega\gamma\tilde{x_0} + \omega_0^2\tilde{x_0} &= qE_0/m \\ \tilde{x_0} &= \frac{q/m}{-\omega^2 + i\omega\gamma + \omega_0^2}E_0 \end{aligned} \tag{A.42}$$

The polarization $\tilde{\mathbf{P}}$, which is the dipole per unit volume, is found by summing over all populations of electrons with a given frequency and damping coefficient, subscripted j:

$$\tilde{\mathbf{P}} = \frac{Nq^2}{m}\left(\sum_j \frac{f_j}{-\omega^2 + i\omega\gamma_j + \omega_j^2}\right)\tilde{\mathbf{E}} \tag{A.43}$$

where f_j is the size of each population. And for linear media:

$$\tilde{\mathbf{P}} = \varepsilon_0\tilde{\chi_e}\tilde{\mathbf{E}} \tag{A.44}$$

and as $\varepsilon_R = 1 + \tilde{\chi_e}$,

$$\varepsilon_R = 1 + \frac{Nq^2}{m}\left(\sum_j \frac{f_j}{-\omega^2 + i\omega\gamma_j + \omega_j^2}\right) \tag{A.45}$$

giving us our non-constant ε as a function of ω.

APPENDIX B

Signac Cookbook

B1. Tips for Running HOOMD Simulations with *signac*

1. Statepoints and Documents

I find it very useful to mold my HOOMD simulations around the signac infrastructure.[10] For this, I'll distinguish between the static and dynamic data storage for signac. The ensemble-defining parameters should go in the signac statepoint, so a typical $NVT\mu$ ensemble simulation may have a statepoint like:

```
{
   "phi": 0.6,\ #running our simulation at a filling fraction of 0.6 (analogous to constant volume)
   "N": 512,\
   "target": "sc", #the target we are trying to optimize
}
```

The signac document can be used to store the dynamic data from a simulation:

```
{
   "pressure": 100,\ # such as when calculated using the sdf analyzer
   "vertices": {"A": [...], "B":[...]},\ #dictionary of vertices for a DA simulation
   "MC_sweep": 20001000,\ #current mc sweep, as gotten by hoomd.get\_step()
   "total_run": 40000000,\ #target number of MC sweeps to run for, can be increased if equilibrium isn't
       reached
   "random_seed": 5003452,\ #random seed to be used in simulation. I like to put it in the document so that
       my searching of statepoints doesn't have to account for random seeds
```

```
   "output_file": "...",\ #current output file, if file type is rewrite only
}
```

2. Using Signac Operations for Code Reusability

Often times we have sections of our simulations that require the same type of code. I like to use signac operations to avoid code duplication:

```
##operations.py

def __simulate__(job, mode, dump_period = 1e3):
   #names outputs with the given mode
   restart = 'restart.{}.gsd'.format(mode)

   #code that runs the simulation, dumping restart or data at the prescribed dump_period

def compress(job):
   #do what I need to do to compress
   __simulate__(job, "compress", 1e2)

def equilibrate(job):
   __simulate__(job, "equilibrate", 1e4)

def collect_data(job):
   #do what I need to do to set up data collection
   __simulate__(job, "collect")

if __name__=="__main__":
   import flow
   flow.run()
```

B2. Multi-Level Projects

During my doctoral work, I used a data management framework *signac* to organize, develop, and conduct my work. Some of my signac usage is quite textbook, however for a few projects I employed multi-level projects, as I will detail here.

For the projects covered in Chapters VII-VIII, it was appropriate to conduct computations/calculations on two levels: "sub-job" and "super-jobs". The super-job would correspond to the structures, *e.g.* $cF8$-C or $cP1$-Po and the sub-jobs would correspond to individual states, such as with different materials or filling fraction. A snapshot of this file structure is given in Fig. 7.6.

1. The Project.py Files and Status Calls

The *signac* super-project file can look like this:[i]

```
##super_project.py
from flow import FlowProject, staticlabel
import signac
class Project(FlowProject):
        @staticlabel()
        def Progress(job):
            return '{}\%'.format(round( 100*len( signac.get_project(job.workspace()).find_jobs(
                 doc_filter={"calculations_done":True))/len(signac.get_project(job.workspace()).find_jobs()),2))
        @staticlabel()
        def finished(job):
            return len(signac.get_project(job.workspace()).find_jobs(
                 doc_filter={"calculations_done":True))==len(signac.get_project(job.workspace()).find_jobs())
        def __init__(self, *args, **kwargs):
                super(Project, self).__init__(*args, **kwargs)
                self.add_operation(name='store_BZ', post=[lambda job: 'BZ' in job.document]
                       cmd='python super_operations.py store_BZ {job._id}')
                self.add_operation(name='store_spacegroup', post=[lambda job: 'spacegroup' in job.document]
                    cmd='python super_operations.py store_spacegroup {job._id}')
                self.add_operation(name='submit_subjobs',\
                    cmd='cd {job.ws}; python ../../../sub_project.py submit -o compute; cd {job.ws}/../../',
                    post=[Project.finished])

if __name__=="__main__":
    Project().main()
```

when invoked with "python super_project.py status -d –skip-overview" gives:

```
job_id                           operation                structure      labels
-------------------------------- -----------------------  -------------   ------------------------------
11259c0c710cd3c07e81d726342e695d                          Structure1      finished
96ca3ebafaf0627e74cde058fc7746a6 store_spacegroup [U]     Structure2      70.0\%
                                 submit_subjobs [U]
b35947d0db87e3390b271cd5f43eab9c store_BZ [U]              Structure3      65.0\%
                                 submit_subjobs [U]
                                 store_spacegroup [U]
[U]:unknown [R]:registered [Q]:queued [A]:active [I]:inactive [!]:requires_attention
```

[i]Notes: I use the old signac API, but this can be converted to the currect API easily.

The sub-project file can look like this:

```
##sub_project.py
from flow import FlowProject
from flow import staticlabel

class Project(FlowProject):

       def __init__(self, *args, **kwargs):
              super(Project, self).__init__(*args, **kwargs)
              self.add_operation(name='compute',\
                     cmd='python sub_operations.py compute {job._id}',
                     post=[lambda job: job.document.get('calculations_done')==True])
              self.add_operation(name='store_filling_fraction',\
                  cmd='python sub_operations.py store_ff {job._id}',
                  post=[lambda job: 'fill_fraction' in job.document])

if __name__=="__main__":
    Project().main()
```

which when invoked from within a sub-project folder gives:

```
# Detailed View:
job_id                           operation                  radius   dielectric   labels
-------------------------------- -------------------------- -------- ------------ ----------------
2cbe92bbb74043e72907d43adf8f3ba9 compute [U]                     0.1           12  ff_stored
bcb2395eec03cb18f8cd851b1846783b store_filling_fraction [U]      0.8            4  computed
bcaa1c1e7ea6056543f32b1bccbbd4c6 store_filling_fraction [U]      0.3            4  computed
37f881c6005d89be2720fe69c654950d compute [U]                     0.2           16  ff_stored
195bf8408e8cd408cec4f3141a7c6476 store_filling_fraction [U]      0.1            4  computed
9a48843751347716110c1027c64428d9 store_filling_fraction [U]      0.5           12  computed
e4f9ba06c9d24d4c0774677a99a591c7 compute [U]                     0.8            8  ff_stored
14db7dc600abf0e52e347bca16413ce8 store_filling_fraction [U]      0.9            4  computed
28ac8f460bb11eee31aa6f7ef3748d44 compute [U]                     0.6           16  ff_stored
a846799094f74807c4e417ad87072e22 compute [U]                     0.8           12  ff_stored
c3724f79137862cddca38c9c7bff47ee store_filling_fraction [U]      0.4           16  computed
[U]:unknown [R]:registered [Q]:queued [A]:active [I]:inactive [!]:requires_attention
```

2. Aggregating and Submitting at the Super Project Level

Computations could also be aggregated and submitted from the super project level:

```
python super_project.py submit -o submit_subjobs -j 96ca --pretend
Using environment configuration: UnknownEnvironment
Submitting cluster job 'super_projec/96ca3eba/submit_subjo/0000/7b49e8103b9cf86db2f80c915113b93f':
 - Operation: submit_subjobs(96ca3ebafaf0627e74cde058fc7746a6)

cd my_project

# submit_subjobs(96ca3ebafaf0627e74cde058fc7746a6)
cd my_project/workspace/96ca3ebafaf0627e74cde058fc7746a6
python ../../../sub_project.py submit -o compute -w 12 --nn 1
cd my_project/workspace/96ca3ebafaf0627e74cde058fc7746a6/../../
```

3. Multi-Level Data Analysis

This structure also allows for cross-structural data analysis, such as that in Fig. 7.12(c). We could generate a similar figure showing individual statepoints that have a PBG for every ε using this code snippet[ii]:

```
##agg_plot.py
from matplotlib import pyplot, rcParams
import signac
project = signac.get_project()
structure_projects = [signac.get_project(structure.workspace()) for structure in project.find_jobs()]
sub_jobs = [jobs for sproj in structure_projects for jobs in sproj.find_jobs(doc_filter={"has_gap":True})]
dielectrics = [4, 6, 8, 10, 12, 14, 16]
band_gaps = [(band, job.sp.dielectric) for job in sub_jobs for band in job.document.band_nos]
for bn in range(2,20):
    pyplot.plot(dielectrics, [band_gaps.count((bn,d)) for d in dielectrics])
pyplot.show()
```

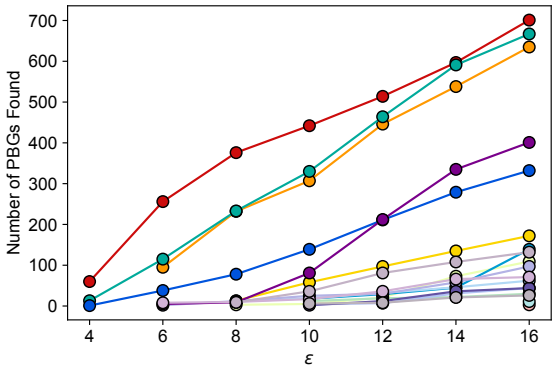

Figure B.1: **The Resulting Figure from our Code Snippet**

References

[1] Gauss, C. F. Theoria attractionis corporum sphaeroidicorum ellipticorum homogeneorum methodo nova tractata.. *Optics Express* **8**, 173 (2001).

[2] Lagrange, J.-L. Nouvelles recherches sur la nature et la propagation du son (1760).

[ii] This is not the most efficient way to do this, but the most demonstrative. I have omitted a bit of code for clarity corresponding to getting and setting colors, labels, font sizes, etc.

[3] Green, G. Essay on the Mathematical Theory of Electricity and Magnetism.(1823).

[4] Ostrogradsky, M.(1826).

[5] Peregrinus de Maricourt, P. Actum in castris in obsidione Luceriae anno domini.(1269).

[6] Faraday, M. (1831).

[7] Maxwell, J. C. On Physical Lines of Force (1861).

[8] Joannopoulos, J. *Photonic Crystals: Molding the Flow of Light, 2nd Edition* (Princeton University Press, 2008).

[9] Johnson, S. & Joannopoulos, J. Block-iterative frequency-domain methods for Maxwell's equations in a planewave basis. *Optics Express* **8**, 173 (2001).

[10] Adorf, C. S., Dodd, P. M., Ramasubramani, V. & Glotzer, S. C. Simple data and workflow management with the signac framework. *Computational Materials Science* **146**, 220–229 (2018). 1611.03543.

APPENDIX C

Glossary of Photonic Band Structures from Chapter VII

For each of these crystal structures, the photonic band structure for each gap location (*e.g.* between bands 2-3) is given for the filling fraction ϕ that maximizes gap size and for all ε computed in Chapter VII where gap size is greater than 0.

2-Connected Diamond ($cF40$-ZnC_2N_2), Bands 2 - 3
Structure file taken from `https://doi.org/10.1021/ja4012707`.

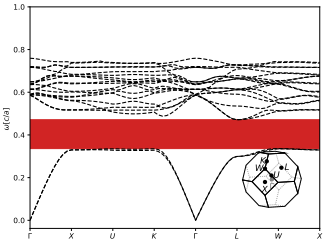

$\varepsilon = 16$, $\phi = 0.19$. 34.45% gap.

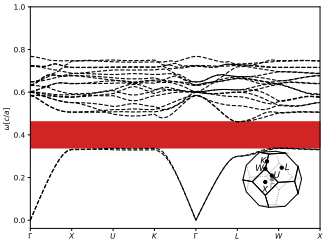

$\varepsilon = 14$, $\phi = 0.21$. 31.54% gap.

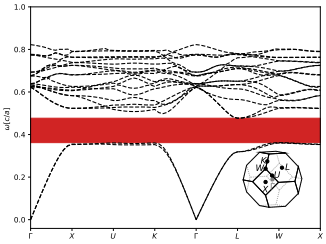

$\varepsilon = 12$, $\phi = 0.21$. 28.14% gap.

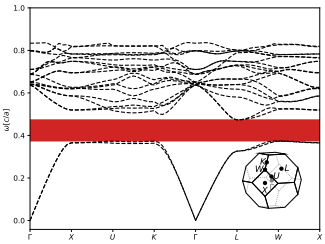

$\varepsilon = 10$, $\phi = 0.24$. 23.9% gap.

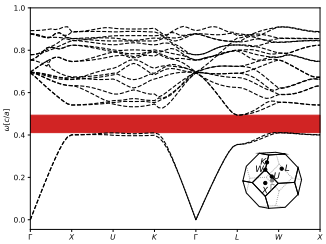

$\varepsilon = 8$, $\phi = 0.24$. 18.6% gap.

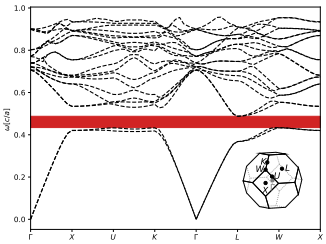

$\varepsilon = 6$, $\phi = 0.3$. 11.88% gap.

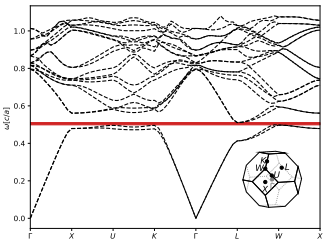

$\varepsilon = 4$, $\phi = 0.33$. 2.61% gap.

Inverse Clathrate-II (*cF* 136-Si), Bands 2 - 3

Structure file taken from `https://doi.org/10.1103/PhysRevB.60.950`.

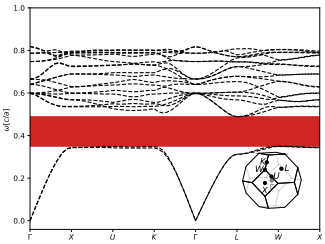

$\varepsilon = 16$, $\phi = 0.15$. 33.9% gap.

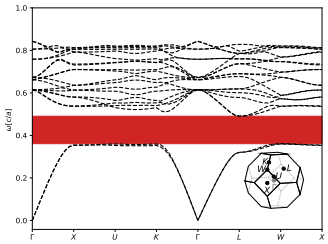

$\varepsilon = 14$, $\phi = 0.17$. 30.94% gap.

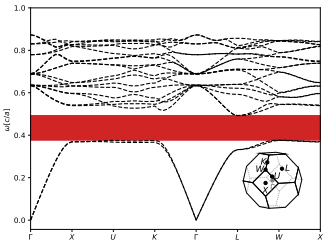

$\varepsilon = 12$, $\phi = 0.18$. 27.23% gap.

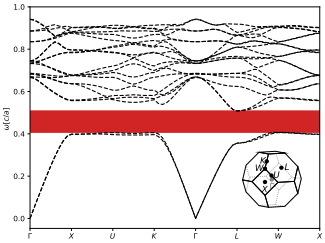

$\varepsilon = 10$, $\phi = 0.18$. 22.66% gap.

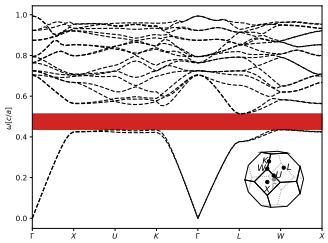

$\varepsilon = 8$, $\phi = 0.2$. 16.9% gap.

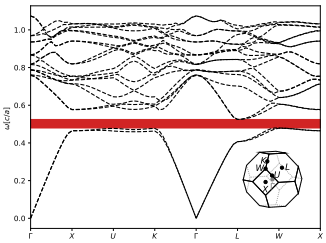

$\varepsilon = 6$, $\phi = 0.21$. 9.41% gap.

Inverse Diamond ($cF8$-C), Bands 2 - 3

Structure file taken from `https://doi.org/10.1107/S0108768195010810`.

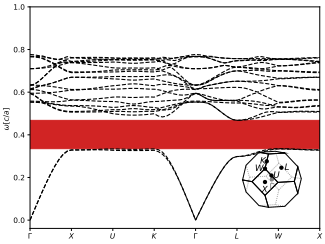

$\varepsilon = 16$, $\phi = 0.17$. 33.84% gap.

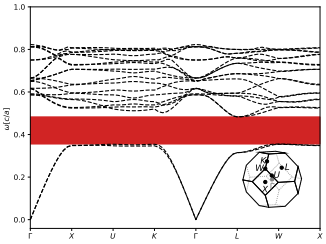

$\varepsilon = 14$, $\phi = 0.17$. 31.18% gap.

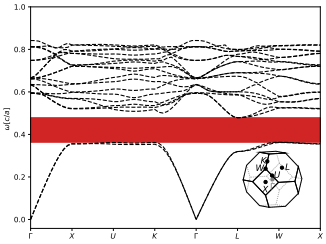

$\varepsilon = 12$, $\phi = 0.19$. 27.98% gap.

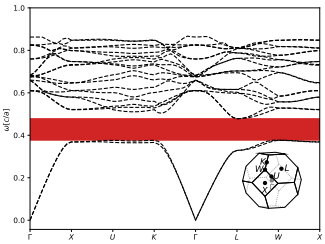

$\varepsilon = 10$, $\phi = 0.22$. 23.99% gap.

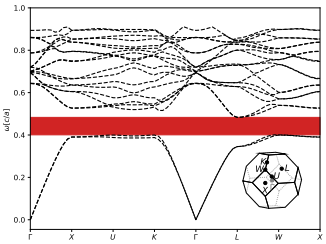

$\varepsilon = 8$, $\phi = 0.24$. 18.93% gap.

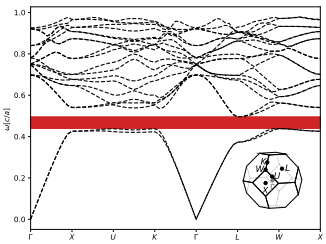

$\varepsilon = 6$, $\phi = 0.27$. 12.31% gap.

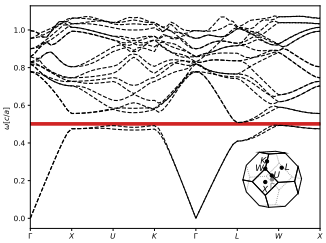

$\varepsilon = 4$, $\phi = 0.33$. 2.89% gap.

Inverse Tetraarsenic Oxide ($cF80$-As_2O_3), Bands 2 - 3

Structure file taken from `https://doi.org/10.1021/ja01660a006`.

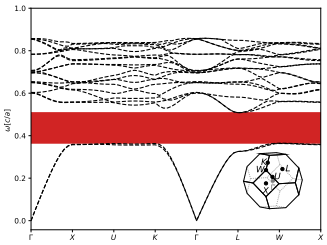

$\varepsilon = 16$, $\phi = 0.14$. 33.79% gap.

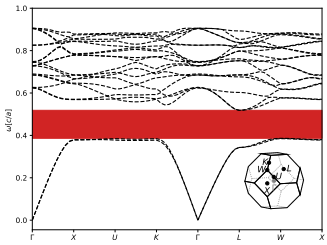

$\varepsilon = 14$, $\phi = 0.14$. 30.13% gap.

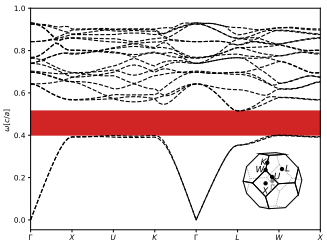

$\varepsilon = 12$, $\phi = 0.15$. 25.82% gap.

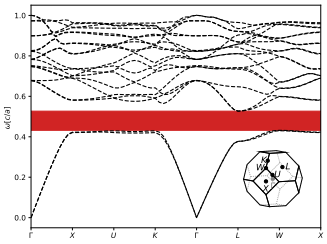

$\varepsilon = 10$, $\phi = 0.15$. 20.6% gap.

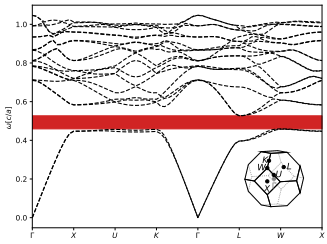

$\varepsilon = 8$, $\phi = 0.17$. 14.27% gap.

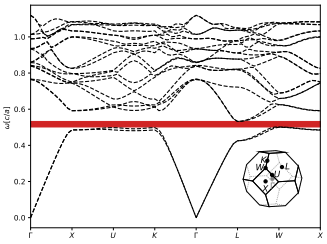

$\varepsilon = 6$, $\phi = 0.19$. 6.4% gap.

Inverse Senarmontite ($cF80$-Sb_2O_3), Bands 2 - 3

Structure file taken from `https://doi.org/10.1107/S0567740875006759`.

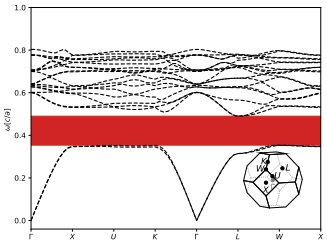

$\varepsilon = 16$, $\phi = 0.16$. 33.03% gap.

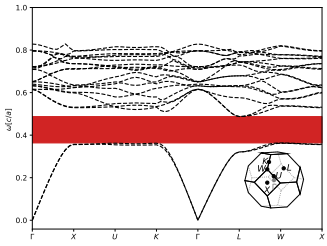

$\varepsilon = 14$, $\phi = 0.17$. 29.82% gap.

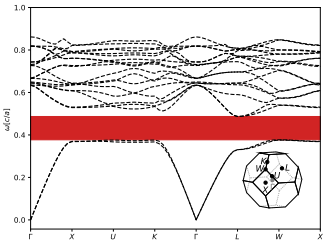

$\varepsilon = 12$, $\phi = 0.19$. 25.96% gap.

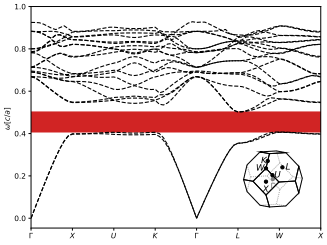

$\varepsilon = 10$, $\phi = 0.19$. 21.32% gap.

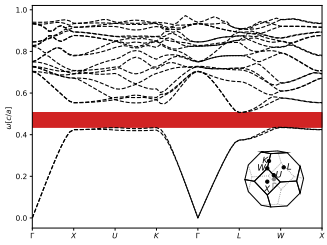

$\varepsilon = 8$, $\phi = 0.21$. 15.53% gap.

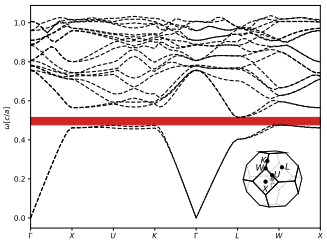

$\varepsilon = 6$, $\phi = 0.23$. 8.0% gap.

Inverse 2-Connected Diamond ($cF40$-ZnC_2N_2), Bands 2 - 3
Structure file taken from `https://doi.org/10.1021/ja4012707`.

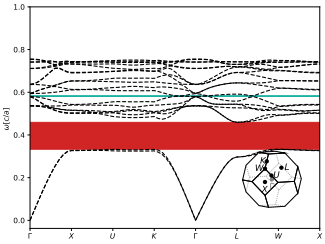

$\varepsilon = 16$, $\phi = 0.17$. 32.36% gap.

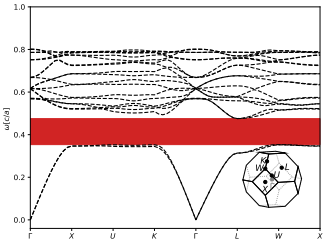

$\varepsilon = 14$, $\phi = 0.17$. 30.01% gap.

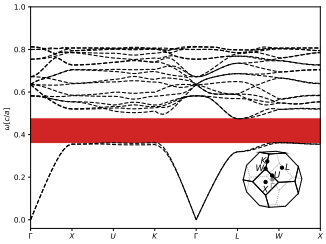

$\varepsilon = 12$, $\phi = 0.19$. 27.13% gap.

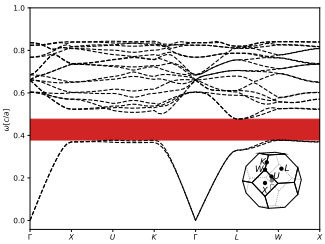

$\varepsilon = 10$, $\phi = 0.22$. 23.48% gap.

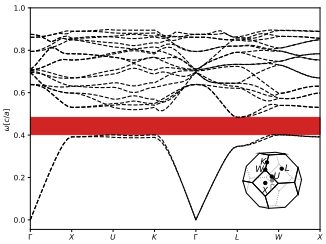

$\varepsilon = 8$, $\phi = 0.24$. 18.72% gap.

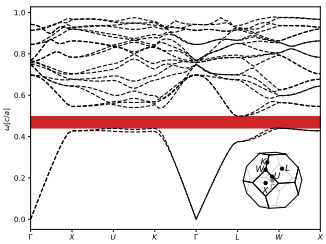

$\varepsilon = 6$, $\phi = 0.27$. 12.28% gap.

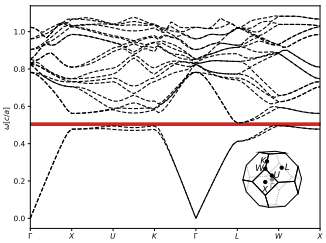

$\varepsilon = 4$, $\phi = 0.32$. 3.01% gap.

Cristobalite (beta) (cF24-SiO_2), Bands 2 - 3

Structure file taken from `https://doi.org/10.1524/zkri.1992.201.1-2.125`.

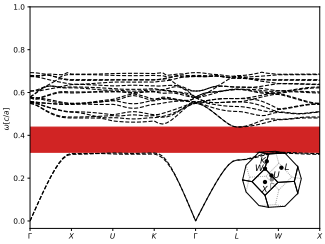

$\varepsilon = 16$, $\phi = 0.23$. 31.79% gap.

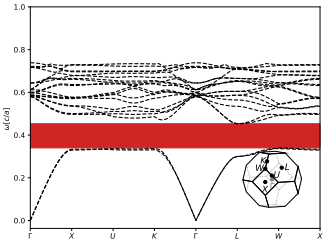

$\varepsilon = 14$, $\phi = 0.23$. 29.27% gap.

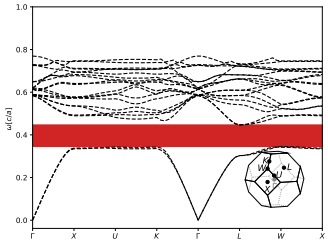

$\varepsilon = 12$, $\phi = 0.26$. 26.16% gap.

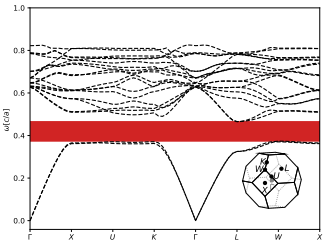

$\varepsilon = 10$, $\phi = 0.26$. 22.4% gap.

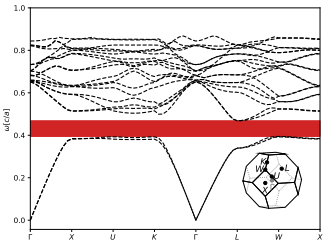

$\varepsilon = 8$, $\phi = 0.29$. 17.46% gap.

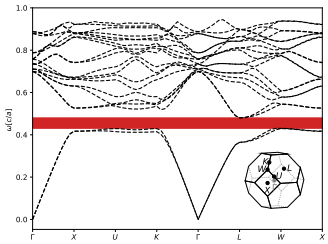

$\varepsilon = 6$, $\phi = 0.32$. 10.95% gap.

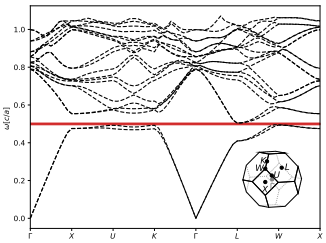

$\varepsilon = 4$, $\phi = 0.35$. 1.92% gap.

Inverse Cobalt Copper Silicon Sulfide ($tI16$-$CoSiCu_2S_4$), Bands 8 - 9
Structure file taken from `https://doi.org/10.1016/j.jallcom.2004.02.004`.

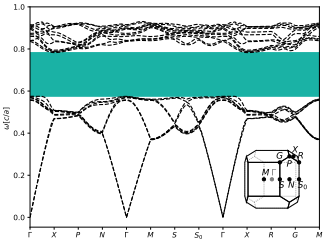

$\varepsilon = 16$, $\phi = 0.18$. 31.48% gap.

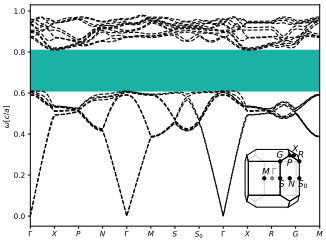

$\varepsilon = 14$, $\phi = 0.18$. 29.14% gap.

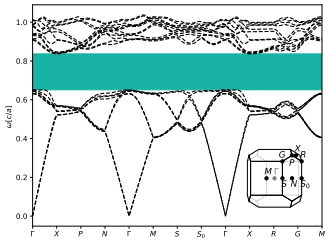

$\varepsilon = 12$, $\phi = 0.18$. 26.07% gap.

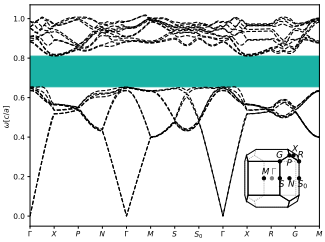

$\varepsilon = 10$, $\phi = 0.22$. 22.37% gap.

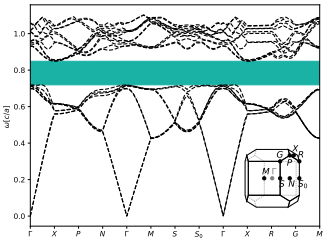

$\varepsilon = 8$, $\phi = 0.22$. 17.65% gap.

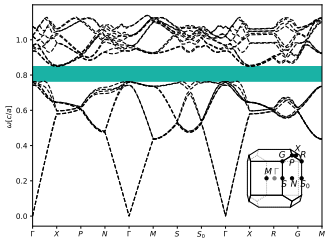

$\varepsilon = 6$, $\phi = 0.27$. 11.36% gap.

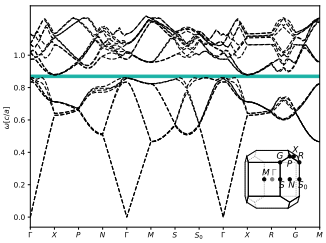

$\varepsilon = 4$, $\phi = 0.32$. 2.48% gap.

Inverse Cristobalite (beta) (cF24-SiO_2), Bands 2 - 3

Structure file taken from `https://doi.org/10.1524/zkri.1992.201.1-2.125`.

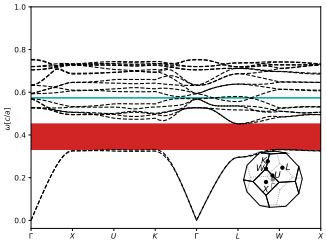

$\varepsilon = 16$, $\phi = 0.18$. 31.25% gap.

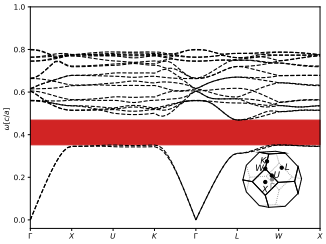

$\varepsilon = 14$, $\phi = 0.18$. 29.05% gap.

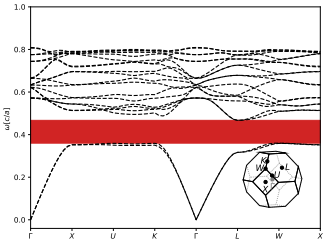

$\varepsilon = 12$, $\phi = 0.2$. 26.36% gap.

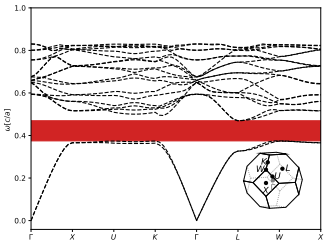

$\varepsilon = 10$, $\phi = 0.23$. 22.8% gap.

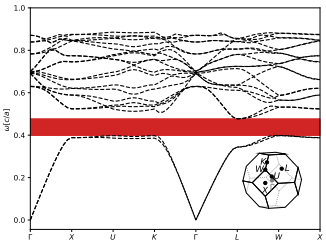

$\varepsilon = 8$, $\phi = 0.25$. 18.15% gap.

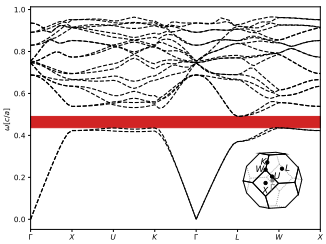

$\varepsilon = 6$, $\phi = 0.28$. 11.84% gap.

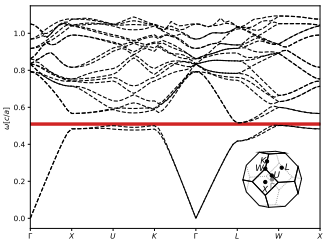

$\varepsilon = 4$, $\phi = 0.31$. 2.7% gap.

Inverse Indium Silver Telluride ($tI16$-$In_{4.8}Ag_{1.6}Te_8$), Bands 8 - 9
Structure file taken from `https://doi.org/10.1021/acs.inorgchem.5b00433`.

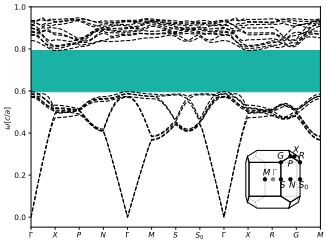

$\varepsilon = 16$, $\phi = 0.17$. 29.8% gap.

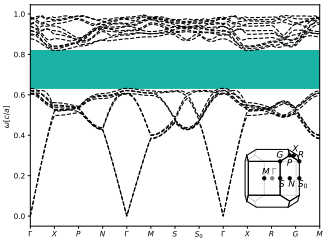

$\varepsilon = 14$, $\phi = 0.17$. 27.43% gap.

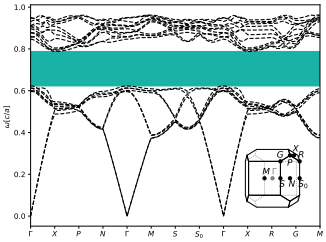

$\varepsilon = 12$, $\phi = 0.21$. 24.62% gap.

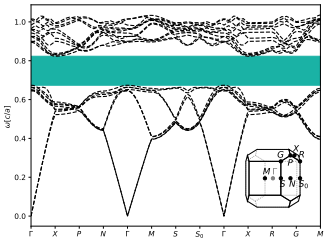

$\varepsilon = 10$, $\phi = 0.21$. 21.19% gap.

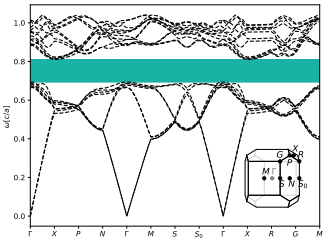

$\varepsilon = 8$, $\phi = 0.26$. 16.54% gap.

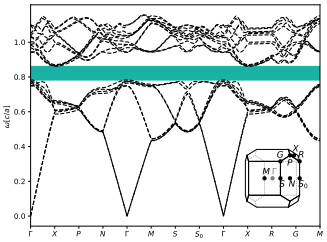

$\varepsilon = 6$, $\phi = 0.26$. 10.5% gap.

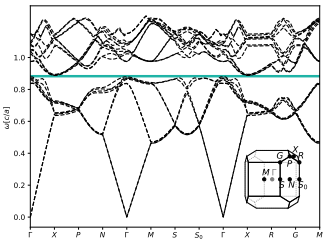

$\varepsilon = 4$, $\phi = 0.31$. 1.77% gap.

Inverse Chalkogenide With Pyrite Structure ($tI16$-$AlAgS_2$), Bands 8 - 9

Structure file taken from `https://doi.org/10.1002/zaac.19532710307`.

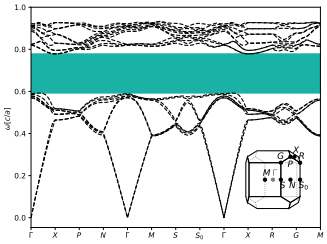

$\varepsilon = 16$, $\phi = 0.16$. 28.12% gap.

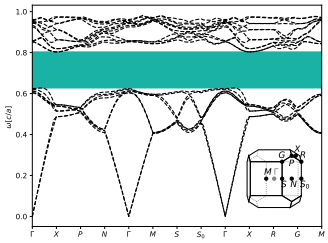

$\varepsilon = 14$, $\phi = 0.16$. 25.67% gap.

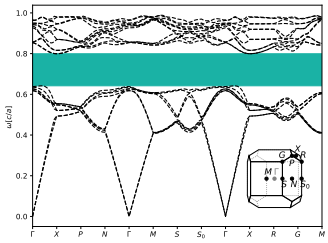

$\varepsilon = 12$, $\phi = 0.18$. 22.77% gap.

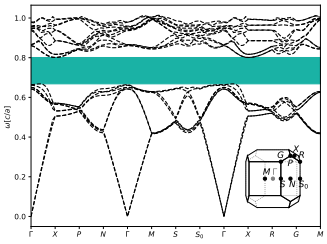

$\varepsilon = 10$, $\phi = 0.21$. 19.16% gap.

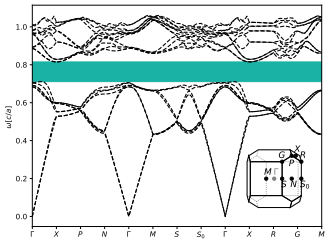

$\varepsilon = 8$, $\phi = 0.23$. 14.51% gap.

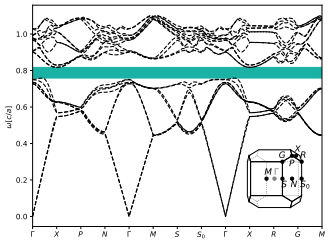

$\varepsilon = 6$, $\phi = 0.27$. 8.31% gap.

Inverse Simple Chiral Cubic ($cP4$-X), Bands 4 - 5

Structure file taken from `https://doi.org/10.1103/PhysRevLett.115.158303`.

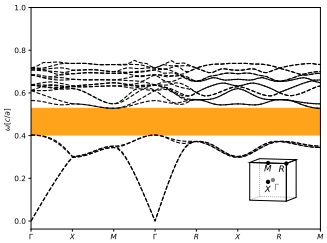

$\varepsilon = 16$, $\phi = 0.16$. 27.58% gap.

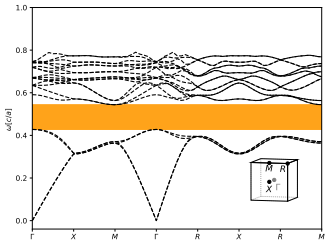

$\varepsilon = 14$, $\phi = 0.16$. 24.62% gap.

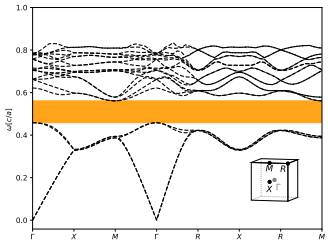

$\varepsilon = 12$, $\phi = 0.16$. 20.88% gap.

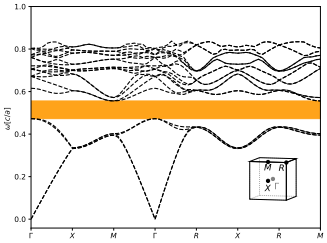

$\varepsilon = 10$, $\phi = 0.19$. 16.56% gap.

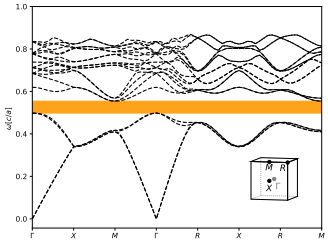

$\varepsilon = 8$, $\phi = 0.22$. 11.05% gap.

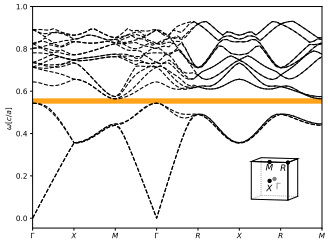

$\varepsilon = 6$, $\phi = 0.26$. 3.85% gap.

Inverse Zeolite- type Chalcogenide ($tI48$-GeS_2), Bands 2 - 3
Structure file taken from `https://doi.org/10.1021/jacs.5b03550`.

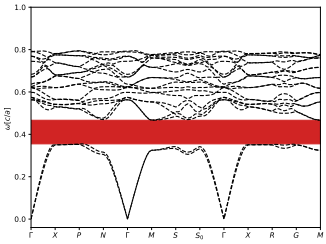

$\varepsilon = 16$, $\phi = 0.18$. 27.43% gap.

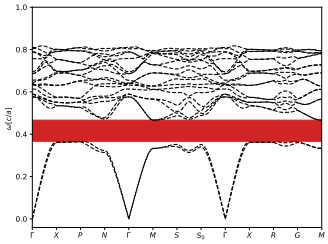

$\varepsilon = 14$, $\phi = 0.2$. 24.53% gap.

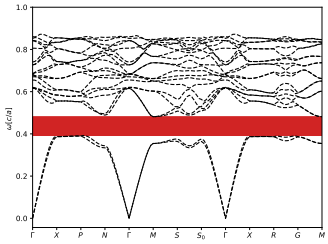

$\varepsilon = 12$, $\phi = 0.2$. 20.9% gap.

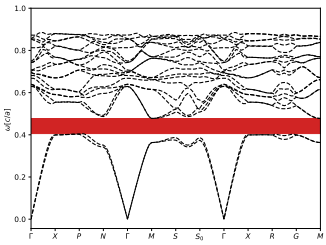

$\varepsilon = 10$, $\phi = 0.23$. 16.6% gap.

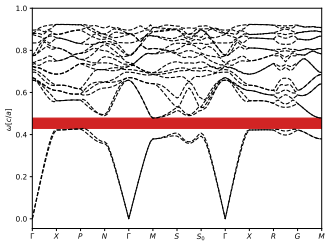

$\varepsilon = 8$, $\phi = 0.26$. 11.21% gap.

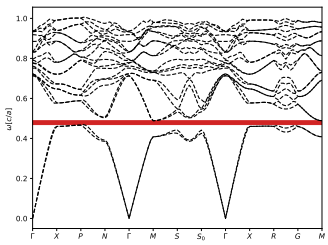

$\varepsilon = 6$, $\phi = 0.29$. 4.32% gap.

Cristobalite (beta, with defects) ($cP24$-SiO_2), Bands 8 - 9
Structure file taken from `https://doi.org/10.2475/ajs.s5-23.136.350`.

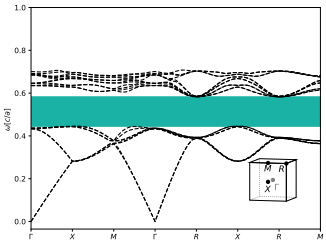

$\varepsilon = 16$, $\phi = 0.26$. 27.35% gap.

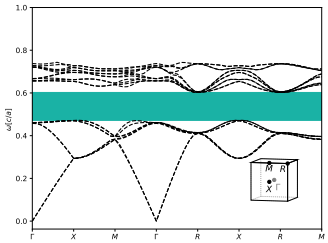

$\varepsilon = 14$, $\phi = 0.26$. 24.85% gap.

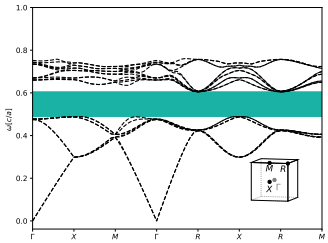

$\varepsilon = 12$, $\phi = 0.28$. 21.87% gap.

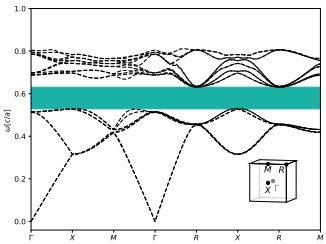

$\varepsilon = 10$, $\phi = 0.28$. 18.2% gap.

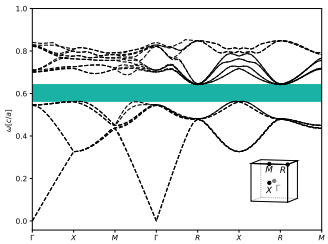

$\varepsilon = 8$, $\phi = 0.3$. 13.58% gap.

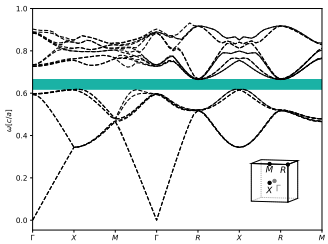

$\varepsilon = 6$, $\phi = 0.33$. 7.58% gap.

Ice Ih (hP20-H_3O), Bands 4 - 5

Structure file taken from `https://doi.org/10.1063/1.1765099`.

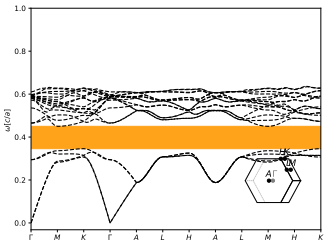

$\varepsilon = 16$, $\phi = 0.19$. 27.3% gap.

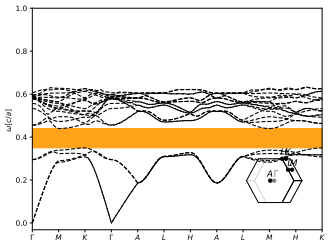

$\varepsilon = 14$, $\phi = 0.22$. 23.76% gap.

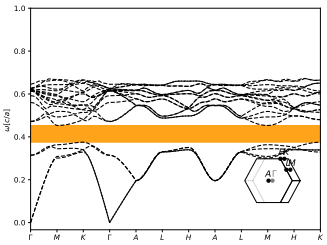

$\varepsilon = 12$, $\phi = 0.22$. 19.71% gap.

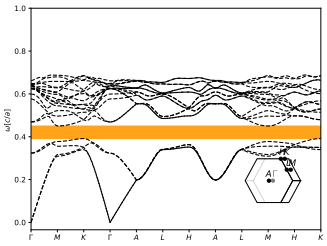

$\varepsilon = 10$, $\phi = 0.25$. 14.82% gap.

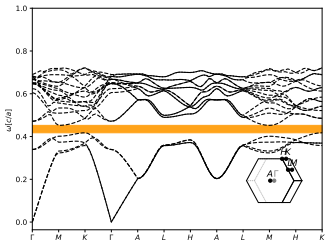

$\varepsilon = 8$, $\phi = 0.27$. 8.64% gap.

Inverse Lithium (aP4-Li), Bands 4 - 5

Structure file taken from `https://doi.org/10.1021/nn204012y`.

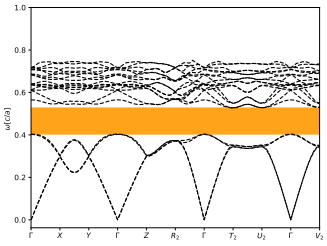

$\varepsilon = 16$, $\phi = 0.16$. 27.07% gap.

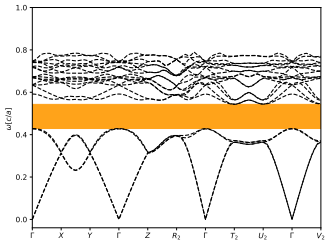

$\varepsilon = 14$, $\phi = 0.16$. 24.12% gap.

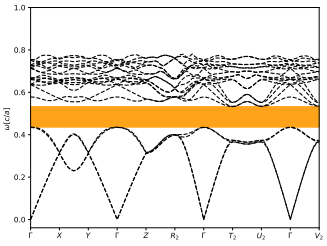

$\varepsilon = 12$, $\phi = 0.19$. 20.45% gap.

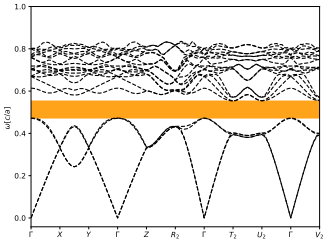

$\varepsilon = 10$, $\phi = 0.19$. 16.17% gap.

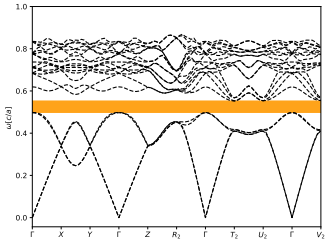

$\varepsilon = 8$, $\phi = 0.23$. 10.69% gap.

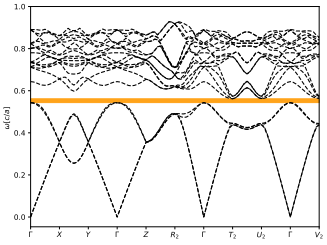

$\varepsilon = 6$, $\phi = 0.26$. 3.52% gap.

Inverse Iron Trifluoride (Pyrochlore- Type) (cF64-FeF_3), Bands 2 - 3
Structure file taken from `https://doi.org/10.1016/0025-5408(86)90134-0`.

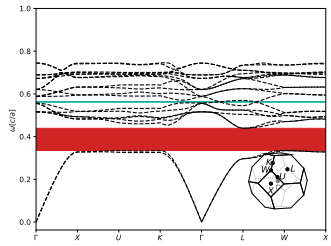

$\varepsilon = 16$, $\phi = 0.19$. 26.94% gap.

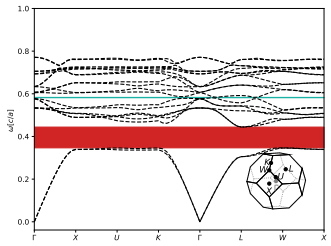

$\varepsilon = 14$, $\phi = 0.21$. 25.05% gap.

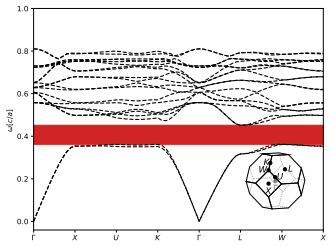

$\varepsilon = 12$, $\phi = 0.22$. 22.55% gap.

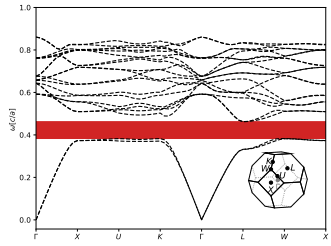

$\varepsilon = 10$, $\phi = 0.24$. 19.3% gap.

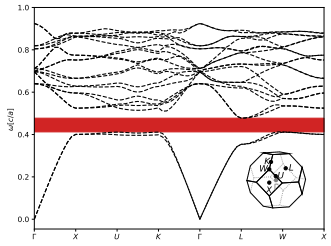

$\varepsilon = 8$, $\phi = 0.25$. 14.96% gap.

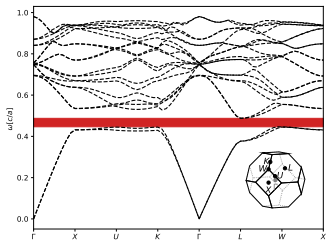

$\varepsilon = 6$, $\phi = 0.28$. 9.01% gap.

Inverse Iron Trifluoride (Pyrochlore- Type) (cF64-FeF_3), Bands 18 - 19
Structure file taken from `https://doi.org/10.1016/0025-5408(86)90134-0`.

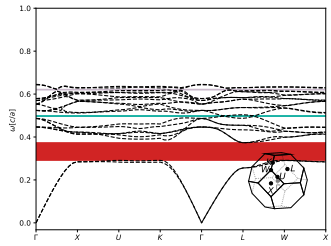

$\varepsilon = 16$, $\phi = 0.28$. (1) 24.94% gap between bands 2-3, and (3) 1.11% gap between bands 18-19.

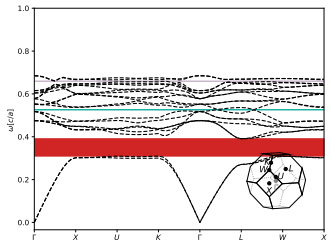

$\varepsilon = 14$, $\phi = 0.28$. (1) 23.42% gap between bands 2-3, and (2) 1.23% gap between bands 18-19.

Inverse 576-Particle Zeolite Network ($cF2304\text{-}SiO_2$), Bands 8 - 9

Structure file taken from `https://doi.org/10.1021/ja048685g`.

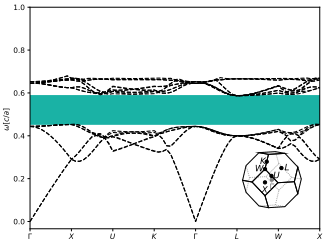

$\varepsilon = 16$, $\phi = 0.21$. 25.93% gap.

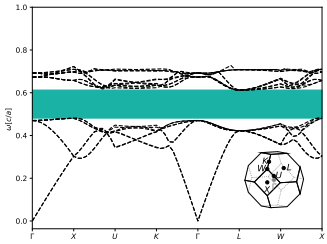

$\varepsilon = 14$, $\phi = 0.21$. 24.3% gap.

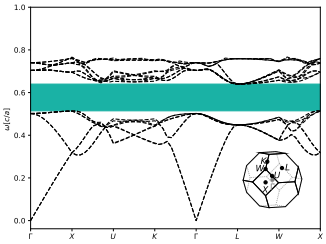

$\varepsilon = 12$, $\phi = 0.21$. 22.07% gap.

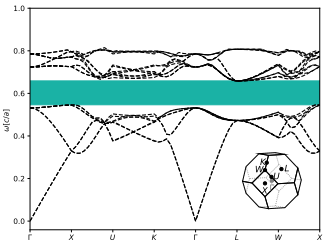

$\varepsilon = 10$, $\phi = 0.23$. 19.06% gap.

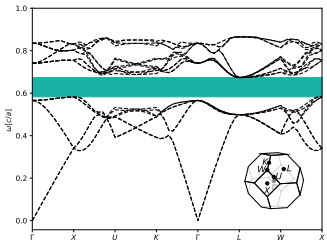

$\varepsilon = 8$, $\phi = 0.25$. 14.98% gap.

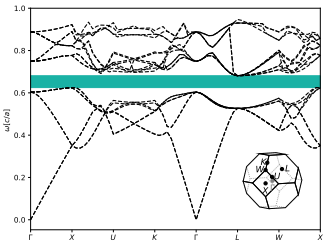

$\varepsilon = 6$, $\phi = 0.3$. 9.22% gap.

Inverse Germanium Indium Selenide ($oF96\text{-}In_2S_5$), Bands 2 - 3

Structure file taken from `https://doi.org/10.1107/S0108768104003878`.

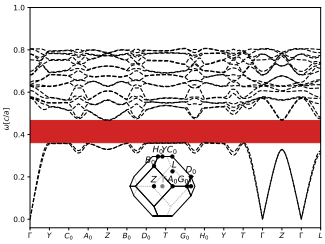

$\varepsilon = 16$, $\phi = 0.18$. 25.68% gap.

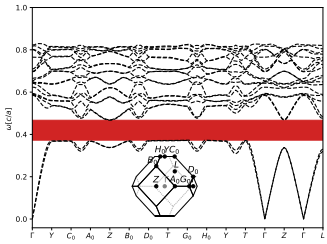

$\varepsilon = 14$, $\phi = 0.2$. 22.64% gap.

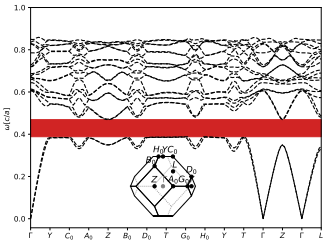

$\varepsilon = 12$, $\phi = 0.21$. 19.02% gap.

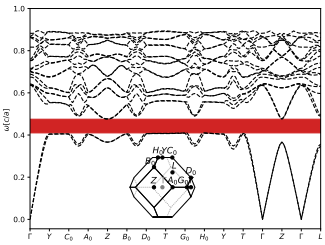

$\varepsilon = 10$, $\phi = 0.23$. 14.65% gap.

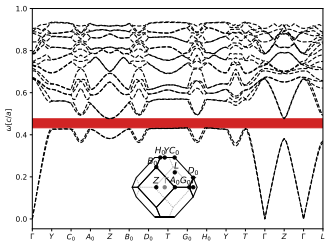

$\varepsilon = 8$, $\phi = 0.26$. 9.27% gap.

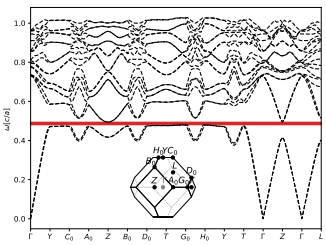

$\varepsilon = 6$, $\phi = 0.28$. 2.47% gap.

2-Connected Hexagonal Diamond ($hP20$-ZnC_2N_2), Bands 4 - 5

Structure file taken from `https://doi.org/10.1021/ja4012707`.

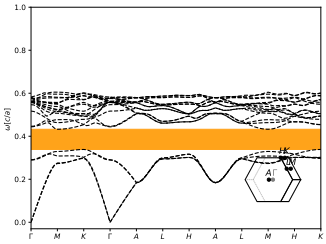

$\varepsilon = 16$, $\phi = 0.22$. 25.32% gap.

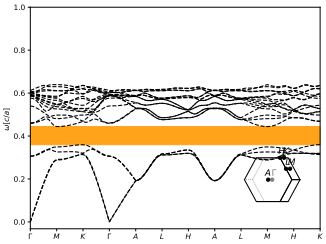

$\varepsilon = 14$, $\phi = 0.22$. 21.97% gap.

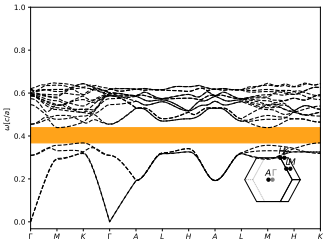

$\varepsilon = 12$, $\phi = 0.24$. 17.94% gap.

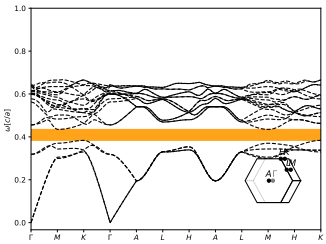

$\varepsilon = 10$, $\phi = 0.27$. 13.14% gap.

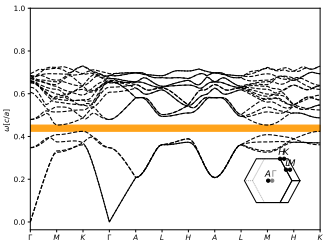

$\varepsilon = 8$, $\phi = 0.27$. 7.23% gap.

Inverse Manganese Yttrium ($tI8$-YMn_2), Bands 2 - 3

Structure file taken from `https://doi.org/10.1088/0953-8984/3/33/023`.

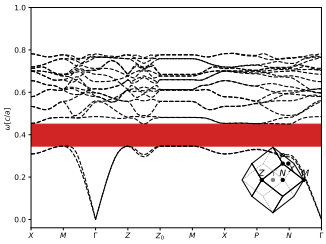

$\varepsilon = 16$, $\phi = 0.16$. 25.08% gap.

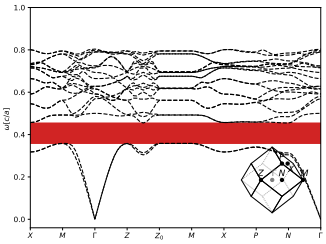

$\varepsilon = 14$, $\phi = 0.17$. 22.57% gap.

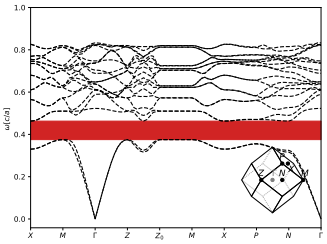

$\varepsilon = 12$, $\phi = 0.18$. 19.48% gap.

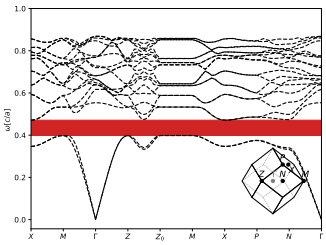

$\varepsilon = 10$, $\phi = 0.2$. 15.66% gap.

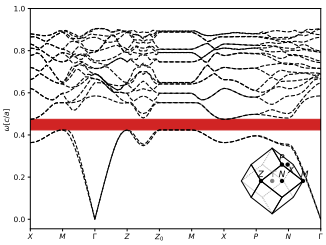

$\varepsilon = 8$, $\phi = 0.22$. 10.91% gap.

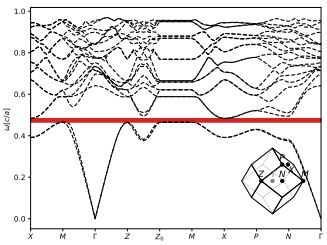

$\varepsilon = 6$, $\phi = 0.25$. 4.06% gap.

Inverse Lautite ($oP12$-CuAsS), Bands 12 - 13

Structure file taken from `https://doi.org/10.1107/S1600536808004492`.

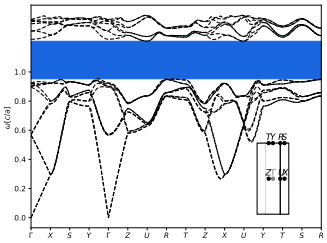

$\varepsilon = 16$, $\phi = 0.21$. 24.96% gap.

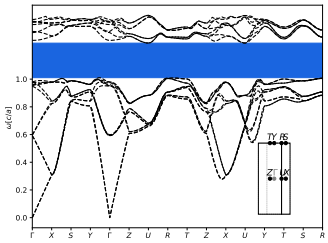

$\varepsilon = 14$, $\phi = 0.21$. 23.29% gap.

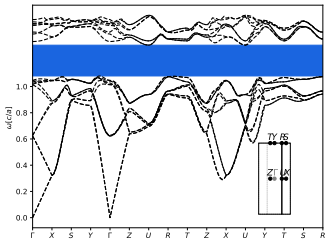

$\varepsilon = 12$, $\phi = 0.21$. 21.06% gap.

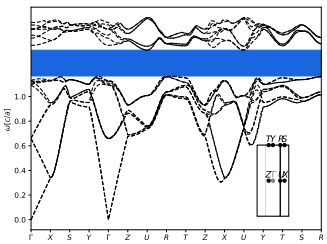

$\varepsilon = 10$, $\phi = 0.21$. 18.02% gap.

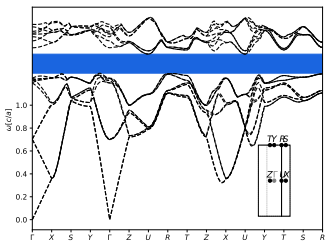

$\varepsilon = 8$, $\phi = 0.21$. 13.76% gap.

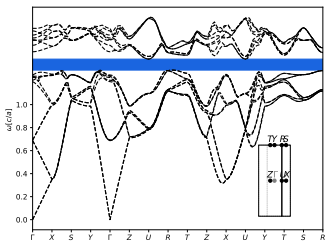

$\varepsilon = 6$, $\phi = 0.3$. 8.41% gap.

Orthorhombic Tridymite (HT) ($oC48$-SiO_2), Bands 8 - 9

Structure file taken from `https://doi.org/10.1107/S0365110X67003287`.

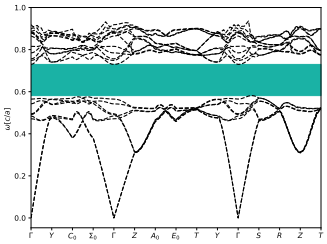

$\varepsilon = 16$, $\phi = 0.23$. 24.61% gap.

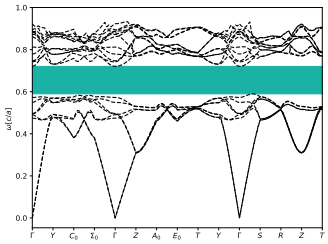

$\varepsilon = 14$, $\phi = 0.25$. 21.5% gap.

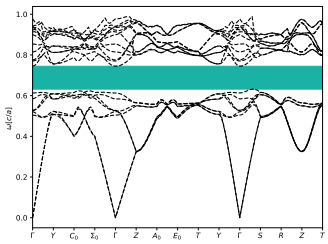

$\varepsilon = 12$, $\phi = 0.25$. 17.82% gap.

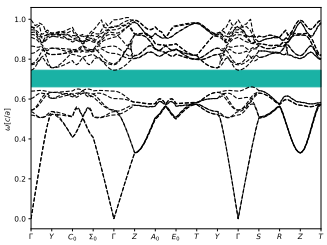

$\varepsilon = 10$, $\phi = 0.28$. 13.17% gap.

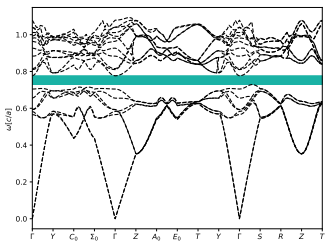

$\varepsilon = 8$, $\phi = 0.28$. 7.4% gap.

Cristobalite (alpha, HT) ($tP12$-SiO_2), Bands 4 - 5

Structure file taken from `https://doi.org/10.1524/zkri.1973.138.jg.274`.

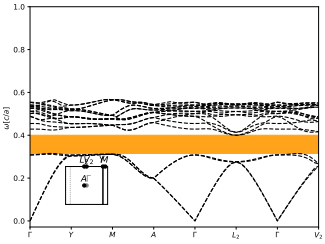

$\varepsilon = 16$, $\phi = 0.27$. 24.44% gap.

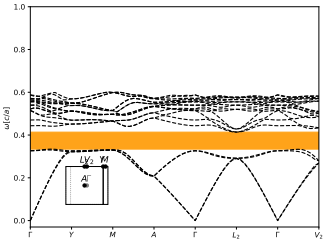

$\varepsilon = 14$, $\phi = 0.27$. 21.94% gap.

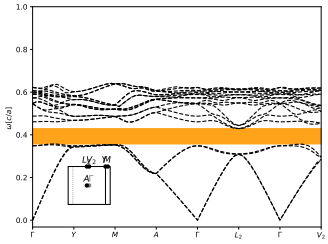

$\varepsilon = 12$, $\phi = 0.27$. 18.93% gap.

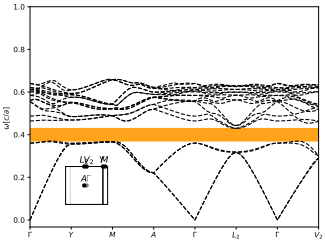

$\varepsilon = 10$, $\phi = 0.3$. 15.38% gap.

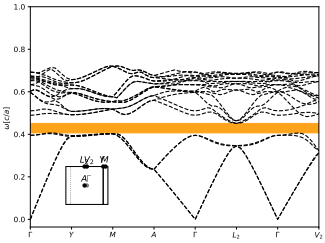

$\varepsilon = 8$, $\phi = 0.3$. 10.98% gap.

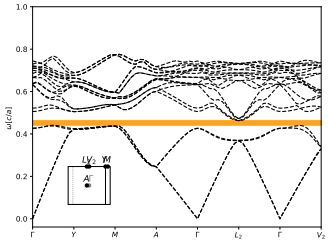

$\varepsilon = 6$, $\phi = 0.33$. 5.39% gap.

Tridymite 2H ($hP12$-SiO), Bands 4 - 5

Structure file taken from `https://doi.org/10.1524/zkri.1978.147.3-4.159`.

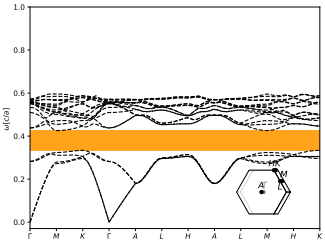

$\varepsilon = 16$, $\phi = 0.23$. 24.17% gap.

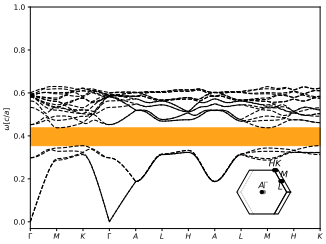

$\varepsilon = 14$, $\phi = 0.23$. 20.97% gap.

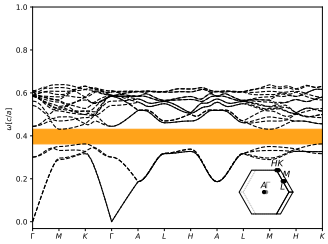

$\varepsilon = 12$, $\phi = 0.26$. 17.01% gap.

Monoclinic Tridymite ($mP12$-SiO_2), Bands 4 - 5

Structure file taken from `https://doi.org/10.17188/1269045`.

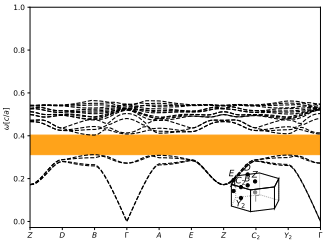

$\varepsilon = 16$, $\phi = 0.26$. 23.94% gap.

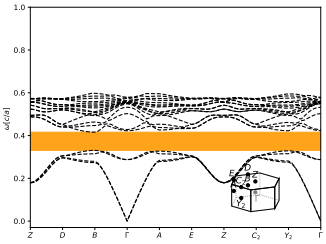

$\varepsilon = 14$, $\phi = 0.26$. 21.0% gap.

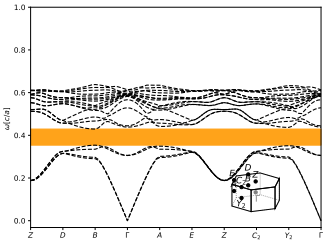

$\varepsilon = 12$, $\phi = 0.26$. 17.33% gap.

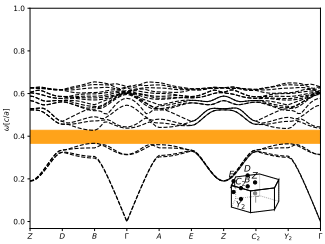

$\varepsilon = 10$, $\phi = 0.29$. 12.86% gap.

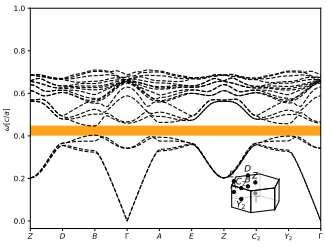

$\varepsilon = 8$, $\phi = 0.29$. 7.31% gap.

Monoclinic Tridymite ($mP24$-SiO_2), Bands 8 - 9

Structure file taken from `https://doi.org/10.17188/1269045`.

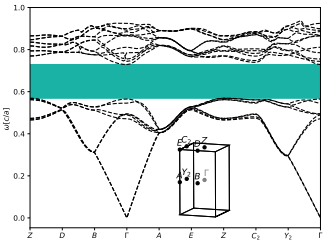

$\varepsilon = 16$, $\phi = 0.23$. 23.78% gap.

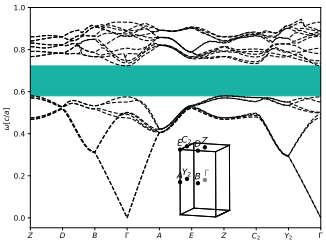

$\varepsilon = 14$, $\phi = 0.26$. 20.8% gap.

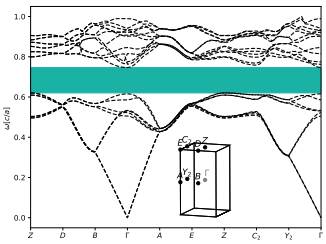

$\varepsilon = 12$, $\phi = 0.26$. 17.14% gap.

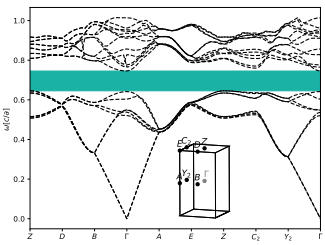

$\varepsilon = 10$, $\phi = 0.29$. 12.64% gap.

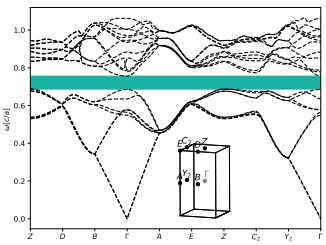

$\varepsilon = 8$, $\phi = 0.31$. 7.07% gap.

Phosphorus Oxonitride (cristobalite- like) (tI12-PNO), Bands 2 - 3
Structure file taken from `https://doi.org/10.1107/S205698901501899X`.

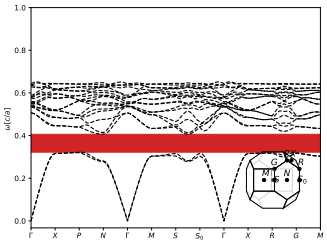

$\varepsilon = 16$, $\phi = 0.28$. 23.52% gap.

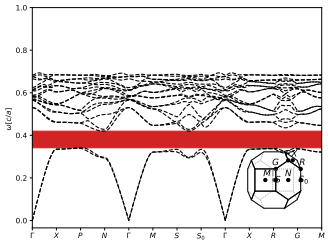

$\varepsilon = 14$, $\phi = 0.28$. 20.98% gap.

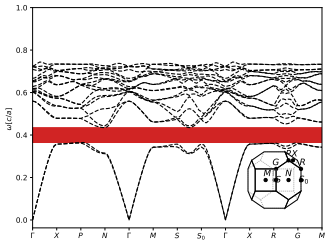

$\varepsilon = 12$, $\phi = 0.28$. 17.87% gap.

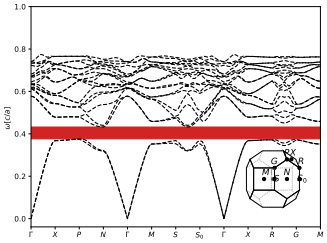

$\varepsilon = 10$, $\phi = 0.31$. 14.16% gap.

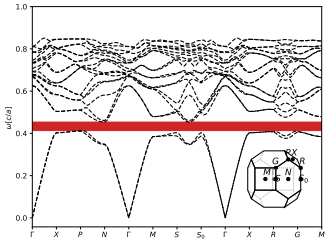

$\varepsilon = 8$, $\phi = 0.31$. 9.59% gap.

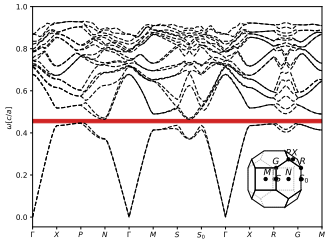

$\varepsilon = 6$, $\phi = 0.35$. 3.69% gap.

Gallium Boron Phosphate (beta cristobalite- like) (tP12-$Ga_{0.71}B_{0.29}PO_4$), Bands 4 - 5
Structure file taken from `https://doi.org/10.1107/S1600536810000358`.

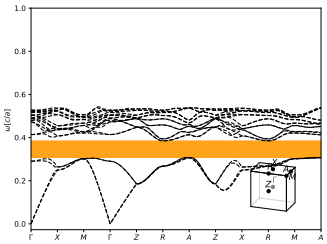

$\varepsilon = 16$, $\phi = 0.29$. 23.19% gap.

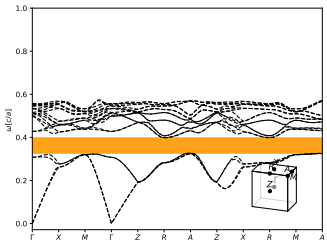

$\varepsilon = 14$, $\phi = 0.29$. 20.81% gap.

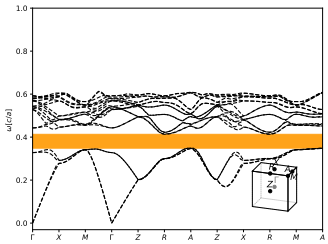

$\varepsilon = 12$, $\phi = 0.29$. 17.88% gap.

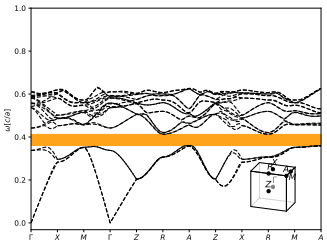

$\varepsilon = 10$, $\phi = 0.32$. 14.23% gap.

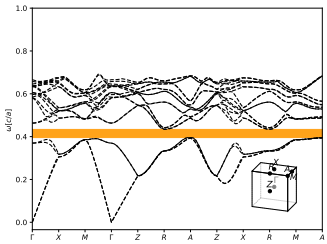

$\varepsilon = 8$, $\phi = 0.32$. 9.81% gap.

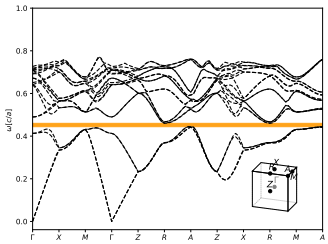

$\varepsilon = 6$, $\phi = 0.32$. 3.98% gap.

Boron Phosphate (tI12-BPO_4), Bands 2 - 3

Structure file taken from `https://doi.org/10.17188/1207092`.

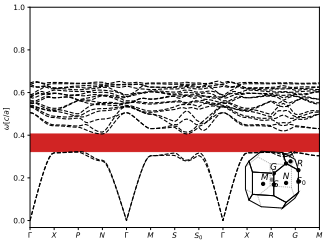

$\varepsilon = 16$, $\phi = 0.28$. 23.13% gap.

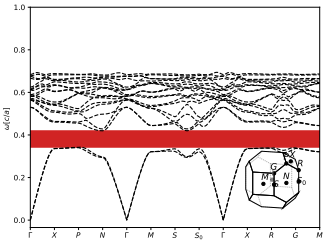

$\varepsilon = 14$, $\phi = 0.28$. 20.61% gap.

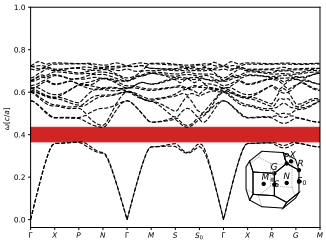

$\varepsilon = 12$, $\phi = 0.28$. 17.54% gap.

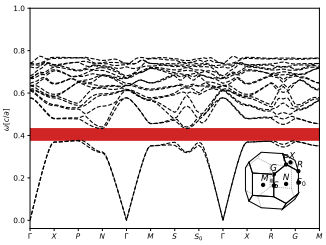

$\varepsilon = 10$, $\phi = 0.31$. 13.89% gap.

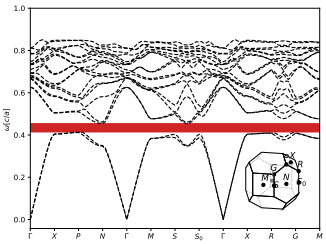

$\varepsilon = 8$, $\phi = 0.31$. 9.35% gap.

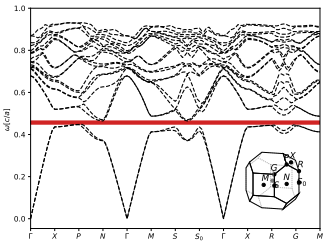

$\varepsilon = 6$, $\phi = 0.35$. 3.49% gap.

Phosphorus Oxide Nitride (tP12-PNO), Bands 4 - 5

Structure file taken from `https://doi.org/10.1002/chin.199030021`.

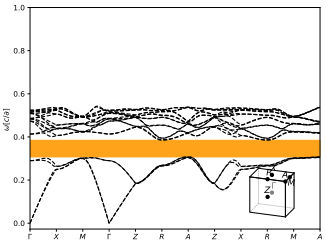

$\varepsilon = 16$, $\phi = 0.29$. 22.95% gap.

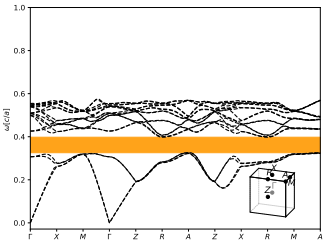

$\varepsilon = 14$, $\phi = 0.29$. 20.46% gap.

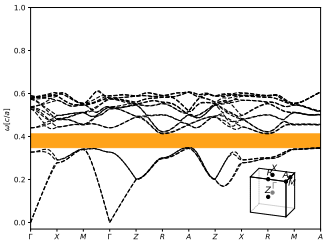

$\varepsilon = 12$, $\phi = 0.29$. 17.42% gap.

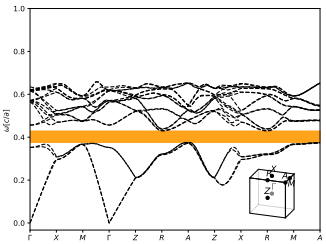

$\varepsilon = 10$, $\phi = 0.29$. 13.66% gap.

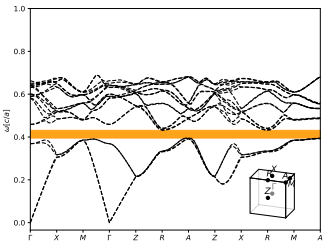

$\varepsilon = 8$, $\phi = 0.32$. 9.16% gap.

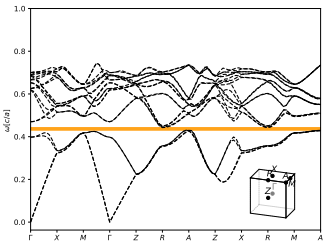

$\varepsilon = 6$, $\phi = 0.36$. 3.33% gap.

Inverse Silver Indium Germanium Selenide (tI28-InAgGeSe$_4$), Bands 16 - 17
Structure file taken from `https://doi.org/10.1016/S0925-8388(01)01945-4`.

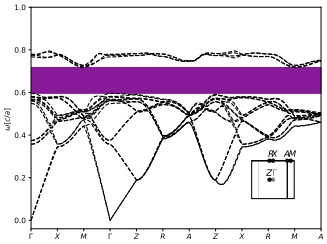

$\varepsilon = 16$, $\phi = 0.13$. 22.47% gap.

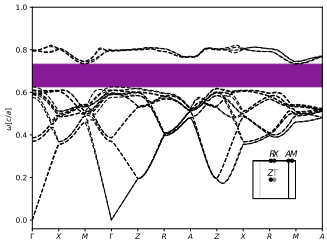

$\varepsilon = 14$, $\phi = 0.13$. 19.56% gap.

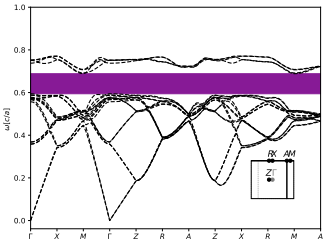

$\varepsilon = 12$, $\phi = 0.16$. 16.4% gap.

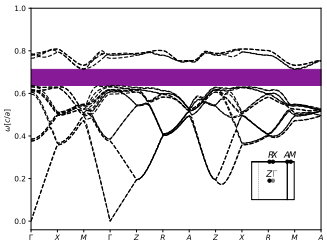

$\varepsilon = 10$, $\phi = 0.16$. 12.89% gap.

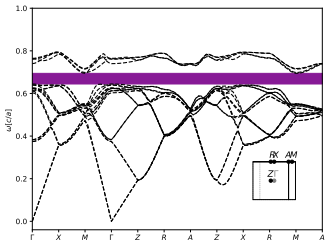

$\varepsilon = 8$, $\phi = 0.2$. 8.43% gap.

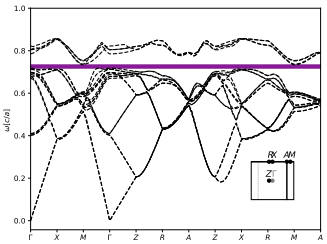

$\varepsilon = 6$, $\phi = 0.2$. 3.16% gap.

Inverse Phosphorus Oxonitride (cristobalite- like) (tI12-PNO), Bands 2 - 3
Structure file taken from `https://doi.org/10.1107/S205698901501899X`.

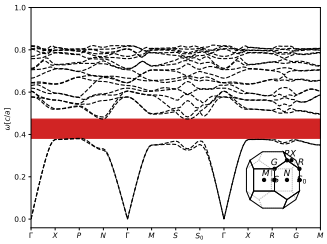

$\varepsilon = 16$, $\phi = 0.16$. 21.86% gap.

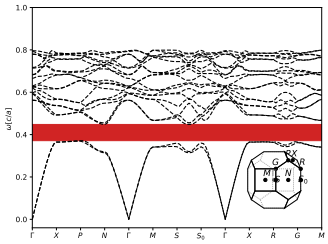

$\varepsilon = 14$, $\phi = 0.19$. 19.2% gap.

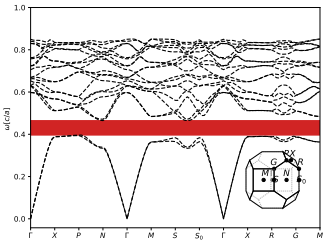

$\varepsilon = 12$, $\phi = 0.19$. 16.45% gap.

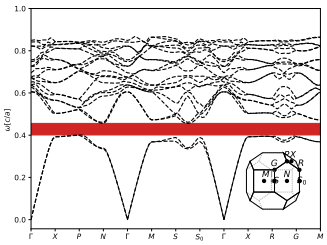

$\varepsilon = 10$, $\phi = 0.23$. 13.07% gap.

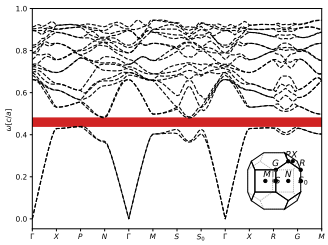

$\varepsilon = 8$, $\phi = 0.23$. 8.98% gap.

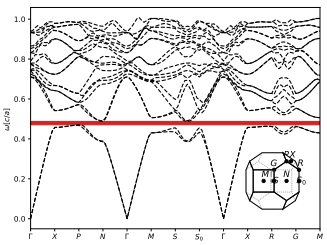

$\varepsilon = 6$, $\phi = 0.27$. 3.72% gap.

Inverse Boron Phosphate ($tI12$-BPO_4), Bands 2 - 3

Structure file taken from `https://doi.org/10.17188/1207092`.

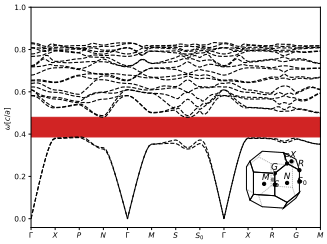

$\varepsilon = 16$, $\phi = 0.15$. 21.77% gap.

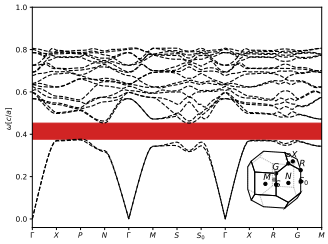

$\varepsilon = 14$, $\phi = 0.19$. 18.98% gap.

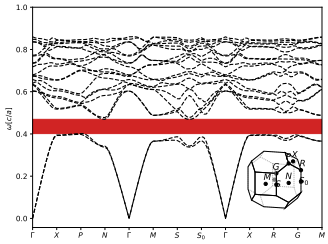

$\varepsilon = 12$, $\phi = 0.19$. 16.18% gap.

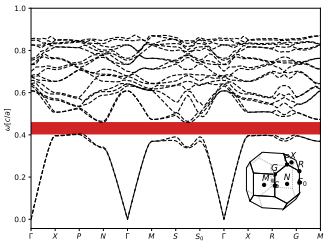

$\varepsilon = 10$, $\phi = 0.23$. 12.81% gap.

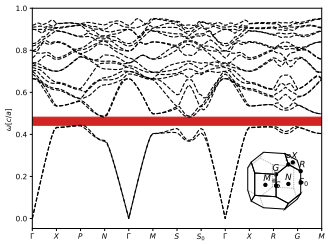

$\varepsilon = 8$, $\phi = 0.23$. 8.7% gap.

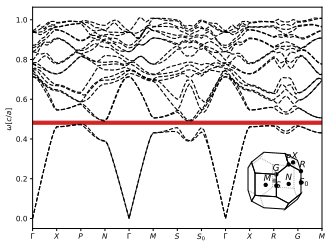

$\varepsilon = 6$, $\phi = 0.27$. 3.47% gap.

Inverse Dinitrogen Tetraoxide ($cI36$-NO_2), Bands 2 - 3

Structure file taken from `https://doi.org/10.1007/BF01390966`.

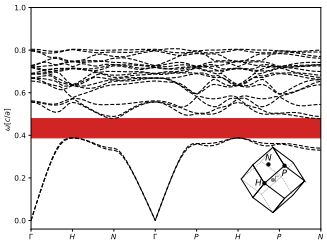

$\varepsilon = 16$, $\phi = 0.14$. 21.35% gap.

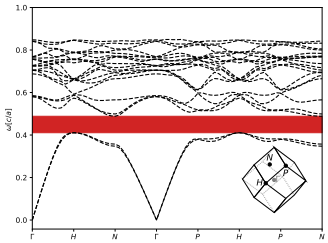

$\varepsilon = 14$, $\phi = 0.14$. 17.67% gap.

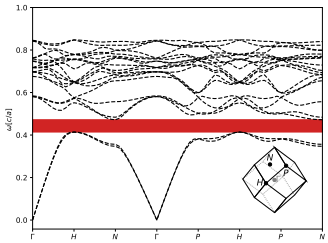

$\varepsilon = 12$, $\phi = 0.17$. 13.46% gap.

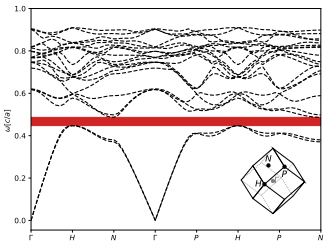

$\varepsilon = 10$, $\phi = 0.17$. 8.7% gap.

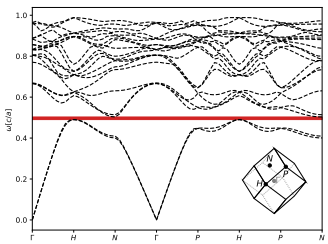

$\varepsilon = 8$, $\phi = 0.17$. 2.9% gap.

Inverse Gallium Boron Phosphate (beta cristobalite- like) ($tP12$-$Ga_{0.71}B_{0.29}PO_4$), Bands 4 - 5

Structure file taken from `https://doi.org/10.1107/S1600536810000358`.

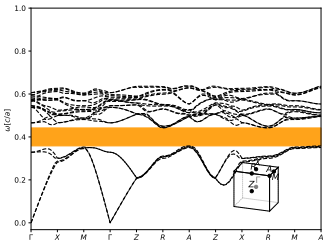

$\varepsilon = 16$, $\phi = 0.17$. 21.14% gap.

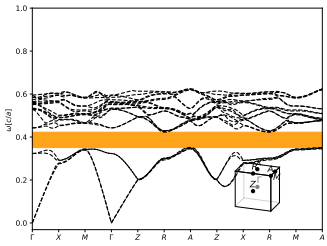

$\varepsilon = 14$, $\phi = 0.21$. 18.94% gap.

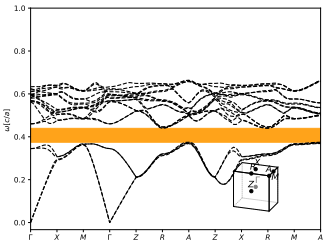

$\varepsilon = 12$, $\phi = 0.21$. 16.43% gap.

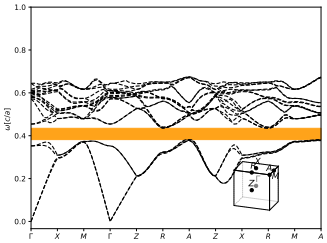

$\varepsilon = 10$, $\phi = 0.24$. 13.23% gap.

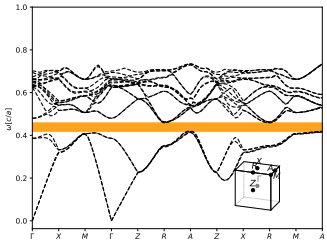

$\varepsilon = 8$, $\phi = 0.24$. 9.32% gap.

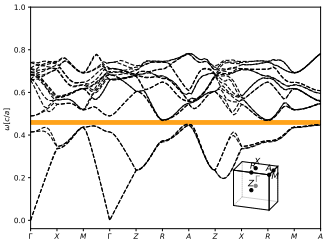

$\varepsilon = 6$, $\phi = 0.28$. 4.14% gap.

Inverse Cristobalite (beta, with defects) ($cP24$-SiO_2), Bands 8 - 9

Structure file taken from `https://doi.org/10.2475/ajs.s5-23.136.350`.

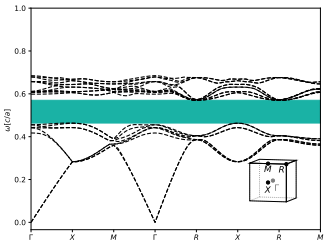

$\varepsilon = 16$, $\phi = 0.22$. 20.95% gap.

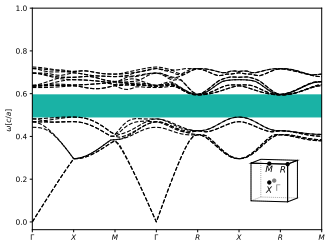

$\varepsilon = 14$, $\phi = 0.22$. 19.48% gap.

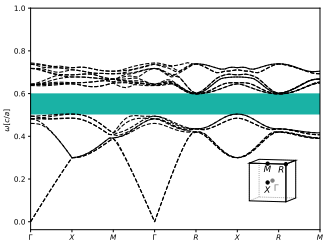

$\varepsilon = 12$, $\phi = 0.24$. 17.51% gap.

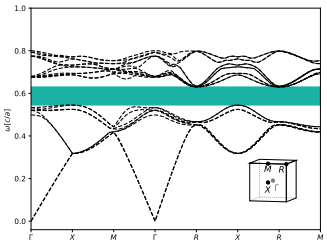

$\varepsilon = 10$, $\phi = 0.24$. 14.97% gap.

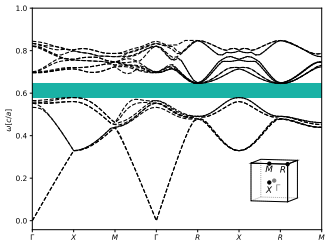

$\varepsilon = 8$, $\phi = 0.27$. 11.47% gap.

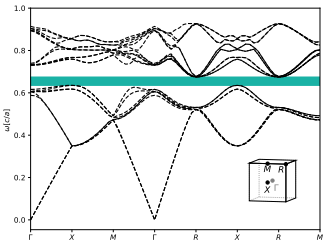

$\varepsilon = 6$, $\phi = 0.29$. 6.49% gap.

Inverse Platinum Hexaindium Germanate Oxide (cF72-$In_6Ge_2PtO_9$), Bands 10 - 11

Structure file taken from `https://doi.org/10.1021/ja053280x`.

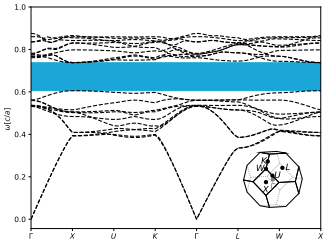

$\varepsilon = 16$, $\phi = 0.19$. 20.42% gap.

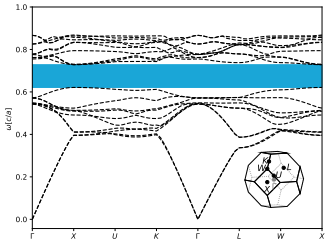

$\varepsilon = 14$, $\phi = 0.21$. 16.66% gap.

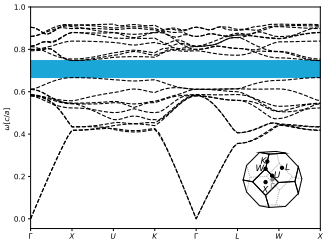

$\varepsilon = 12$, $\phi = 0.21$. 12.2% gap.

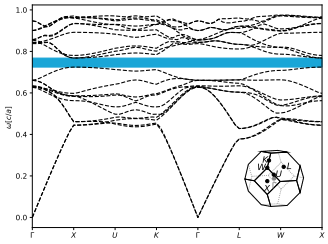

$\varepsilon = 10$, $\phi = 0.21$. 6.6% gap.

Inverse Platinum Hexaindium Germanate Oxide (cF72-$In_6Ge_2PtO_9$), Bands 13 - 14

Structure file taken from `https://doi.org/10.1021/ja053280x`.

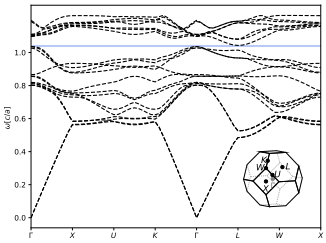

$\varepsilon = 16$, $\phi = 0.06$. 2.91% gap.

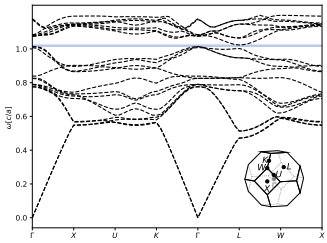

$\varepsilon = 14$, $\phi = 0.07$. 1.78% gap.

Inverse Germanium Mercury Selenium ($tI14$-Hg_2GeSe_4), Bands 8 - 9
Structure file taken from `https://doi.org/10.1107/S1600536804034105`.

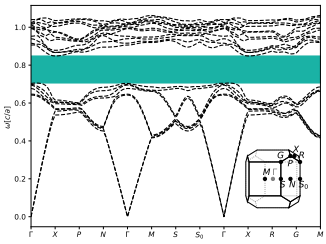

$\varepsilon = 16$, $\phi = 0.12$. 19.2% gap.

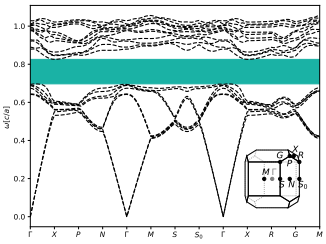

$\varepsilon = 14$, $\phi = 0.15$. 17.05% gap.

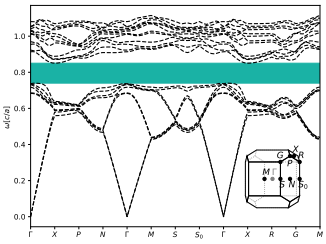

$\varepsilon = 12$, $\phi = 0.15$. 14.32% gap.

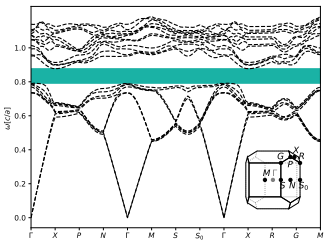

$\varepsilon = 10$, $\phi = 0.15$. 10.83% gap.

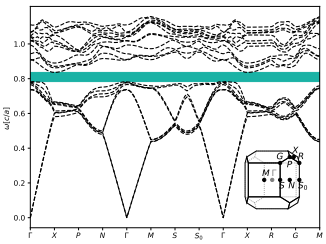

$\varepsilon = 8$, $\phi = 0.19$. 6.9% gap.

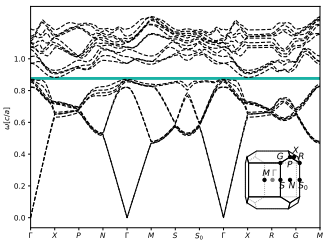

$\varepsilon = 6$, $\phi = 0.19$. 1.93% gap.

Inverse Germanium Mercury Selenium ($tI14$-Hg_2GeSe_4), Bands 11 - 12
Structure file taken from `https://doi.org/10.1107/S1600536804034105`.

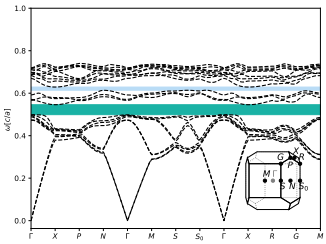

$\varepsilon = 16$, $\phi = 0.3$. (1) 8.43% gap between bands 8-9, and (2) 3.58% gap between bands 11-12.

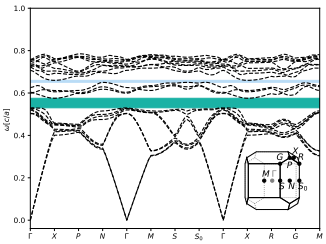

$\varepsilon = 14$, $\phi = 0.3$. (1) 7.74% gap between bands 8-9, and (2) 2.59% gap between bands 11-12.

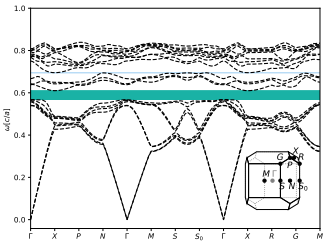

$\varepsilon = 12$, $\phi = 0.3$. (1) 6.84% gap between bands 8-9, and (2) 1.25% gap between bands 11-12.

Inverse Cristobalite (alpha, HT) ($tP12$-SiO_2), Bands 4 - 5
Structure file taken from `https://doi.org/10.1524/zkri.1973.138.jg.274`.

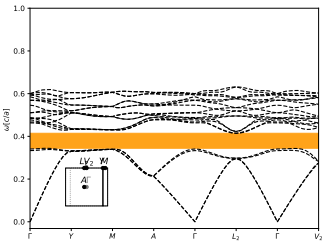

$\varepsilon = 16$, $\phi = 0.19$. 19.23% gap.

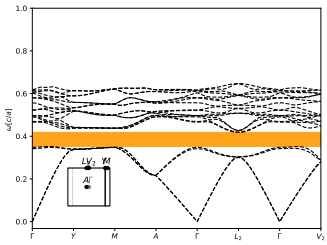

$\varepsilon = 14$, $\phi = 0.21$. 17.64% gap.

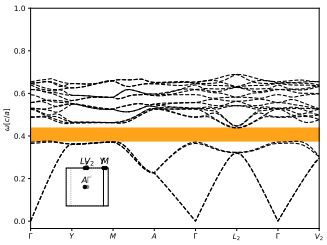

$\varepsilon = 12$, $\phi = 0.21$. 15.67% gap.

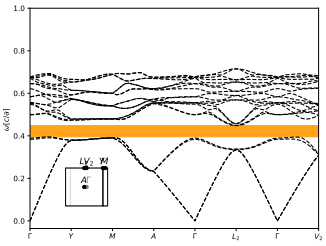

$\varepsilon = 10$, $\phi = 0.23$. 13.11% gap.

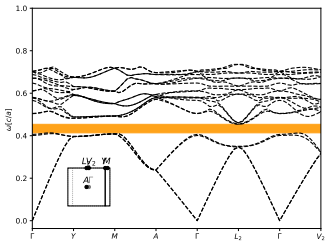

$\varepsilon = 8$, $\phi = 0.26$. 9.75% gap.

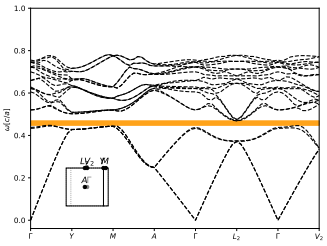

$\varepsilon = 6$, $\phi = 0.29$. 5.1% gap.

Inverse Beryllium Sulfate Tetrahydrate ($tI40$-$BeSO_8$), Bands 12 - 13
Structure file taken from `https://doi.org/10.1524/zkri.1932.82.1.297`.

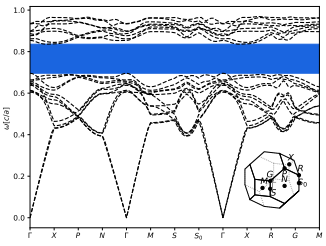

$\varepsilon = 16$, $\phi = 0.14$. 19.21% gap.

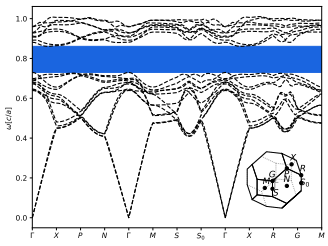

$\varepsilon = 14$, $\phi = 0.14$. 17.44% gap.

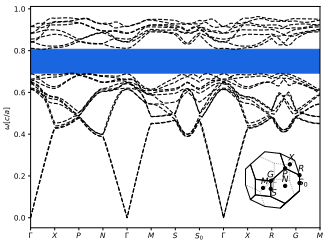

$\varepsilon = 12$, $\phi = 0.19$. 15.31% gap.

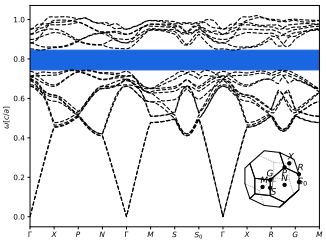

$\varepsilon = 10$, $\phi = 0.19$. 12.65% gap.

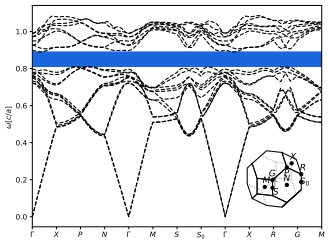

$\varepsilon = 8$, $\phi = 0.19$. 9.28% gap.

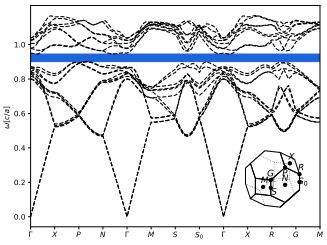

$\varepsilon = 6$, $\phi = 0.19$. 4.83% gap.

Inverse Complex Polymeric Telluridoindates ($tI280$-$In_{12}Te_{23}$), Bands 2 - 3
Structure file taken from `https://doi.org/10.1107/S0108767383001762`.

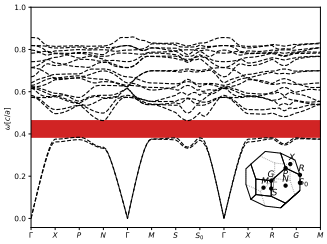

$\varepsilon = 16$, $\phi = 0.14$. 19.06% gap.

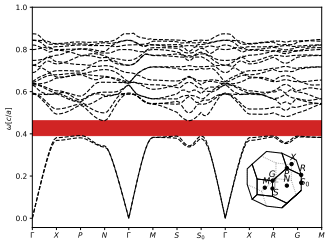

$\varepsilon = 14$, $\phi = 0.16$. 16.8% gap.

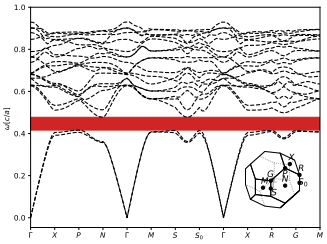

$\varepsilon = 12$, $\phi = 0.16$. 13.97% gap.

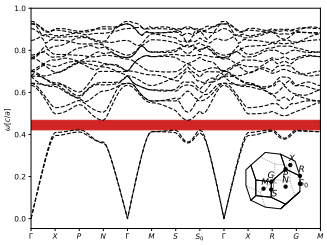

$\varepsilon = 10$, $\phi = 0.19$. 10.52% gap.

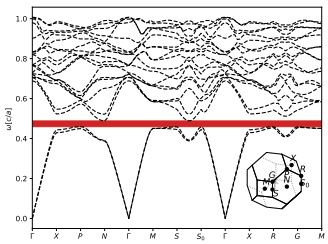

$\varepsilon = 8$, $\phi = 0.19$. 6.39% gap.

Inverse Trisilver Vanadate (beta) ($tI16$-VAg_3O_4), Bands 8 - 9
Structure file taken from `https://doi.org/10.1021/cm301119c`.

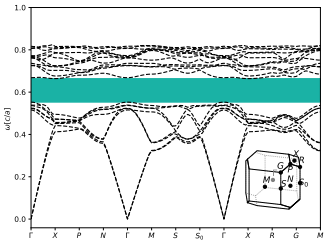

$\varepsilon = 16$, $\phi = 0.22$. 18.9% gap.

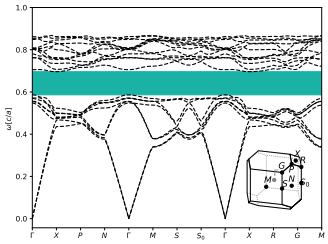

$\varepsilon = 14$, $\phi = 0.22$. 17.8% gap.

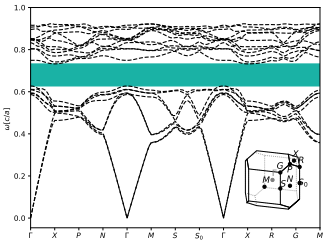

$\varepsilon = 12$, $\phi = 0.22$. 16.25% gap.

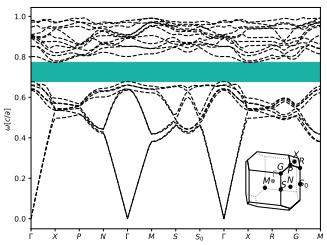

$\varepsilon = 10$, $\phi = 0.22$. 13.98% gap.

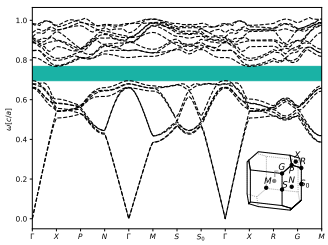

$\varepsilon = 8$, $\phi = 0.27$. 10.87% gap.

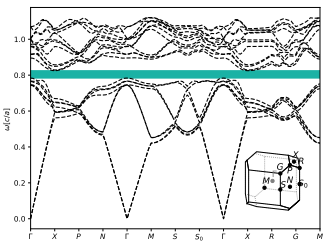

$\varepsilon = 6$, $\phi = 0.27$. 6.1% gap.

Inverse Uranium Borohydride (tP20-UB_4), Bands 4 - 5

Structure file taken from `https://doi.org/10.1021/ic50118a027`.

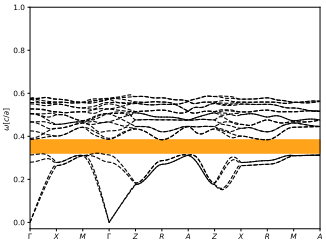

$\varepsilon = 16$, $\phi = 0.19$. 18.88% gap.

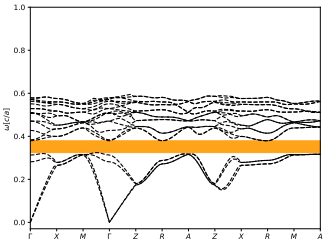

$\varepsilon = 14$, $\phi = 0.22$. 17.26% gap.

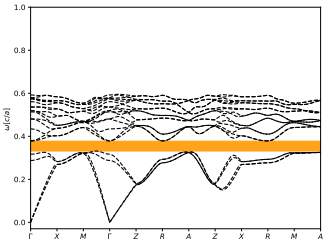

$\varepsilon = 12$, $\phi = 0.25$. 14.64% gap.

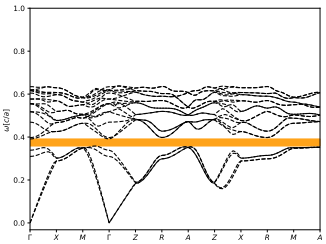

$\varepsilon = 10$, $\phi = 0.25$. 10.12% gap.

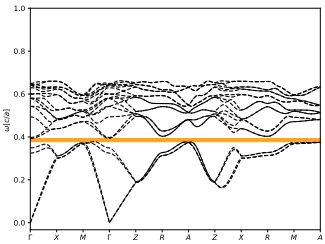

$\varepsilon = 8$, $\phi = 0.29$. 4.64% gap.

Ice II (hR72-H_2O), Bands 12 - 13

Structure file taken from `https://doi.org/10.1107/S0365110X64003553`.

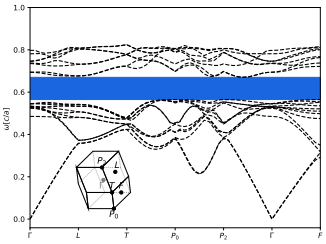

$\varepsilon = 16$, $\phi = 0.29$. 18.52% gap.

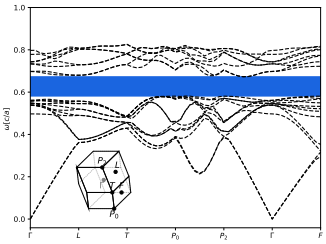

$\varepsilon = 14$, $\phi = 0.32$. 16.15% gap.

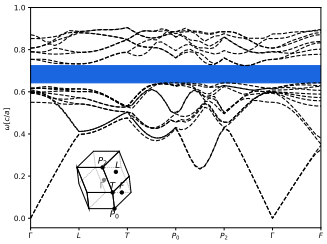

$\varepsilon = 12$, $\phi = 0.29$. 13.39% gap.

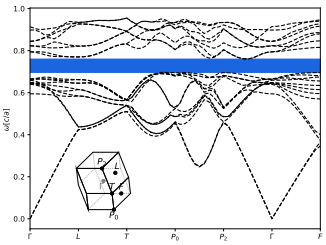

$\varepsilon = 10$, $\phi = 0.29$. 10.21% gap.

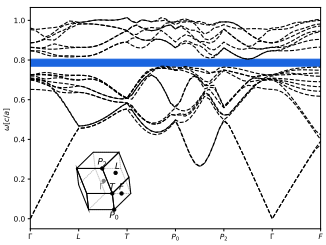

$\varepsilon = 8$, $\phi = 0.29$. 6.11% gap.

Inverse Silicon (II) ($cI16$-Si), Bands 12 - 13

Structure file taken from `https://doi.org/10.1107/S0365110X64001840`.

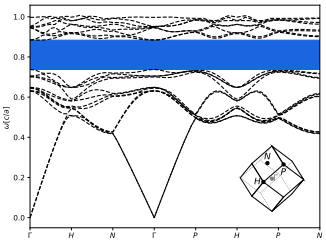

$\varepsilon = 16$, $\phi = 0.11$. 17.85% gap.

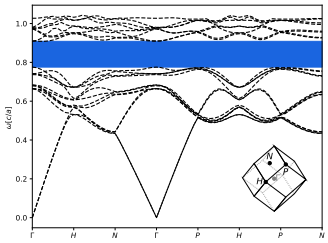

$\varepsilon = 14$, $\phi = 0.11$. 16.31% gap.

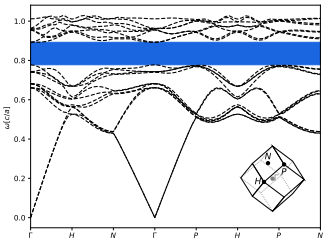

$\varepsilon = 12$, $\phi = 0.13$. 13.87% gap.

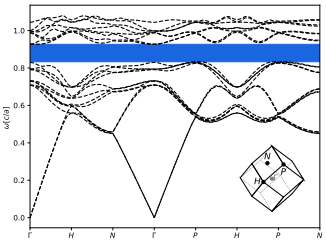

$\varepsilon = 10$, $\phi = 0.13$. 11.22% gap.

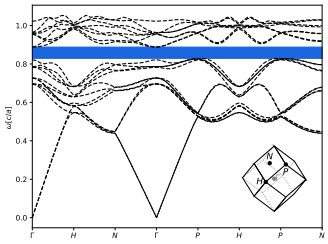

$\varepsilon = 8$, $\phi = 0.18$. 7.38% gap.

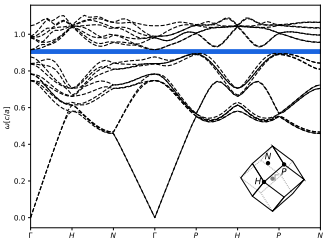

$\varepsilon = 6$, $\phi = 0.2$. 2.77% gap.

Inverse Silica (HP, Pyrite- type) ($cP12$-SiO_2), Bands 16 - 17

Structure file taken from `https://doi.org/10.1126/science.1114879`.

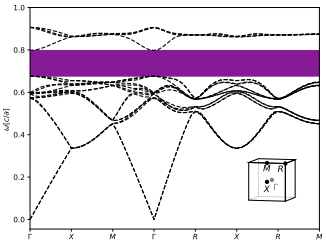

$\varepsilon = 16$, $\phi = 0.15$. 18.32% gap.

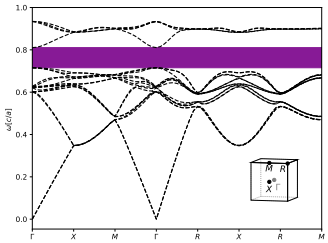

$\varepsilon = 14$, $\phi = 0.15$. 14.32% gap.

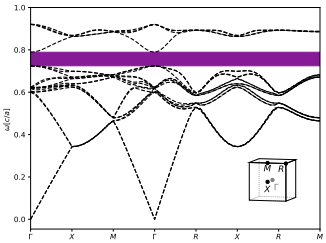

$\varepsilon = 12$, $\phi = 0.17$. 9.73% gap.

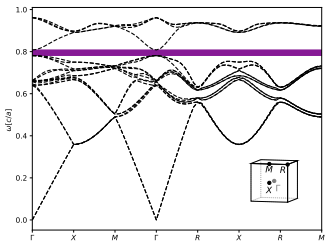

$\varepsilon = 10$, $\phi = 0.17$. 4.55% gap.

Ice Ih ($hP30$-H_5O_2), Bands 4 - 5

Structure file taken from `https://doi.org/10.1063/1.1699206`.

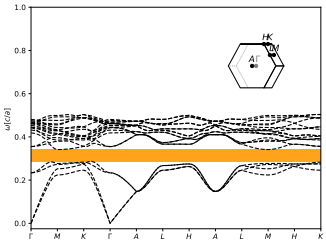

$\varepsilon = 16$, $\phi = 0.33$. 17.75% gap.

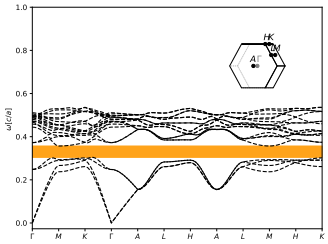

$\varepsilon = 14$, $\phi = 0.33$. 16.37% gap.

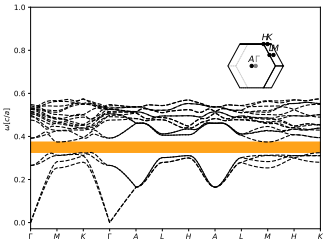

$\varepsilon = 12$, $\phi = 0.33$. 14.56% gap.

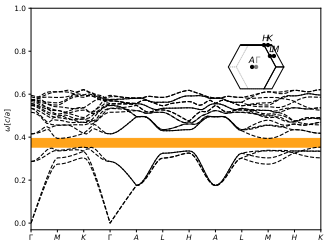

$\varepsilon = 10$, $\phi = 0.33$. 11.62% gap.

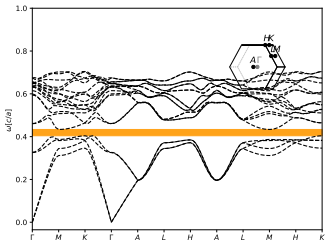

$\varepsilon = 8$, $\phi = 0.3$. 7.84% gap.

Inverse Phosphorus Oxide Nitride ($tP12$-PNO), Bands 4 - 5

Structure file taken from `https://doi.org/10.1002/chin.199030021`.

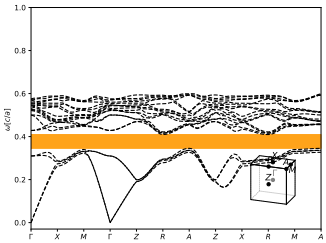

$\varepsilon = 16$, $\phi = 0.2$. 17.42% gap.

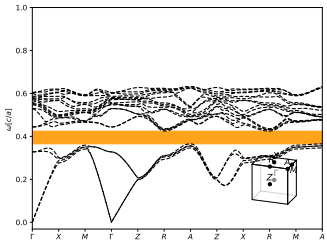

$\varepsilon = 14$, $\phi = 0.2$. 15.53% gap.

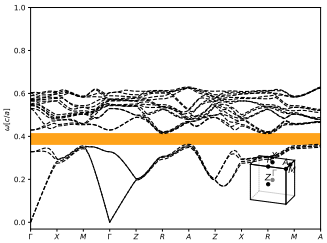

$\varepsilon = 12$, $\phi = 0.24$. 13.23% gap.

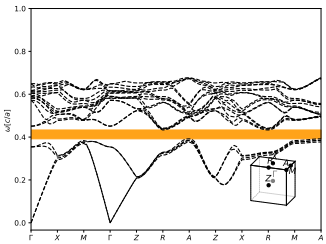

$\varepsilon = 10$, $\phi = 0.24$. 10.51% gap.

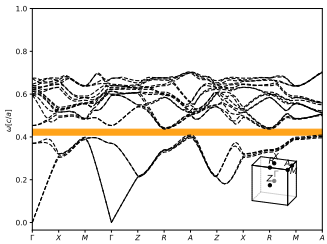

$\varepsilon = 8$, $\phi = 0.27$. 6.99% gap.

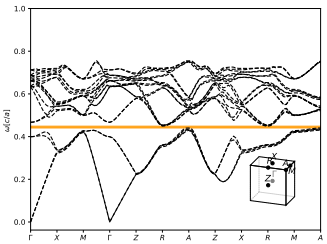

$\varepsilon = 6$, $\phi = 0.31$. 2.29% gap.

Inverse Monoclinic Cristobalite (II) ($mP24$-SiO_2), Bands 8 - 9
Structure file taken from `https://doi.org/10.1180/002646100549436`.

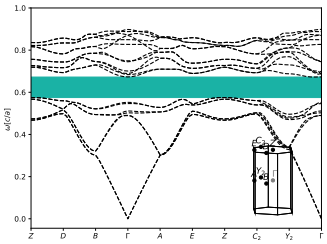

$\varepsilon = 16$, $\phi = 0.3$. 16.25% gap.

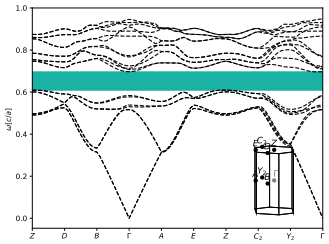

$\varepsilon = 14$, $\phi = 0.3$. 13.91% gap.

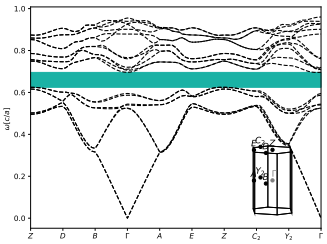

$\varepsilon = 12$, $\phi = 0.33$. 11.21% gap.

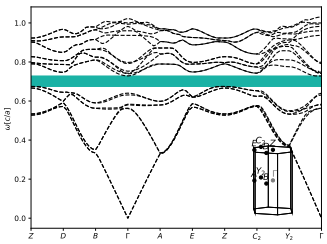

$\varepsilon = 10$, $\phi = 0.33$. 8.02% gap.

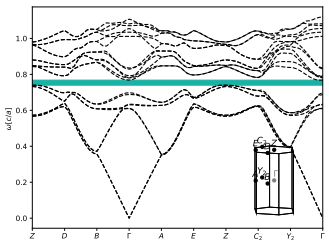

$\varepsilon = 8$, $\phi = 0.33$. 4.05% gap.

Inverse Octahedral Hexasilver Molecule ($cP86$-$Al_{12}Si_{12}Ag_{11.48}O_{48}$), Bands 5 - 6
Structure file taken from `https://doi.org/10.1021/ja00490a035`.

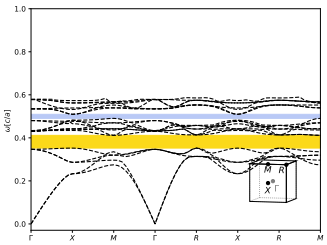

$\varepsilon = 16$, $\phi = 0.27$. (1) 15.63% gap between bands 5-6, and (2) 3.83% gap between bands 13-14.

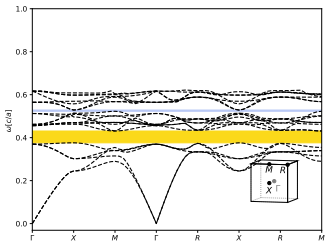

$\varepsilon = 14$, $\phi = 0.27$. (1) 13.75% gap between bands 5-6, and (2) 1.23% gap between bands 13-14.

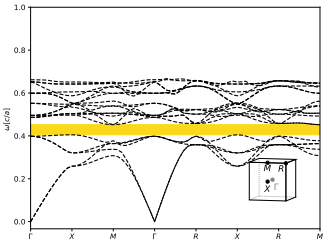

$\varepsilon = 12$, $\phi = 0.27$. 11.13% gap.

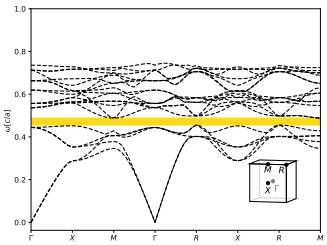

$\varepsilon = 10$, $\phi = 0.25$. 7.77% gap.

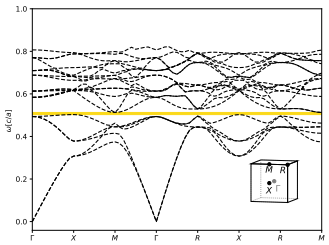

$\varepsilon = 8$, $\phi = 0.25$. 2.08% gap.

Inverse Octahedral Hexasilver Molecule (cP86-$Al_{12}Si_{12}Ag_{11.48}O_{48}$), Bands 13 - 14

Structure file taken from `https://doi.org/10.1021/ja00490a035`.

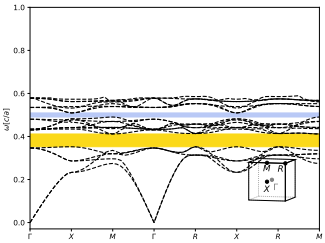

$\varepsilon = 16$, $\phi = 0.27$. (1) 15.63% gap between bands 5-6, and (2) 3.83% gap between bands 13-14.

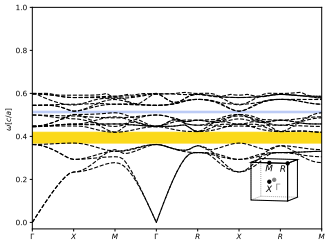

$\varepsilon = 14$, $\phi = 0.29$. (1) 12.79% gap between bands 5-6, and (2) 1.44% gap between bands 13-14.

Inverse Zeolite (CIT-I) (mC336-SO_2), Bands 4 - 5

Structure file taken from `https://doi.org/10.1021/ja00118a013`.

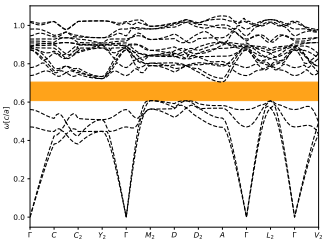

$\varepsilon = 16$, $\phi = 0.19$. 15.57% gap.

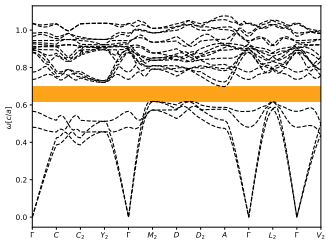

$\varepsilon = 14$, $\phi = 0.21$. 13.57% gap.

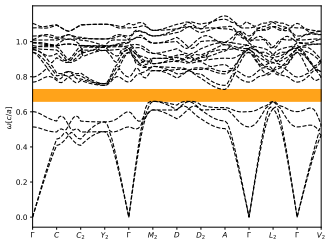

$\varepsilon = 12$, $\phi = 0.21$. 11.14% gap.

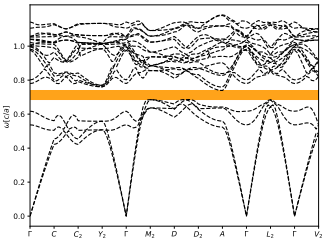

$\varepsilon = 10$, $\phi = 0.23$. 8.02% gap.

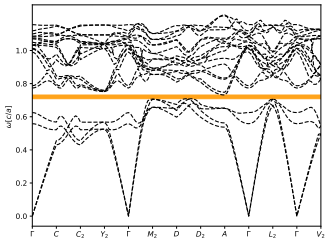

$\varepsilon = 8$, $\phi = 0.28$. 3.88% gap.

Inverse Copper Nitride ($cP4$-Cu_3N), Bands 5 - 6

Structure file taken from `https://doi.org/10.1016/j.ssc.2010.06.012`.

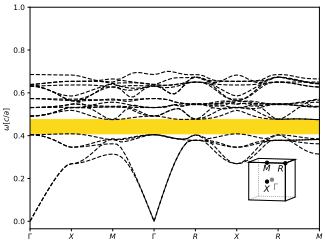

$\varepsilon = 16$, $\phi = 0.17$. 15.04% gap.

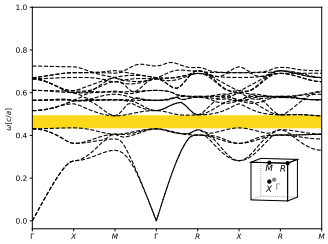

$\varepsilon = 14$, $\phi = 0.17$. 12.21% gap.

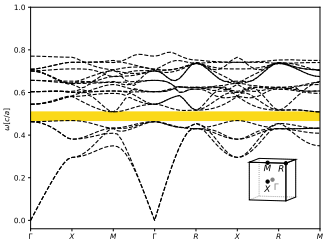

$\varepsilon = 12$, $\phi = 0.17$. 8.43% gap.

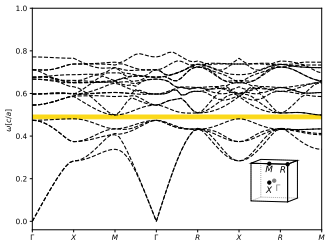

$\varepsilon = 10$, $\phi = 0.22$. 3.7% gap.

Inverse Cobalt pentlandite ($cF68$-Co_9S_8), Bands 10 - 11

Structure file taken from `https://doi.org/10.17188/1191033`.

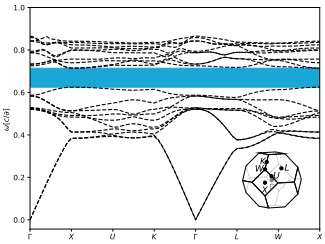

$\varepsilon = 16$, $\phi = 0.2$. 14.77% gap.

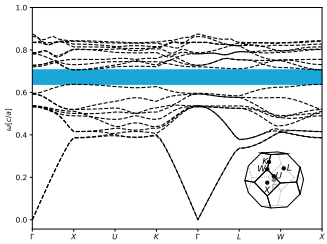

$\varepsilon = 14$, $\phi = 0.22$. 12.04% gap.

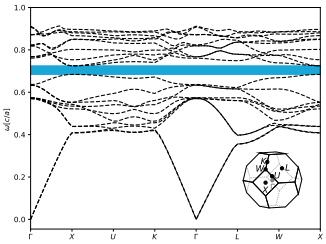

$\varepsilon = 12$, $\phi = 0.22$. 7.45% gap.

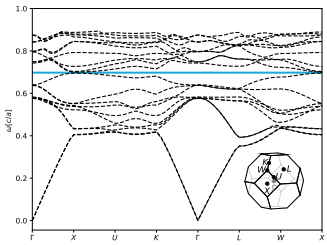

$\varepsilon = 10$, $\phi = 0.27$. 2.18% gap.

Inverse Cobalt pentlandite ($cF68$-Co_9S_8), Bands 13 - 14
Structure file taken from `https://doi.org/10.17188/1191033`.

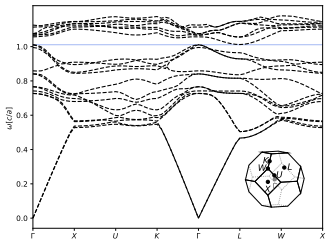

$\varepsilon = 16$, $\phi = 0.07$. 1.07% gap.

Diamond ($cF8$-C), Bands 2 - 3
Structure file taken from `https://doi.org/10.1107/S0108768195010810`.

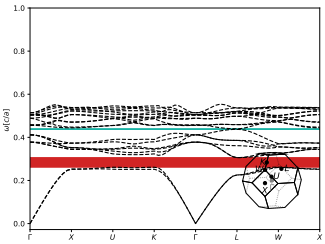

$\varepsilon = 16$, $\phi = 0.42$. 14.74% gap.

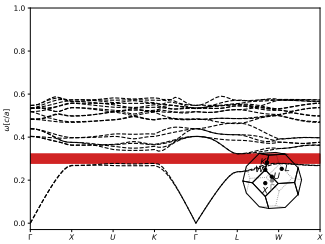

$\varepsilon = 14$, $\phi = 0.42$. 13.92% gap.

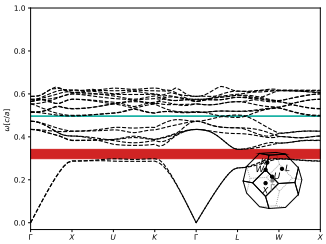

$\varepsilon = 12$, $\phi = 0.42$. 12.82% gap.

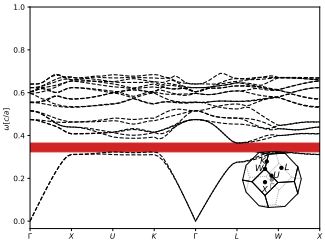

$\varepsilon = 10$, $\phi = 0.42$. 11.27% gap.

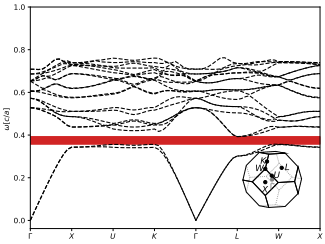

$\varepsilon = 8$, $\phi = 0.42$. 8.98% gap.

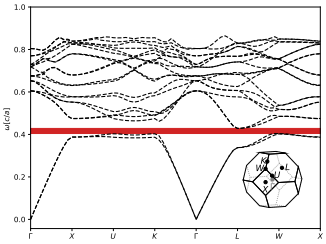

$\varepsilon = 6$, $\phi = 0.42$. 5.37% gap.

Diamond (cF8-C), Bands 8 - 9

Structure file taken from `https://doi.org/10.1107/S0108768195010810`.

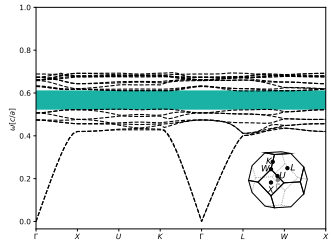

$\varepsilon = 16$, $\phi = 0.21$. 14.34% gap.

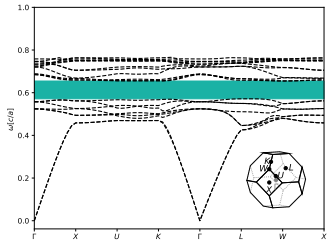

$\varepsilon = 14$, $\phi = 0.19$. 13.38% gap.

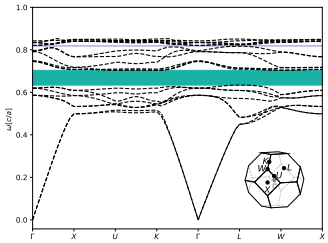

$\varepsilon = 12$, $\phi = 0.16$. 10.35% gap.

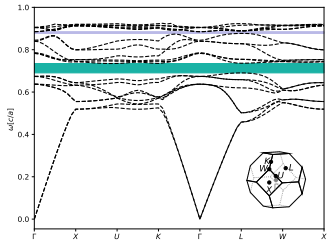

$\varepsilon = 10$, $\phi = 0.16$. (1) 6.07% gap between bands 8-9, and (2) 1.13% gap between bands 14-15.

Diamond (cF8-C), Bands 14 - 15

Structure file taken from `https://doi.org/10.1107/S0108768195010810`.

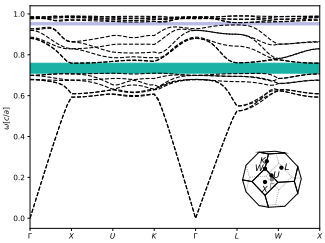

$\varepsilon = 16$, $\phi = 0.07$. (1) 6.65% gap between bands 8-9, and (2) 1.85% gap between bands 14-15.

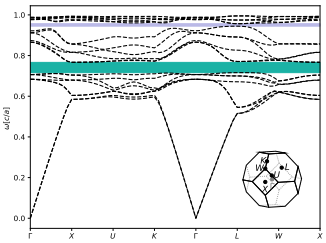

$\varepsilon = 14$, $\phi = 0.08$. (1) 6.9% gap between bands 8-9, and (2) 2.12% gap between bands 14-15.

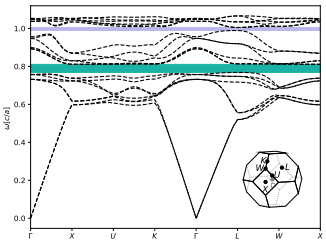

$\varepsilon = 12$, $\phi = 0.08$. (1) 5.36% gap between bands 8-9, and (2) 2.3% gap between bands 14-15.

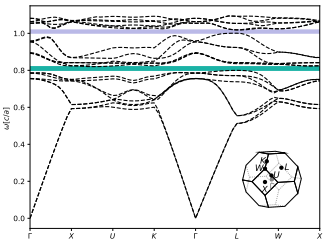

$\varepsilon = 10$, $\phi = 0.09$. (1) 3.1% gap between bands 8-9, and (2) 2.21% gap between bands 14-15.

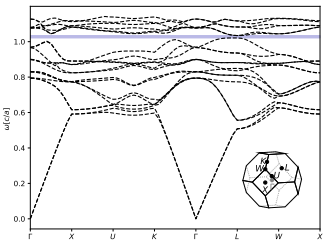

$\varepsilon = 8$, $\phi = 0.11$. 1.56% gap.

Ice Ih ($hP36$-H_2O), Bands 12 - 13

Structure file taken from `https://doi.org/10.1063/1.1749327`.

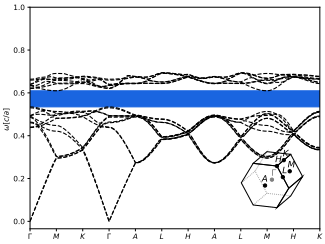

$\varepsilon = 16$, $\phi = 0.32$. 14.17% gap.

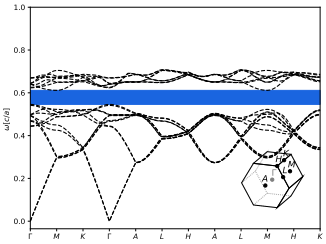

$\varepsilon = 14$, $\phi = 0.35$. 12.41% gap.

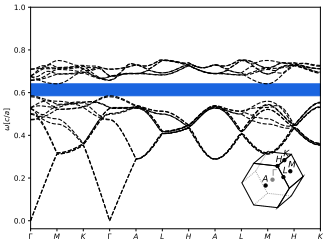

$\varepsilon = 12$, $\phi = 0.35$. 10.18% gap.

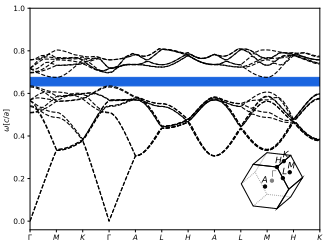

$\varepsilon = 10$, $\phi = 0.35$. 7.14% gap.

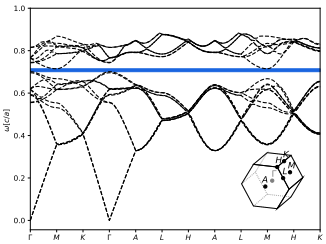

$\varepsilon = 8$, $\phi = 0.35$. 2.85% gap.

Ice Ih ($hP36$-H_2O), Bands 12 - 13

Structure file taken from `https://doi.org/10.1063/1.1749327`.

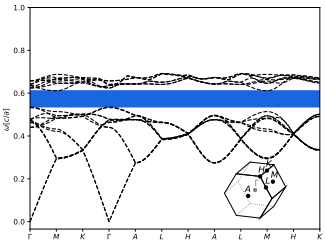

$\varepsilon = 16$, $\phi = 0.32$. 14.17% gap.

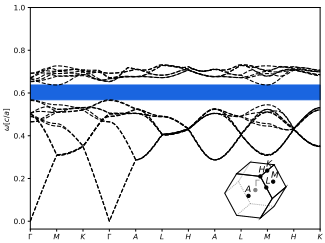

$\varepsilon = 14$, $\phi = 0.32$. 12.45% gap.

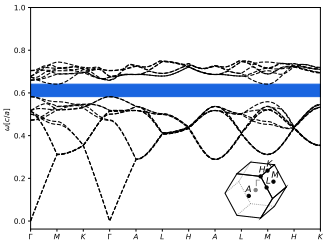

$\varepsilon = 12$, $\phi = 0.35$. 10.2% gap.

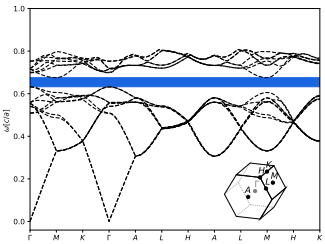

$\varepsilon = 10$, $\phi = 0.35$. 7.15% gap.

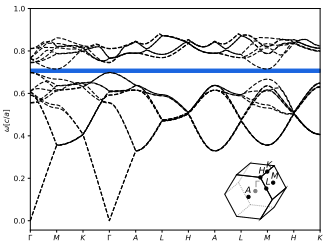

$\varepsilon = 8$, $\phi = 0.35$. 2.85% gap.

Sodium Alumosilicate Eu-doped ($hP21$-$NaAlSiO_4$), Bands 6 - 7
Structure file taken from `https://doi.org/10.1021/acs.chemmater.7b02548`.

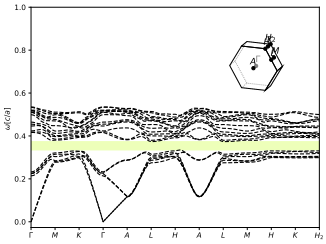

$\varepsilon = 16$, $\phi = 0.32$. 13.97% gap.

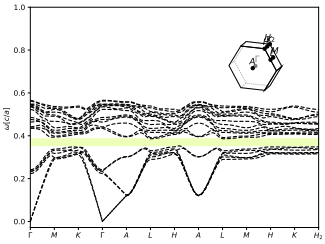

$\varepsilon = 14$, $\phi = 0.32$. 11.67% gap.

Silver Copper Oxide ($tI28$-$Cu_2Ag_2O_3$), Bands 2 - 3
Structure file taken from `https://doi.org/10.1021/ic025872b`.

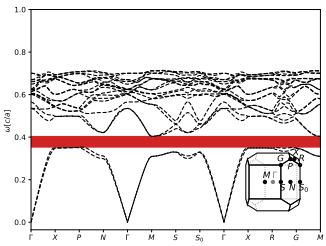

$\varepsilon = 16$, $\phi = 0.34$. 13.96% gap.

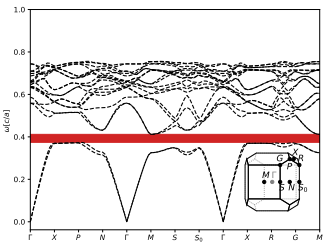

$\varepsilon = 14$, $\phi = 0.34$. 10.17% gap.

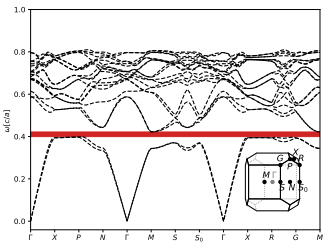

$\varepsilon = 12$, $\phi = 0.34$. 5.83% gap.

Inverse Gallium Chalkogenide ($tI14$-Ga_2HgSe_4), Bands 8 - 9
Structure file taken from `https://doi.org/10.1002/zaac.19552790502`.

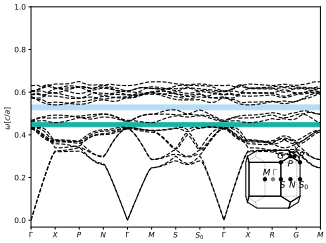

$\varepsilon = 16$, $\phi = 0.4$. (1) 4.93% gap between bands 8-9, and (2) 4.96% gap between bands 11-12.

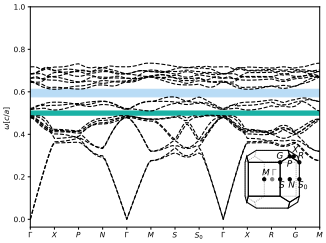

$\varepsilon = 14$, $\phi = 0.35$. (1) 4.7% gap between bands 8-9, and (2) 6.52% gap between bands 11-12.

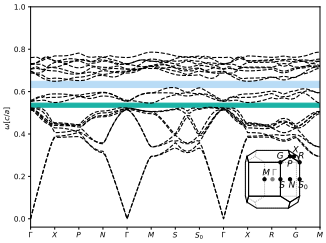

$\varepsilon = 12$, $\phi = 0.35$. (1) 4.42% gap between bands 8-9, and (2) 5.4% gap between bands 11-12.

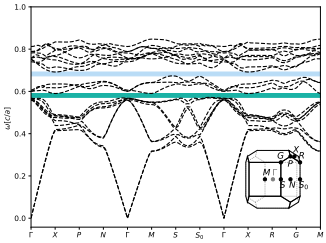

$\varepsilon = 10$, $\phi = 0.35$. (1) 3.92% gap between bands 8-9, and (2) 3.52% gap between bands 11-12.

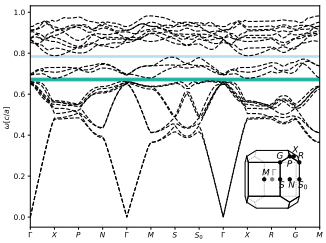

$\varepsilon = 8$, $\phi = 0.3$. (1) 2.79% gap between bands 8-9, and (2) 1.99% gap between bands 11-12.

Inverse Gallium Chalkogenide ($tI14$-Ga_2HgSe_4), Bands 11 - 12
Structure file taken from `https://doi.org/10.1002/zaac.19552790502`.

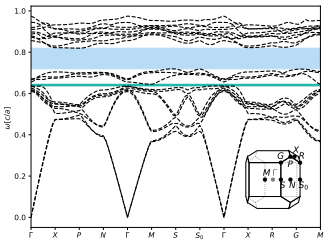

$\varepsilon = 16$, $\phi = 0.16$. (1) 2.02% gap between bands 8-9, and (2) 13.93% gap between bands 11-12.

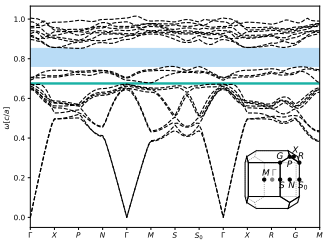

$\varepsilon = 14$, $\phi = 0.16$. (1) 1.74% gap between bands 8-9, and (2) 12.36% gap between bands 11-12.

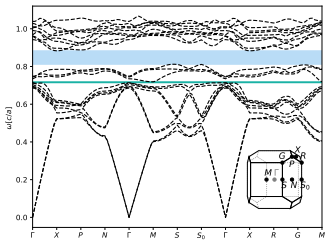

$\varepsilon = 12$, $\phi = 0.16$. (1) 1.36% gap between bands 8-9, and (2) 10.17% gap between bands 11-12.

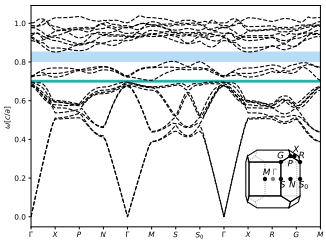

$\varepsilon = 10$, $\phi = 0.2$. (1) 1.99% gap between bands 8-9, and (2) 7.17% gap between bands 11-12.

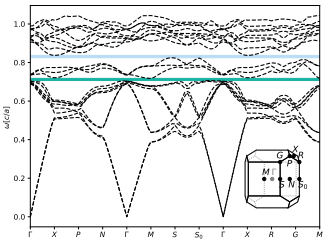

$\varepsilon = 8$, $\phi = 0.25$. (1) 2.24% gap between bands 8-9, and (2) 2.67% gap between bands 11-12.

Silver Chlorate (VII) (cF24-$AgClO_4$), Bands 2 - 3

Structure file taken from `https://doi.org/10.1515/zkri-1930-0105`.

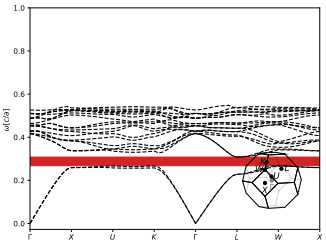

$\varepsilon = 16$, $\phi = 0.49$. 13.91% gap.

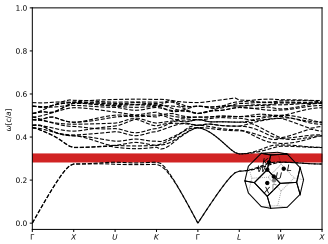

$\varepsilon = 14$, $\phi = 0.49$. 12.28% gap.

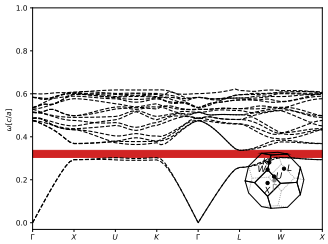

$\varepsilon = 12$, $\phi = 0.49$. 10.22% gap.

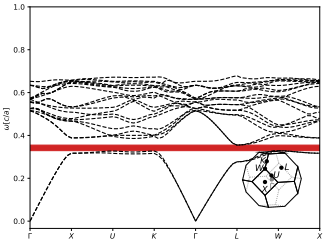

$\varepsilon = 10$, $\phi = 0.49$. 7.61% gap.

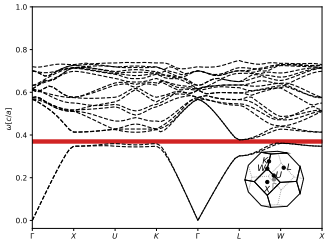

$\varepsilon = 8$, $\phi = 0.49$. 4.19% gap.

Zeolite- type Chalcogenide ($tI48$-GeS_2), Bands 2 - 3
Structure file taken from `https://doi.org/10.1021/jacs.5b03550`.

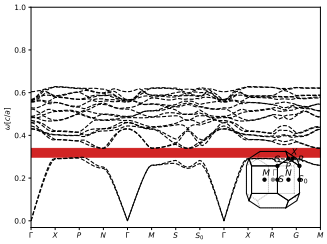

$\varepsilon = 16$, $\phi = 0.39$. 13.75% gap.

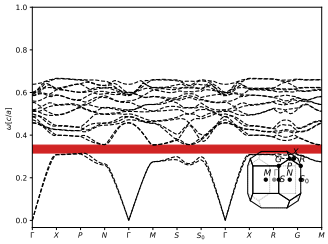

$\varepsilon = 14$, $\phi = 0.39$. 12.28% gap.

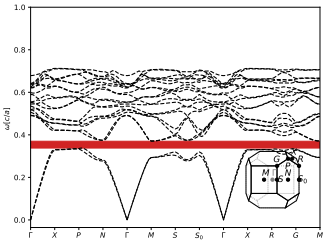

$\varepsilon = 12$, $\phi = 0.39$. 10.01% gap.

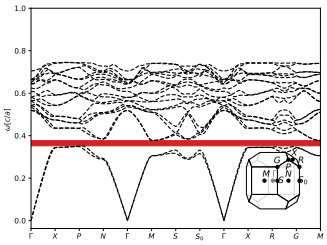

$\varepsilon = 10$, $\phi = 0.42$. 7.25% gap.

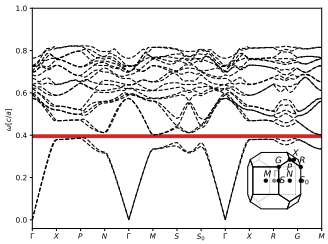

$\varepsilon = 8$, $\phi = 0.42$. 3.73% gap.

Inverse Cadmium Selenide ($cP138$-Cd_6Se_7O), Bands 5 - 6
Structure file taken from `https://doi.org/10.1021/jacs.6b10490`.

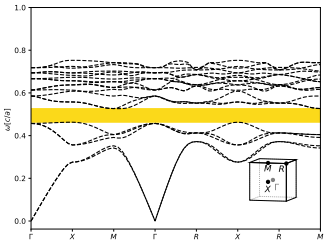

$\varepsilon = 16$, $\phi = 0.16$. 13.68% gap.

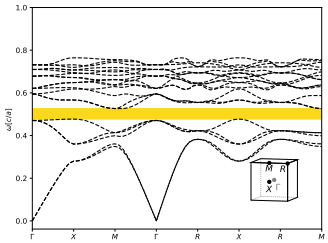

$\varepsilon = 14$, $\phi = 0.17$. 10.27% gap.

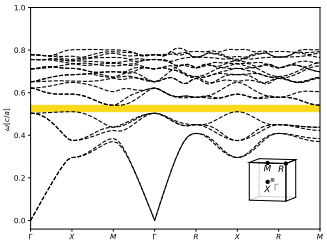

$\varepsilon = 12$, $\phi = 0.17$. 6.27% gap.

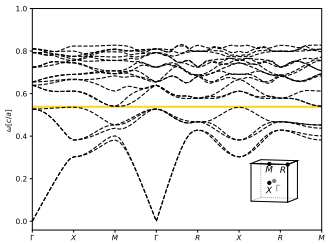

$\varepsilon = 10$, $\phi = 0.19$. 1.39% gap.

Inverse Cadmium Selenide (cP138-Cd_6Se_7O), Bands 8 - 9
Structure file taken from `https://doi.org/10.1021/jacs.6b10490`.

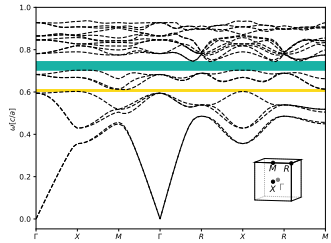

$\varepsilon = 16$, $\phi = 0.08$. (1) 2.71% gap between bands 5-6, and (2) 6.44% gap between bands 8-9.

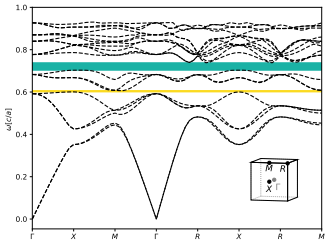

$\varepsilon = 14$, $\phi = 0.09$. (1) 1.88% gap between bands 5-6, and (2) 5.77% gap between bands 8-9.

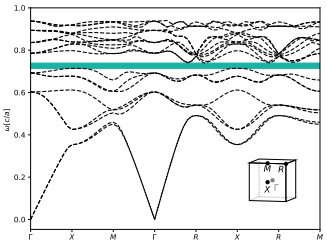

$\varepsilon = 12$, $\phi = 0.1$. 4.34% gap.

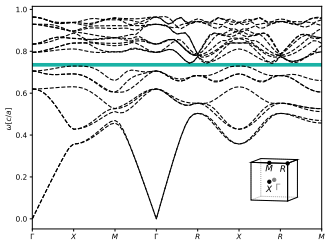

$\varepsilon = 10$, $\phi = 0.11$. 2.22% gap.

Inverse AB13 (cP26-UBe$_{13}$), Bands 5 - 6

Structure file taken from `https://doi.org/10.1103/PhysRevB.32.6042`.

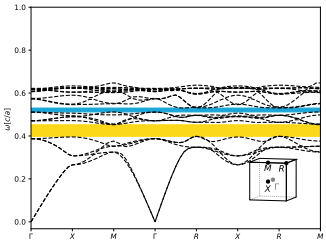

$\varepsilon = 16$, $\phi = 0.21$. (1) 13.3% gap between bands 5-6, and (2) 3.12% gap between bands 10-11.

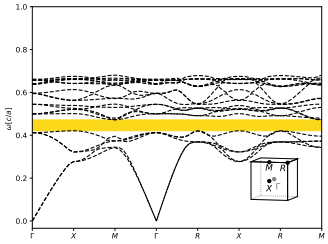

$\varepsilon = 14$, $\phi = 0.21$. 11.76% gap.

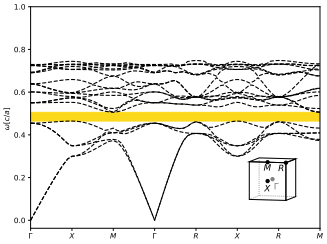

$\varepsilon = 12$, $\phi = 0.2$. 8.99% gap.

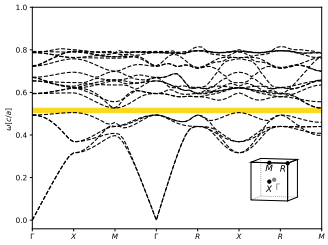

$\varepsilon = 10$, $\phi = 0.2$. 4.61% gap.

Inverse AB13 (cP26-UBe$_{13}$), Bands 10 - 11

Structure file taken from `https://doi.org/10.1103/PhysRevB.32.6042`.

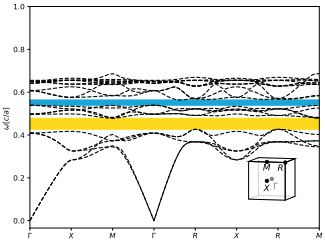

$\varepsilon = 16$, $\phi = 0.18$. (1) 11.71% gap between bands 5-6, and (2) 4.77% gap between bands 10-11.

Ice II ($oC48$-H_2O), Bands 8 - 9

Structure file taken from `https://doi.org/10.1063/1.1749748`.

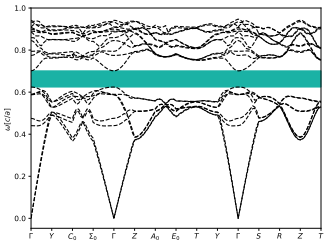

$\varepsilon = 16$, $\phi = 0.27$. 13.3% gap.

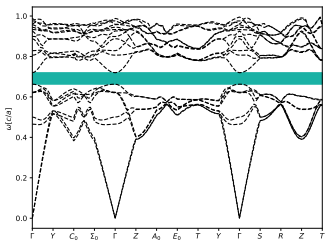

$\varepsilon = 14$, $\phi = 0.27$. 9.81% gap.

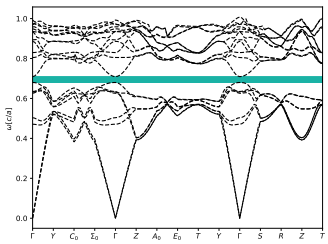

$\varepsilon = 12$, $\phi = 0.3$. 5.66% gap.

Ice II ($oC48$-H_2O), Bands 8 - 9

Structure file taken from `https://doi.org/10.1063/1.1749748`.

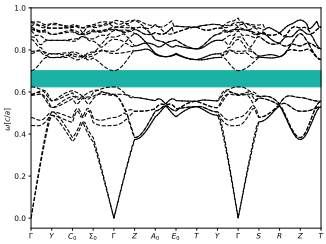

$\varepsilon = 16$, $\phi = 0.27$. 13.24% gap.

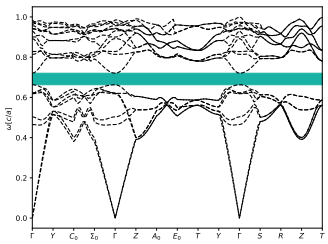

$\varepsilon = 14$, $\phi = 0.27$. 9.75% gap.

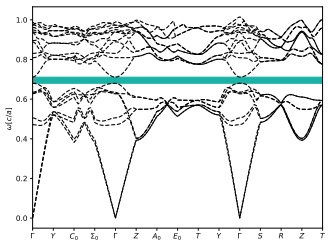

$\varepsilon = 12$, $\phi = 0.3$. 5.66% gap.

Hexagonal Diamond ($hP4$-Ge), Bands 4 - 5

Structure file taken from `https://doi.org/10.17188/1324726`.

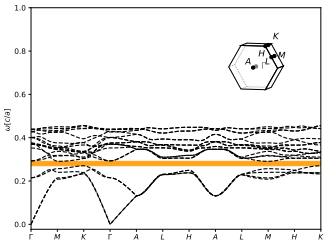

$\varepsilon = 16$, $\phi = 0.45$. 7.33% gap.

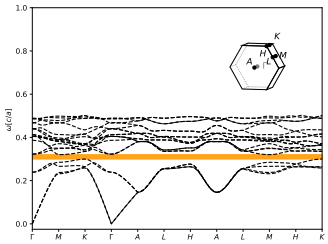

$\varepsilon = 14$, $\phi = 0.41$. 6.52% gap.

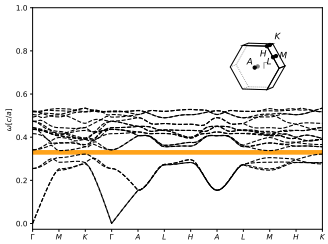

$\varepsilon = 12$, $\phi = 0.41$. 4.89% gap.

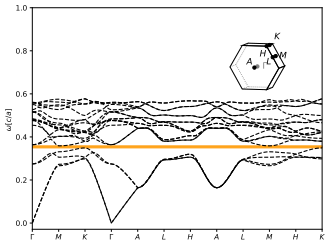

$\varepsilon = 10$, $\phi = 0.41$. 2.62% gap.

Hexagonal Diamond ($hP4$-Ge), Bands 16 - 17
Structure file taken from `https://doi.org/10.17188/1324726`.

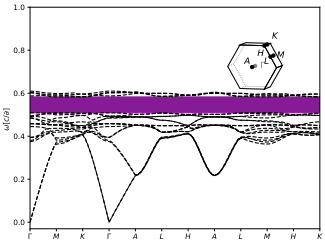

$\varepsilon = 16$, $\phi = 0.23$. 13.2% gap.

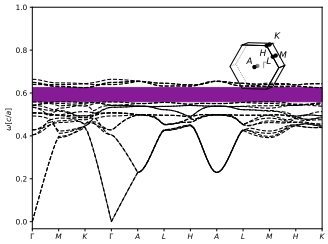

$\varepsilon = 14$, $\phi = 0.2$. 11.05% gap.

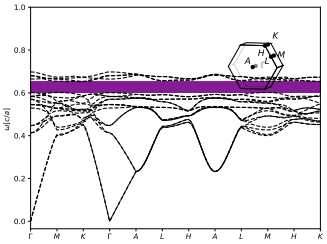

$\varepsilon = 12$, $\phi = 0.2$. 8.16% gap.

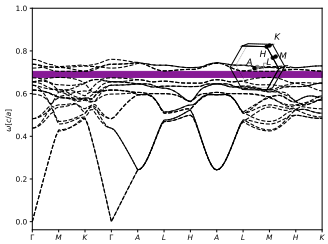

$\varepsilon = 10$, $\phi = 0.18$. 4.09% gap.

Inverse Ternary Thiostannate ($cF184$-$Cu_8Sn_3S_{12}$), Bands 10 - 11
Structure file taken from `https://doi.org/10.1021/acs.inorgchem.6b02012`.

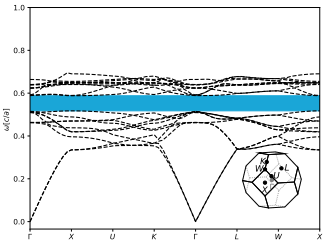

$\varepsilon = 16$, $\phi = 0.26$. 13.13% gap.

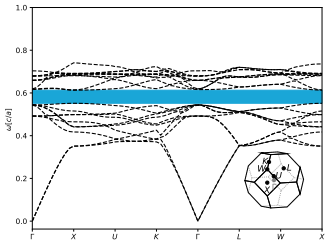

$\varepsilon = 14$, $\phi = 0.26$. 10.93% gap.

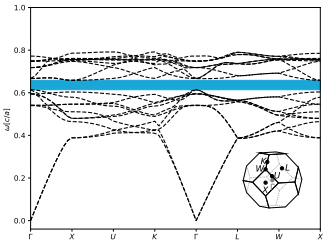

$\varepsilon = 12$, $\phi = 0.24$. 8.1% gap.

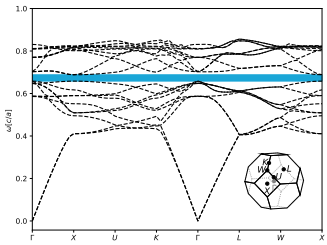

$\varepsilon = 10$, $\phi = 0.24$. 4.9% gap.

Inverse Manganese Gallium Sulfide ($tI14$-$Mn_{1.5}Ga_{4.34}S_8$), Bands 8 - 9
Structure file taken from `https://doi.org/10.1016/0025-5408(78)90086-7`.

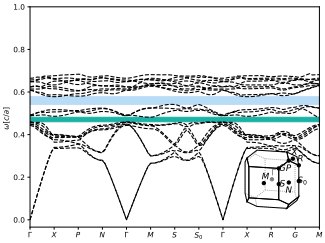

$\varepsilon = 16$, $\phi = 0.35$. (1) 4.82% gap between bands 8-9, and (2) 7.05% gap between bands 11-12.

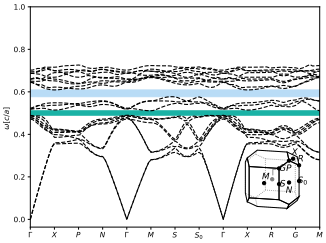

$\varepsilon = 14$, $\phi = 0.35$. (1) 4.55% gap between bands 8-9, and (2) 6.09% gap between bands 11-12.

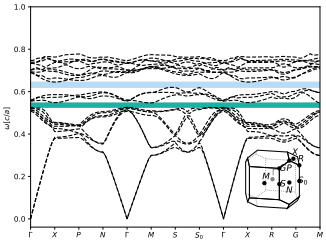

$\varepsilon = 12$, $\phi = 0.35$. (1) 4.2% gap between bands 8-9, and (2) 4.75% gap between bands 11-12.

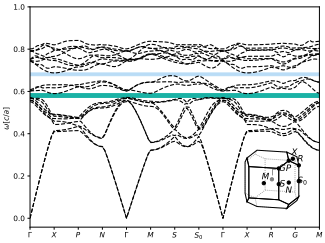

$\varepsilon = 10$, $\phi = 0.35$. (1) 3.44% gap between bands 8-9, and (2) 2.81% gap between bands 11-12.

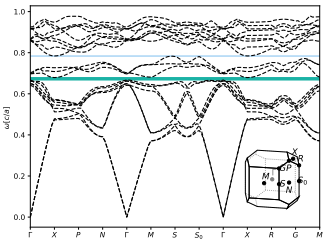

$\varepsilon = 8$, $\phi = 0.3$. (1) 2.15% gap between bands 8-9, and (2) 1.23% gap between bands 11-12.

Inverse Manganese Gallium Sulfide (tI14-$Mn_{1.5}Ga_{4.34}S_8$), Bands 11 - 12
Structure file taken from `https://doi.org/10.1016/0025-5408(78)90086-7`.

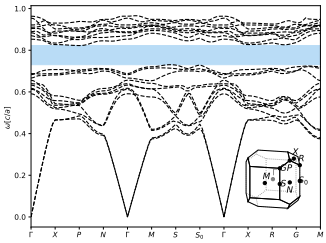

$\varepsilon = 16$, $\phi = 0.16$. 13.07% gap.

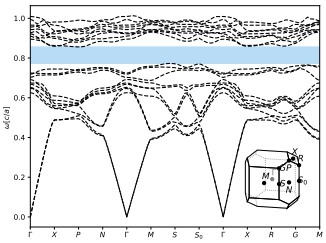

$\varepsilon = 14$, $\phi = 0.16$. 11.61% gap.

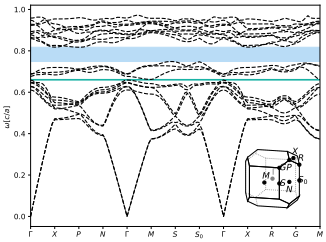

$\varepsilon = 12$, $\phi = 0.2$. (1) 1.25% gap between bands 8-9, and (2) 9.44% gap between bands 11-12.

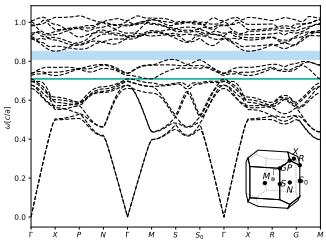

$\varepsilon = 10$, $\phi = 0.2$. 6.46% gap.

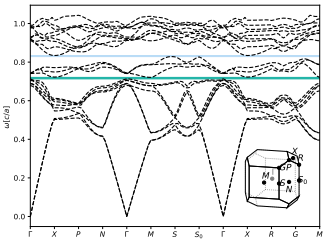

$\varepsilon = 8$, $\phi = 0.25$. (1) 1.55% gap between bands 8-9, and (2) 1.88% gap between bands 11-12.

Inverse Rhodium Telluride (Pyrite- like) (cP12-Te_2Rh), Bands 16 - 17
Structure file taken from `https://doi.org/10.3891/acta.chem.scand.32a-0209`.

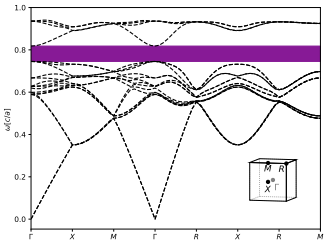

$\varepsilon = 16$, $\phi = 0.12$. 12.64% gap.

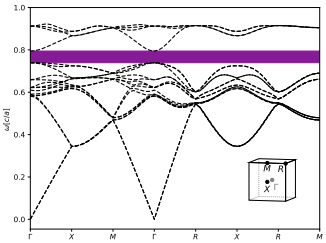

$\varepsilon = 14$, $\phi = 0.15$. 8.98% gap.

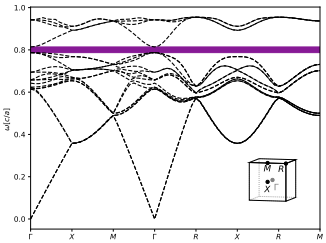

$\varepsilon = 12$, $\phi = 0.15$. 5.16% gap.

Germanium Indium Selenide (oF96-In_2S_5), Bands 2 - 3

Structure file taken from `https://doi.org/10.1107/S0108768104003878`.

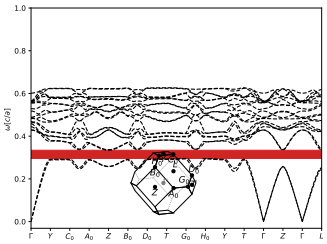

$\varepsilon = 16$, $\phi = 0.4$. 12.28% gap.

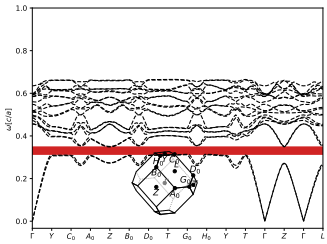

$\varepsilon = 14$, $\phi = 0.4$. 10.45% gap.

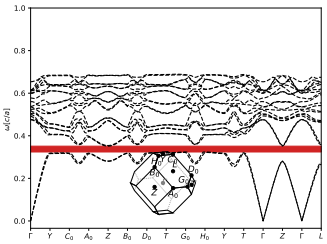

$\varepsilon = 12$, $\phi = 0.43$. 8.26% gap.

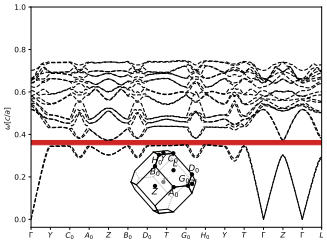

$\varepsilon = 10$, $\phi = 0.43$. 5.57% gap.

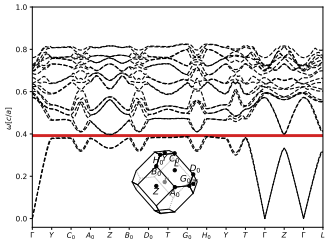

$\varepsilon = 8$, $\phi = 0.43$. 2.04% gap.

Cobalt Copper Silicon Sulfide (tI16-$CoSiCu_2S_4$), Bands 8 - 9

Structure file taken from `https://doi.org/10.1016/j.jallcom.2004.02.004`.

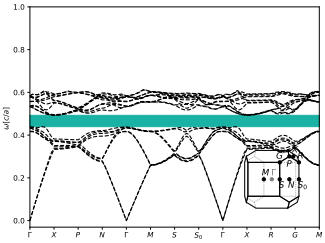

$\varepsilon = 16$, $\phi = 0.46$. 12.26% gap.

Ammonium Fluoride (hP12-H_2NF), Bands 4 - 5

Structure file taken from `https://doi.org/10.1107/S0567740870003898`.

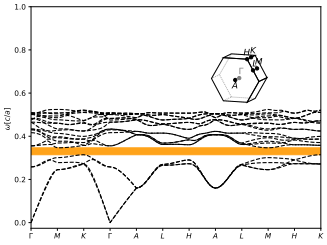

$\varepsilon = 14$, $\phi = 0.35$. 10.51% gap.

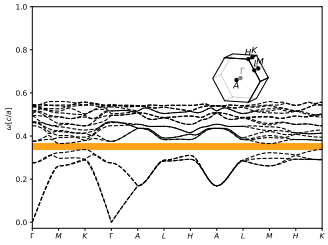

$\varepsilon = 12$, $\phi = 0.35$. 8.63% gap.

Indium Silver Telluride ($tI16$-$In_{4.8}Ag_{1.6}Te_8$), Bands 8 - 9

Structure file taken from `https://doi.org/10.1021/acs.inorgchem.5b00433`.

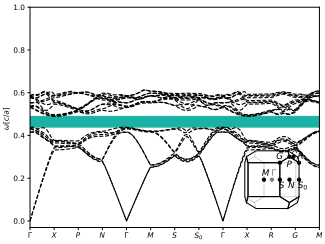

$\varepsilon = 16$, $\phi = 0.47$. 11.71% gap.

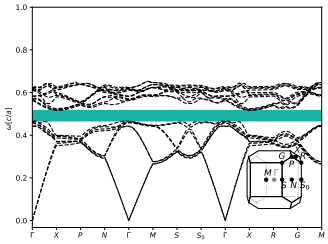

$\varepsilon = 14$, $\phi = 0.47$. 10.98% gap.

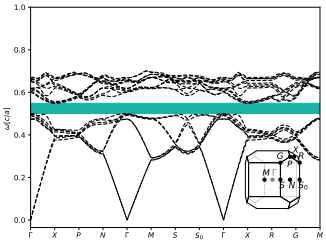

$\varepsilon = 12$, $\phi = 0.47$. 9.99% gap.

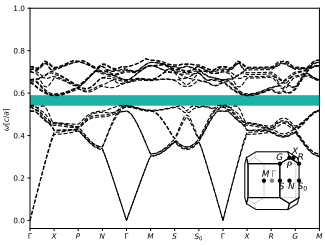

$\varepsilon = 10$, $\phi = 0.47$. 8.62% gap.

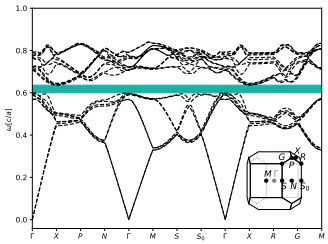

$\varepsilon = 8$, $\phi = 0.47$. 6.59% gap.

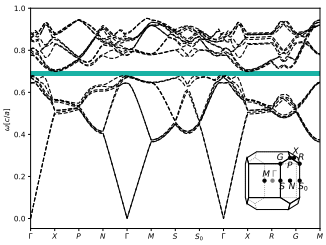

$\varepsilon = 6$, $\phi = 0.47$. 3.4% gap.

Inverse Simple Cubic ($cP1$-Po), Bands 5 - 6

Structure file taken from `https://doi.org/10.1016/0022-1902(66)80270-1`.

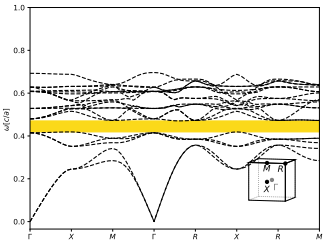

$\varepsilon = 16$, $\phi = 0.18$. 11.58% gap.

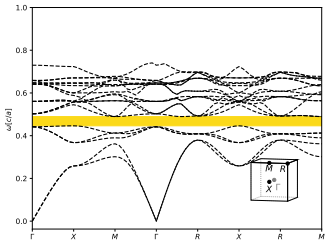

$\varepsilon = 14$, $\phi = 0.18$. 9.25% gap.

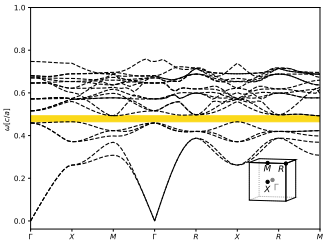

$\varepsilon = 12$, $\phi = 0.2$. 5.81% gap.

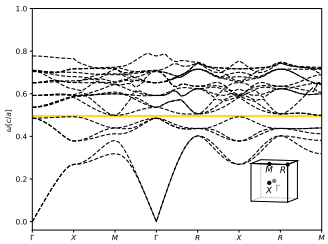

$\varepsilon = 10$, $\phi = 0.22$. 1.39% gap.

Hoffman- type Framework (tP20-$ZnNiC_4N_4$), Bands 4 - 5
Structure file taken from `https://doi.org/10.1039/c1ce05699a`.

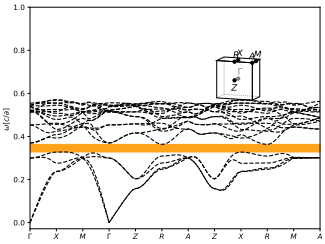

$\varepsilon = 16$, $\phi = 0.21$. 11.42% gap.

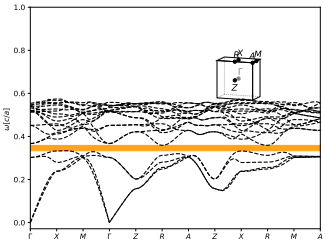

$\varepsilon = 14$, $\phi = 0.23$. 8.67% gap.

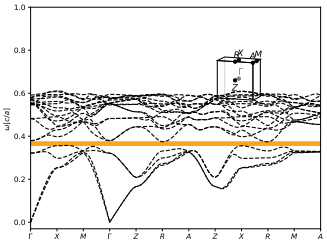

$\varepsilon = 12$, $\phi = 0.23$. 6.05% gap.

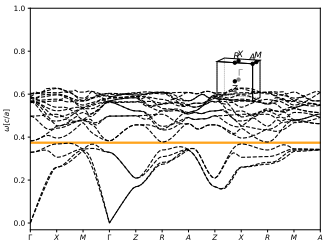

$\varepsilon = 10$, $\phi = 0.26$. 2.84% gap.

Inverse Borphosphide (hR14-$B_{12.64}P_{1.36}$), Bands 7 - 8
Structure file taken from `https://doi.org/10.1107/S0567740874007576`.

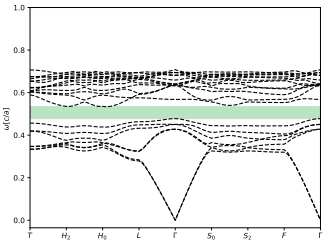

$\varepsilon = 16$, $\phi = 0.22$. 11.39% gap.

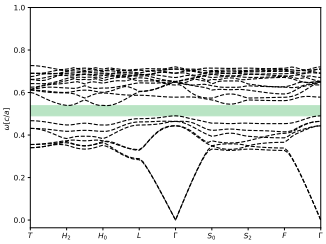

$\varepsilon = 14$, $\phi = 0.24$. 9.52% gap.

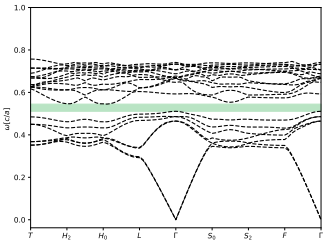

$\varepsilon = 12$, $\phi = 0.26$. 7.09% gap.

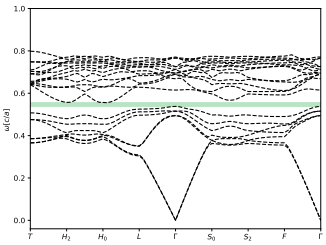

$\varepsilon = 10$, $\phi = 0.28$. 3.88% gap.

Silica Sodalite (cI36-SiO_2), Bands 6 - 7
Structure file taken from `https://doi.org/10.1016/j.micromeso.2011.10.042`.

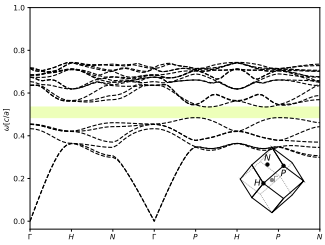

$\varepsilon = 16$, $\phi = 0.24$. 10.71% gap.

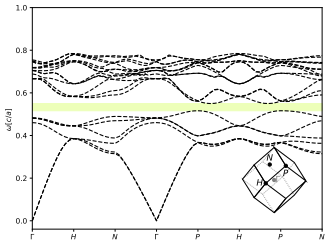

$\varepsilon = 14$, $\phi = 0.24$. 7.23% gap.

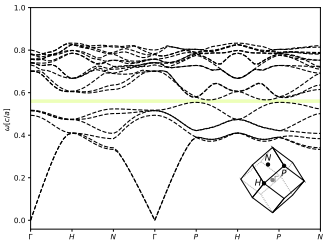

$\varepsilon = 12$, $\phi = 0.24$. 2.89% gap.

Ice II (HP) (hR36-H_2O), Bands 12 - 13
Structure file taken from `https://doi.org/10.1107/S0365110X64003553`.

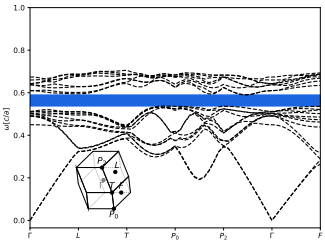

$\varepsilon = 16$, $\phi = 0.4$. 10.65% gap.

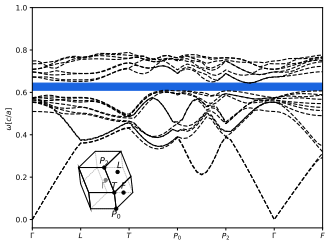

$\varepsilon = 12$, $\phi = 0.4$. 7.07% gap.

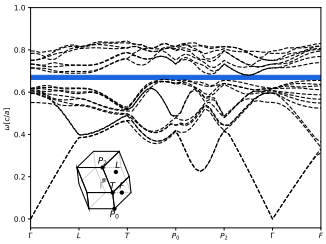

$\varepsilon = 10$, $\phi = 0.4$. 4.78% gap.

Inverse Triammonium Heptafluorozirconate (cF360-$Zr_4H_{47.99936}N_{12}F_{28.0032}$), Bands 10 - 11
Structure file taken from `https://doi.org/10.1007/s10947-008-0066-8`.

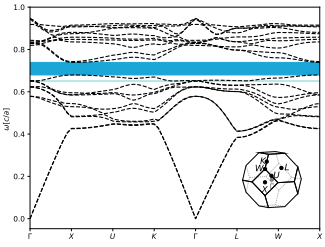

$\varepsilon = 16$, $\phi = 0.15$. 10.24% gap.

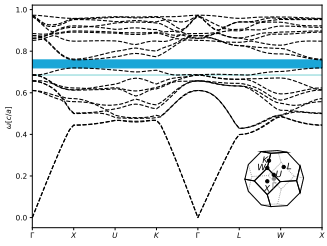

$\varepsilon = 14$, $\phi = 0.15$. 7.13% gap.

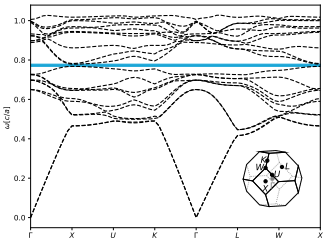

$\varepsilon = 12$, $\phi = 0.15$. 3.24% gap.

Iron Trifluoride (Pyrochlore- Type) (cF64-FeF_3), Bands 2 - 3
Structure file taken from `https://doi.org/10.1016/0025-5408(86)90134-0`.

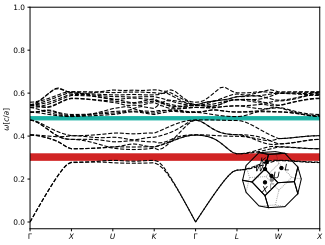

$\varepsilon = 16$, $\phi = 0.42$. (1) 10.14% gap between bands 2-3, and (2) 3.72% gap between bands 8-9.

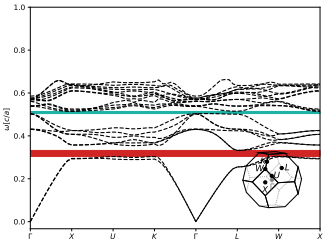

$\varepsilon = 14$, $\phi = 0.42$. (1) 8.96% gap between bands 2-3, and (2) 2.68% gap between bands 8-9.

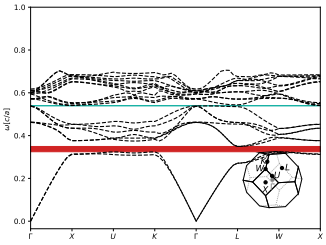

$\varepsilon = 12$, $\phi = 0.42$. (1) 7.47% gap between bands 2-3, and (2) 1.19% gap between bands 8-9.

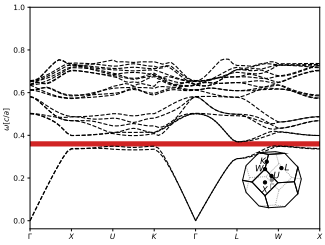

$\varepsilon = 10$, $\phi = 0.42$. 5.55% gap.

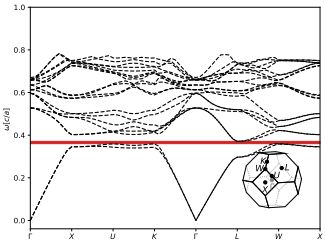

$\varepsilon = 8$, $\phi = 0.47$. 3.09% gap.

Iron Trifluoride (Pyrochlore- Type) (cF64-FeF_3), Bands 8 - 9
Structure file taken from `https://doi.org/10.1016/0025-5408(86)90134-0`.

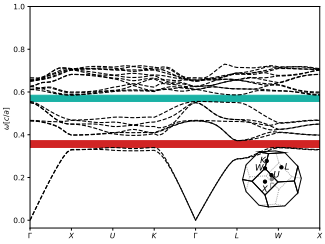

$\varepsilon = 16$, $\phi = 0.31$. (1) 9.23% gap between bands 2-3, and (2) 6.13% gap between bands 8-9.

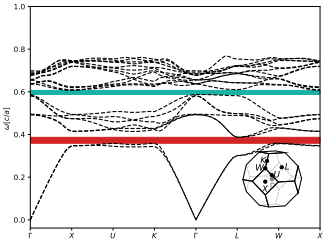

$\varepsilon = 14$, $\phi = 0.31$. (1) 7.81% gap between bands 2-3, and (2) 4.32% gap between bands 8-9.

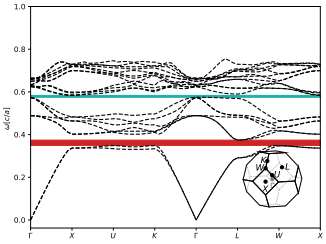

$\varepsilon = 12$, $\phi = 0.36$. (1) 7.14% gap between bands 2-3, and (2) 2.26% gap between bands 8-9.

Inverse Ammonia ($cP16$-H_3N), Bands 4 - 5

Structure file taken from `https://doi.org/10.1021/jp970580v`.

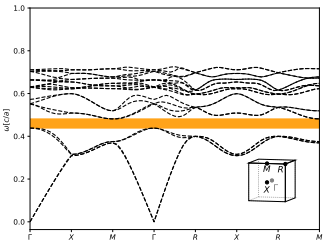

$\varepsilon = 16$, $\phi = 0.17$. 10.06% gap.

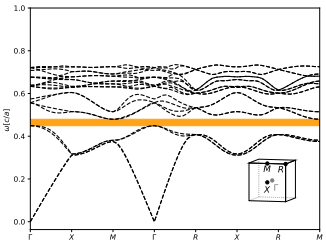

$\varepsilon = 14$, $\phi = 0.19$. 7.24% gap.

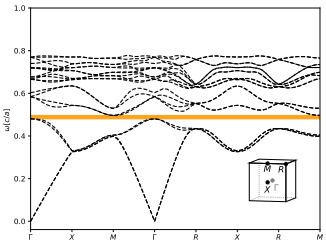

$\varepsilon = 12$, $\phi = 0.19$. 4.0% gap.

Lautite ($oP12$-CuAsS), Bands 12 - 13

Structure file taken from `https://doi.org/10.1107/S1600536808004492`.

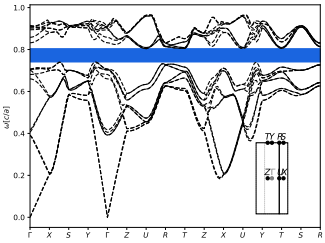

$\varepsilon = 16$, $\phi = 0.51$. 10.0% gap.

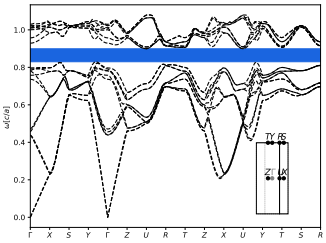

$\varepsilon = 14$, $\phi = 0.46$. 9.29% gap.

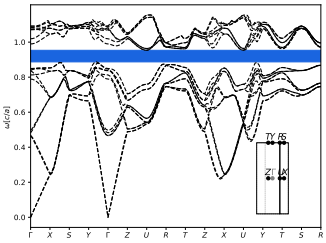

$\varepsilon = 12$, $\phi = 0.46$. 8.5% gap.

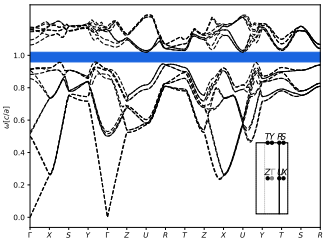

$\varepsilon = 10$, $\phi = 0.46$. 7.35% gap.

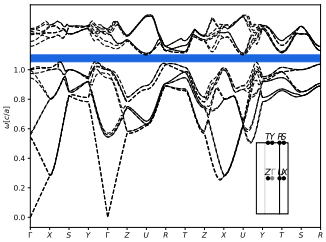

$\varepsilon = 8$, $\phi = 0.46$. 5.59% gap.

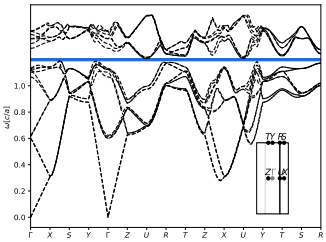

$\varepsilon = 6$, $\phi = 0.46$. 2.77% gap.

Potassium Magnesium Silicide ($tI60$-K_2MgO_2), Bands 8 - 9

Structure file taken from `https://doi.org/10.1107/S0108768196004594`.

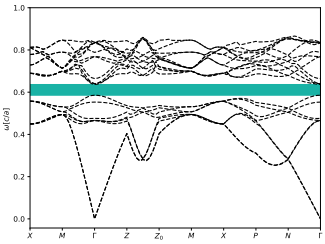

$\varepsilon = 16$, $\phi = 0.31$. 9.96% gap.

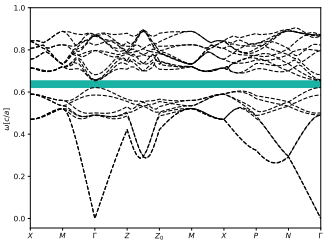

$\varepsilon = 14$, $\phi = 0.31$. 6.49% gap.

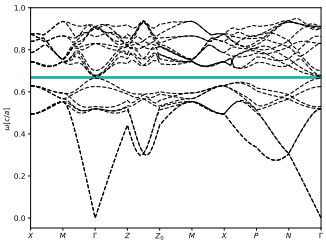

$\varepsilon = 12$, $\phi = 0.31$. 2.42% gap.

Inverse Trilead Germanate ($mP9$-$GePb_3O_5$), Bands 5 - 6
Structure file taken from `https://doi.org/10.17188/1272330`.

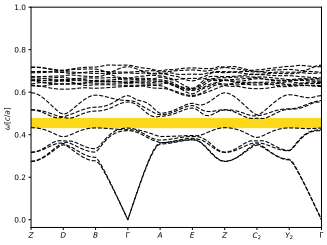

$\varepsilon = 16$, $\phi = 0.19$. 9.89% gap.

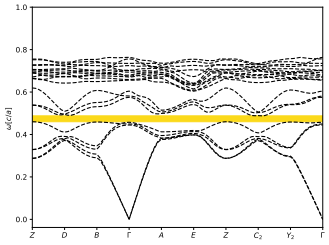

$\varepsilon = 14$, $\phi = 0.19$. 6.21% gap.

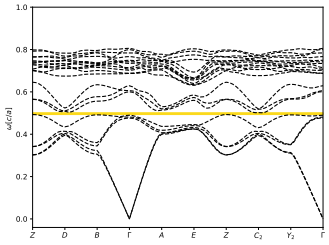

$\varepsilon = 12$, $\phi = 0.19$. 1.97% gap.

Inverse Trilead Germanate ($mP9$-$GePb_3O_5$), Bands 8 - 9
Structure file taken from `https://doi.org/10.17188/1272330`.

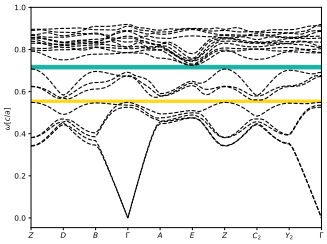

$\varepsilon = 16$, $\phi = 0.09$. (1) 3.27% gap between bands 5-6, and (2) 3.48% gap between bands 8-9.

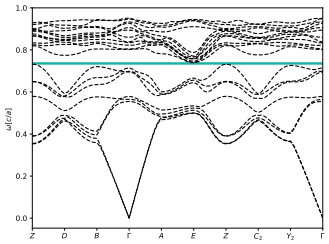

$\varepsilon = 14$, $\phi = 0.09$. 2.06% gap.

Rblicro 4 Crystals ($hP14$-$RbLiCrO_4$), Bands 4 - 5
Structure file taken from `https://doi.org/10.1107/S0108768192006141`.

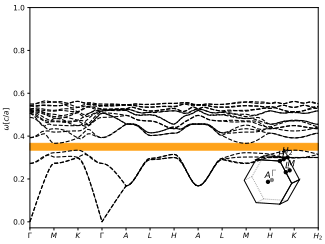

$\varepsilon = 16$, $\phi = 0.3$. 9.78% gap.

Keatite ($mP36$-SiO_2), Bands 12 - 13
Structure file taken from `https://doi.org/10.1524/zkri.1959.112.jg.409`.

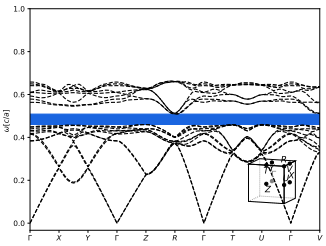

$\varepsilon = 16$, $\phi = 0.32$. 9.69% gap.

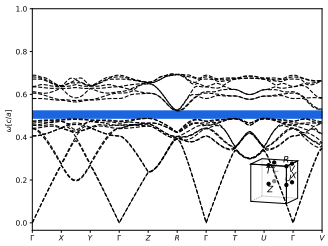

$\varepsilon = 14$, $\phi = 0.32$. 6.52% gap.

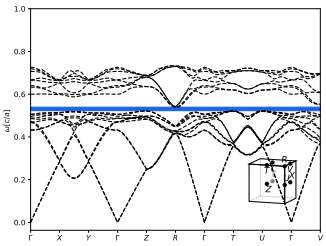

$\varepsilon = 12$, $\phi = 0.32$. 2.87% gap.

Inverse Hexagonal Diamond ($hP4$-Ge), Bands 4 - 5
Structure file taken from `https://doi.org/10.17188/1324726`.

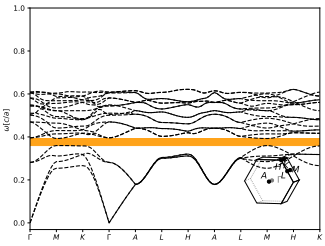

$\varepsilon = 16$, $\phi = 0.2$. 9.32% gap.

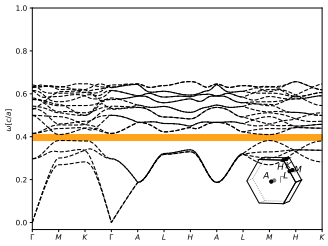

$\varepsilon = 14$, $\phi = 0.2$. 7.69% gap.

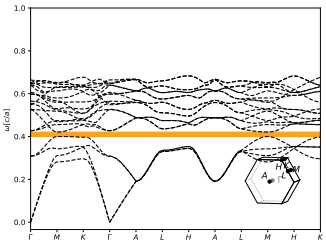

$\varepsilon = 12$, $\phi = 0.21$. 5.46% gap.

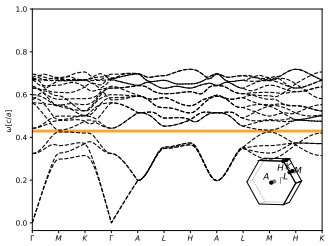

$\varepsilon = 10$, $\phi = 0.22$. 2.55% gap.

Inverse Copper (I) Tetraiodomercurate ($tP7$-Cu_2HgI_4), Bands 8 - 9
Structure file taken from `https://doi.org/10.1524/zkri.1931.80.1.190`.

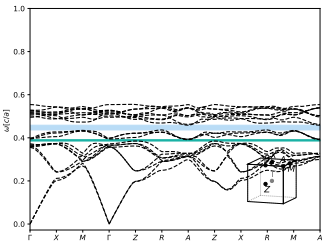

$\varepsilon = 16$, $\phi = 0.36$. (1) 1.8% gap between bands 8-9, and (2) 5.1% gap between bands 11-12.

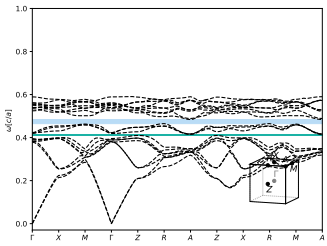

$\varepsilon = 14$, $\phi = 0.36$. (1) 1.33% gap between bands 8-9, and (2) 4.25% gap between bands 11-12.

Inverse Copper (I) Tetraiodomercurate ($tP7$-Cu_2HgI_4), Bands 11 - 12
Structure file taken from `https://doi.org/10.1524/zkri.1931.80.1.190`.

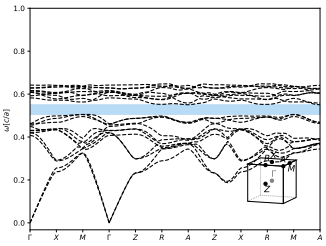

$\varepsilon = 16$, $\phi = 0.24$. 9.03% gap.

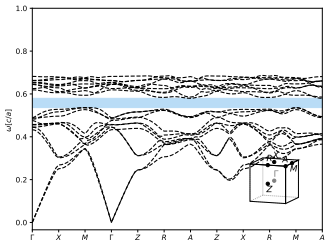

$\varepsilon = 14$, $\phi = 0.24$. 8.29% gap.

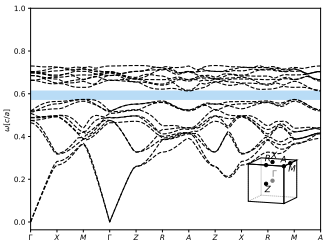

$\varepsilon = 12$, $\phi = 0.24$. 7.17% gap.

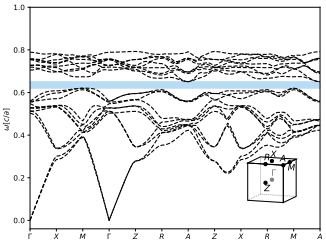

$\varepsilon = 10$, $\phi = 0.24$. 5.39% gap.

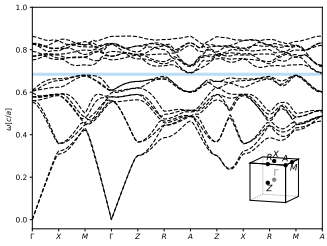

$\varepsilon = 8$, $\phi = 0.24$. 2.06% gap.

Inverse Metal Chalcogenide Supertetrahedral Nanocluster (mP212-$Zn_4In_{16}S_{33}$), Bands 6 - 7

Structure file taken from `https://doi.org/10.1021/jacs.7b12092`.

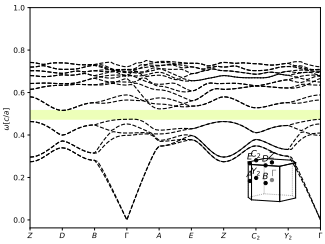

$\varepsilon = 16$, $\phi = 0.16$. 8.82% gap.

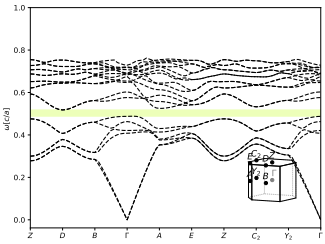

$\varepsilon = 14$, $\phi = 0.18$. 6.4% gap.

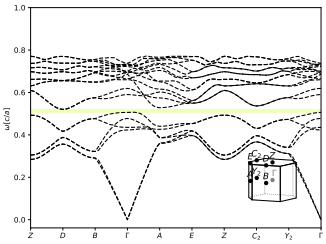

$\varepsilon = 12$, $\phi = 0.2$. 3.3% gap.

Inverse Opal (FCC) (cF4-Cu), Bands 8 - 9

Structure file taken from `https://doi.org/10.1063/1.1728392`.

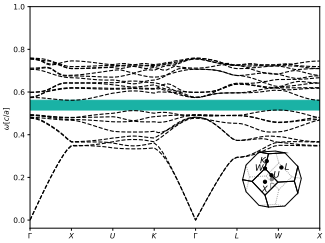

$\varepsilon = 16$, $\phi = 0.22$. 8.76% gap.

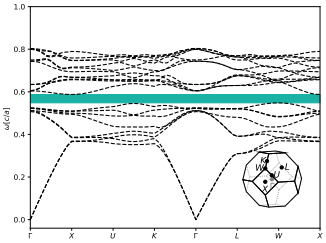

$\varepsilon = 14$, $\phi = 0.22$. 7.21% gap.

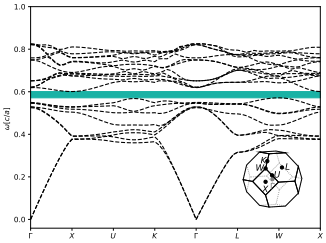

$\varepsilon = 12$, $\phi = 0.24$. 5.34% gap.

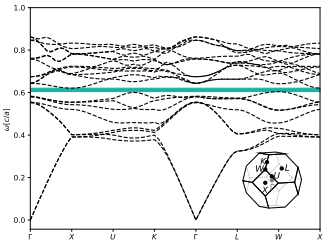

$\varepsilon = 10$, $\phi = 0.26$. 2.92% gap.

Phosphorus (V) Nitride (alpha) (mC64-P_3N_5), Bands 12 - 13
Structure file taken from `https://doi.org/10.1002/(SICI)1521-3749(199804)624:4<620::AID-ZAAC620>3.0.CO;2-K`.

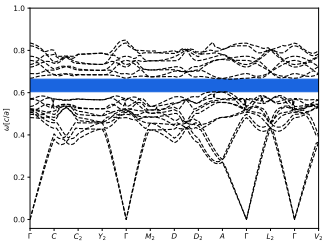

$\varepsilon = 16$, $\phi = 0.27$. 8.53% gap.

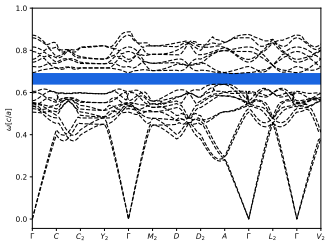

$\varepsilon = 14$, $\phi = 0.27$. 6.65% gap.

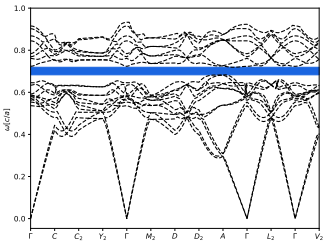

$\varepsilon = 12$, $\phi = 0.27$. 4.26% gap.

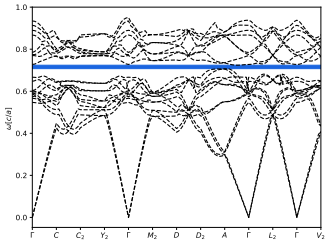

$\varepsilon = 10$, $\phi = 0.3$. 1.32% gap.

Inverse Gallium Selenide (mC20-Ga_2Se_3), Bands 12 - 13
Structure file taken from `https://doi.org/10.1107/S0108270183007039`.

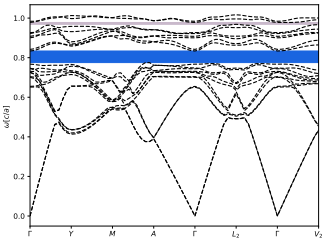

$\varepsilon = 16$, $\phi = 0.1$. (1) 7.17% gap between bands 12-13, and (2) 2.35% gap between bands 18-19.

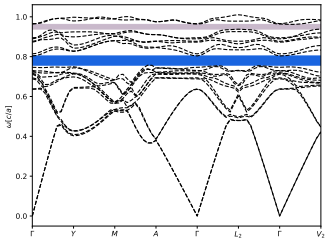

$\varepsilon = 14$, $\phi = 0.12$. (1) 6.41% gap between bands 12-13, and (2) 3.72% gap between bands 18-19.

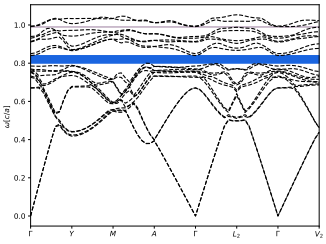

$\varepsilon = 12$, $\phi = 0.12$. (1) 5.44% gap between bands 12-13, and (2) 1.4% gap between bands 18-19.

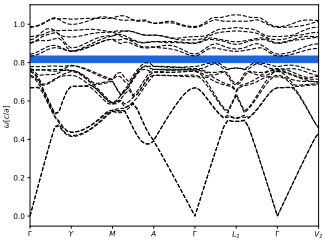

$\varepsilon = 10$, $\phi = 0.15$. 4.29% gap.

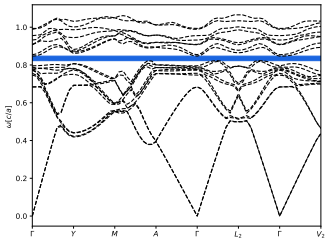

$\varepsilon = 8$, $\phi = 0.17$. 2.69% gap.

Inverse Gallium Selenide (mC20-Ga_2Se_3), Bands 18 - 19
Structure file taken from `https://doi.org/10.1107/S0108270183007039`.

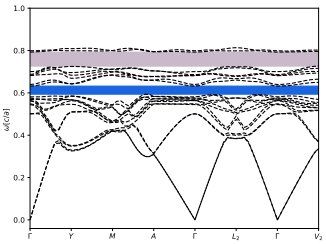

$\varepsilon = 16$, $\phi = 0.2$. (1) 5.28% gap between bands 12-13, and (2) 8.29% gap between bands 18-19.

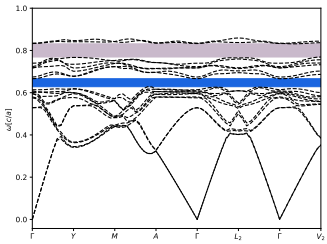

$\varepsilon = 14$, $\phi = 0.2$. (1) 4.96% gap between bands 12-13, and (2) 7.69% gap between bands 18-19.

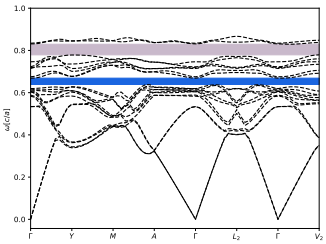

$\varepsilon = 12$, $\phi = 0.22$. (1) 4.26% gap between bands 12-13, and (2) 6.62% gap between bands 18-19.

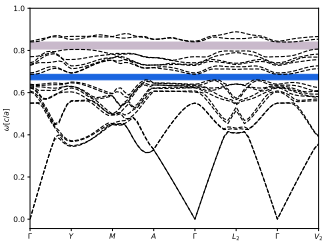

$\varepsilon = 10$, $\phi = 0.25$. (1) 3.37% gap between bands 12-13, and (2) 4.51% gap between bands 18-19.

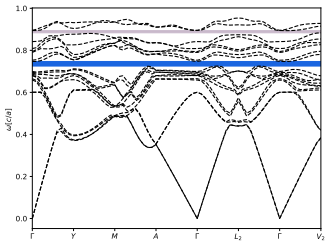

$\varepsilon = 8$, $\phi = 0.25$. (1) 2.55% gap between bands 12-13, and (2) 1.44% gap between bands 18-19.

Inverse Nickel Antimonide Sulfide (cP12-NiSbS), Bands 16 - 17
Structure file taken from `https://doi.org/10.1006/jssc.2001.9342`.

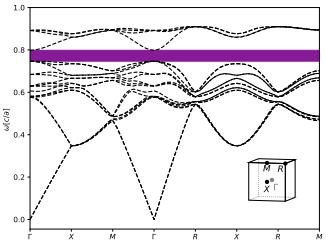

$\varepsilon = 16$, $\phi = 0.13$. 8.28% gap.

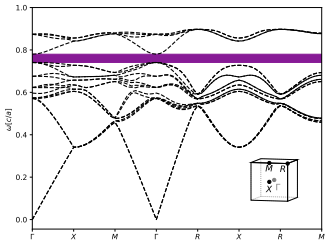

$\varepsilon = 14$, $\phi = 0.15$. 5.48% gap.

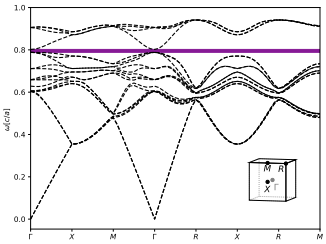

$\varepsilon = 12$, $\phi = 0.15$. 2.42% gap.

Inverse Aluminum Cobalt Phosphate (mC384-$Al_{19.2}Co_{12.8}P_{32}O_{128}$), Bands 16 - 17

Structure file taken from `https://doi.org/10.1021/ja057933l`.

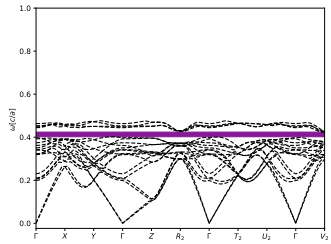

$\varepsilon = 16$, $\phi = 0.23$. 8.17% gap.

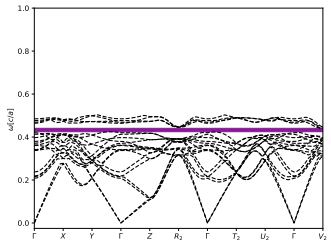

$\varepsilon = 14$, $\phi = 0.23$. 6.58% gap.

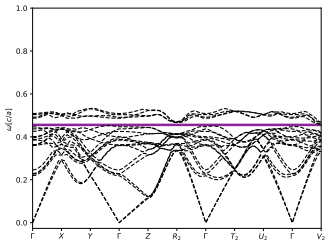

$\varepsilon = 12$, $\phi = 0.23$. 4.37% gap.

Inverse Zeolite ZSM-11 (tI576-SiO_2), Bands 4 - 5

Structure file taken from `https://doi.org/10.1021/ja00189a016`.

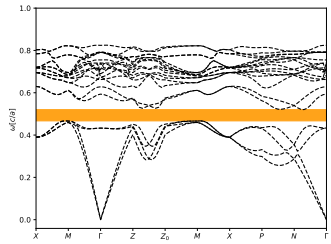

$\varepsilon = 16$, $\phi = 0.2$. 8.13% gap.

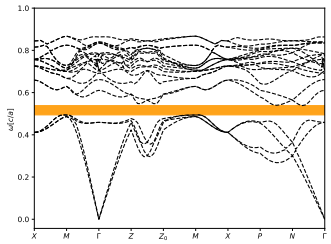

$\varepsilon = 14$, $\phi = 0.2$. 4.34% gap.

Inverse Heazlewoodite (hR5-Ni_3S_2), Bands 2 - 3

Structure file taken from `https://doi.org/10.1002/zaac.19382390109`.

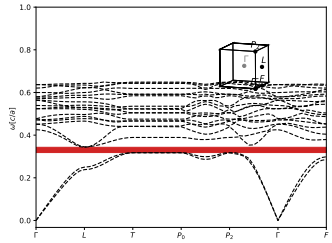

$\varepsilon = 16$, $\phi = 0.22$. 8.07% gap.

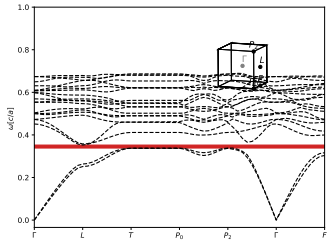

$\varepsilon = 14$, $\phi = 0.22$. 4.67% gap.

Inverse Rhenium Disulfide ($mC4$-ReS_2), Bands 16 - 17

Structure file taken from `https://doi.org/10.1021/ic00097a037`.

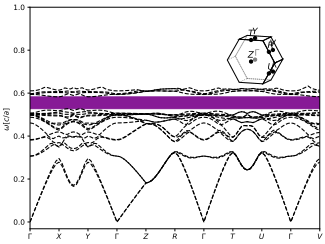

$\varepsilon = 16$, $\phi = 0.21$. 8.05% gap.

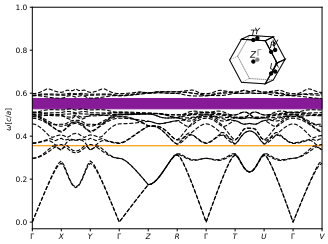

$\varepsilon = 14$, $\phi = 0.25$. 6.5% gap.

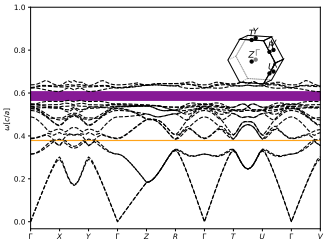

$\varepsilon = 12$, $\phi = 0.25$. 4.71% gap.

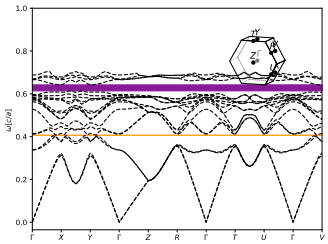

$\varepsilon = 10$, $\phi = 0.25$. 2.19% gap.

Inverse HCP ($hP2$-Be), Bands 16 - 17

Structure file taken from `https://doi.org/10.1107/S0567739478000121`.

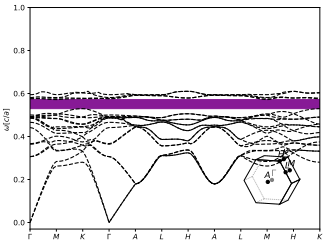

$\varepsilon = 16$, $\phi = 0.23$. 7.79% gap.

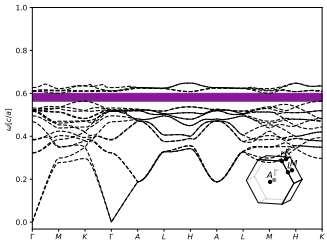

$\varepsilon = 14$, $\phi = 0.23$. 6.64% gap.

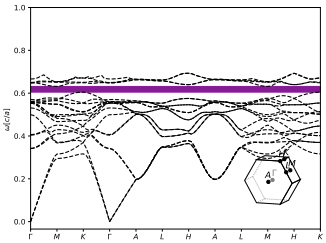

$\varepsilon = 12$, $\phi = 0.23$. 4.79% gap.

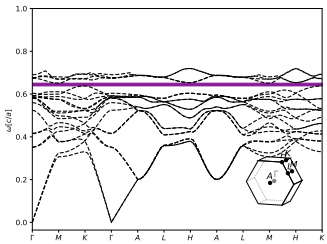

$\varepsilon = 10$, $\phi = 0.25$. 2.35% gap.

Inverse Uranium Boride (cF52-UB_{12}), Bands 5 - 6

Structure file taken from `https://doi.org/10.1107/S0365110X54000151`.

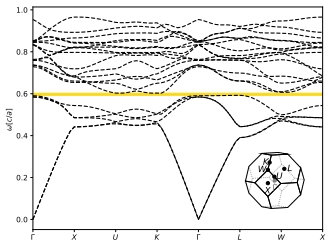

$\varepsilon = 16$, $\phi = 0.13$. 3.84% gap.

Inverse Uranium Boride (cF52-UB_{12}), Bands 8 - 9

Structure file taken from `https://doi.org/10.1107/S0365110X54000151`.

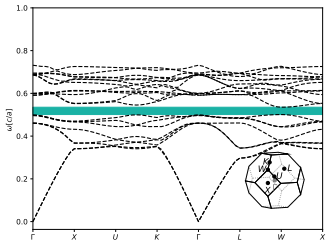

$\varepsilon = 16$, $\phi = 0.25$. 7.78% gap.

Dinitrogen Tetraoxide (cI36-NO_2), Bands 8 - 9

Structure file taken from `https://doi.org/10.1007/BF01390966`.

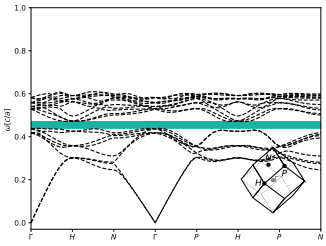

$\varepsilon = 16$, $\phi = 0.41$. 7.66% gap.

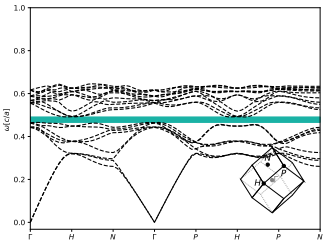

$\varepsilon = 14$, $\phi = 0.41$. 5.94% gap.

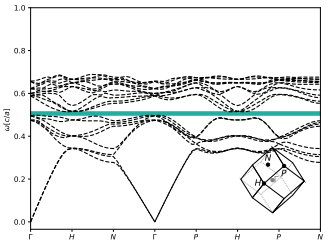

$\varepsilon = 12$, $\phi = 0.41$. 3.75% gap.

Inverse Ice Ih ($hP30$-H_5O_2), Bands 4 - 5

Structure file taken from `https://doi.org/10.1063/1.1699206`.

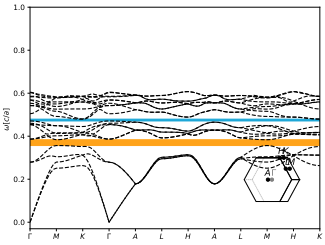

$\varepsilon = 16$, $\phi = 0.21$. (1) 7.52% gap between bands 4-5, and (2) 1.89% gap between bands 10-11.

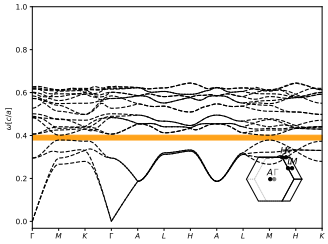

$\varepsilon = 14$, $\phi = 0.21$. 6.05% gap.

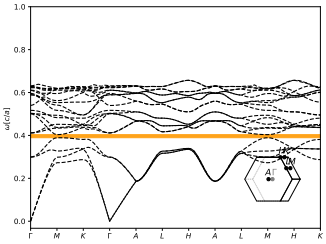

$\varepsilon = 12$, $\phi = 0.24$. 4.08% gap.

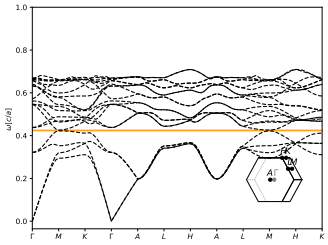

$\varepsilon = 10$, $\phi = 0.24$. 1.36% gap.

Inverse Ice Ih ($hP30$-H_5O_2), Bands 10 - 11

Structure file taken from `https://doi.org/10.1063/1.1699206`.

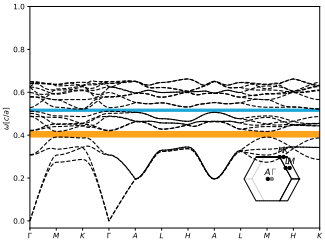

$\varepsilon = 16$, $\phi = 0.17$. (1) 6.68% gap between bands 4-5, and (2) 2.7% gap between bands 10-11.

Uranium Borohydride (tP20-UB_4), Bands 4 - 5

Structure file taken from `https://doi.org/10.1021/ic50118a027`.

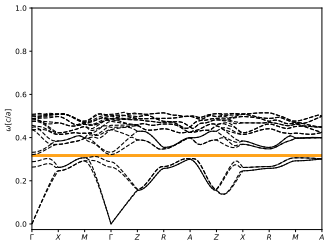

$\varepsilon = 14$, $\phi = 0.36$. 4.96% gap.

Chalkogenide With Pyrite Structure (tI16-$AlAgS_2$), Bands 8 - 9

Structure file taken from `https://doi.org/10.1002/zaac.19532710307`.

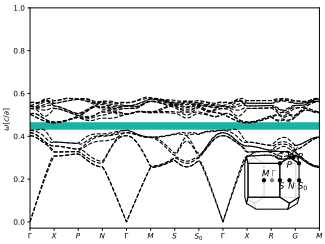

$\varepsilon = 16$, $\phi = 0.49$. 7.41% gap.

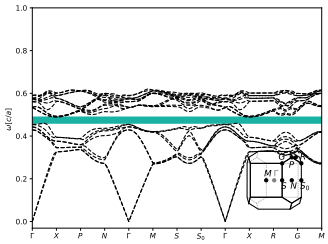

$\varepsilon = 14$, $\phi = 0.49$. 6.84% gap.

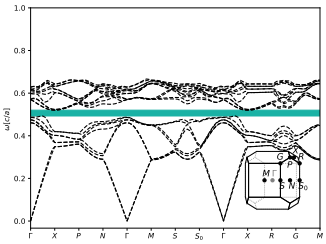

$\varepsilon = 12$, $\phi = 0.49$. 6.06% gap.

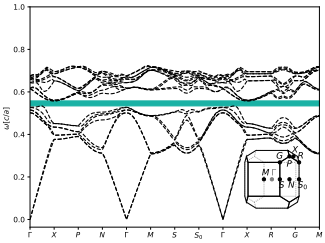

$\varepsilon = 10$, $\phi = 0.49$. 4.94% gap.

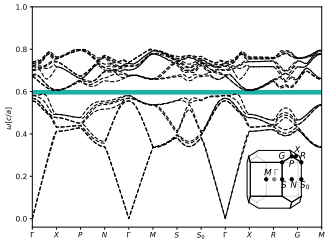

$\varepsilon = 8$, $\phi = 0.49$. 3.26% gap.

Inverse Heazlewoodite (hR5-Ni_3S_2), Bands 2 - 3

Structure file taken from `https://doi.org/10.1107/S0567740880005523`.

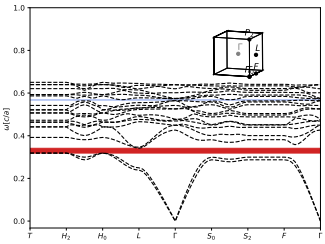

$\varepsilon = 16$, $\phi = 0.22$. 7.31% gap.

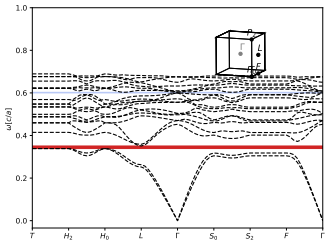

$\varepsilon = 14$, $\phi = 0.22$. 3.99% gap.

Hexadeuteriodi - amminedeuterium iodide (cP8-DIN$_6$), Bands 5 - 6

Structure file taken from `https://doi.org/10.1524/zkri.1992.200.3-4.225`.

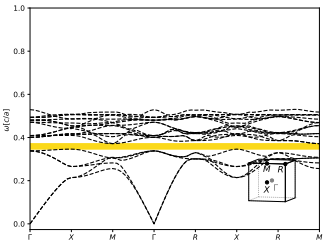

$\varepsilon = 16$, $\phi = 0.39$. 7.26% gap.

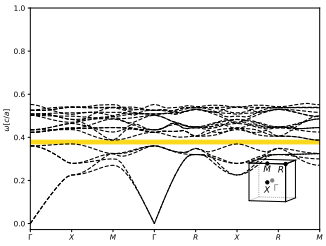

$\varepsilon = 14$, $\phi = 0.39$. 4.79% gap.

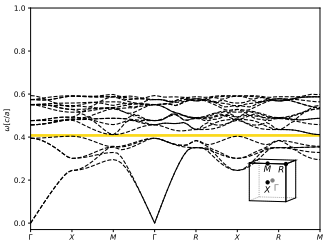

$\varepsilon = 12$, $\phi = 0.37$. 1.93% gap.

Inverse BCC (cI2-D), Bands 6 - 7

Structure file taken from `https://doi.org/10.1063/1.1727691`.

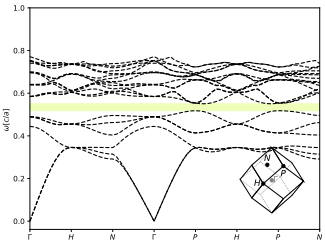

$\varepsilon = 16$, $\phi = 0.19$. 7.18% gap.

Inverse Ice Ih (hP20-H$_3$O), Bands 4 - 5

Structure file taken from `https://doi.org/10.1063/1.1765099`.

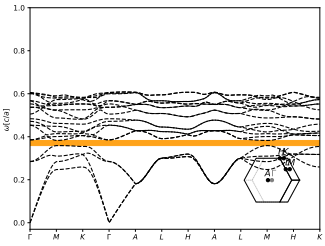

$\varepsilon = 16$, $\phi = 0.21$. 7.08% gap.

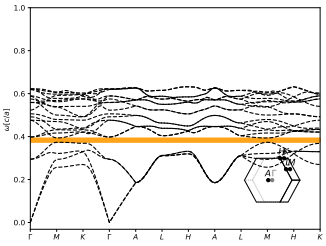

$\varepsilon = 14$, $\phi = 0.22$. 5.67% gap.

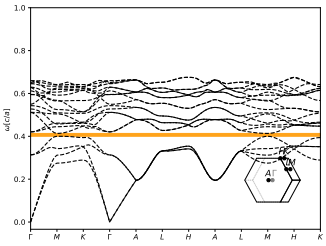

$\varepsilon = 12$, $\phi = 0.22$. 3.75% gap.

Inverse Ice Ih ($hP36$-H_2O), Bands 12 - 13
Structure file taken from `https://doi.org/10.1063/1.1749327`.

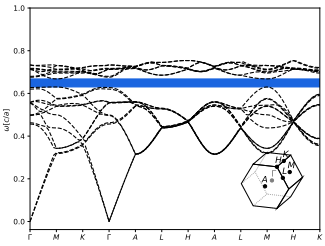

$\varepsilon = 16$, $\phi = 0.21$. 6.89% gap.

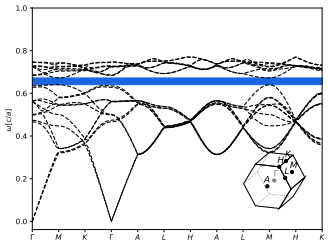

$\varepsilon = 14$, $\phi = 0.23$. 5.43% gap.

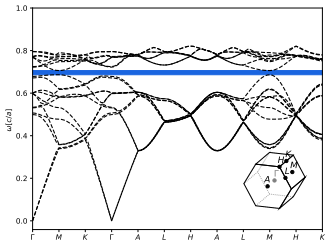

$\varepsilon = 12$, $\phi = 0.23$. 3.5% gap.

Inverse Ice Ih ($hP36$-H_2O), Bands 12 - 13
Structure file taken from `https://doi.org/10.1063/1.1749327`.

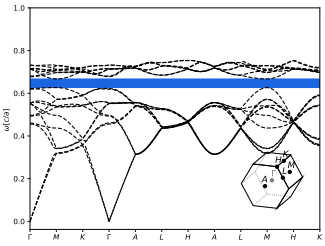

$\varepsilon = 16$, $\phi = 0.21$. 6.85% gap.

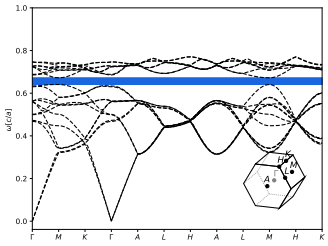

$\varepsilon = 14$, $\phi = 0.23$. 5.39% gap.

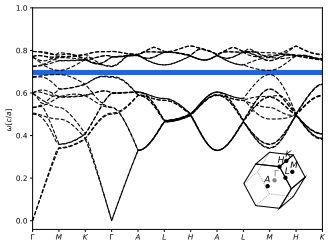

$\varepsilon = 12$, $\phi = 0.23$. 3.46% gap.

Inverse Copper Cadnium Germanium Sulfide ($oP16$-$CdCu_2GeS_4$), Bands 16 - 17
Structure file taken from `https://doi.org/10.1107/S0567740869003670`.

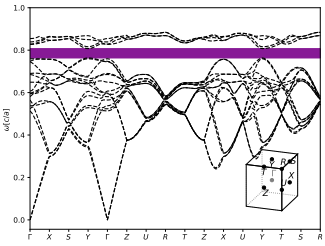

$\varepsilon = 16$, $\phi = 0.18$. 6.75% gap.

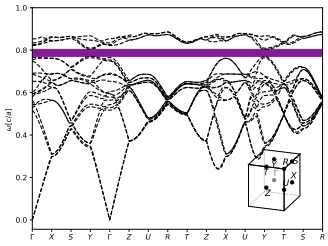

$\varepsilon = 14$, $\phi = 0.21$. 5.21% gap.

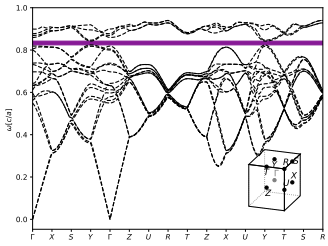

$\varepsilon = 12$, $\phi = 0.21$. 3.22% gap.

Aluminum Fluoride (cF288-$AlH_{2.25}O_{1.875}F_{1.5}$), Bands 8 - 9
Structure file taken from `https://doi.org/10.1021/ja01181a030`.

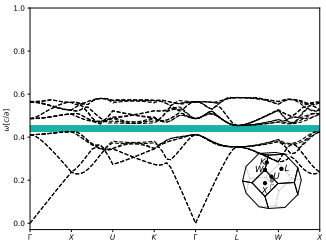

$\varepsilon = 16$, $\phi = 0.43$. 6.7% gap.

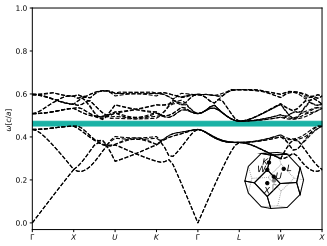

$\varepsilon = 14$, $\phi = 0.43$. 5.21% gap.

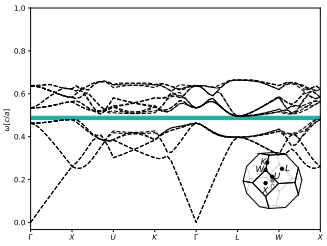

$\varepsilon = 12$, $\phi = 0.43$. 3.37% gap.

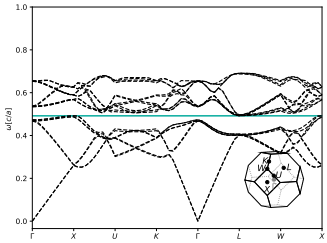

$\varepsilon = 10$, $\phi = 0.47$. 1.08% gap.

Beryllium Catena Phosphate (II) (mP36-BeP_2O_6), Bands 12 - 13
Structure file taken from `https://doi.org/10.1107/S0567740877011200`.

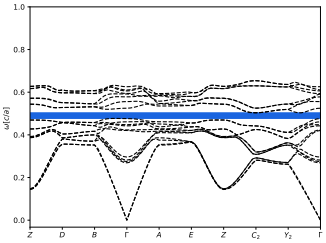

$\varepsilon = 16$, $\phi = 0.34$. 6.69% gap.

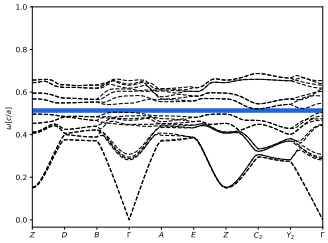

$\varepsilon = 14$, $\phi = 0.34$. 4.4% gap.

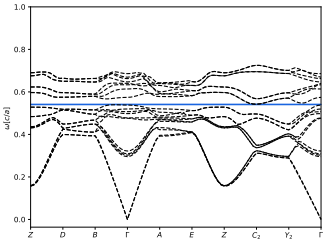

$\varepsilon = 12$, $\phi = 0.34$. 2.01% gap.

Aluminum Silicate (oI108-SiO_2), Bands 18 - 19
Structure file taken from `https://doi.org/10.1021/ja0292400`.

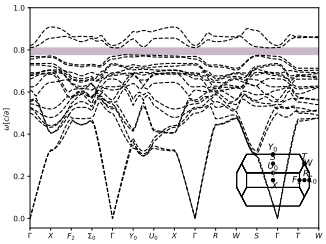

$\varepsilon = 16$, $\phi = 0.27$. 6.64% gap.

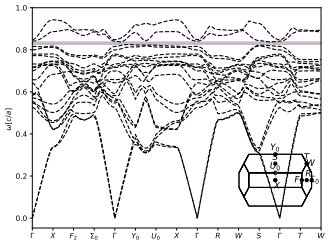

$\varepsilon = 14$, $\phi = 0.27$. 4.0% gap.

Inverse Erbium Oxide ($cI80$-Er_2O_3), Bands 12 - 13
Structure file taken from `https://doi.org/10.17188/1283440`.

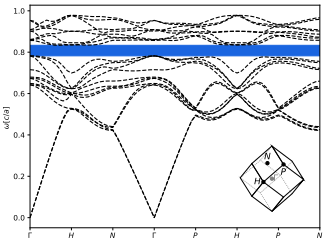

$\varepsilon = 16$, $\phi = 0.14$. 6.64% gap.

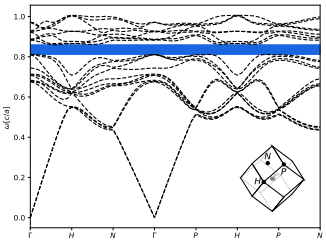

$\varepsilon = 14$, $\phi = 0.14$. 6.16% gap.

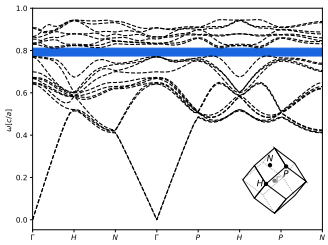

$\varepsilon = 12$, $\phi = 0.19$. 5.07% gap.

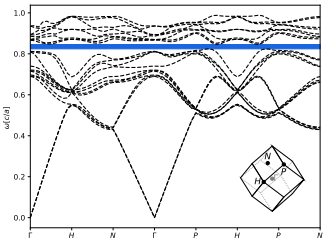

$\varepsilon = 10$, $\phi = 0.19$. 3.31% gap.

Inverse Cerium (alpha, HP) ($mC4$-Ce), Bands 16 - 17
Structure file taken from `https://doi.org/10.1107/S0567739477000321`.

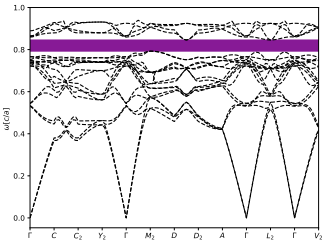

$\varepsilon = 16$, $\phi = 0.2$. 6.62% gap.

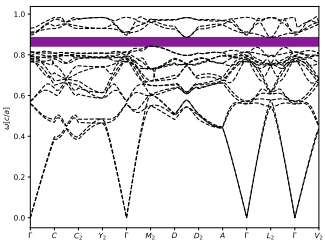

$\varepsilon = 14$, $\phi = 0.2$. 5.19% gap.

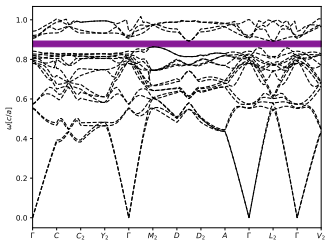

$\varepsilon = 12$, $\phi = 0.23$. 3.48% gap.

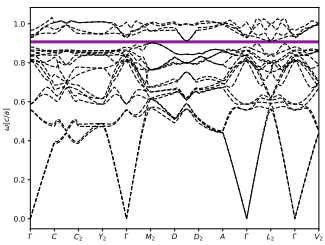

$\varepsilon = 10$, $\phi = 0.26$. 1.3% gap.

Mixed- metal Oxynitrides (cF88-$Pr_2Zr_2O_7$), Bands 2 - 3
Structure file taken from `https://doi.org/10.1021/ic902020r`.

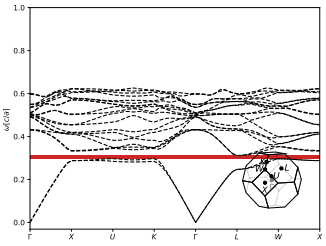

$\varepsilon = 16$, $\phi = 0.47$. 6.52% gap.

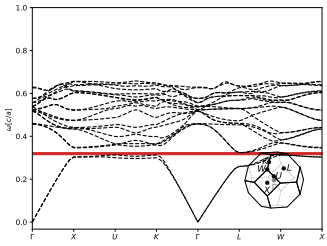

$\varepsilon = 14$, $\phi = 0.47$. 4.71% gap.

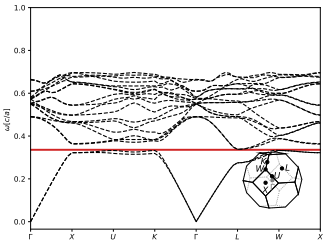

$\varepsilon = 12$, $\phi = 0.47$. 2.59% gap.

Inverse Sperrylite (cP12-As_2Pt), Bands 16 - 17
Structure file taken from `https://pubs.geoscienceworld.org/canmin/article/17/1/117/11304/the-crystal-structure-of-platarsite-pt-as-s-2-and`.

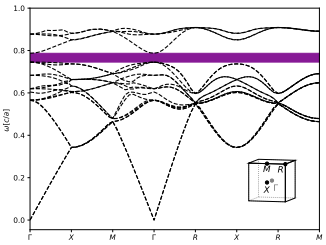

$\varepsilon = 16$, $\phi = 0.13$. 6.49% gap.

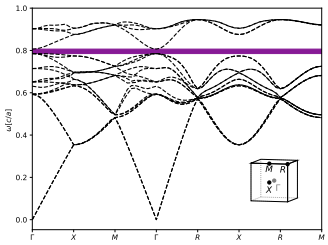

$\varepsilon = 14$, $\phi = 0.13$. 3.78% gap.

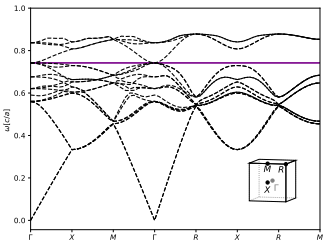

$\varepsilon = 12$, $\phi = 0.18$. 1.06% gap.

Inverse 2-Connected Hexagonal Diamond (hP20-ZnC_2N_2), Bands 4 - 5
Structure file taken from `https://doi.org/10.1021/ja4012707`.

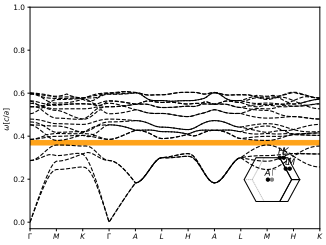

$\varepsilon = 16$, $\phi = 0.21$. 6.44% gap.

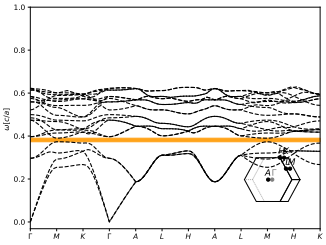

$\varepsilon = 14$, $\phi = 0.23$. 5.02% gap.

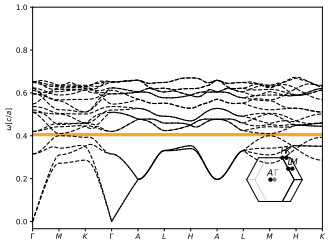

$\varepsilon = 12$, $\phi = 0.23$. 3.11% gap.

Inverse 2-Connected Hexagonal Diamond (hP20-ZnC_2N_2), Bands 10 - 11
Structure file taken from `https://doi.org/10.1021/ja4012707`.

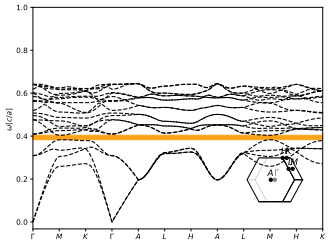

$\varepsilon = 16$, $\phi = 0.18$. (1) 5.74% gap between bands 4-5, and (2) 1.07% gap between bands 10-11.

Silicon (II) (cI16-Si), Bands 8 - 9
Structure file taken from `https://doi.org/10.1107/S0365110X64001840`.

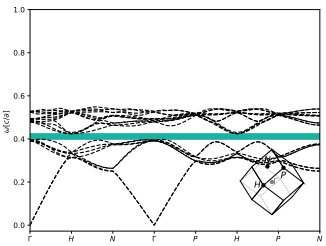

$\varepsilon = 16$, $\phi = 0.49$. 6.39% gap.

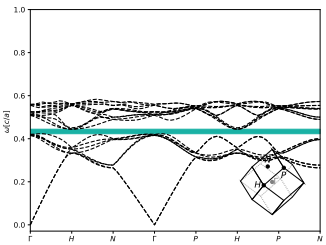

$\varepsilon = 14$, $\phi = 0.49$. 4.91% gap.

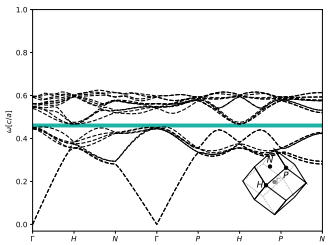

$\varepsilon = 12$, $\phi = 0.49$. 3.04% gap.

Inverse Tridymite 2H ($hP12$-SiO), Bands 4 - 5
Structure file taken from `https://doi.org/10.1524/zkri.1978.147.3-4.159`.

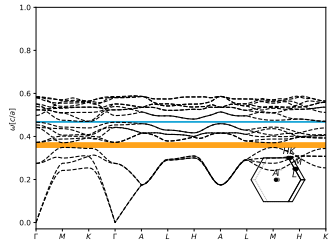

$\varepsilon = 16$, $\phi = 0.23$. (1) 6.38% gap between bands 4-5, and (2) 1.29% gap between bands 10-11.

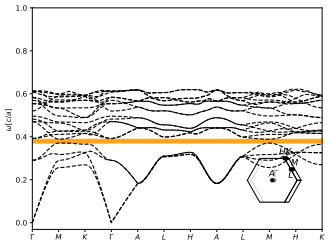

$\varepsilon = 14$, $\phi = 0.23$. 5.02% gap.

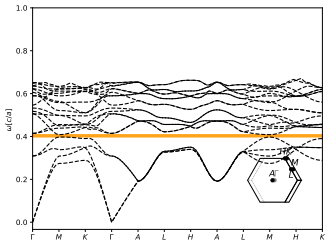

$\varepsilon = 12$, $\phi = 0.23$. 3.15% gap.

Inverse Tridymite 2H ($hP12$-SiO), Bands 10 - 11
Structure file taken from `https://doi.org/10.1524/zkri.1978.147.3-4.159`.

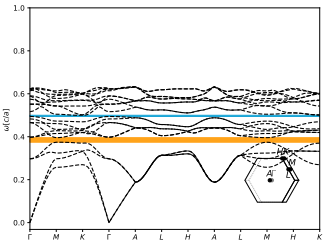

$\varepsilon = 16$, $\phi = 0.19$. (1) 6.11% gap between bands 4-5, and (2) 2.07% gap between bands 10-11.

Inverse Zeolite ITQ-34 ($oC672$-$Si_{0.91}Ge_{0.09}O_2$), Bands 8 - 9
Structure file taken from `https://doi.org/10.1021/ja806903c`.

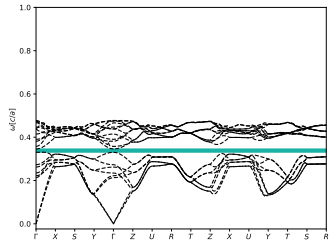

$\varepsilon = 16$, $\phi = 0.19$. 6.09% gap.

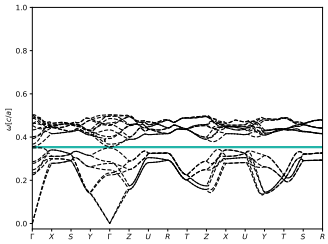

$\varepsilon = 14$, $\phi = 0.19$. 3.23% gap.

Manganese Yttrium (tI8-YMn_2), Bands 2 - 3

Structure file taken from `https://doi.org/10.1088/0953-8984/3/33/023`.

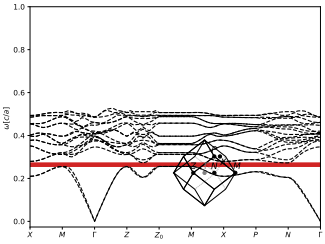

$\varepsilon = 16$, $\phi = 0.5$. 6.01% gap.

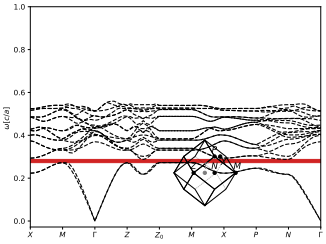

$\varepsilon = 14$, $\phi = 0.5$. 5.13% gap.

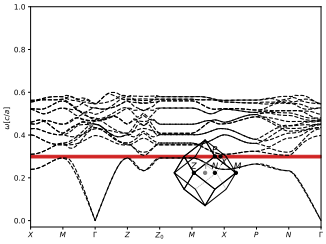

$\varepsilon = 12$, $\phi = 0.5$. 3.97% gap.

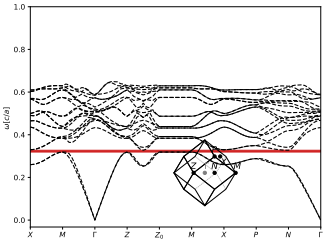

$\varepsilon = 10$, $\phi = 0.5$. 2.42% gap.

Manganese Yttrium (tI8-YMn_2), Bands 14 - 15

Structure file taken from `https://doi.org/10.1088/0953-8984/3/33/023`.

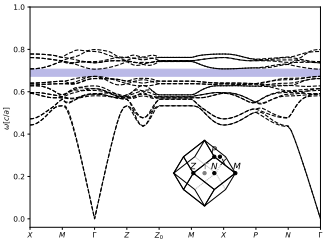

$\varepsilon = 16$, $\phi = 0.17$. 4.82% gap.

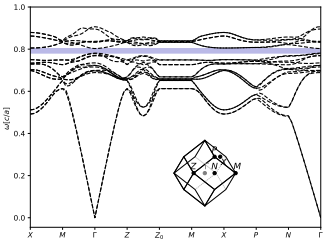

$\varepsilon = 14$, $\phi = 0.13$. 2.72% gap.

Inverse Silver Chlorate (VII) (cF24-$AgClO_4$), Bands 5 - 6
Structure file taken from `https://doi.org/10.1515/zkri-1930-0105`.

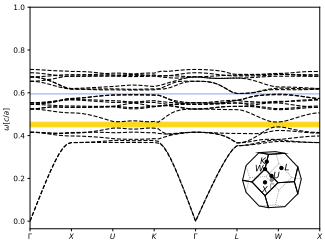

$\varepsilon = 16$, $\phi = 0.23$. (1) 6.01% gap between bands 5-6, and (2) 1.09% gap between bands 13-14.

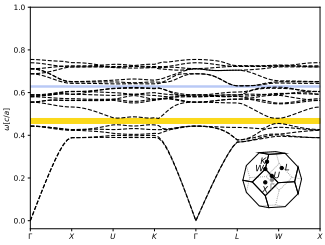

$\varepsilon = 14$, $\phi = 0.23$. (1) 5.96% gap between bands 5-6, and (2) 1.42% gap between bands 13-14.

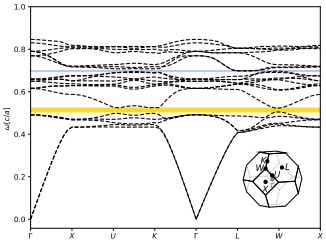

$\varepsilon = 12$, $\phi = 0.2$. 3.88% gap.

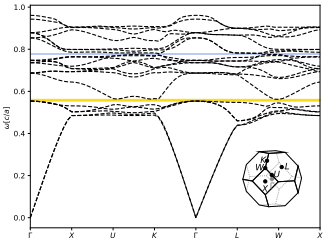

$\varepsilon = 10$, $\phi = 0.17$. 1.58% gap.

Inverse Silver Chlorate (VII) (cF24-$AgClO_4$), Bands 13 - 14
Structure file taken from `https://doi.org/10.1515/zkri-1930-0105`.

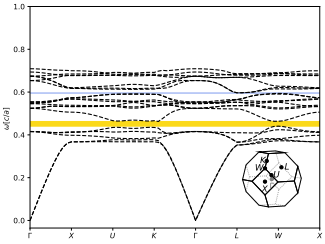

$\varepsilon = 16$, $\phi = 0.23$. (1) 6.01% gap between bands 5-6, and (2) 1.09% gap between bands 13-14.

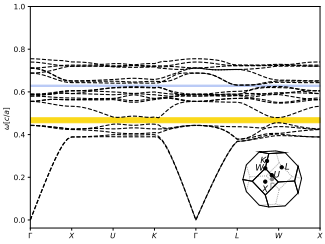

$\varepsilon = 14$, $\phi = 0.23$. (1) 5.96% gap between bands 5-6, and (2) 1.42% gap between bands 13-14.

Inverse Copper Iron Selenide ($tP16$-$FeCuSe_2$), Bands 16 - 17
Structure file taken from `https://doi.org/10.1007/BF02398194`.

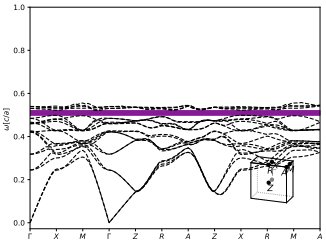

$\varepsilon = 16$, $\phi = 0.22$. 6.0% gap.

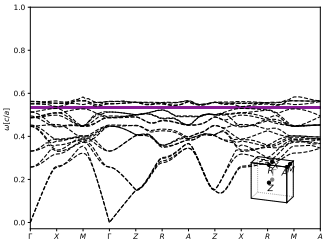

$\varepsilon = 14$, $\phi = 0.22$. 3.7% gap.

Lithium Oxide ($cF12$-Li_2O), Bands 8 - 9
Structure file taken from `https://doi.org/10.1021/ja066016s`.

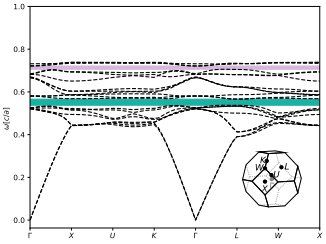

$\varepsilon = 14$, $\phi = 0.28$. (1) 5.09% gap between bands 8-9, and (2) 2.11% gap between bands 17-18.

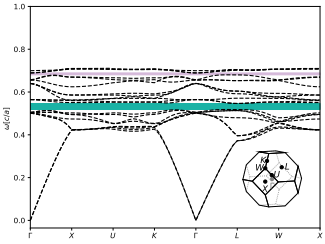

$\varepsilon = 14$, $\phi = 0.31$. (1) 5.05% gap between bands 8-9, and (2) 1.36% gap between bands 17-18.

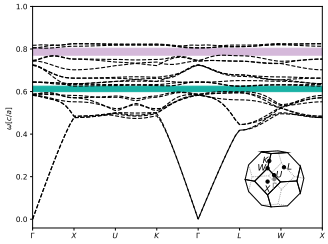

$\varepsilon = 12$, $\phi = 0.25$. (1) 4.15% gap between bands 8-9, and (2) 4.08% gap between bands 17-18.

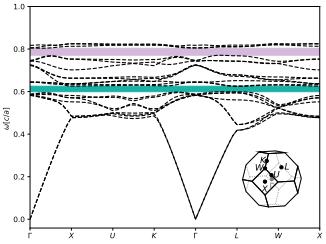

$\varepsilon = 12$, $\phi = 0.25$. (1) 4.15% gap between bands 8-9, and (2) 4.08% gap between bands 17-18.

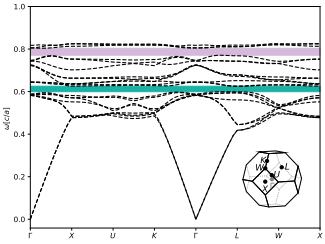

$\varepsilon = 12$, $\phi = 0.25$. (1) 4.15% gap between bands 8-9, and (2) 4.08% gap between bands 17-18.

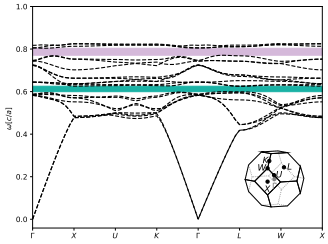

$\varepsilon = 12$, $\phi = 0.25$. (1) 4.15% gap between bands 8-9, and (2) 4.08% gap between bands 17-18.

Lithium Oxide (cF12-Li_2O), Bands 17 - 18
Structure file taken from `https://doi.org/10.1021/ja066016s`.

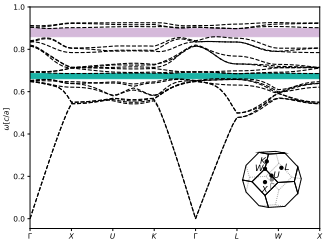

$\varepsilon = 14$, $\phi = 0.14$. (1) 3.48% gap between bands 8-9, and (2) 4.01% gap between bands 17-18.

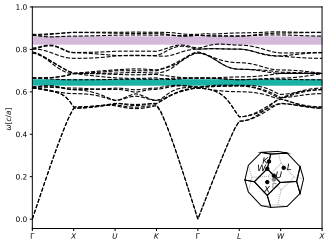

$\varepsilon = 14$, $\phi = 0.16$. (1) 3.83% gap between bands 8-9, and (2) 4.07% gap between bands 17-18.

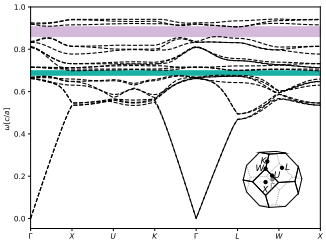

$\varepsilon = 12$, $\phi = 0.16$. (1) 2.95% gap between bands 8-9, and (2) 5.02% gap between bands 17-18.

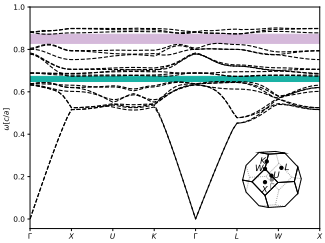

$\varepsilon = 12$, $\phi = 0.19$. (1) 3.5% gap between bands 8-9, and (2) 5.12% gap between bands 17-18.

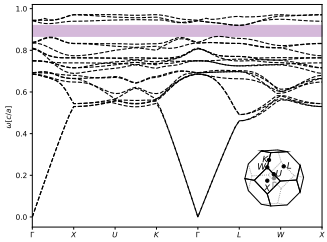

$\varepsilon = 10$, $\phi = 0.19$. 6.39% gap.

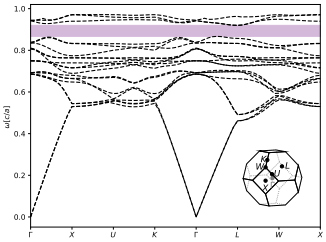

$\varepsilon = 10$, $\phi = 0.19$. 6.39% gap.

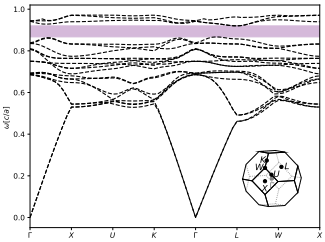

$\varepsilon = 10$, $\phi = 0.19$. 6.39% gap.

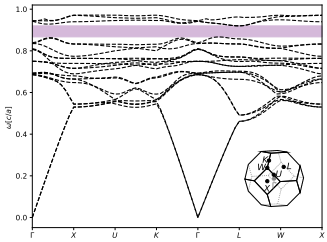

$\varepsilon = 10$, $\phi = 0.19$. 6.39% gap.

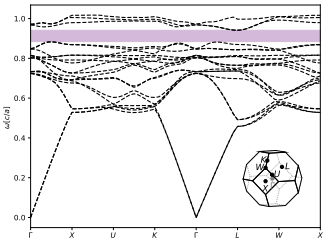

$\varepsilon = 8$, $\phi = 0.22$. 6.15% gap.

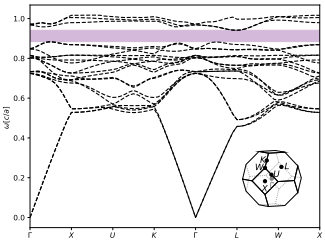

$\varepsilon = 8$, $\phi = 0.22$. 6.15% gap.

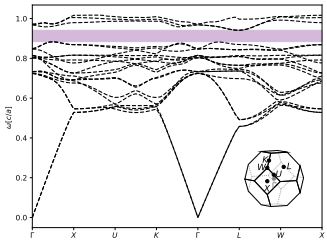

$\varepsilon = 8$, $\phi = 0.22$. 6.15% gap.

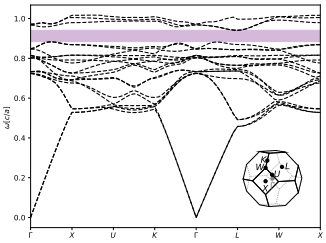

$\varepsilon = 8$, $\phi = 0.22$. 6.15% gap.

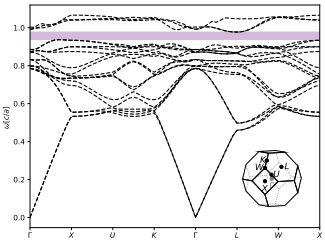

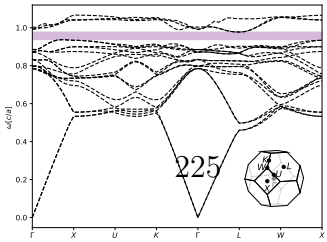

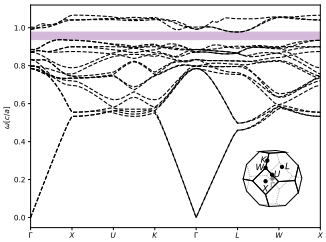

Beryllium Tellurate (cF48-Be_4TeO_7), Bands 10 - 11

Structure file taken from `https://doi.org/10.1107/S0567740877012606`.

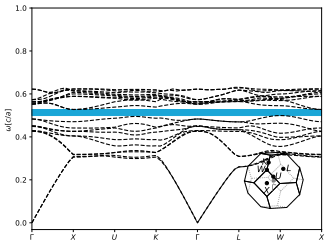

$\varepsilon = 16$, $\phi = 0.4$. 5.89% gap.

Inverse Plutonium (gamma) (oF8-Pu), Bands 12 - 13

Structure file taken from `https://doi.org/10.1107/S0365110X55001357`.

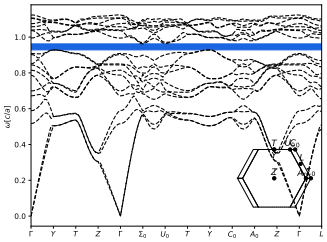

$\varepsilon = 16$, $\phi = 0.22$. 5.87% gap.

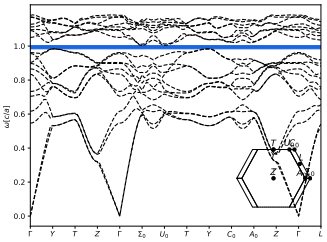

$\varepsilon = 14$, $\phi = 0.22$. 3.97% gap.

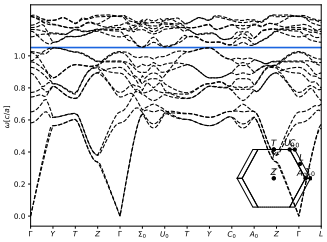

$\varepsilon = 12$, $\phi = 0.22$. 1.94% gap.

Inverse Pyrite (cP12-FeS_2), Bands 16 - 17

Structure file taken from `https://doi.org/10.17188/1183906`.

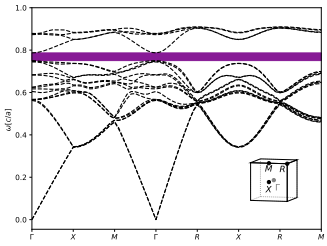

$\varepsilon = 16$, $\phi = 0.13$. 5.86% gap.

Inverse Hexachloroborazol (hR18-BNCl), Bands 5 - 6
Structure file taken from `https://doi.org/10.1107/S0567740871005235`.

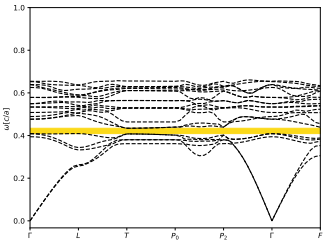

$\varepsilon = 16$, $\phi = 0.19$. 5.82% gap.

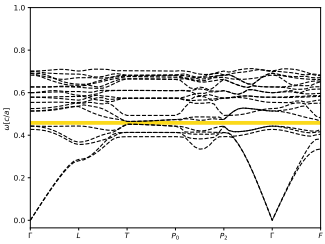

$\varepsilon = 14$, $\phi = 0.18$. 3.82% gap.

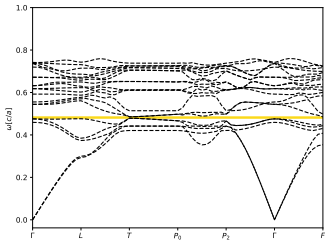

$\varepsilon = 12$, $\phi = 0.18$. 1.86% gap.

Inverse Ammonium Fluoride (hP12-H_2NF), Bands 4 - 5
Structure file taken from `https://doi.org/10.1107/S0567740870004624`.

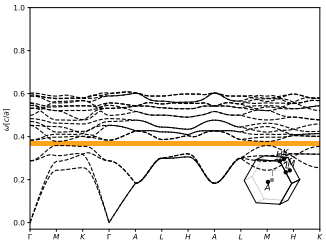

$\varepsilon = 16$, $\phi = 0.21$. 5.75% gap.

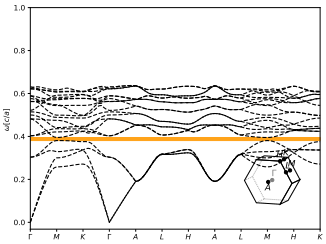

$\varepsilon = 14$, $\phi = 0.21$. 4.35% gap.

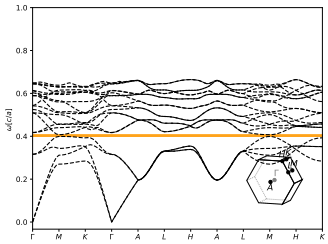

$\varepsilon = 12$, $\phi = 0.23$. 2.49% gap.

Inverse Potassium Sulfate -High-temperature Phase (hP22-$K_4S_3O_{12}$), Bands 16 - 17
Structure file taken from `https://doi.org/10.1107/S0567740880003779`.

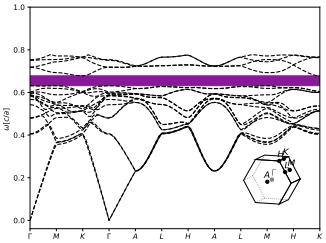

$\varepsilon = 16$, $\phi = 0.15$. 5.74% gap.

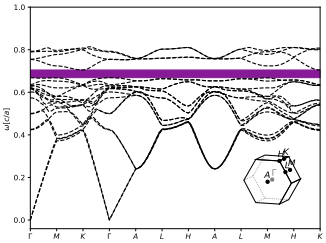

$\varepsilon = 14$, $\phi = 0.15$. 4.4% gap.

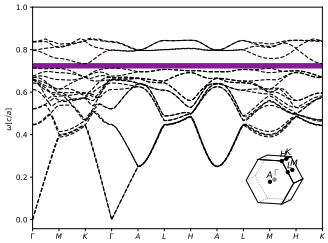

$\varepsilon = 12$, $\phi = 0.15$. 2.55% gap.

Inverse Chabazite (hR108-Si_2O_5), Bands 15 - 16

Structure file taken from `https://doi.org/10.1039/A804800B`.

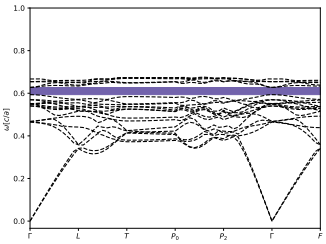

$\varepsilon = 16$, $\phi = 0.22$. 5.73% gap.

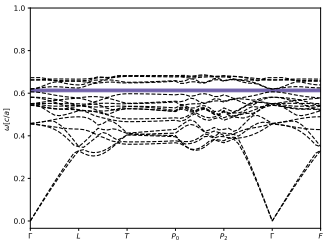

$\varepsilon = 14$, $\phi = 0.25$. 2.53% gap.

Inverse Zeolite ITQ-24 (oA336-SiO_2), Bands 4 - 5

Structure file taken from `https://doi.org/10.1021/ja0603599`.

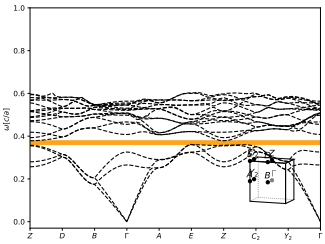

$\varepsilon = 16$, $\phi = 0.21$. 5.62% gap.

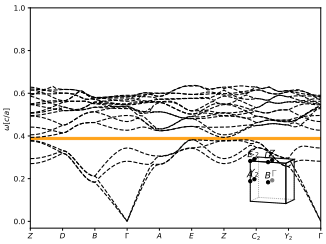

$\varepsilon = 14$, $\phi = 0.21$. 3.62% gap.

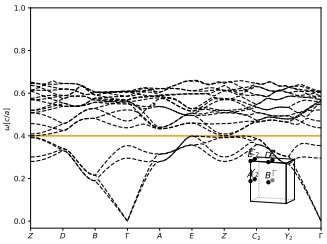

$\varepsilon = 12$, $\phi = 0.23$. 1.0% gap.

Inverse Lead Molybdate (Wulfenite) (tI2-$MoPbO_4$), Bands 8 - 9

Structure file taken from `https://doi.org/10.1021/ja01446a012`.

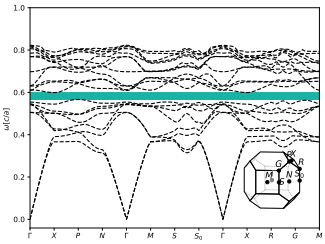

$\varepsilon = 16$, $\phi = 0.18$. 5.37% gap.

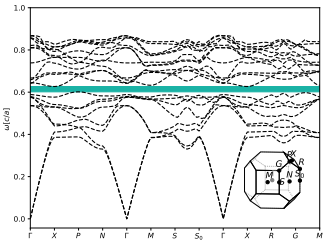

$\varepsilon = 14$, $\phi = 0.18$. 4.03% gap.

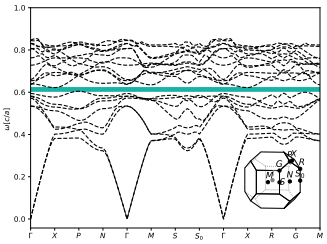

$\varepsilon = 12$, $\phi = 0.22$. 2.56% gap.

Vanadium Phosphate (V) (tI80-VP_2O_7), Bands 16 - 17

Structure file taken from `http://crystallography-online.com/structure/1530205`.

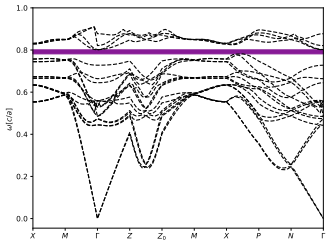

$\varepsilon = 16$, $\phi = 0.39$. 5.31% gap.

Inverse Sakhaite (cF264-$Ca_{24}Mg_8B_{16}C_8O_{73}$), Bands 8 - 9
Structure file taken from `http://icsd.kisti.re.kr/icsd/icsd_view1.jsp?board=icsd&num=6398&pg=399`.

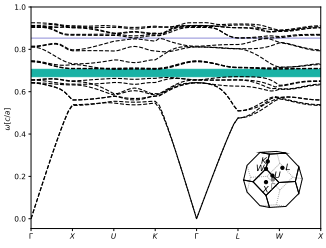

$\varepsilon = 16$, $\phi = 0.11$. 5.23% gap.

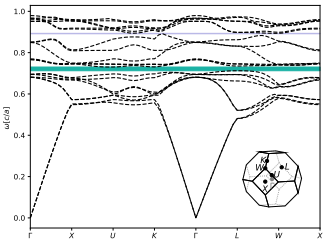

$\varepsilon = 14$, $\phi = 0.11$. (1) 2.68% gap between bands 8-9, and (2) 1.13% gap between bands 14-15.

Inverse Sakhaite (cF264-$Ca_{24}Mg_8B_{16}C_8O_{73}$), Bands 14 - 15
Structure file taken from `http://icsd.kisti.re.kr/icsd/icsd_view1.jsp?board=icsd&num=6398&pg=399`.

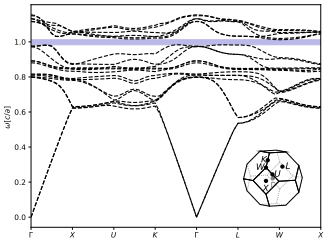

$\varepsilon = 16$, $\phi = 0.05$. (1) 1.05% gap between bands 8-9, and (2) 3.24% gap between bands 14-15.

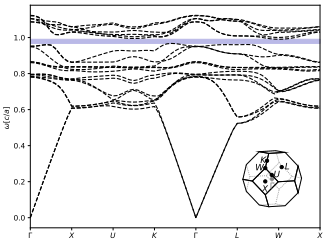

$\varepsilon = 14$, $\phi = 0.07$. 3.29% gap.

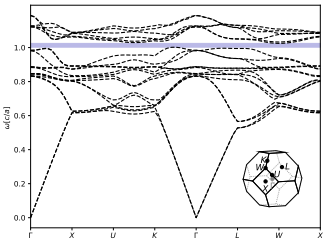

$\varepsilon = 12$, $\phi = 0.07$. 3.01% gap.

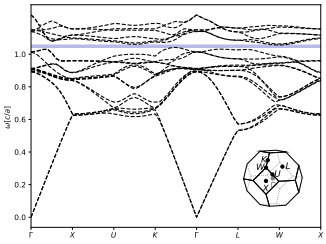

$\varepsilon = 10$, $\phi = 0.07$. 2.48% gap.

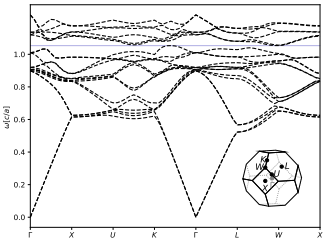

$\varepsilon = 8$, $\phi = 0.09$. 1.33% gap.

Ytterbium Indium Rhodium Tetracopper (cF24-$YbIn_{0.81}Cu_4Rh_{0.19}$), Bands 2 - 3

Structure file taken from `https://doi.org/10.1107/S1600536806029941`.

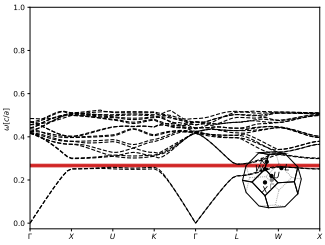

$\varepsilon = 16$, $\phi = 0.62$. 5.17% gap.

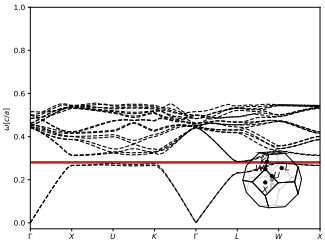

$\varepsilon = 14$, $\phi = 0.62$. 3.05% gap.

Inverse Clathrate II (cF136-Ge), Bands 8 - 9

Structure file taken from `https://doi.org/10.1002/anie.200800914`.

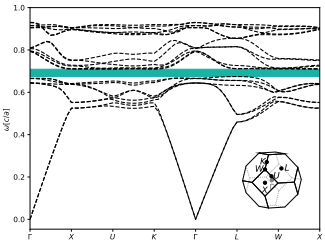

$\varepsilon = 16$, $\phi = 0.14$. 5.09% gap.

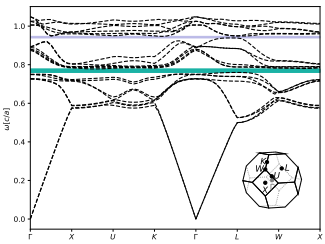

$\varepsilon = 14$, $\phi = 0.11$. 3.09% gap.

Inverse Clathrate II (cF136-Ge), Bands 14 - 15

Structure file taken from `https://doi.org/10.1002/anie.200800914`.

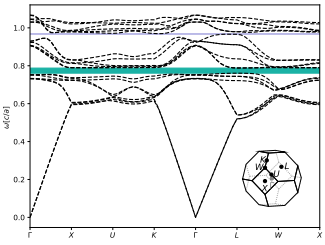

$\varepsilon = 16$, $\phi = 0.09$. (1) 3.67% gap between bands 8-9, and (2) 1.53% gap between bands 14-15.

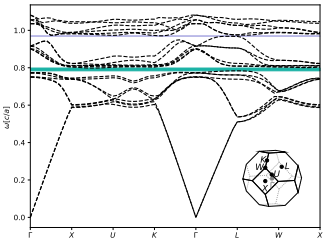

$\varepsilon = 14$, $\phi = 0.1$. (1) 3.0% gap between bands 8-9, and (2) 1.11% gap between bands 14-15.

Indium Phosphorous Chalkogenide ($tI12$-$InPS_4$), Bands 2 - 3

Structure file taken from `https://doi.org/10.1107/S0567740878005002`.

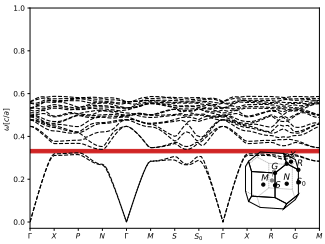

$\varepsilon = 16$, $\phi = 0.41$. 5.04% gap.

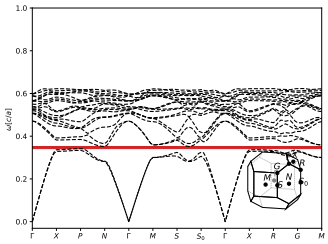

$\varepsilon = 14$, $\phi = 0.41$. 2.99% gap.

Silica Sodalite ($cI36$-SiO_2), Bands 14 - 15

Structure file taken from `https://doi.org/10.1016/j.micromeso.2011.10.042`.

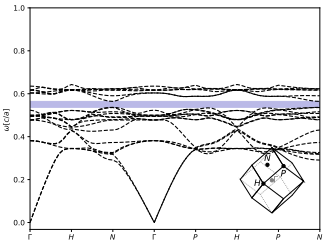

$\varepsilon = 16$, $\phi = 0.28$. 4.99% gap.

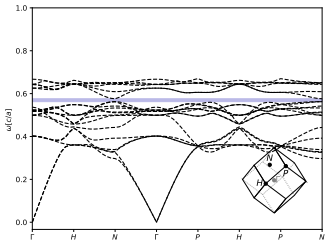

$\varepsilon = 14$, $\phi = 0.29$. 2.19% gap.

Inverse Orthorhombic Tridymite (HT) ($oC48$-SiO_2), Bands 8 - 9

Structure file taken from `https://doi.org/10.1107/S0365110X67003287`.

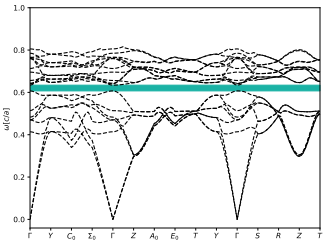

$\varepsilon = 16$, $\phi = 0.24$. 4.99% gap.

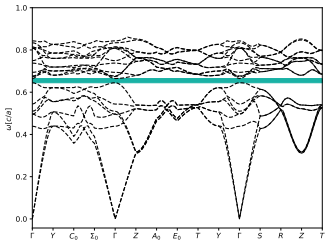

$\varepsilon = 14$, $\phi = 0.24$. 3.69% gap.

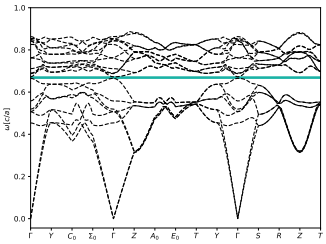

$\varepsilon = 12$, $\phi = 0.26$. 1.92% gap.

Inverse Gold Silver Selenide ($cI48$-Ag_3AuSe_2), Bands 2 - 3

Structure file taken from `https://doi.org/10.1002/zaac.19673560110`.

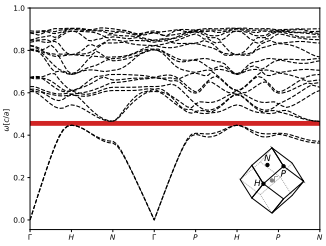

$\varepsilon = 16$, $\phi = 0.16$. 4.95% gap.

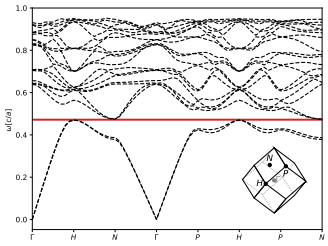

$\varepsilon = 14$, $\phi = 0.16$. 1.76% gap.

Sodium Diplatinum ($cF24$-$NaPt_2$), Bands 2 - 3

Structure file taken from `https://doi.org/10.1107/S0108270189000351`.

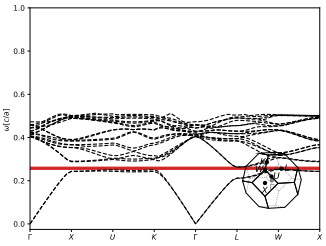

$\varepsilon = 16$, $\phi = 0.66$. 4.87% gap.

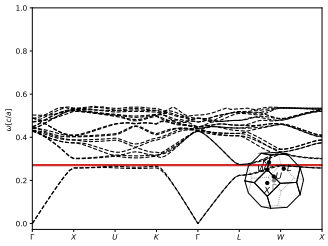

$\varepsilon = 14$, $\phi = 0.66$. 2.76% gap.

Hafnium Vanadide ($tI12$-HfV_2), Bands 2 - 3

Structure file taken from `https://doi.org/10.1107/S0108768100003633`.

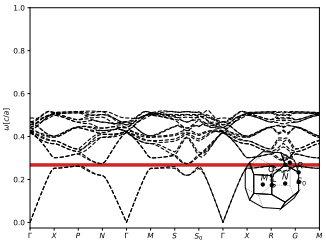

$\varepsilon = 16$, $\phi = 0.62$. 4.84% gap.

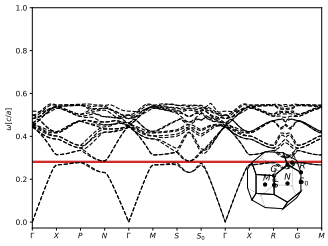

$\varepsilon = 14$, $\phi = 0.62$. 2.73% gap.

Inverse Beryllium Floride (hR108-Be_9F_{26}), Bands 15 - 16
Structure file taken from `https://doi.org/10.1021/ja8026967`.

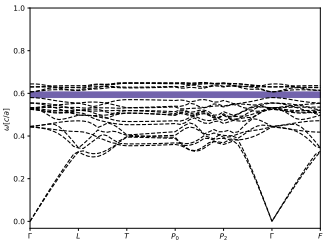

$\varepsilon = 16$, $\phi = 0.24$. 4.8% gap.

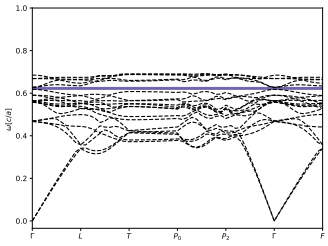

$\varepsilon = 14$, $\phi = 0.24$. 1.69% gap.

Copper Nitride (cP4-Cu_3N), Bands 2 - 3
Structure file taken from `https://doi.org/10.1016/j.ssc.2010.06.012`.

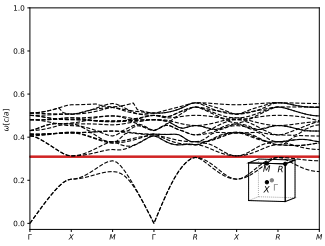

$\varepsilon = 16$, $\phi = 0.34$. 1.48% gap.

Copper Nitride (cP4-Cu_3N), Bands 14 - 15
Structure file taken from `https://doi.org/10.1016/j.ssc.2010.06.012`.

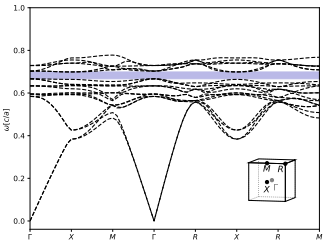

$\varepsilon = 16$, $\phi = 0.13$. 4.77% gap.

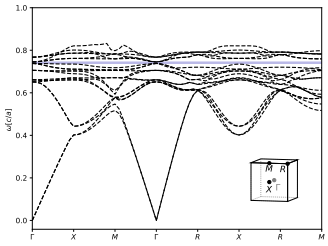

$\varepsilon = 14$, $\phi = 0.11$. 1.17% gap.

Silver Cadmium Gallium Sulfide ($oP16$-Cd_2GaAgS_4), Bands 16 - 17
Structure file taken from `https://doi.org/10.1107/S1600536805012341`.

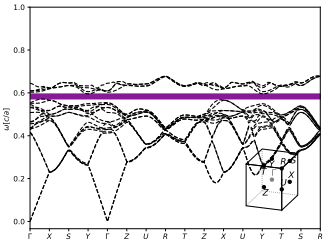

$\varepsilon = 16$, $\phi = 0.43$. 4.69% gap.

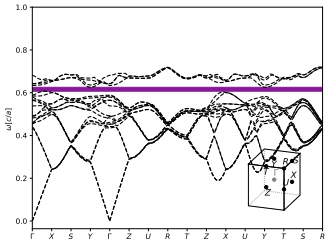

$\varepsilon = 14$, $\phi = 0.43$. 3.58% gap.

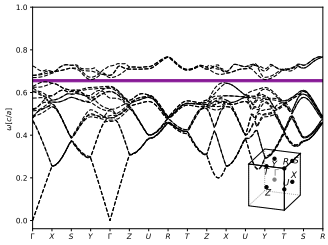

$\varepsilon = 12$, $\phi = 0.43$. 2.09% gap.

Inverse Dicopper (I) Zinc Silicon Tetrasulfide ($oP16$-$ZnSiCu_2S_4$), Bands 16 - 17
Structure file taken from `https://doi.org/10.1107/S1600536811008889`.

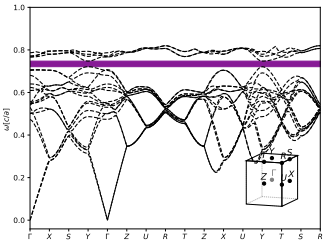

$\varepsilon = 16$, $\phi = 0.22$. 4.67% gap.

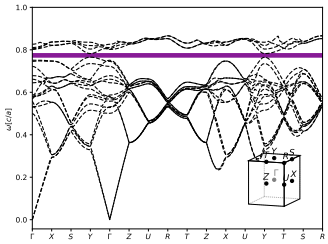

$\varepsilon = 14$, $\phi = 0.22$. 3.34% gap.

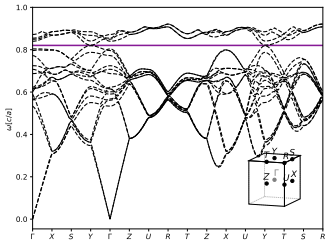

$\varepsilon = 12$, $\phi = 0.22$. 1.5% gap.

Inverse Caesium Duo-disulfate ($hP20$-$CsSO_3$), Bands 12 - 13
Structure file taken from `https://doi.org/10.1515/zpch-1932-1825`.

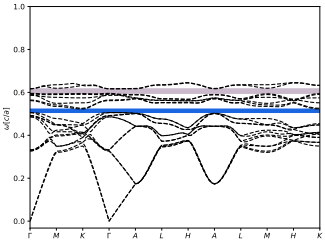

$\varepsilon = 16$, $\phi = 0.23$. (1) 4.65% gap between bands 12-13, and (2) 3.19% gap between bands 18-19.

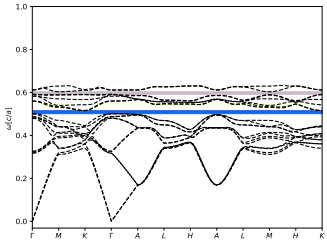

$\varepsilon = 14$, $\phi = 0.23$. (1) 3.69% gap between bands 12-13, and (2) 2.82% gap between bands 18-19.

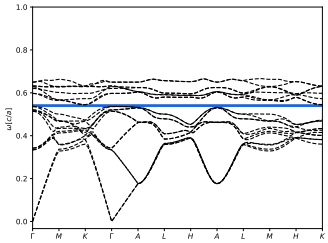

$\varepsilon = 12$, $\phi = 0.23$. 2.38% gap.

Inverse Caesium Duo-disulfate (hP20-$CsSO_3$), Bands 18 - 19

Structure file taken from `https://doi.org/10.1515/zpch-1932-1825`.

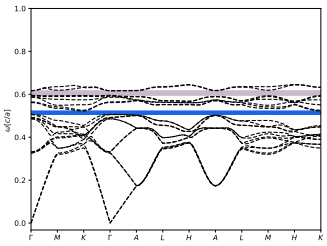

$\varepsilon = 16$, $\phi = 0.19$. (1) 4.52% gap between bands 12-13, and (2) 3.19% gap between bands 18-19.

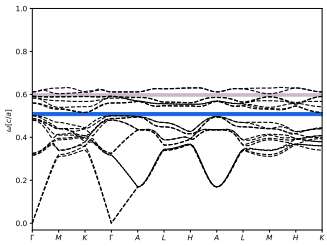

$\varepsilon = 14$, $\phi = 0.23$. (1) 3.69% gap between bands 12-13, and (2) 2.82% gap between bands 18-19.

Inverse Scandium Oxide (cI80-Sc_2O_3), Bands 12 - 13

Structure file taken from `https://doi.org/10.17188/1197026`.

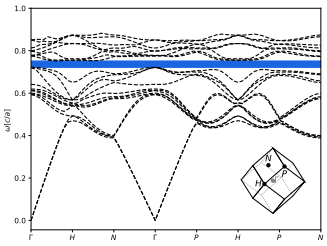

$\varepsilon = 16$, $\phi = 0.18$. 4.62% gap.

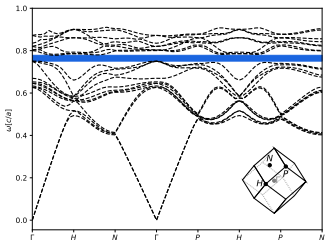

$\varepsilon = 14$, $\phi = 0.18$. 4.05% gap.

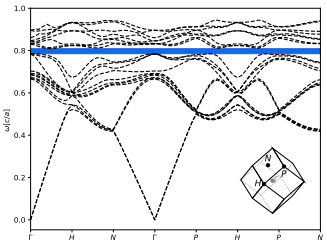

$\varepsilon = 12$, $\phi = 0.18$. 3.4% gap.

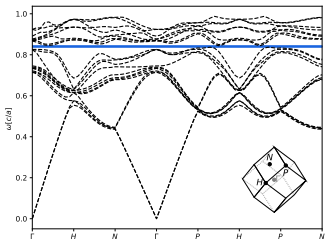

$\varepsilon = 10$, $\phi = 0.18$. 1.45% gap.

Trisilver Vanadate (beta) (tI16-VAg_3O_4), Bands 8 - 9
Structure file taken from `https://doi.org/10.1021/cm301119c`.

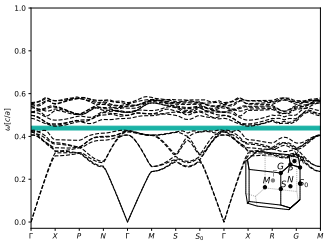

$\varepsilon = 16$, $\phi = 0.51$. 4.61% gap.

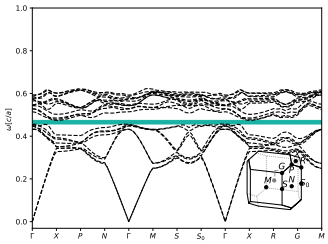

$\varepsilon = 14$, $\phi = 0.51$. 4.12% gap.

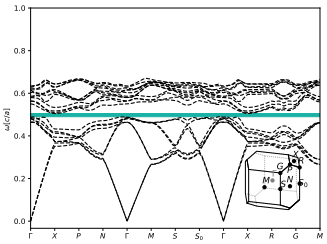

$\varepsilon = 12$, $\phi = 0.51$. 3.45% gap.

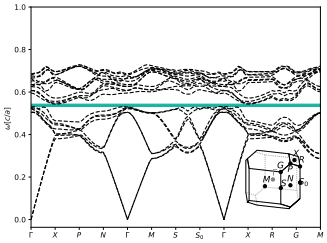

$\varepsilon = 10$, $\phi = 0.51$. 2.5% gap.

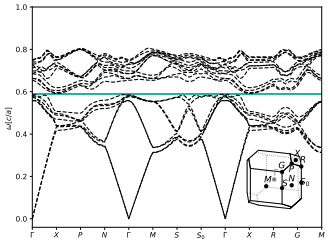

$\varepsilon = 8$, $\phi = 0.51$. 1.07% gap.

Copper Chloride (cP16-CuBr), Bands 16 - 17
Structure file taken from `https://doi.org/10.1103/PhysRevB.50.5868`.

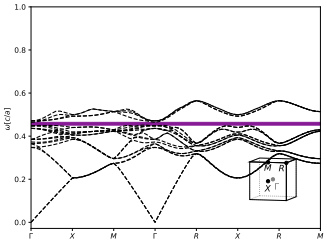

$\varepsilon = 16$, $\phi = 0.52$. 4.6% gap.

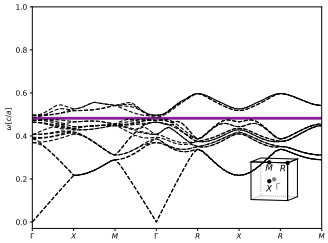

$\varepsilon = 14$, $\phi = 0.52$. 3.42% gap.

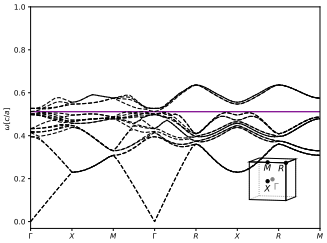

$\varepsilon = 12$, $\phi = 0.52$. 2.09% gap.

Inverse Silver Cadmium Gallium Sulfide (oP16-Cd_2GaAgS_4), Bands 16 - 17
Structure file taken from `https://doi.org/10.1107/S1600536805012341`.

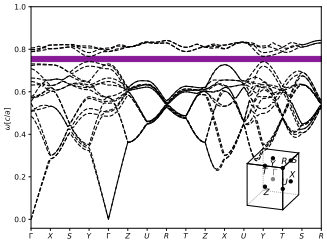

$\varepsilon = 16$, $\phi = 0.21$. 4.57% gap.

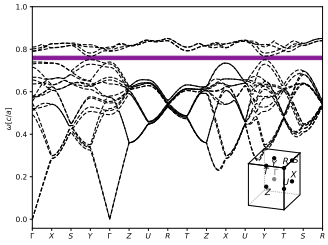

$\varepsilon = 14$, $\phi = 0.23$. 3.19% gap.

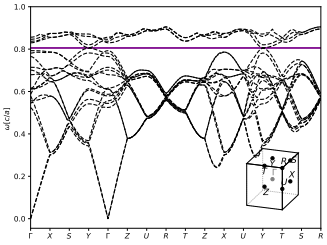

$\varepsilon = 12$, $\phi = 0.23$. 1.36% gap.

Inverse Zeolite With Three- dimensional Intersecting Straight- channel ($tP96$-SiO_2), Bands 2 - 3

Structure file taken from `https://doi.org/10.1021/ja0107778`.

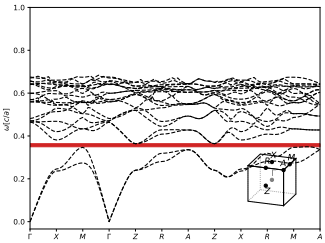

$\varepsilon = 16$, $\phi = 0.17$. 4.49% gap.

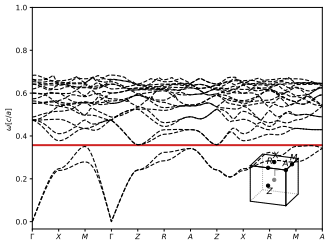

$\varepsilon = 14$, $\phi = 0.19$. 1.27% gap.

Pyrochlore- like ($cF72$-$CsAl_{0.38}Te_{1.62}O_6$), Bands 2 - 3

Structure file taken from `https://doi.org/10.1021/ic200574v`.

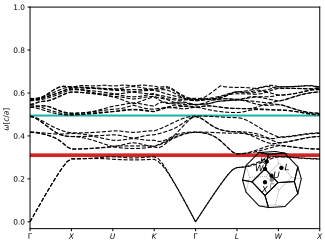

$\varepsilon = 16$, $\phi = 0.45$. (1) 4.46% gap between bands 2-3, and (2) 2.02% gap between bands 8-9.

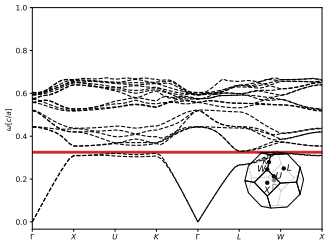

$\varepsilon = 14$, $\phi = 0.45$. 2.99% gap.

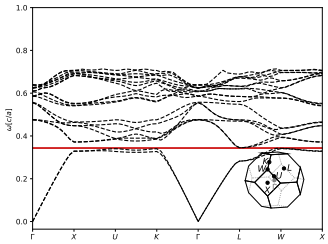

$\varepsilon = 12$, $\phi = 0.45$. 1.19% gap.

Pyrochlore- like ($cF72$-$CsAl_{0.38}Te_{1.62}O_6$), Bands 8 - 9

Structure file taken from `https://doi.org/10.1021/ic200574v`.

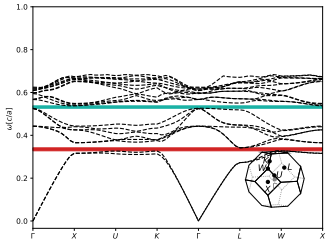

$\varepsilon = 16$, $\phi = 0.38$. (1) 4.21% gap between bands 2-3, and (2) 2.83% gap between bands 8-9.

Dicopper (I) Zinc Silicon Tetrasulfide ($oP16$-$ZnSiCu_2S_4$), Bands 16 - 17
Structure file taken from `https://doi.org/10.1107/S1600536811008889`.

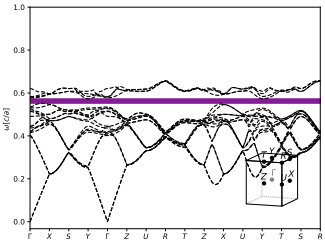

$\varepsilon = 16$, $\phi = 0.45$. 4.41% gap.

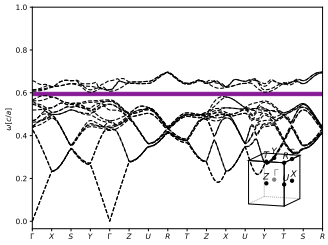

$\varepsilon = 14$, $\phi = 0.45$. 3.33% gap.

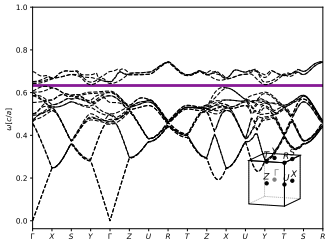

$\varepsilon = 12$, $\phi = 0.45$. 1.87% gap.

Pyrochlore- Related Cesium Tellurium Oxide ($oP44$-Te_4CO_6), Bands 4 - 5
Structure file taken from `https://doi.org/10.1021/ic2010375`.

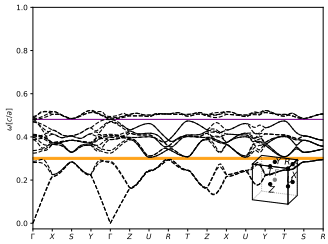

$\varepsilon = 16$, $\phi = 0.46$. 4.32% gap.

Pyrochlore- Related Cesium Tellurium Oxide ($oP44$-Te_4CO_6), Bands 16 - 17
Structure file taken from `https://doi.org/10.1021/ic2010375`.

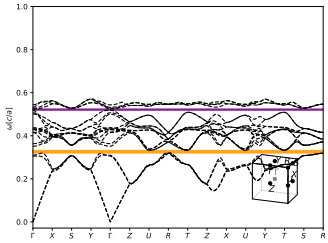

$\varepsilon = 16$, $\phi = 0.4$. (1) 4.09% gap between bands 4-5, and (2) 1.59% gap between bands 16-17.

Inverse High- temperature Order- disorder Transition In Cocr2se4 (cF56-$Cr_2Co_{0.2}Cu_{0.8}Se_4$), Bands 8 - 9
Structure file taken from `https://doi.org/10.1021/ic900264x`.

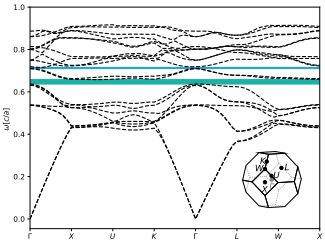

$\varepsilon = 16$, $\phi = 0.16$. 4.32% gap.

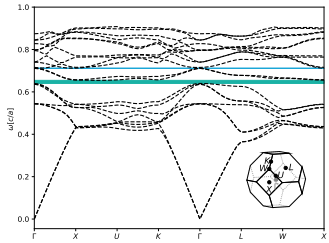

$\varepsilon = 14$, $\phi = 0.19$. 3.0% gap.

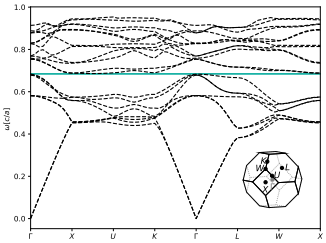

$\varepsilon = 12$, $\phi = 0.19$. 1.33% gap.

Inverse Aluminum Fluoride (cF288-$AlH_{2.25}O_{1.875}F_{1.5}$), Bands 8 - 9
Structure file taken from `https://doi.org/10.1021/ja01181a030`.

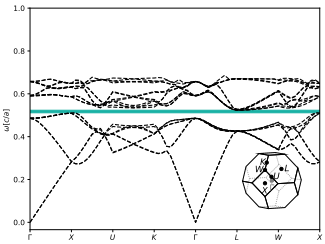

$\varepsilon = 16$, $\phi = 0.25$. 4.31% gap.

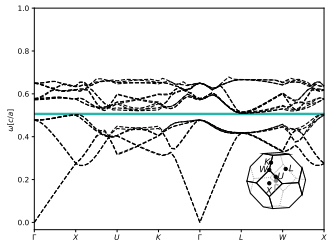

$\varepsilon = 14$, $\phi = 0.29$. 3.1% gap.

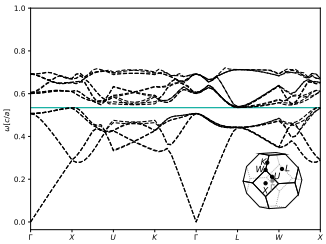

$\varepsilon = 12$, $\phi = 0.29$. 1.97% gap.

Zirconium Tungstate (cP44-ZrW_2O_8), Bands 16 - 17
Structure file taken from `https://doi.org/10.1107/S0108270195001545`.

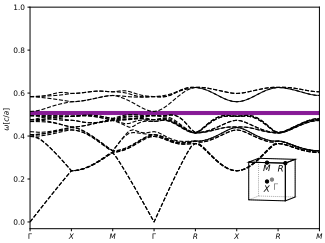

$\varepsilon = 16$, $\phi = 0.41$. 4.3% gap.

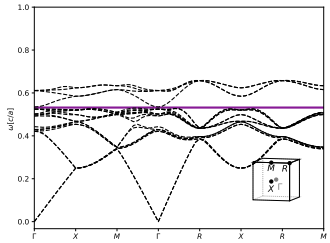

$\varepsilon = 14$, $\phi = 0.41$. 2.27% gap.

Inverse Silicon Phosphide ($cP12$-SiP_2), Bands 16 - 17

Structure file taken from `https://doi.org/10.1524/zkri.1984.167.14.1.`.

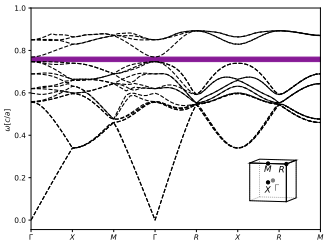

$\varepsilon = 16$, $\phi = 0.14$. 4.24% gap.

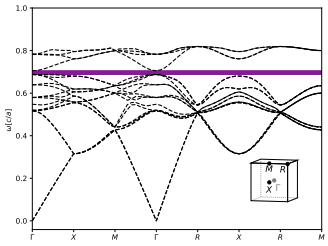

$\varepsilon = 14$, $\phi = 0.19$. 2.18% gap.

Inverse Gold Silver Selenide ($cI48$-Ag_3AuSe_2), Bands 2 - 3

Structure file taken from `http://crystallography-online.com/structure/1509884`.

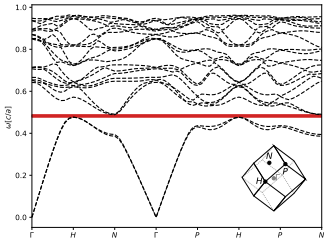

$\varepsilon = 16$, $\phi = 0.13$. 4.15% gap.

Inverse Hydrogen Peroxide ($tP16$-HO), Bands 12 - 13

Structure file taken from `https://doi.org/10.1021/ja00524a012`.

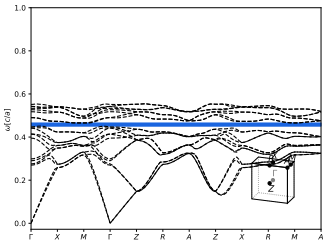

$\varepsilon = 16$, $\phi = 0.23$. 4.08% gap.

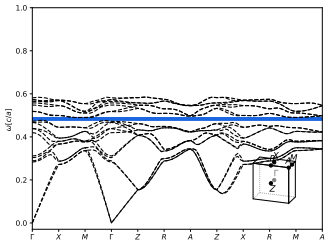

$\varepsilon = 14$, $\phi = 0.23$. 3.61% gap.

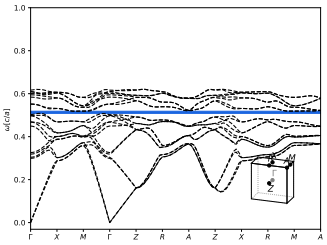

$\varepsilon = 12$, $\phi = 0.23$. 2.91% gap.

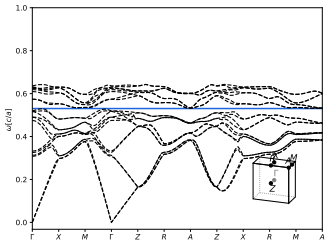

$\varepsilon = 10$, $\phi = 0.25$. 1.27% gap.

Calcium Boride (cP7-SiB_6), Bands 5 - 6

Structure file taken from `https://doi.org/10.17188/1299378`.

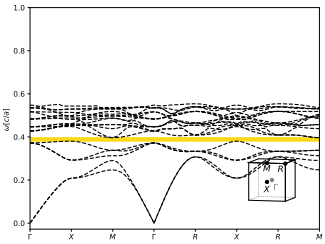

$\varepsilon = 16$, $\phi = 0.34$. 4.07% gap.

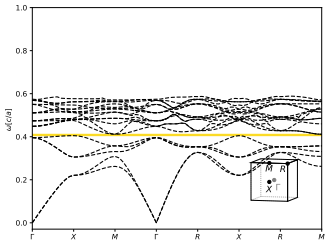

$\varepsilon = 14$, $\phi = 0.34$. 1.52% gap.

High- temperature Order- disorder Transition In Cocr2se4 (cF56-$Cr_2Co_{0.2}Cu_{0.8}Se_4$), Bands 18 - 19

Structure file taken from `https://doi.org/10.1021/ic900264x`.

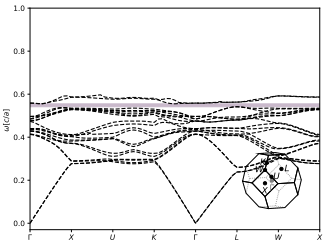

$\varepsilon = 16$, $\phi = 0.51$. 3.92% gap.

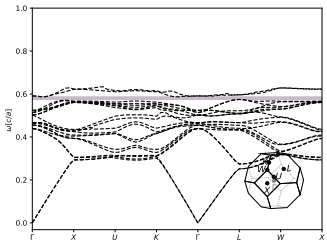

$\varepsilon = 14$, $\phi = 0.51$. 3.44% gap.

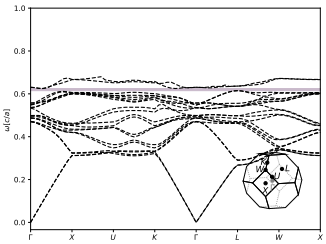

$\varepsilon = 12$, $\phi = 0.51$. 2.79% gap.

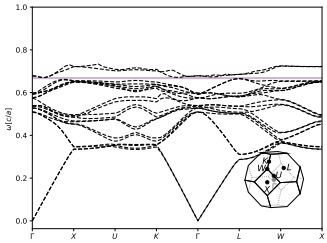

$\varepsilon = 10$, $\phi = 0.51$. 1.83% gap.

Inverse Titanium Tellerium Oxide (cI96-$TiTe_3O_8$), Bands 12 - 13

Structure file taken from `https://doi.org/10.1107/S0567740871002620`.

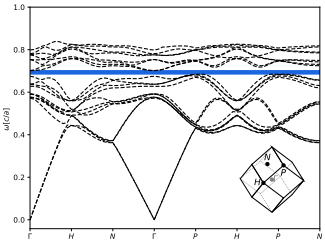

$\varepsilon = 16$, $\phi = 0.21$. 3.9% gap.

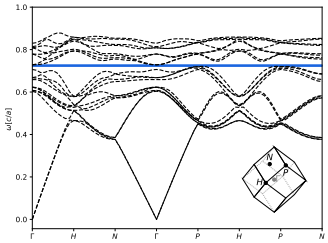

$\varepsilon = 14$, $\phi = 0.21$. 2.45% gap.

Aluminum Silver Disulfide ($hP4$-$AlAgS_2$), Bands 18 - 19
Structure file taken from `https://doi.org/10.1515/znb-1974-3-411`.

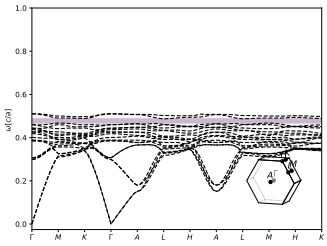

$\varepsilon = 16$, $\phi = 0.32$. 3.9% gap.

Inverse Thiospinelle ($tI28$-Fe_2SnS_4), Bands 8 - 9
Structure file taken from `https://doi.org/10.1107/S0567740877012205`.

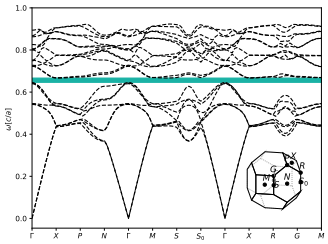

$\varepsilon = 16$, $\phi = 0.16$. 3.89% gap.

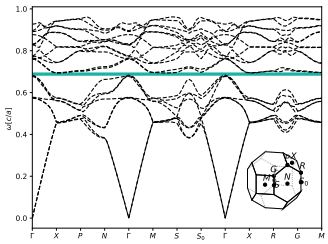

$\varepsilon = 14$, $\phi = 0.16$. 2.5% gap.

Inverse Erbium Iron Deuteride ($cF120$-$Er_8Fe_{16}D_{23.52}$), Bands 11 - 12
Structure file taken from `https://doi.org/10.1016/j.jallcom.2012.05.107`.

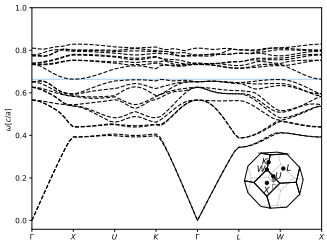

$\varepsilon = 12$, $\phi = 0.26$. 1.23% gap.

Inverse Erbium Iron Deuteride (cF120-$Er_8Fe_{16}D_{23.52}$), Bands 16 - 17
Structure file taken from `https://doi.org/10.1016/j.jallcom.2012.05.107`.

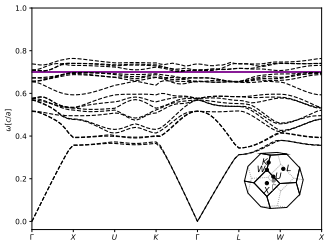

$\varepsilon = 12$, $\phi = 0.33$. 1.35% gap.

Silicon Nitride (beta) (hP14-SiN_2), Bands 10 - 11
Structure file taken from `https://doi.org/10.1107/S0567740879004933`.

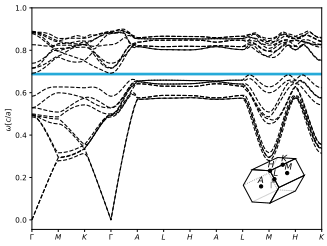

$\varepsilon = 16$, $\phi = 0.34$. 3.87% gap.

Cadium (alpha) (oP12-CdP_2), Bands 12 - 13
Structure file taken from `https://doi.org/10.1107/S0567740869005723`.

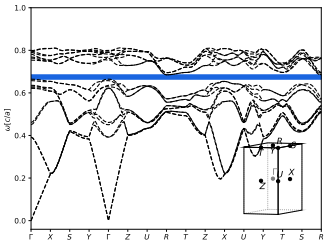

$\varepsilon = 16$, $\phi = 0.46$. 3.85% gap.

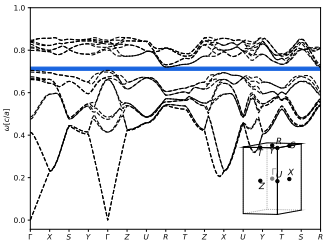

$\varepsilon = 14$, $\phi = 0.46$. 2.95% gap.

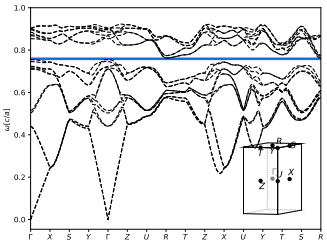

$\varepsilon = 12$, $\phi = 0.46$. 1.74% gap.

Rubidium Nitrate (V) - HT (cP33-$RbNO_3$), Bands 5 - 6
Structure file taken from `https://doi.org/10.1107/S0108270187095660`.

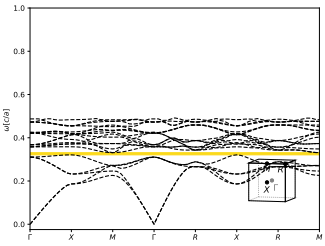

$\varepsilon = 16$, $\phi = 0.49$. 3.82% gap.

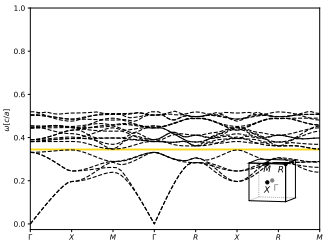

$\varepsilon = 14$, $\phi = 0.49$. 1.85% gap.

Rubidium Nitrate (V) - HT (cP33-$RbNO_3$), Bands 16 - 17
Structure file taken from `https://doi.org/10.1107/S0108270187095660`.

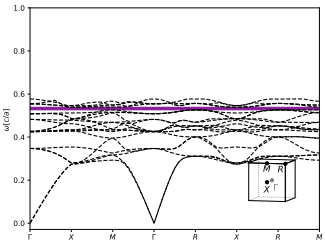

$\varepsilon = 16$, $\phi = 0.32$. 2.59% gap.

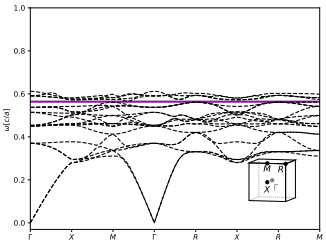

$\varepsilon = 14$, $\phi = 0.32$. 2.23% gap.

Inverse Tin (HP) (oI2-Sn), Bands 6 - 7
Structure file taken from `https://doi.org/10.1103/PhysRevB.88.104104`.

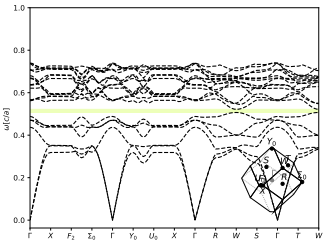

$\varepsilon = 16$, $\phi = 0.2$. 3.68% gap.

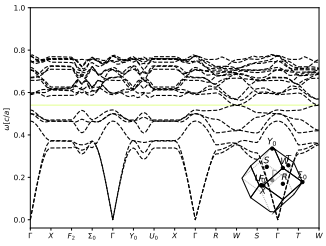

$\varepsilon = 14$, $\phi = 0.2$. 1.16% gap.

Silicon (XII, HP) ($hR8$-Si), Bands 8 - 9

Structure file taken from `https://doi.org/10.1103/PhysRevB.50.13043`.

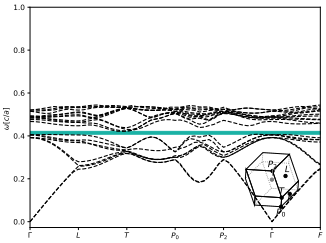

$\varepsilon = 16$, $\phi = 0.5$. 3.65% gap.

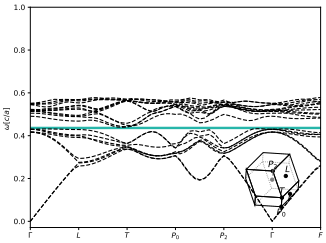

$\varepsilon = 14$, $\phi = 0.5$. 1.9% gap.

Tin Oxide (HP) ($oP4$-SnO), Bands 16 - 17

Structure file taken from `https://doi.org/10.17188/1267079`.

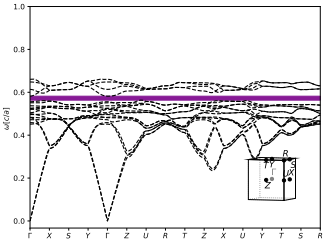

$\varepsilon = 16$, $\phi = 0.25$. 3.62% gap.

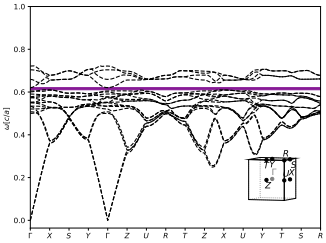

$\varepsilon = 14$, $\phi = 0.22$. 1.79% gap.

Inverse Hypothetical Uninodal Zeolite (tP24-SiO_2), Bands 10 - 11
Structure file taken from `https://doi.org/10.1021/ja037334j`.

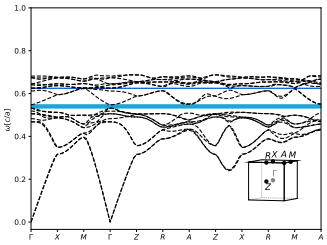

$\varepsilon = 16$, $\phi = 0.19$. 3.61% gap.

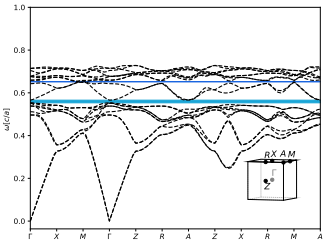

$\varepsilon = 14$, $\phi = 0.19$. (1) 2.63% gap between bands 10-11, and (2) 1.03% gap between bands 12-13.

Inverse Hypothetical Uninodal Zeolite (tP24-SiO_2), Bands 12 - 13
Structure file taken from `https://doi.org/10.1021/ja037334j`.

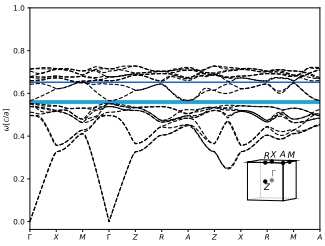

$\varepsilon = 14$, $\phi = 0.19$. (1) 2.63% gap between bands 10-11, and (2) 1.03% gap between bands 12-13.

Cesium Tellurate (hR54-$CsTe_2O_6$), Bands 6 - 7
Structure file taken from `https://doi.org/10.1021/ic2010375`.

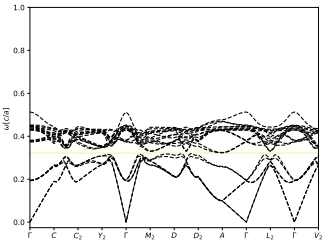

$\varepsilon = 16$, $\phi = 0.41$. 3.46% gap.

Inverse Cobalt (II) Dicarbonate Trisodium Chloride (cF208-$Na_3CoC_2ClO_6$), Bands 2 - 3

Structure file taken from `https://doi.org/10.1107/S0108270111043605`.

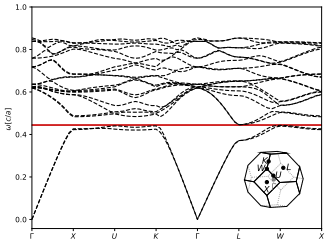

$\varepsilon = 16$, $\phi = 0.18$. 1.1% gap.

Inverse Cobalt (II) Dicarbonate Trisodium Chloride (cF208-$Na_3CoC_2ClO_6$), Bands 14 - 15

Structure file taken from `https://doi.org/10.1107/S0108270111043605`.

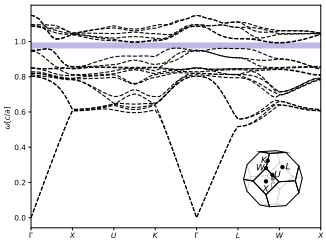

$\varepsilon = 16$, $\phi = 0.06$. 3.45% gap.

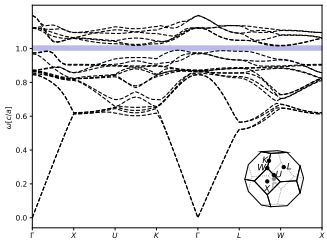

$\varepsilon = 14$, $\phi = 0.06$. 3.16% gap.

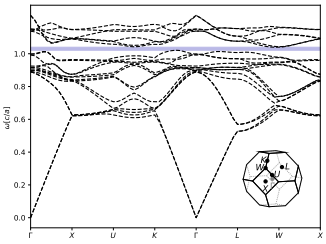

$\varepsilon = 12$, $\phi = 0.06$. 2.63% gap.

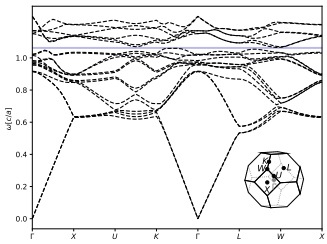

$\varepsilon = 10$, $\phi = 0.06$. 1.28% gap.

Simple Chiral Cubic ($cP4$-X), Bands 16 - 17
Structure file taken from `https://doi.org/10.1103/PhysRevLett.115.158303`.

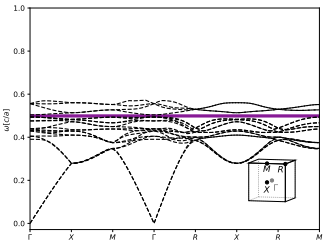

$\varepsilon = 16$, $\phi = 0.39$. 3.42% gap.

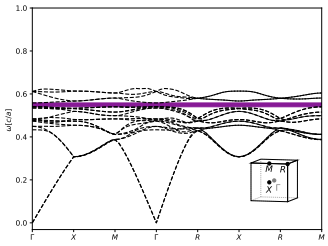

$\varepsilon = 14$, $\phi = 0.35$. 3.42% gap.

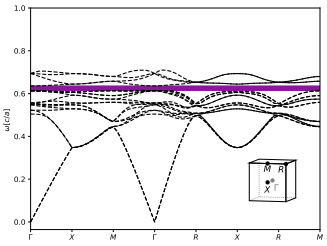

$\varepsilon = 12$, $\phi = 0.28$. 3.33% gap.

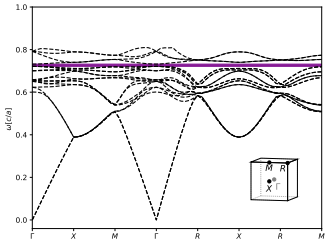

$\varepsilon = 10$, $\phi = 0.2$. 1.45% gap.

Inverse Gallium Tellurium Selenide ($tI20$-Ga_2TeSe_2), Bands 2 - 3
Structure file taken from `https://doi.org/10.17188/1202536`.

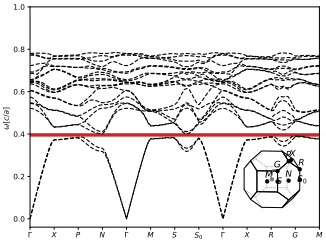

$\varepsilon = 16$, $\phi = 0.19$. 3.33% gap.

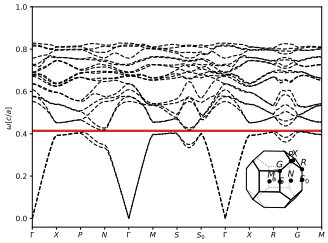

$\varepsilon = 14$, $\phi = 0.19$. 1.96% gap.

Inverse Monoclinic Tridymite ($mP12$-SiO_2), Bands 4 - 5
Structure file taken from `https://doi.org/10.17188/1269045`.

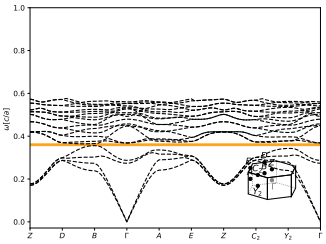

$\varepsilon = 14$, $\phi = 0.26$. 2.75% gap.

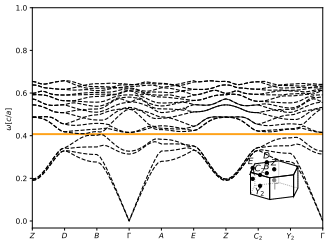

$\varepsilon = 10$, $\phi = 0.26$. 1.84% gap.

Lithium ($aP4$-Li), Bands 16 - 17
Structure file taken from `https://doi.org/10.1021/nn204012y`.

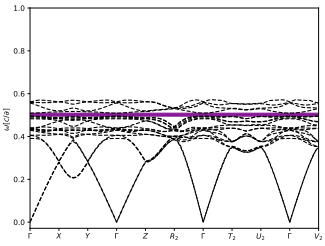

$\varepsilon = 16$, $\phi = 0.39$. 3.28% gap.

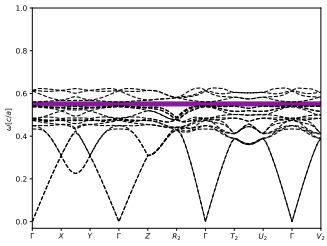

$\varepsilon = 14$, $\phi = 0.35$. 3.22% gap.

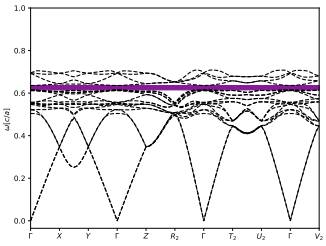

$\varepsilon = 12$, $\phi = 0.28$. 3.1% gap.

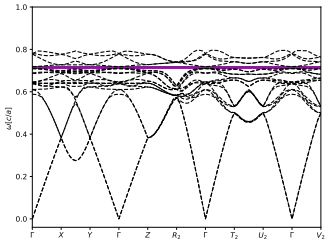

$\varepsilon = 10$, $\phi = 0.22$. 1.21% gap.

Inverse Hydrogen Peroxide ($tP8$-O), Bands 12 - 13
Structure file taken from `https://doi.org/10.1107/S0365110X51000039`.

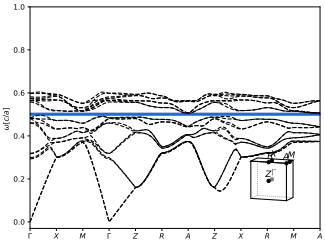

$\varepsilon = 16$, $\phi = 0.18$. 3.2% gap.

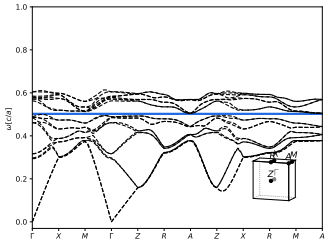

$\varepsilon = 14$, $\phi = 0.2$. 1.56% gap.

Inverse Cobalt Dimanganese (III) Oxide ($tI28$-Mn_2CoO_4), Bands 8 - 9
Structure file taken from `https://doi.org/10.1021/ic501134y`.

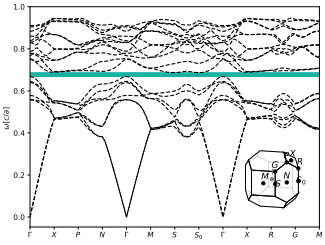

$\varepsilon = 16$, $\phi = 0.16$. 3.16% gap.

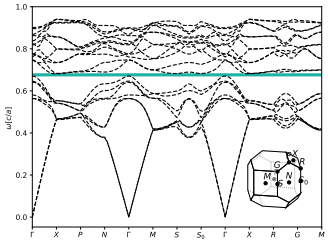

$\varepsilon = 14$, $\phi = 0.18$. 1.91% gap.

Sperrylite ($cP12$-As_2Pt), Bands 16 - 17

Structure file taken from `https://pubs.geoscienceworld.org/canmin/article/17/1/117/11304/the-crystal-structure-of-platarsite-pt-as-s-2-and`.

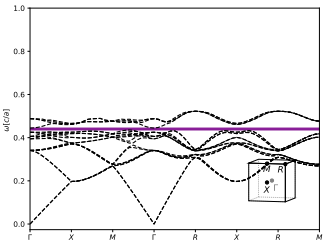

$\varepsilon = 16$, $\phi = 0.56$. 3.14% gap.

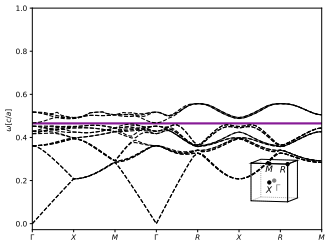

$\varepsilon = 14$, $\phi = 0.56$. 2.21% gap.

Inverse Monoclinic Tridymite ($mP24$-SiO_2), Bands 8 - 9

Structure file taken from `https://doi.org/10.17188/1269045`.

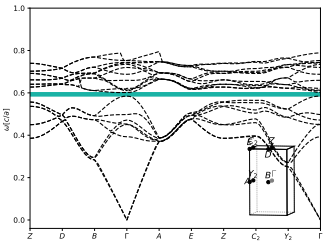

$\varepsilon = 16$, $\phi = 0.27$. 3.13% gap.

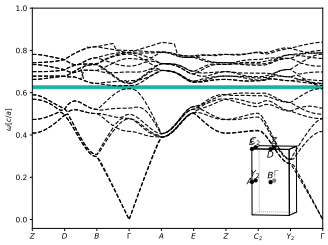

$\varepsilon = 14$, $\phi = 0.27$. 2.32% gap.

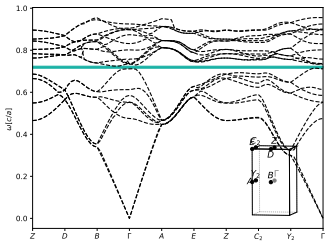

$\varepsilon = 12$, $\phi = 0.22$. 1.59% gap.

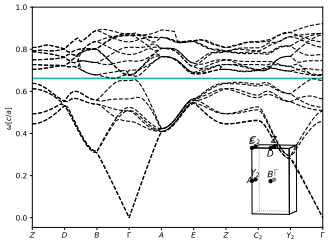

$\varepsilon = 10$, $\phi = 0.32$. 1.33% gap.

Boron Potassium Phosphate ($tI40$-KPD_4O_4), Bands 2 - 3

Structure file taken from `https://doi.org/10.1143/JPSJ.62.959`.

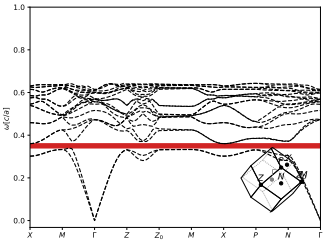

$\varepsilon = 16$, $\phi = 0.34$. 3.06% gap.

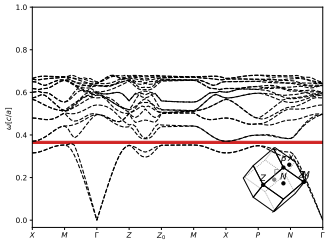

$\varepsilon = 14$, $\phi = 0.34$. 2.88% gap.

Inverse Aluminium Oxide (cF120-$Al_{11}O_4$), Bands 8 - 9
Structure file taken from `https://doi.org/10.2109/jcersj1950.84.976_610`.

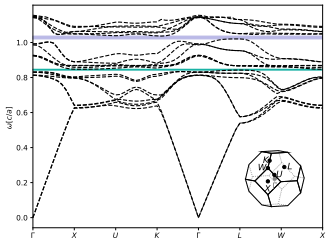

$\varepsilon = 16$, $\phi = 0.05$. (1) 2.13% gap between bands 8-9, and (2) 2.65% gap between bands 14-15.

Inverse Aluminium Oxide (cF120-$Al_{11}O_4$), Bands 14 - 15
Structure file taken from `https://doi.org/10.2109/jcersj1950.84.976_610`.

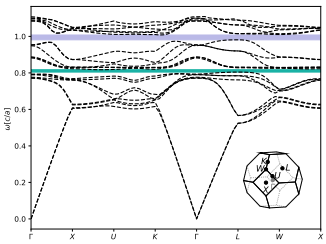

$\varepsilon = 16$, $\phi = 0.06$. (1) 1.9% gap between bands 8-9, and (2) 3.06% gap between bands 14-15.

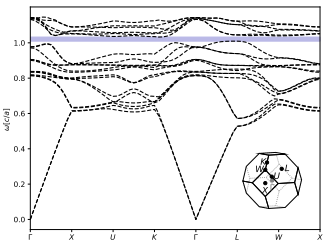

$\varepsilon = 14$, $\phi = 0.06$. 2.66% gap.

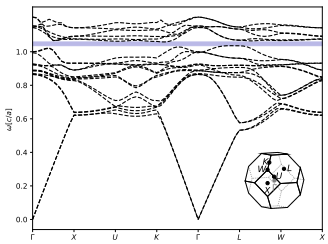

$\varepsilon = 12$, $\phi = 0.06$. 2.43% gap.

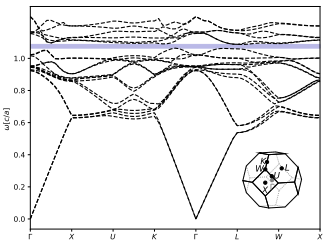

$\varepsilon = 10$, $\phi = 0.06$. 2.09% gap.

Inverse Zn2tio4 Ordered Spinel ($tP28$-$TiZn_2O_4$), Bands 16 - 17
Structure file taken from `https://doi.org/10.1006/jssc.1994.1389`.

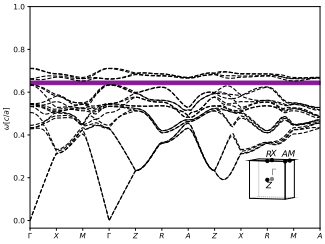

$\varepsilon = 16$, $\phi = 0.16$. 3.04% gap.

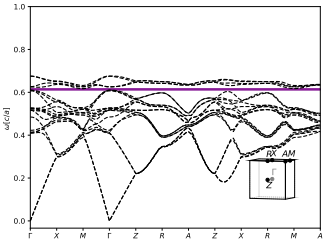

$\varepsilon = 14$, $\phi = 0.21$. 1.87% gap.

Dicopper Selenide (alpha) ($cF44$-$Cu_{10}Se$), Bands 11 - 12
Structure file taken from `https://doi.org/10.1107/S0108768104007475`.

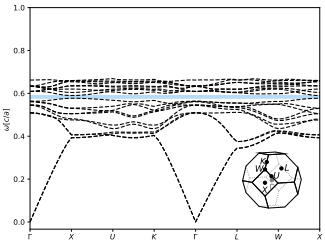

$\varepsilon = 16$, $\phi = 0.34$. 3.01% gap.

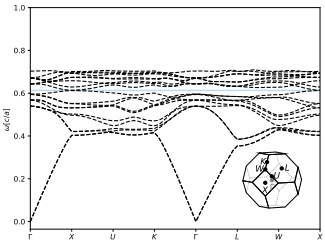

$\varepsilon = 14$, $\phi = 0.34$. 1.15% gap.

Inverse Pyrochlore- Related Cesium Tellurium Oxide ($oP44$-Te_4CO_6), Bands 4 - 5
Structure file taken from `https://doi.org/10.1021/ic2010375`.

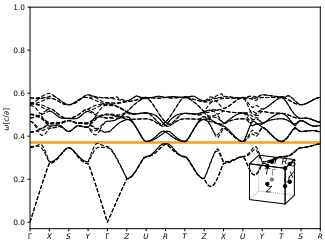

$\varepsilon = 16$, $\phi = 0.25$. 2.94% gap.

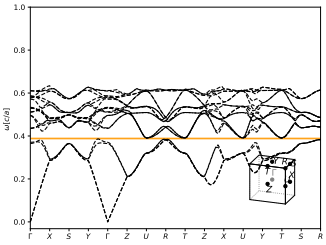

$\varepsilon = 14$, $\phi = 0.25$. 2.09% gap.

Silicon Nitride (beta) ($hP14$-SiN_2), Bands 10 - 11
Structure file taken from `https://doi.org/10.1016/0025-5408(83)90003-X`.

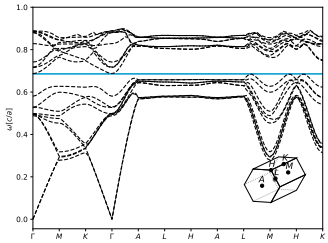

$\varepsilon = 16$, $\phi = 0.34$. 2.93% gap.

Copper (I) Tetraiodomercurate ($tP7$-Cu_2HgI_4), Bands 5 - 6
Structure file taken from `https://doi.org/10.1524/zkri.1931.80.1.190`.

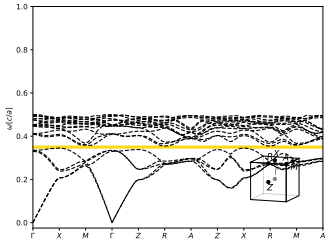

$\varepsilon = 16$, $\phi = 0.43$. 2.91% gap.

Inverse Pyrochlore- like (cF72-$CsAl_{0.38}Te_{1.62}O_6$), Bands 2 - 3
Structure file taken from `https://doi.org/10.1021/ic200574v`.

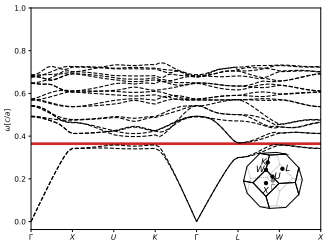

$\varepsilon = 16$, $\phi = 0.25$. 2.9% gap.

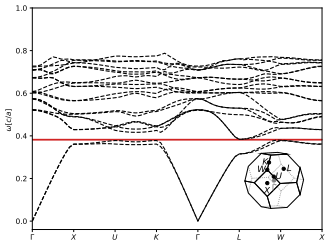

$\varepsilon = 14$, $\phi = 0.25$. 1.64% gap.

Inverse Pyrochlore- like (cF72-$CsAl_{0.38}Te_{1.62}O_6$), Bands 12 - 13
Structure file taken from `https://doi.org/10.1021/ic200574v`.

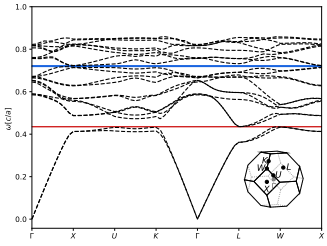

$\varepsilon = 16$, $\phi = 0.16$. (1) 1.01% gap between bands 2-3, and (2) 2.57% gap between bands 12-13.

Inverse Uranium Nitride (cI80-U_2N_3), Bands 12 - 13

Structure file taken from `https://doi.org/10.1021/ja01181a029`.

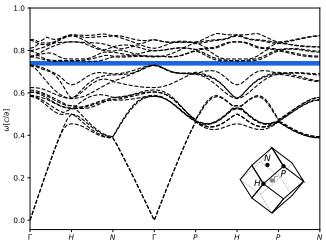

$\varepsilon = 16$, $\phi = 0.19$. 2.9% gap.

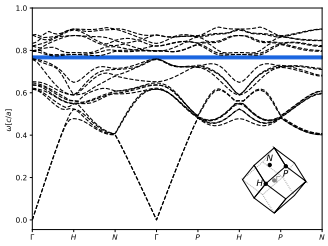

$\varepsilon = 14$, $\phi = 0.19$. 2.39% gap.

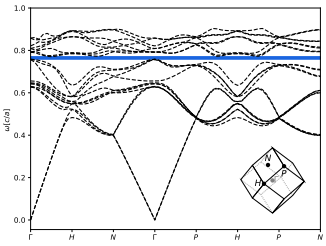

$\varepsilon = 12$, $\phi = 0.23$. 1.91% gap.

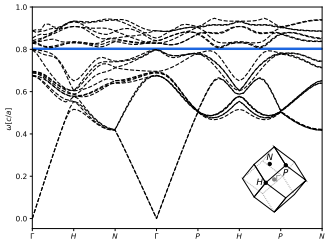

$\varepsilon = 10$, $\phi = 0.23$. 1.24% gap.

Inverse Helical Sulfur (hP9-S), Bands 18 - 19

Structure file taken from `https://doi.org/10.1524/zkri.216.8.417.20360`.

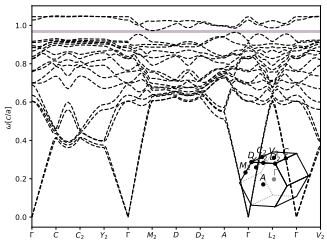

$\varepsilon = 16$, $\phi = 0.14$. 2.89% gap.

Inverse Silicon Nitride (alpha) (hP28-Si_3N_5), Bands 12 - 13

Structure file taken from `https://doi.org/10.1016/0025-5408(83)90003-X`.

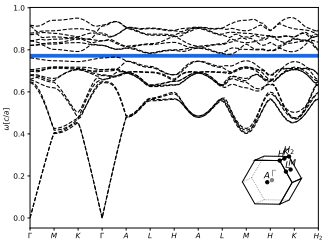

$\varepsilon = 16$, $\phi = 0.15$. 2.86% gap.

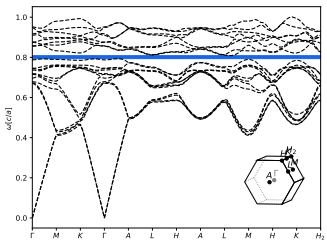

$\varepsilon = 14$, $\phi = 0.15$. 2.76% gap.

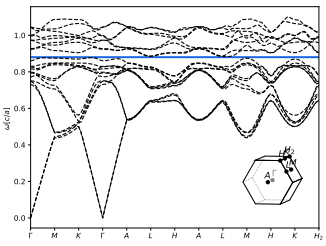

$\varepsilon = 12$, $\phi = 0.12$. 1.66% gap.

Inverse Cooperite ($tP4$-PtS), Bands 4 - 5
Structure file taken from `https://doi.org/10.3891/acta.chem.scand.20-0577`.

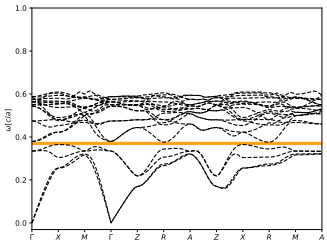

$\varepsilon = 16$, $\phi = 0.15$. 2.85% gap.

Inverse Palladium Oxide ($tP4$-PdO), Bands 4 - 5
Structure file taken from `https://doi.org/10.1107/S0365110X53001800`.

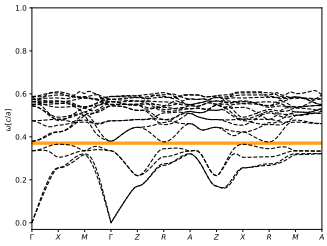

$\varepsilon = 16$, $\phi = 0.15$. 2.85% gap.

Inverse Tin Oxide (HP) ($oP4$-SnO), Bands 4 - 5
Structure file taken from `https://doi.org/10.17188/1267079`.

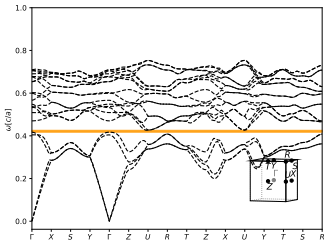

$\varepsilon = 16$, $\phi = 0.17$. 2.84% gap.

Inverse Selenium ($hP3$-Se), Bands 6 - 7
Structure file taken from `https://doi.org/10.1103/PhysRevB.16.4404`.

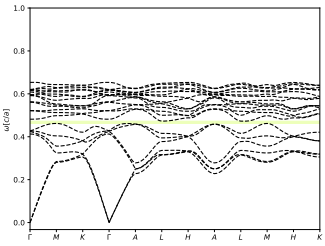

$\varepsilon = 16$, $\phi = 0.22$. 2.83% gap.

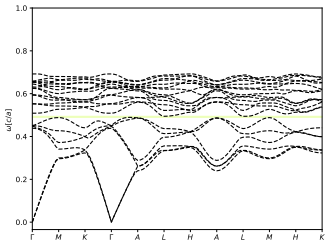

$\varepsilon = 14$, $\phi = 0.22$. 1.54% gap.

Silicon ($oC24$-Si), Bands 12 - 13
Structure file taken from `https://doi.org/10.1038/nmat4140`.

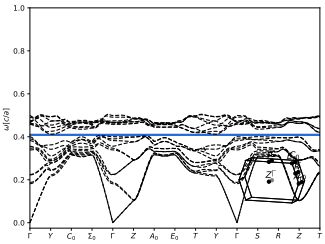

$\varepsilon = 16$, $\phi = 0.42$. 2.82% gap.

Inverse Calcium (IV, HP) ($tP8$-Ca), Bands 12 - 13
Structure file taken from `https://doi.org/10.1103/PhysRevLett.101.095503`.

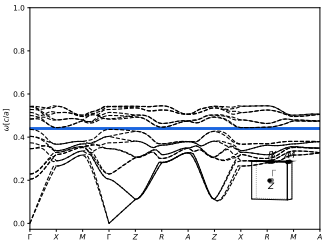

$\varepsilon = 16$, $\phi = 0.21$. 2.81% gap.

Aluminum Lead Oxide (oA28-$AlPbO_3$), Bands 4 - 5

Structure file taken from `https://doi.org/10.1107/S0108768194011857`.

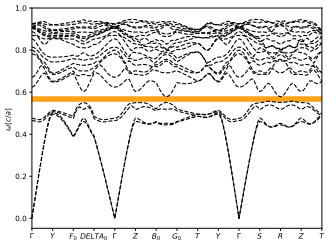

$\varepsilon = 16$, $\phi = 0.3$. 2.76% gap.

Heazlewoodite (hR5-Ni_3S_2), Bands 17 - 18

Structure file taken from `https://doi.org/10.1002/zaac.19382390109`.

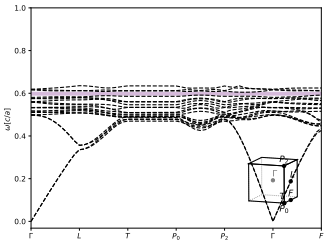

$\varepsilon = 16$, $\phi = 0.25$. 2.75% gap.

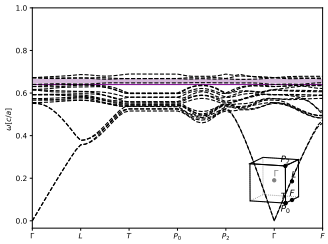

$\varepsilon = 14$, $\phi = 0.22$. 2.38% gap.

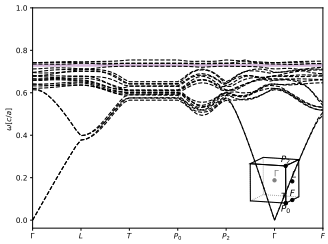

$\varepsilon = 12$, $\phi = 0.19$. 1.25% gap.

Inverse Silicon Nitride (alpha) (hP28-Si_3N_4), Bands 12 - 13

Structure file taken from `https://doi.org/10.1016/0025-5408(83)90003-X`.

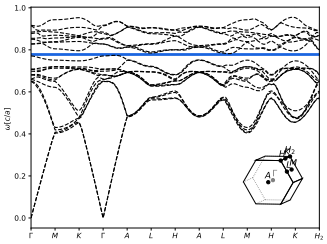

$\varepsilon = 16$, $\phi = 0.15$. 2.7% gap.

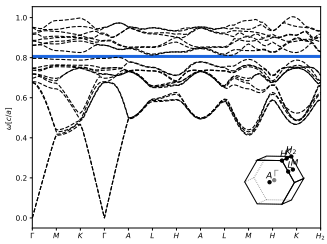

$\varepsilon = 14$, $\phi = 0.15$. 2.62% gap.

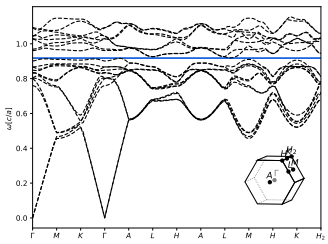

$\varepsilon = 12$, $\phi = 0.1$. 1.39% gap.

Simple Cubic ($cP1$-Po), Bands 5 - 6
Structure file taken from `https://doi.org/10.1016/0022-1902(66)80270-1`.

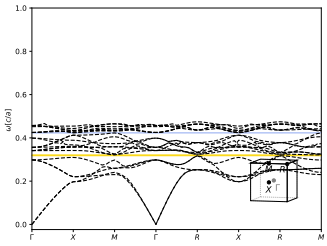

$\varepsilon = 16$, $\phi = 0.51$. 2.69% gap.

Pyrite ($cP12$-FeS_2), Bands 16 - 17
Structure file taken from `https://doi.org/10.17188/1183906`.

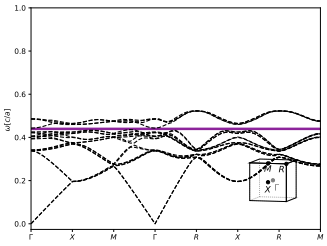

$\varepsilon = 16$, $\phi = 0.56$. 2.68% gap.

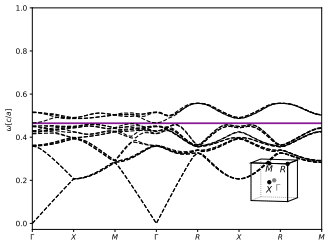

$\varepsilon = 14$, $\phi = 0.56$. 1.82% gap.

Inverse 2-3 Spinel ($tP28$-$Mg(FeO_2)_2$), Bands 16 - 17
Structure file taken from `https://doi.org/10.2138/am.2007.2485`.

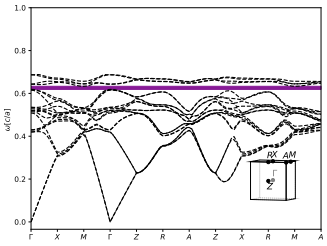

$\varepsilon = 16$, $\phi = 0.17$. 2.68% gap.

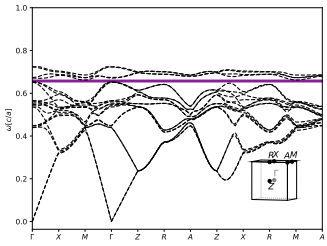

$\varepsilon = 14$, $\phi = 0.17$. 1.77% gap.

Inverse C60 Polymer (oI120-C), Bands 17 - 18
Structure file taken from `https://doi.org/10.1016/S0009-2614(02)00827-8`.

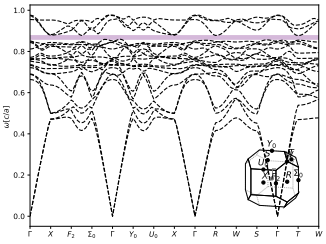

$\varepsilon = 16$, $\phi = 0.12$. 2.64% gap.

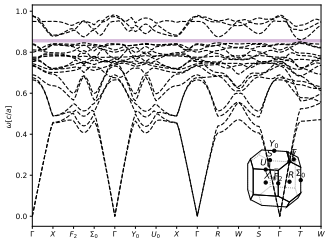

$\varepsilon = 14$, $\phi = 0.14$. 2.73% gap.

Inverse Silver Hexahydroxoantimonate (tP32-$AgSbO_6$), Bands 12 - 13
Structure file taken from `https://doi.org/10.1002/zaac.19382380209`.

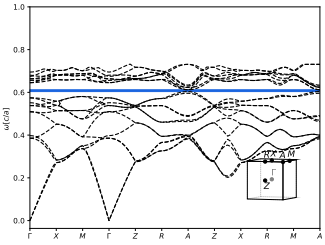

$\varepsilon = 16$, $\phi = 0.21$. 2.64% gap.

Silicon Phosphide (cP12-SiP_2), Bands 16 - 17
Structure file taken from `https://doi.org/10.17188/1196344`.

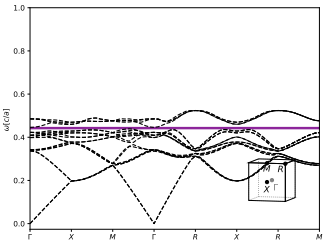

$\varepsilon = 16$, $\phi = 0.56$. 2.62% gap.

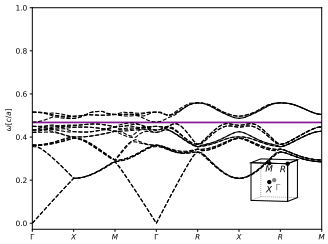

$\varepsilon = 14$, $\phi = 0.56$. 1.82% gap.

Ice III ($tP36$-H_2O), Bands 12 - 13
Structure file taken from `https://doi.org/10.1107/S0567740868004231`.

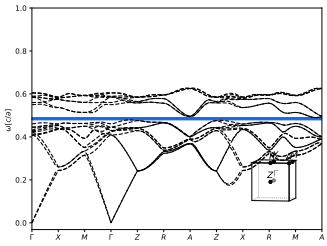

$\varepsilon = 16$, $\phi = 0.38$. 2.53% gap.

Inverse Gallium Tellurium Zinc Oxide ($cI76$-$ZnGa_2Te_4O_{12}$), Bands 10 - 11
Structure file taken from `https://doi.org/10.1021/ic300909s`.

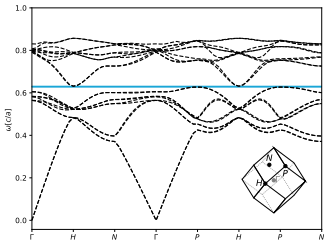

$\varepsilon = 16$, $\phi = 0.18$. 2.51% gap.

Inverse Tellurium (III, HP) ($mC12$-Te), Bands 18 - 19
Structure file taken from `https://doi.org/10.1088/0953-8984/14/44/342`.

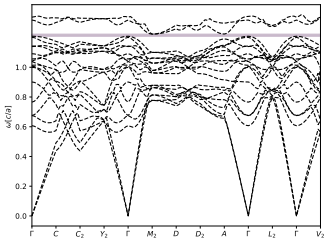

$\varepsilon = 16$, $\phi = 0.14$. 2.5% gap.

Inverse Dilithium Titanium Hexaoxotellurate (oP20-Li_2TiTeO_6), Bands 4 - 5
Structure file taken from `https://doi.org/10.1016/0022-4596(89)90292-2`.

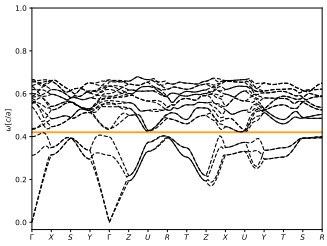

$\varepsilon = 16$, $\phi = 0.15$. 2.44% gap.

Inverse Iron Trifluoride (hR8-FeF_3), Bands 8 - 9
Structure file taken from `https://doi.org/10.17188/1269222`.

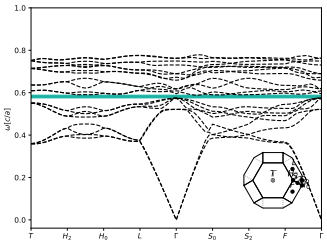

$\varepsilon = 16$, $\phi = 0.2$. 2.44% gap.

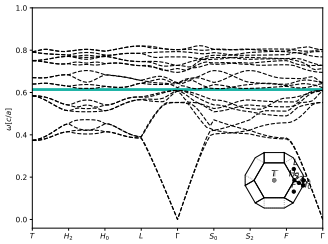

$\varepsilon = 14$, $\phi = 0.2$. 1.25% gap.

Inverse Hypothetical Uninodal Zeolite (oP24-SiO_2), Bands 12 - 13
Structure file taken from `https://doi.org/10.1021/ja037334j`.

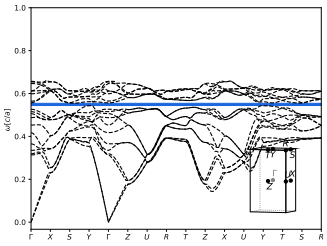

$\varepsilon = 16$, $\phi = 0.31$. 2.4% gap.

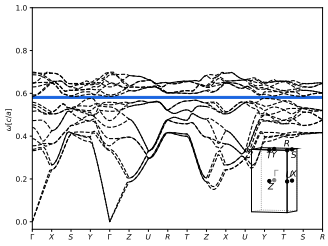

$\varepsilon = 14$, $\phi = 0.31$. 2.17% gap.

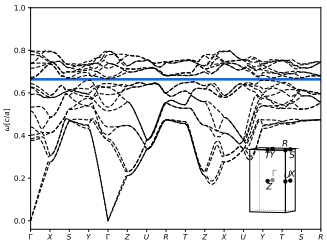

$\varepsilon = 12$, $\phi = 0.26$. 1.64% gap.

Inverse Bismuth Iron (III) Oxide (hR10-$FeBiO_3$), Bands 16 - 17
Structure file taken from `https://doi.org/10.1016/S0022-3697(71)80189-0`.

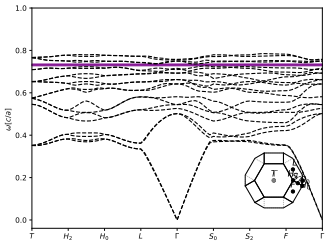

$\varepsilon = 16$, $\phi = 0.22$. 2.36% gap.

Copper Cadnium Germanium Sulfide (oP16-$CdCu_2GeS_4$), Bands 16 - 17
Structure file taken from `https://doi.org/10.1107/S0567740869003670`.

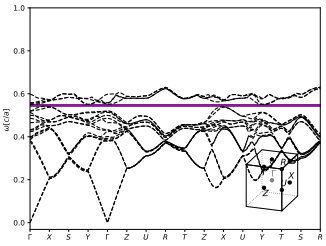

$\varepsilon = 16$, $\phi = 0.49$. 2.36% gap.

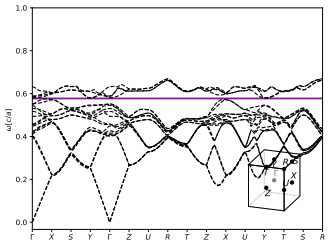

$\varepsilon = 14$, $\phi = 0.49$. 1.39% gap.

Heazlewoodite (hR5-Ni_3S_2), Bands 17 - 18
Structure file taken from `https://doi.org/10.1107/S0567740880005523`.

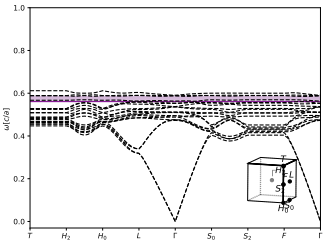

$\varepsilon = 16$, $\phi = 0.29$. 2.34% gap.

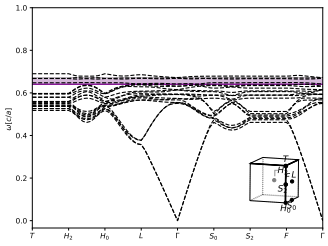

$\varepsilon = 14$, $\phi = 0.22$. 2.12% gap.

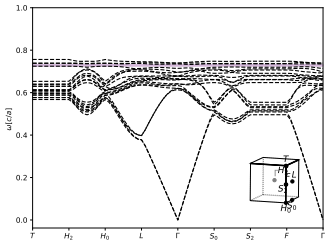

$\varepsilon = 12$, $\phi = 0.19$. 1.22% gap.

Inverse Gallium Selenide (cI144-$GaSe_2$), Bands 14 - 15
Structure file taken from `https://doi.org/10.1126/science.1078663`.

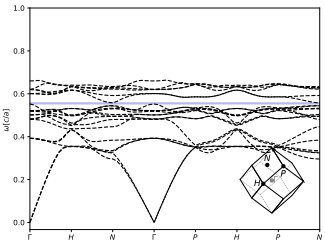

$\varepsilon = 16$, $\phi = 0.27$. 2.33% gap.

Inverse Marcasite (oP6-$CoTe_2$), Bands 8 - 9
Structure file taken from `https://doi.org/10.1021/ic50166a018`.

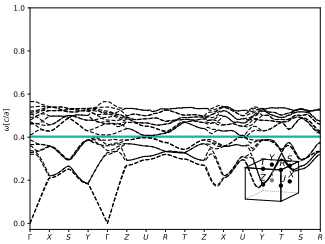

$\varepsilon = 16$, $\phi = 0.4$. 2.32% gap.

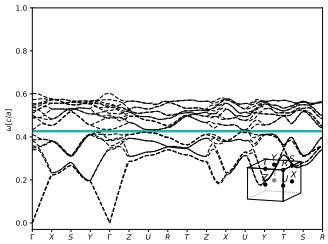

$\varepsilon = 14$, $\phi = 0.4$. 2.65% gap.

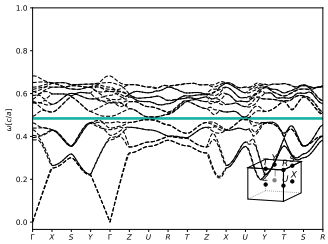

$\varepsilon = 12$, $\phi = 0.35$. 2.41% gap.

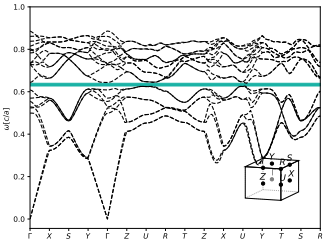

$\varepsilon = 10$, $\phi = 0.21$. 2.8% gap.

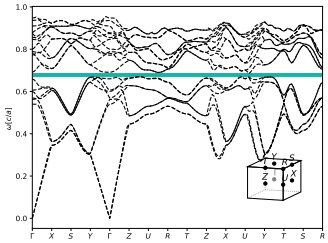

$\varepsilon = 8$, $\phi = 0.21$. 3.66% gap.

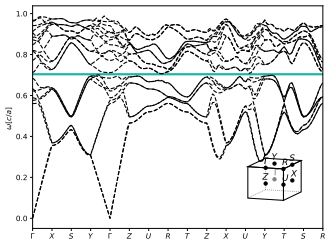

$\varepsilon = 6$, $\phi = 0.25$. 1.27% gap.

576-Particle Zeolite Network (cF2304-SiO_2), Bands 8 - 9
Structure file taken from `https://doi.org/10.1021/ja048685g`.

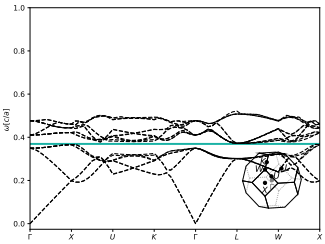

$\varepsilon = 16$, $\phi = 0.49$. 2.29% gap.

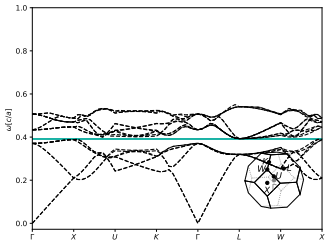

$\varepsilon = 14$, $\phi = 0.49$. 2.03% gap.

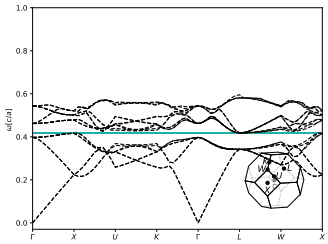

$\varepsilon = 12$, $\phi = 0.49$. 1.29% gap.

Inverse Polonium (beta) (hR1-Po), Bands 3 - 4
Structure file taken from `https://doi.org/10.1016/0022-1902(66)80270-1`.

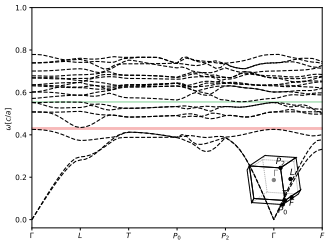

$\varepsilon = 16$, $\phi = 0.13$. 2.28% gap.

Inverse Polonium (beta) (hR1-Po), Bands 7 - 8
Structure file taken from `https://doi.org/10.1016/0022-1902(66)80270-1`.

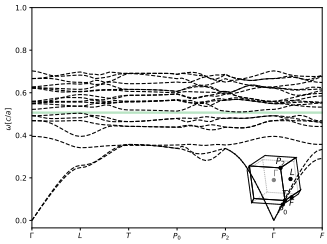

$\varepsilon = 16$, $\phi = 0.17$. 1.25% gap.

Beryllium-free Deep-ultraviolet Nonlinear Optical Crystal (hP42-$Rb_3Al_3B_3O_{10}F$), Bands 10 - 11
Structure file taken from `https://doi.org/10.1021/ja5128314`.

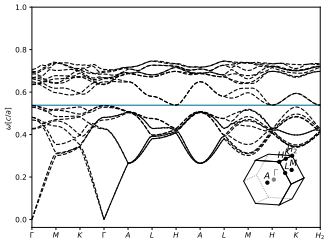

$\varepsilon = 16$, $\phi = 0.31$. 2.22% gap.

Inverse Tetragonal Spinel (tP28-$Ta_{0.6}Ti_{3.4}Zn_{7.7}O_{16}$), Bands 16 - 17
Structure file taken from `https://doi.org/10.2109/jcersj2.115.780`.

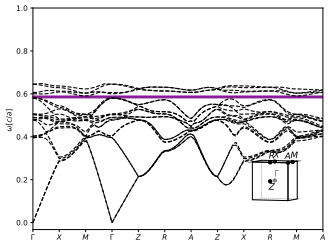

$\varepsilon = 16$, $\phi = 0.21$. 2.2% gap.

Inverse Grey Selenium (hP3-Se), Bands 6 - 7
Structure file taken from `https://doi.org/10.1039/C7CE00863E`.

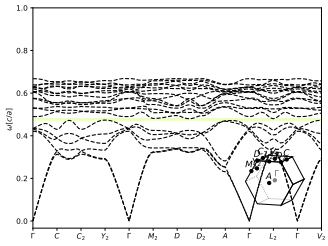

$\varepsilon = 16$, $\phi = 0.21$. 2.13% gap.

Inverse Gold Tellurium Sulfide (mC24-Ag_2TeS_3), Bands 12 - 13
Structure file taken from `https://doi.org/10.1007/BF00807304`.

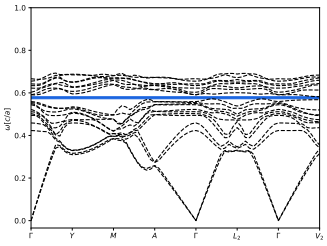

$\varepsilon = 16$, $\phi = 0.24$. 2.1% gap.

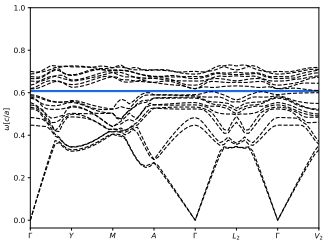

$\varepsilon = 14$, $\phi = 0.24$. 1.37% gap.

Inverse Rubidium Nitrate (V) (HT) (cP33-$RbNO_3$), Bands 17 - 18
Structure file taken from `https://doi.org/10.1107/S0108270187095660`.

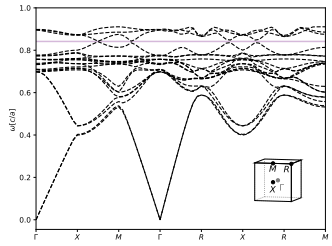

$\varepsilon = 16$, $\phi = 0.08$. 2.05% gap.

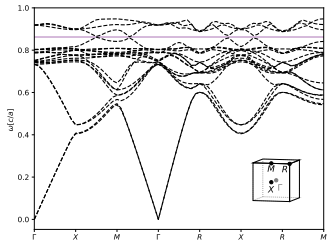

$\varepsilon = 14$, $\phi = 0.08$. 2.26% gap.

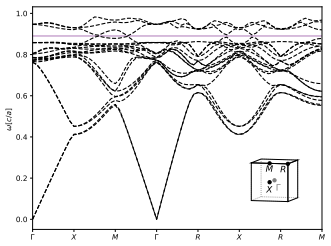

$\varepsilon = 12$, $\phi = 0.08$. 2.04% gap.

Inverse Beryllium Tellurate (cF48-Be_4TeO_7), Bands 18 - 19
Structure file taken from `https://doi.org/10.1107/S0567740877012606`.

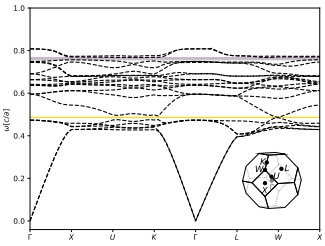

$\varepsilon = 16$, $\phi = 0.17$. 2.01% gap.

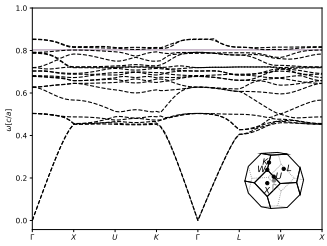

$\varepsilon = 14$, $\phi = 0.17$. 1.0% gap.

Inverse Silver Phosphate (cP16-Ag_3PO_4), Bands 16 - 17
Structure file taken from `https://doi.org/10.1524/zkri.1976.144.16.76`.

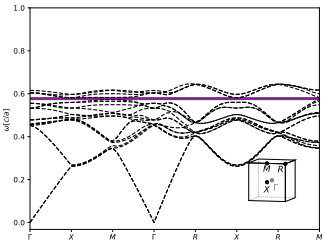

$\varepsilon = 16$, $\phi = 0.26$. 1.97% gap.

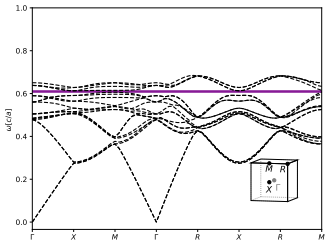

$\varepsilon = 14$, $\phi = 0.26$. 1.5% gap.

Deuterated Sulphuric Acid Tetrahydrate (tP38-$D_{10}SO_8$), Bands 10 - 11
Structure file taken from `https://doi.org/10.1107/S056774087200487X`.

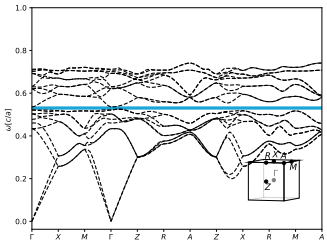

$\varepsilon = 16$, $\phi = 0.3$. 1.94% gap.

Inverse Aluminium trifluoride (tP64-AlF_3), Bands 10 - 11
Structure file taken from `https://doi.org/10.1016/0022-4596(92)90165-R`.

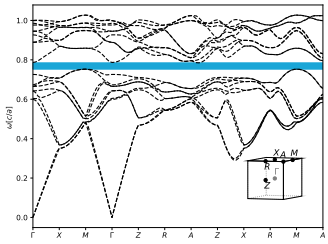

$\varepsilon = 16$, $\phi = 0.13$. 1.94% gap.

Inverse Iodine (HP) (hR6-As), Bands 12 - 13
Structure file taken from `https://doi.org/10.1107/S0021889869006443`.

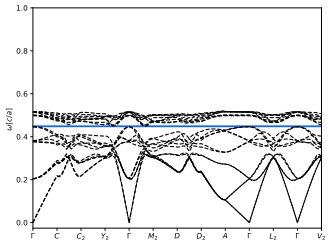

$\varepsilon = 16$, $\phi = 0.22$. 1.89% gap.

Inverse Monoclinic Cristobalite (II) (mP24-SiO_2), Bands 8 - 9
Structure file taken from `https://doi.org/10.1180/002646100549436`.

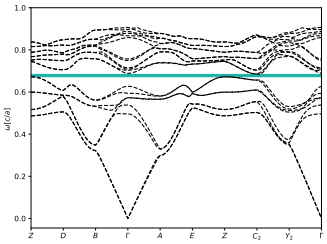

$\varepsilon = 16$, $\phi = 0.21$. 1.88% gap.

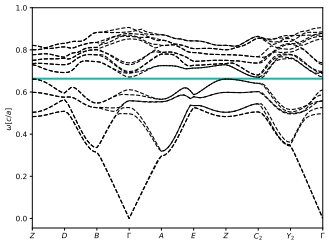

$\varepsilon = 14$, $\phi = 0.25$. 1.1% gap.

Inverse Calcium Bromide Hexahydrate (hP21-$CaH_{12}(BrO_3)_2$), Bands 16 - 17
Structure file taken from `https://doi.org/10.1107/S0567740877009881`.

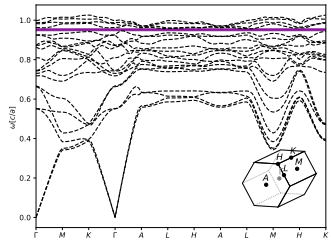

$\varepsilon = 16$, $\phi = 0.17$. 1.85% gap.

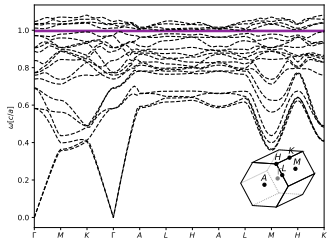

$\varepsilon = 14$, $\phi = 0.17$. 1.93% gap.

Orthorhombic Carbon (oC8-C), Bands 16 - 17
Structure file taken from `https://doi.org/10.1007/s10910-012-0030-x`.

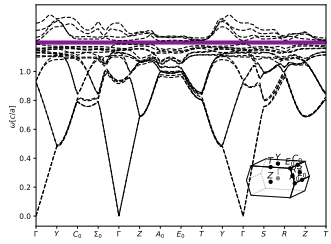

$\varepsilon = 16$, $\phi = 0.06$. 1.81% gap.

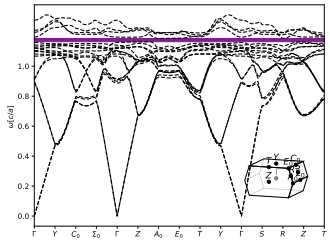

$\varepsilon = 14$, $\phi = 0.08$. 2.44% gap.

Inverse Silicon Oxide - Fibrous (oI12-SiO_2), Bands 14 - 15
Structure file taken from `https://doi.org/10.1002/zaac.19542760110`.

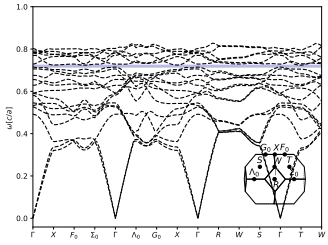

$\varepsilon = 16$, $\phi = 0.2$. 1.77% gap.

Inverse Silver Carbonate (cP6-Ag_2O), Bands 18 - 19
Structure file taken from `https://doi.org/10.1021/ic0111177`.

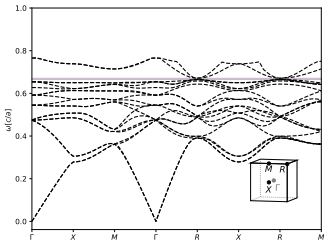

$\varepsilon = 16$, $\phi = 0.2$. 1.75% gap.

Inverse Cuprite (cP6-Cu_2O), Bands 18 - 19
Structure file taken from `https://doi.org/10.1007/BF01390765`.

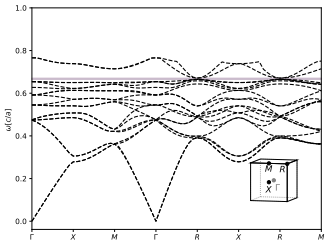

$\varepsilon = 16$, $\phi = 0.2$. 1.75% gap.

Inverse Manganese Nitride (hP12-Mn_3N_7), Bands 12 - 13
Structure file taken from `https://doi.org/10.1107/S0567740877009261`.

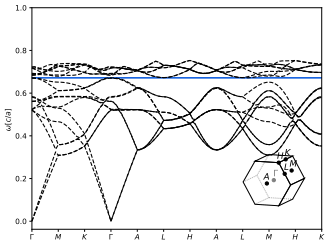

$\varepsilon = 16$, $\phi = 0.23$. 1.71% gap.

Inverse Protactinium (tI2-Pa), Bands 5 - 6
Structure file taken from `https://doi.org/10.1016/0304-8853(82)90252-9`.

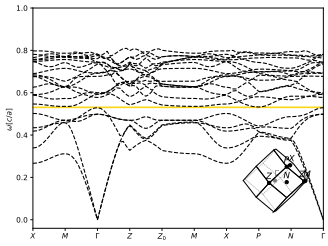

$\varepsilon = 16$, $\phi = 0.16$. 1.65% gap.

Inverse Cinnabar (hP6-HgS), Bands 6 - 7
Structure file taken from `https://doi.org/10.1088/0256-307X/26/4/046402`.

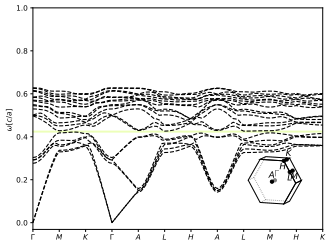

$\varepsilon = 16$, $\phi = 0.16$. 1.59% gap.

Zinc Oxide (hP5-Zn_7O_6), Bands 18 - 19
Structure file taken from `https://doi.org/10.1134/S1063774513020119`.

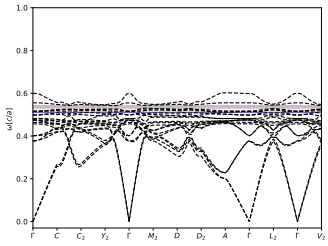

$\varepsilon = 16$, $\phi = 0.27$. 1.58% gap.

Zinc Oxide (hP5-Zn_7O_6), Bands 19 - 20
Structure file taken from `https://doi.org/10.1134/S1063774513020119`.

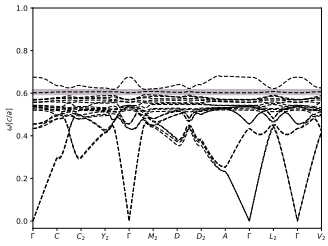

$\varepsilon = 16$, $\phi = 0.18$. 1.5% gap.

Inverse Sodium Superoxide (oP6-NaO_2), Bands 8 - 9
Structure file taken from `https://doi.org/10.1021/ja01117a031`.

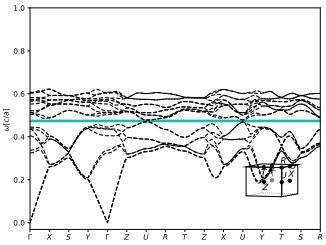

$\varepsilon = 16$, $\phi = 0.25$. 1.55% gap.

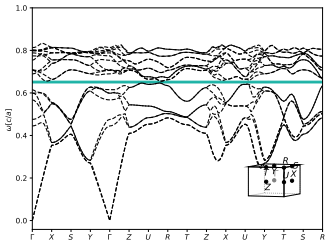

$\varepsilon = 14$, $\phi = 0.13$. 1.42% gap.

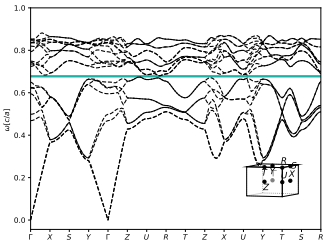

$\varepsilon = 12$, $\phi = 0.13$. 1.68% gap.

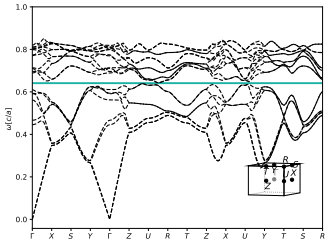

$\varepsilon = 10$, $\phi = 0.18$. 1.71% gap.

Inverse Indium Phosphorous Chalkogenide (tI12-$InPS_4$), Bands 11 - 12
Structure file taken from `https://doi.org/10.1107/S0567740878005002`.

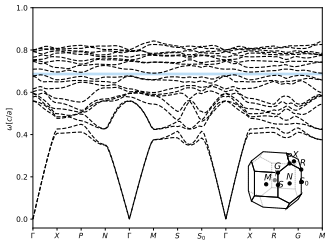

$\varepsilon = 16$, $\phi = 0.18$. 1.48% gap.

Inverse Xenon Trioxide (beta) (hR4-XeO_3), Bands 2 - 3
Structure file taken from `https://doi.org/10.1021/acs.inorgchem.6b02371`.

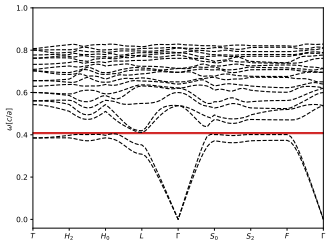

$\varepsilon = 16$, $\phi = 0.12$. 1.47% gap.

Inverse Cobalt Hexafluorozirconate (LT) (hR8-$ZrCoF_6$), Bands 8 - 9
Structure file taken from `https://doi.org/10.1088/0953-8984/2/36/001`.

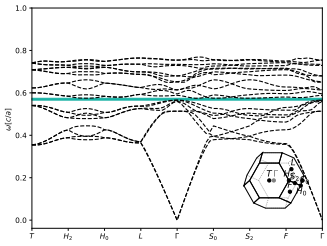

$\varepsilon = 16$, $\phi = 0.21$. 1.47% gap.

Neodymium Oxide (alpha) (hP5-Nd_2O_3), Bands 19 - 20
Structure file taken from `https://doi.org/10.1515/zpch-1926-12309`.

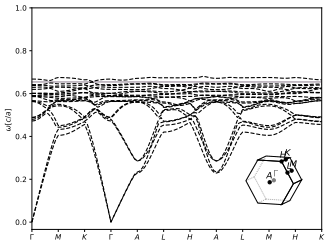

$\varepsilon = 16$, $\phi = 0.14$. 1.44% gap.

Inverse Magnesium Chlorite Hexahydrate (tP26-$Mg(ClO_5)_2$), Bands 10 - 11
Structure file taken from `https://doi.org/10.1107/S010827019000066X`.

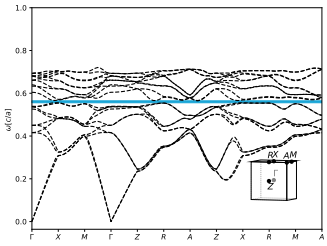

$\varepsilon = 16$, $\phi = 0.16$. 1.41% gap.

Inverse Niobium Oxide Phosphate (HT) (tP14-$NbPO_5$), Bands 8 - 9
Structure file taken from `https://doi.org/10.1006/jssc.1998.8045`.

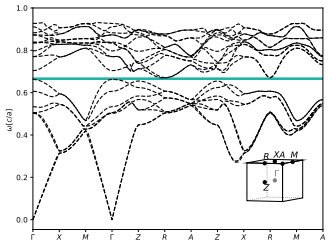

$\varepsilon = 16$, $\phi = 0.16$. 1.38% gap.

Mercury (alpha, LT) (hR1-Hg), Bands 2 - 3
Structure file taken from `https://doi.org/10.1103/PhysRev.19.444.3`.

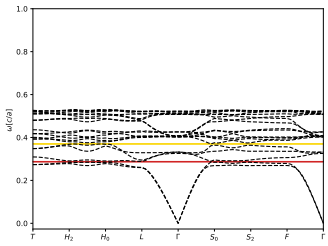

$\varepsilon = 16$, $\phi = 0.39$. (1) 1.11% gap between bands 2-3, and (2) 1.18% gap between bands 5-6.

Mercury (alpha, LT) (hR1-Hg), Bands 5 - 6
Structure file taken from `https://doi.org/10.1103/PhysRev.19.444.3`.

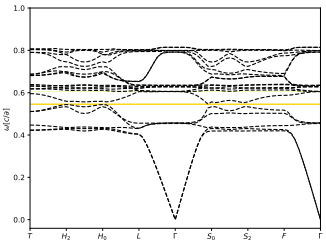

$\varepsilon = 16$, $\phi = 0.11$. 1.36% gap.

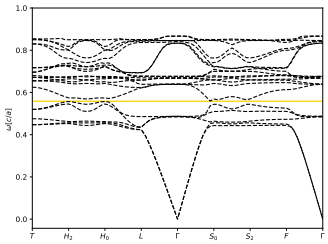

$\varepsilon = 14$, $\phi = 0.11$. 1.57% gap.

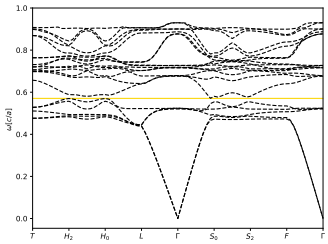

$\varepsilon = 12$, $\phi = 0.11$. 1.66% gap.

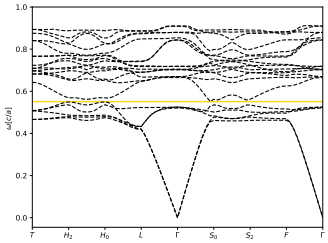

$\varepsilon = 10$, $\phi = 0.14$. 1.82% gap.

Cooperite (tP4-PtS), Bands 18 - 19
Structure file taken from `https://doi.org/10.3891/acta.chem.scand.20-0577`.

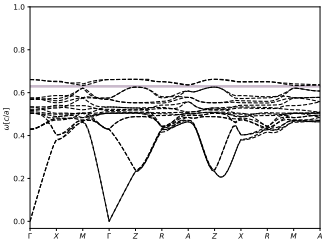

$\varepsilon = 16$, $\phi = 0.14$. 1.34% gap.

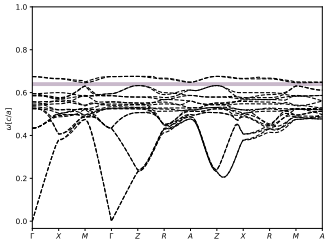

$\varepsilon = 14$, $\phi = 0.15$. 1.97% gap.

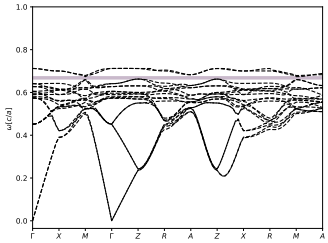

$\varepsilon = 12$, $\phi = 0.14$. 2.74% gap.

Inverse Layered Barium Cobalt Phosphate (hP13-$BaCo_6P_6O_{12}$), Bands 7 - 8
Structure file taken from `https://doi.org/10.1021/ic4009027`.

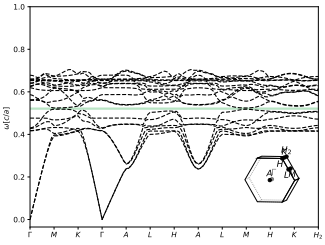

$\varepsilon = 16$, $\phi = 0.12$. 1.32% gap.

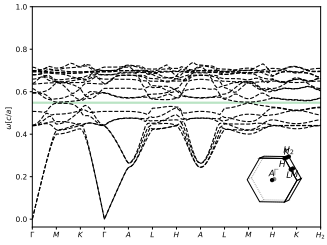

$\varepsilon = 14$, $\phi = 0.12$. 1.17% gap.

Inverse Mattagamite ($oP6$-$CoTe_2$), Bands 8 - 9
Structure file taken from `https://doi.org/10.1002/zaac.19382390203`.

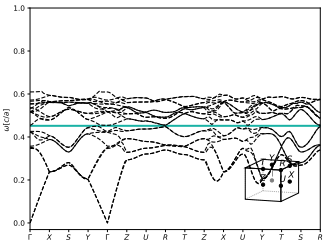

$\varepsilon = 16$, $\phi = 0.32$. 1.28% gap.

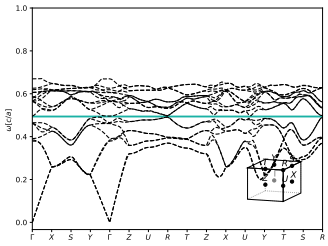

$\varepsilon = 14$, $\phi = 0.3$. 1.24% gap.

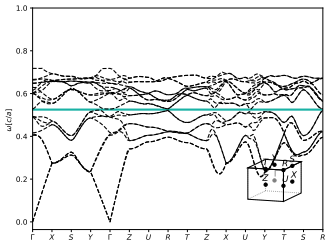

$\varepsilon = 12$, $\phi = 0.3$. 1.17% gap.

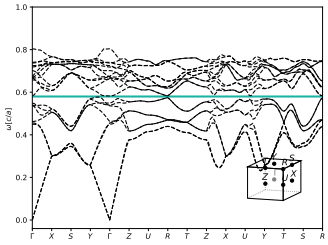

$\varepsilon = 10$, $\phi = 0.28$. 1.08% gap.

Palladium Oxide ($tP4$-PdO), Bands 18 - 19
Structure file taken from `https://doi.org/10.1107/S0365110X53001800`.

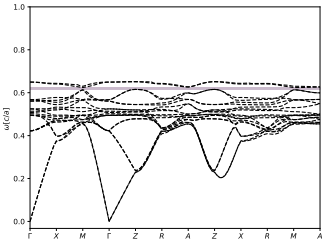

$\varepsilon = 16$, $\phi = 0.15$. 1.28% gap.

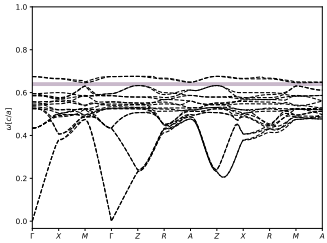

$\varepsilon = 14$, $\phi = 0.15$. 1.97% gap.

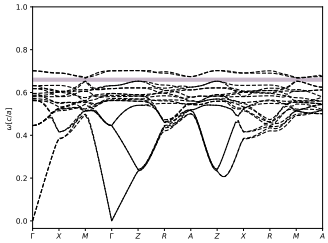

$\varepsilon = 12$, $\phi = 0.15$. 2.56% gap.

Nickel Antimonide Sulfide ($cP12$-NiSbS), Bands 16 - 17
Structure file taken from `https://doi.org/10.1006/jssc.2001.9342`.

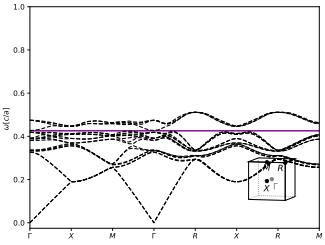

$\varepsilon = 16$, $\phi = 0.59$. 1.26% gap.

Inverse Quartz- like Water Ice (mC80-H_5O_2), Bands 15 - 16
Structure file taken from `https://doi.org/10.1021/jacs.6b06986`.

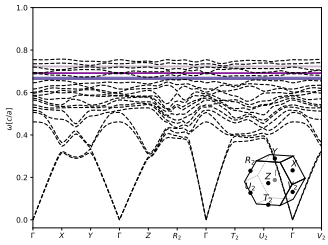

$\varepsilon = 16$, $\phi = 0.2$. 1.25% gap.

Titanium Hydrogen Carbon Nitrogen Oxide (hP72-$TiH_8C_4NO_{10}$), Bands 18 - 19
Structure file taken from `https://doi.org/10.1107/S0108768195012900`.

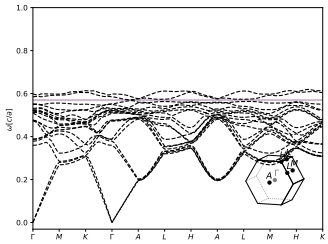

$\varepsilon = 16$, $\phi = 0.39$. 1.25% gap.

Inverse Anhydrous Tetrahedral Halides And Silicon Chalcogenide (hP27-$BeCl_2$), Bands 15 - 16
Structure file taken from `https://doi.org/10.1021/ja8026967`.

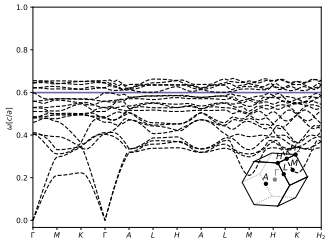

$\varepsilon = 16$, $\phi = 0.31$. 1.22% gap.

Cesium Cadmium Trinitrite (cP20-$CsCd(NO_2)_3$), Bands 17 - 18
Structure file taken from `https://doi.org/10.1016/0022-5088(79)90251-0`.

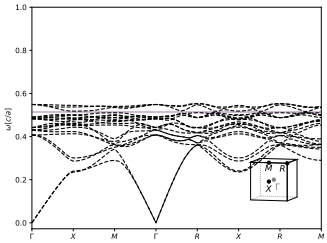

$\varepsilon = 16$, $\phi = 0.42$. 1.14% gap.

Gallium Chalkogenide (tI14-Ga_2HgSe_4), Bands 5 - 6
Structure file taken from `https://doi.org/10.1002/zaac.19552790502`.

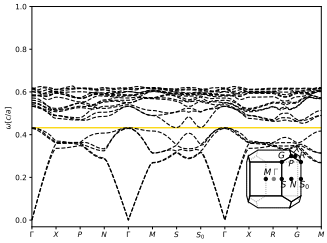

$\varepsilon = 16$, $\phi = 0.4$. 1.1% gap.

Oxygen (eta) ($hP4$-O), Bands 8 - 9
Structure file taken from `https://doi.org/10.1063/1.3118970`.

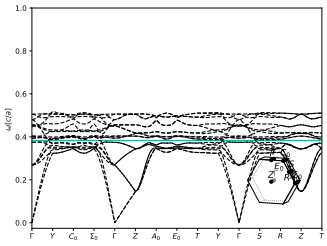

$\varepsilon = 14$, $\phi = 0.25$. 1.7% gap.

Hexagonal Tungsten Trioxide ($hP12$-WO_3), Bands 6 - 7
Structure file taken from `https://doi.org/10.1016/0022-4596(79)90199-3`.

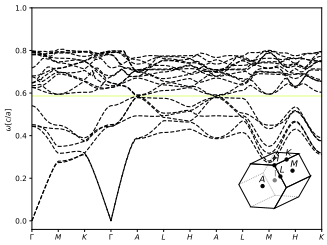

$\varepsilon = 16$, $\phi = 0.32$. 1.01% gap.

Xenon Trioxide (beta) ($hR4$-XeO_3), Bands 16 - 17
Structure file taken from `https://doi.org/10.1021/acs.inorgchem.6b02371`.

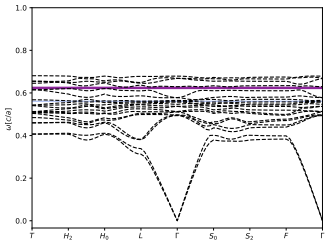

$\varepsilon = 16$, $\phi = 0.21$. 1.0% gap.

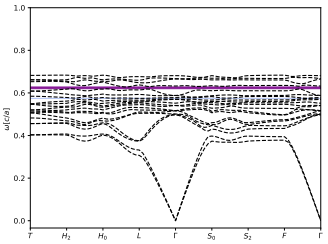

$\varepsilon = 14$, $\phi = 0.24$. 1.33% gap.

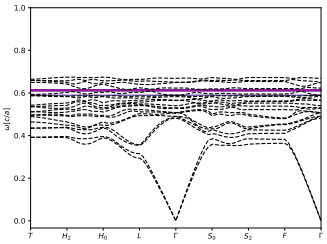

$\varepsilon = 12$, $\phi = 0.3$. 1.29% gap.

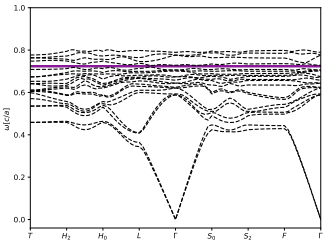

$\varepsilon = 10$, $\phi = 0.21$. 1.03% gap.

APPENDIX D

Glossary of Photonic Band Structures from Section 8.2

For each of these crystal structures, the photonic band structure for each gap location (*e.g.* between bands 2-3) is given for the filling fraction ϕ which maximizes the gap size and all number of additional lattice sites (denoted I) computed in Chapter VIII where gap size is greater than 0. We include multiple ε for select cases of $I = 0$ and $I = 9$.

A15, $\varepsilon = 16$**, Bands 16 - 17**.

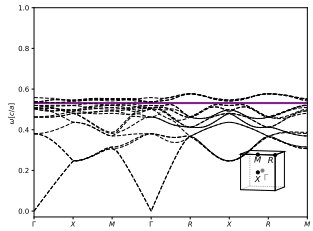

$I = 3$**,** $\phi = 0.32$. 2.47% gap.

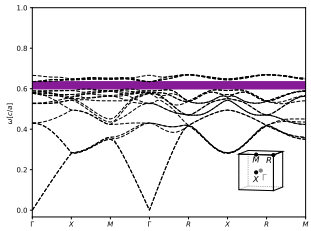

$I = 4$**,** $\phi = 0.23$. 7.08% gap.

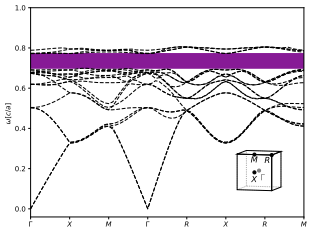

$I = 5$**,** $\phi = 0.15$. 10.59% gap.

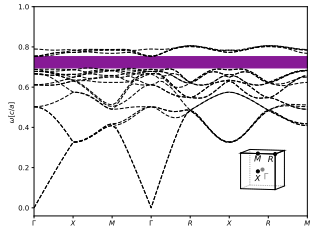

$I = 6$**,** $\phi = 0.15$. 12.65% gap.

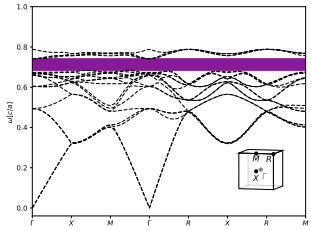

$I = 7$**,** $\phi = 0.16$. 11.48% gap.

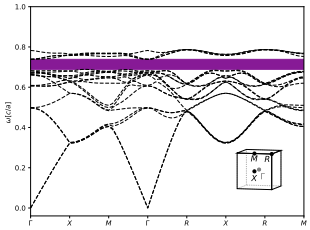

$I = 8$**,** $\phi = 0.16$. 11.6% gap.

A15, $I = 9$, Bands 16 - 17.

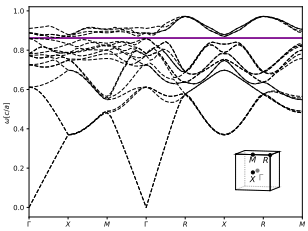

$\varepsilon = 7$, $\phi = 0.21$. 1.68% gap.

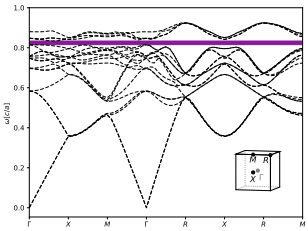

$\varepsilon = 8$, $\phi = 0.21$. 3.43% gap.

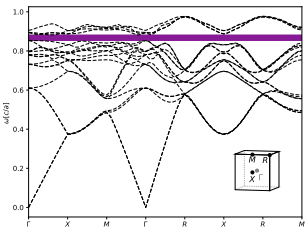

$\varepsilon = 9$, $\phi = 0.16$. 5.04% gap.

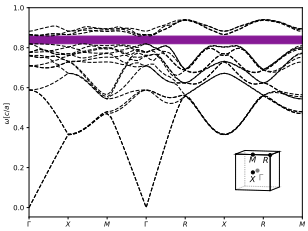

$\varepsilon = 10$, $\phi = 0.16$. 6.66% gap.

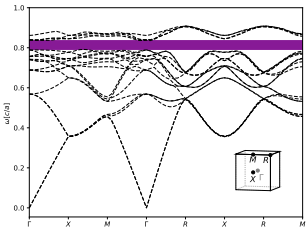

$\varepsilon = 11$, $\phi = 0.16$. 7.99% gap.

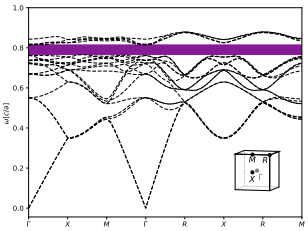

$\varepsilon = 12$, $\phi = 0.16$. 9.2% gap.

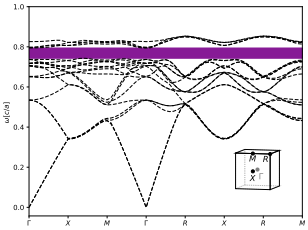

$\varepsilon = 13$, $\phi = 0.16$. 10.18% gap.

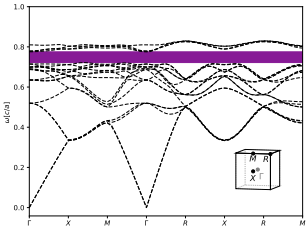

$\varepsilon = 14$, $\phi = 0.16$. 10.85% gap.

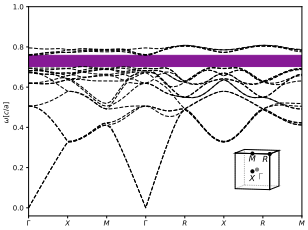

$\varepsilon = 15$, $\phi = 0.16$. 11.45% gap.

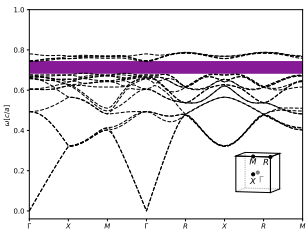

$\varepsilon = 16$, $\phi = 0.16$. 11.98% gap.

Body-Centered Cubic, $\varepsilon = 16$, Bands 6 - 7.

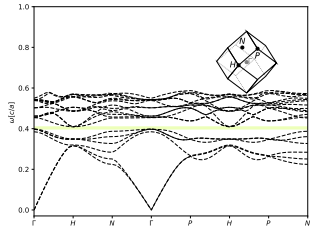

$I = 3$, $\phi = 0.37$. 2.78% gap.

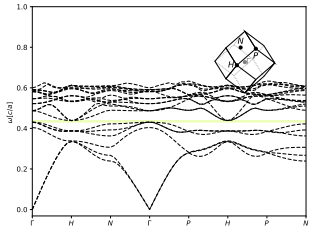

$I = 4$, $\phi = 0.31$. 1.94% gap.

Lithium Oxide, $I = 0$, Bands 17 - 18.

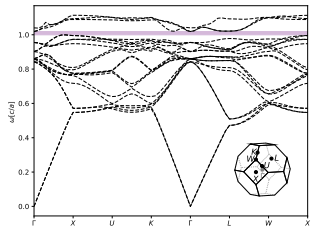

$\varepsilon = 5$, $\phi = 0.25$. 1.94% gap.

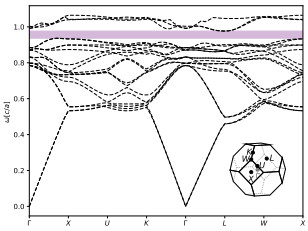

$\varepsilon = 6$, $\phi = 0.25$. 4.07% gap.

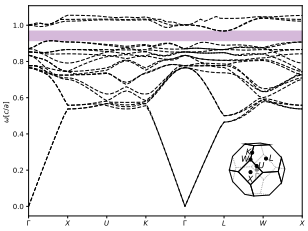

$\varepsilon = 7$, $\phi = 0.22$. 5.51% gap.

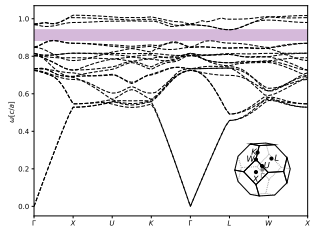

$\varepsilon = 8$, $\phi = 0.22$. 6.15% gap.

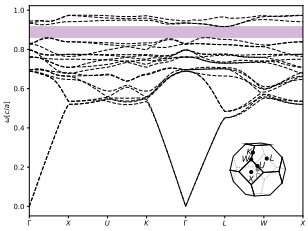

$\varepsilon = 9$, $\phi = 0.22$. 6.11% gap.

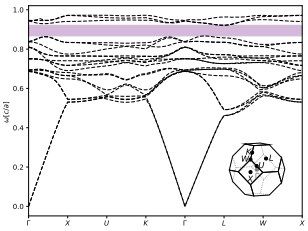

$\varepsilon = 10$, $\phi = 0.19$. 5.85% gap.

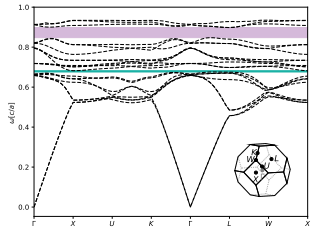

$\varepsilon = 11$, $\phi = 0.19$. 5.51% gap.

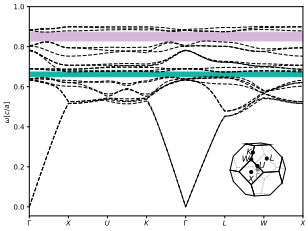

$\varepsilon = 12$, $\phi = 0.19$. (1) 3.5% gap between bands 8-9, and (2) 5.12% gap between bands 17-18.

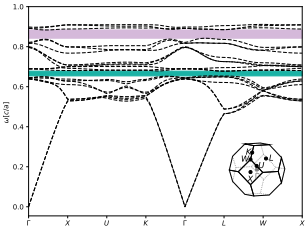

$\varepsilon = 13$, $\phi = 0.16$. (1) 3.48% gap between bands 8-9, and (2) 4.63% gap between bands 17-18.

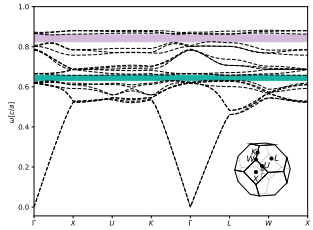

$\varepsilon = 14$, $\phi = 0.16$. (1) 3.83% gap between bands 8-9, and (2) 4.07% gap between bands 17-18.

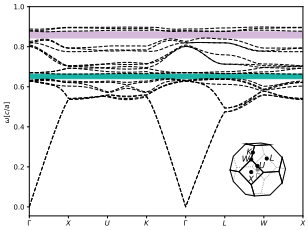

$\varepsilon = 15$, $\phi = 0.14$. (1) 3.5% gap between bands 8-9, and (2) 3.62% gap between bands 17-18.

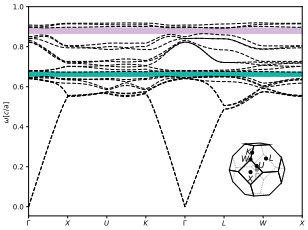

$\varepsilon = 16$, $\phi = 0.12$. (1) 3.15% gap between bands 8-9, and (2) 3.1% gap between bands 17-18.

Lithium Oxide, $I = 0$, Bands 8 - 9.

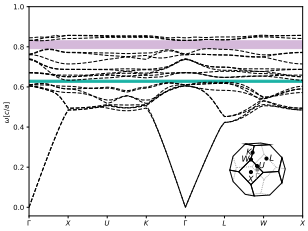

$\varepsilon = 11$, $\phi = 0.25$. (1) 1.66% gap between bands 8-9, and (2) 4.83% gap between bands 17-18.

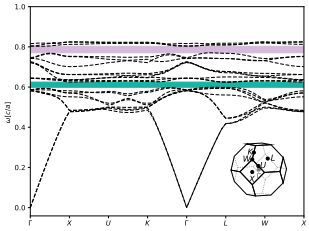

$\varepsilon = 12$, $\phi = 0.25$. (1) 4.15% gap between bands 8-9, and (2) 4.08% gap between bands 17-18.

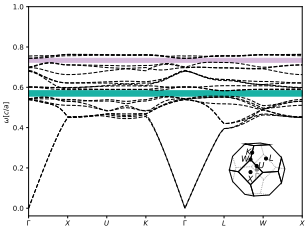

$\varepsilon = 13$, $\phi = 0.28$. (1) 4.67% gap between bands 8-9, and (2) 2.68% gap between bands 17-18.

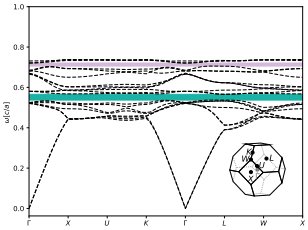

$\varepsilon = 14$, $\phi = 0.28$. (1) 5.09% gap between bands 8-9, and (2) 2.11% gap between bands 17-18.

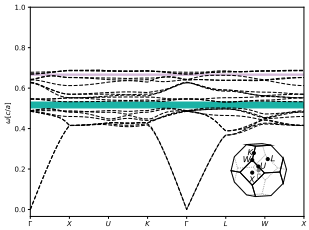

$\varepsilon = 15$, $\phi = 0.31$. 5.46% gap.

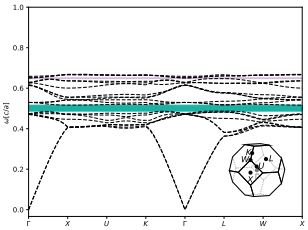

$\varepsilon = 16$, $\phi = 0.31$. 5.86% gap.

Lithium Oxide, $\varepsilon = 16$, Bands 5-6.

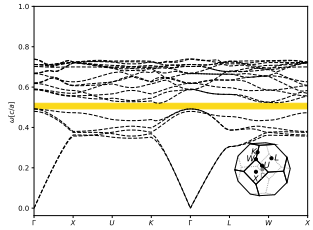

$I = 1$, $\phi = 0.27$. 6.0% gap between bands 5-6.

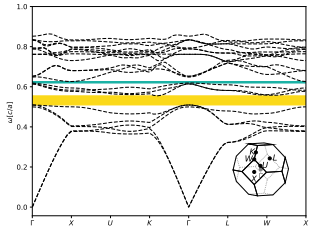

$I = 2$, $\phi = 0.19$. (1) 8.65% gap between bands 5-6, and (2) 1.37% gap between bands 8-9.

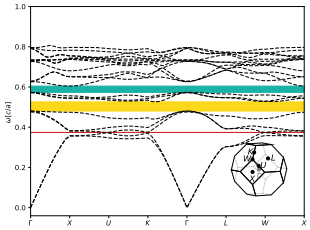

$I = 3$, $\phi = 0.21$. (1) 9.12% gap between bands 5-6, and (2) 5.34% gap between bands 8-9.

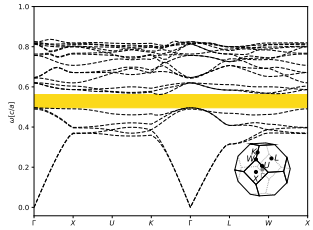

$I = 4$, $\phi = 0.19$. 12.89% gap between bands 5-6.

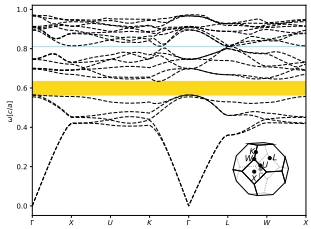

$I = 5$, $\phi = 0.13$. 13.08% gap.

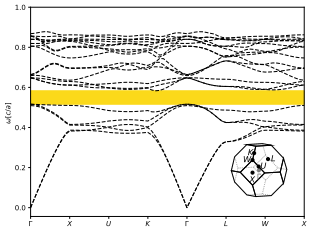

$I = 6$, $\phi = 0.17$. 16.03% gap.

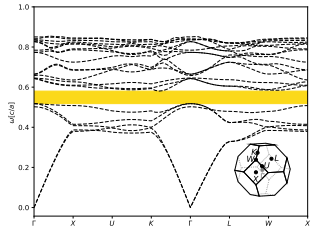

$I = 7$, $\phi = 0.17$. 15.8% gap.

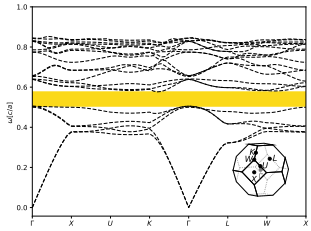

$I = 8$, $\phi = 0.17$. 15.89% gap.

Lithium Oxide, $\varepsilon = 16$, Bands 8-9.

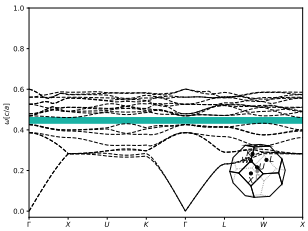

$I = 1$, $\phi = 0.41$. 6.32% gap between bands 8-9.

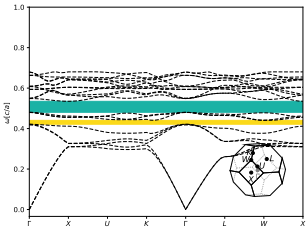

$I = 2$, $\phi = 0.3$. (1) 4.4% gap between bands 5-6, and (2) 10.72% gap between bands 8-9.

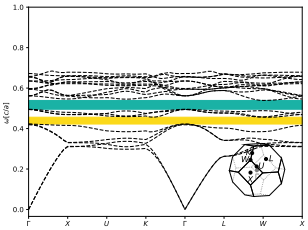

$I = 3$, $\phi = 0.29$. (1) 8.03% gap between bands 5-6, and (2) 8.18% gap between bands 8-9.

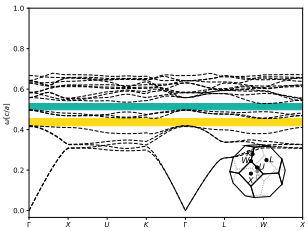

$I = 4$, $\phi = 0.3$. (1) 7.94% gap between bands 5-6, and (2) 6.52% gap between bands 8-9.

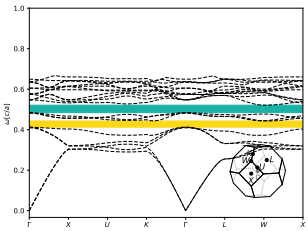

$I = 5$, $\phi = 0.3$. (1) 7.35% gap between bands 5-6, and (2) 7.32% gap between bands 8-9.

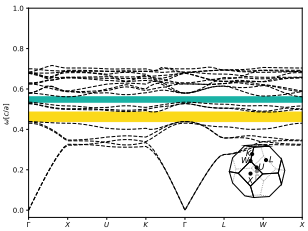

$I = 6$, $\phi = 0.27$. (1) 10.92% gap between bands 5-6, and (2) 7.33% gap between bands 8-9.

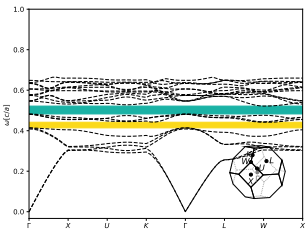

$I = 7$, $\phi = 0.31$. (2) 8.74% gap between bands 5-6, and (3) 7.08% gap between bands 8-9.

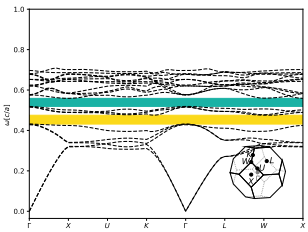

$I = 8$, $\phi = 0.27$. (1) 10.84% gap between bands 5-6, and (2) 7.37% gap between bands 8-9.

Lithium Oxide, $I = 9$, Bands 5-6.

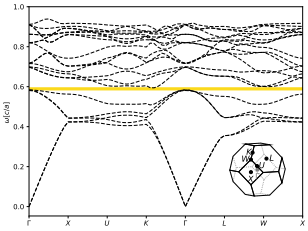

$\varepsilon = 9$, $\phi = 0.24$. 3.32% gap.

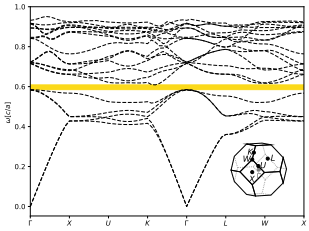

$\varepsilon = 10$, $\phi = 0.2$. 5.78% gap.

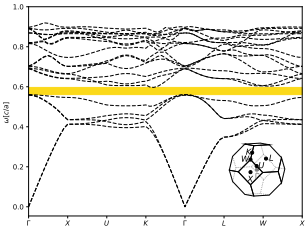

$\varepsilon = 11$, $\phi = 0.2$. 7.97% gap.

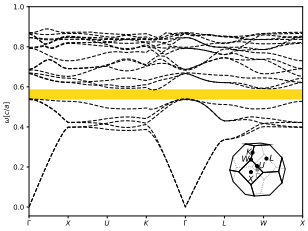

$\varepsilon = 12$, $\phi = 0.2$. 9.83% gap.

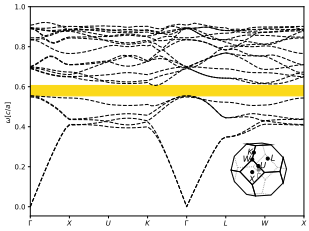

$\varepsilon = 13$, $\phi = 0.17$. 11.66% gap.

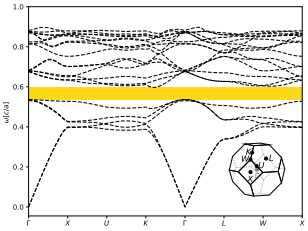

$\varepsilon = 14$, $\phi = 0.17$. 13.36% gap.

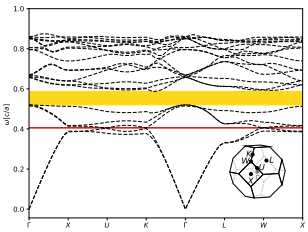

$\varepsilon = 15$, $\phi = 0.17$. 14.85% gap.

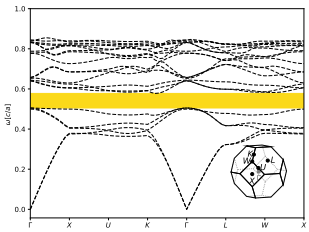

$\varepsilon = 16$, $\phi = 0.17$. 16.13% gap.

Lithium Oxide, $I = 9$, Bands 8-9.

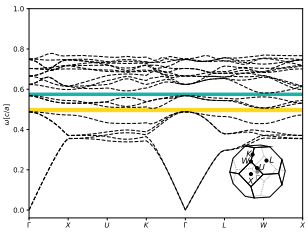

$\varepsilon = 11$, $\phi = 0.31$. (1) 4.66% gap between bands 5-6, and (2) 2.05% gap between bands 8-9.

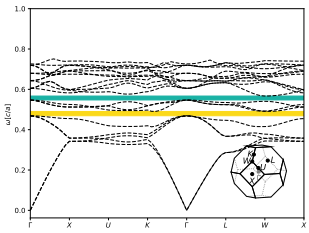

$\varepsilon = 12$, $\phi = 0.31$. (1) 5.76% gap between bands 5-6, and (2) 3.38% gap between bands 8-9.

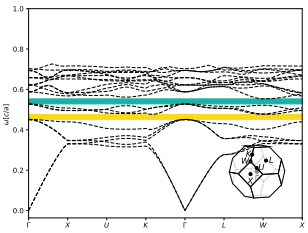

$\varepsilon = 13$, $\phi = 0.31$. (1) 6.68% gap between bands 5-6, and (2) 4.49% gap between bands 8-9.

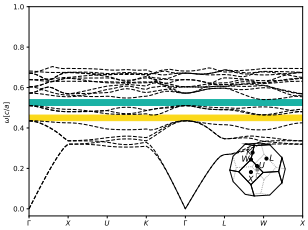

$\varepsilon = 14$, $\phi = 0.31$. (2) 7.46% gap between bands 5-6, and (3) 5.44% gap between bands 8-9.

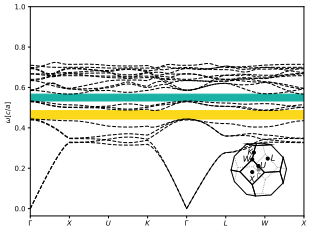

$\varepsilon = 15$, $\phi = 0.27$. (1) 10.26% gap between bands 5-6, and (2) 6.31% gap between bands 8-9.

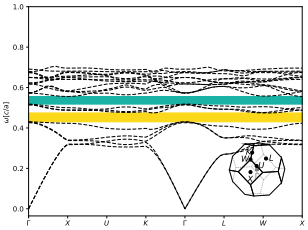

$\varepsilon = 16$, $\phi = 0.27$. (1) 10.93% gap between bands 5-6, and (2) 7.14% gap between bands 8-9.

Simple Chiral Cubic, $I = 0$, Bands 16 - 17.

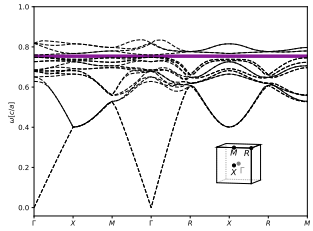

$\varepsilon = 10$, $\phi = 0.18$. 1.59% gap.

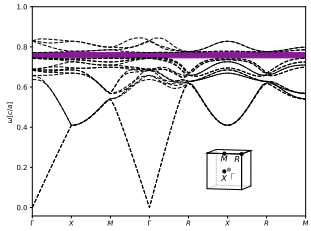

$\varepsilon = 11$, $\phi = 0.16$. 3.52% gap.

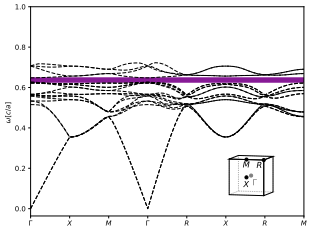

$\varepsilon = 12$, $\phi = 0.26$. 3.38% gap.

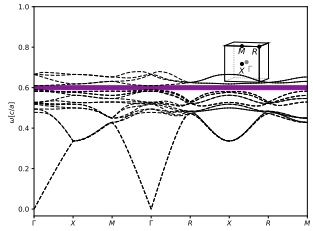

$\varepsilon = 13$, $\phi = 0.29$. 3.27% gap.

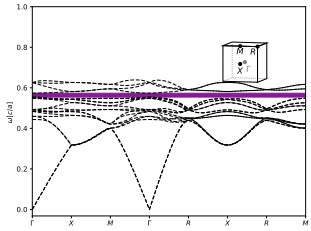

$\varepsilon = 14$, $\phi = 0.33$. 3.5% gap.

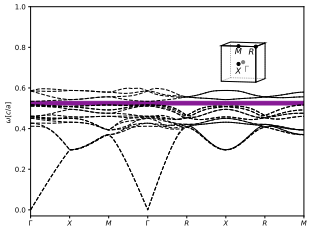

$\varepsilon = 15$, $\phi = 0.37$. 3.23% gap.

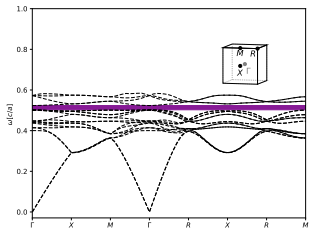

$\varepsilon = 16$, $\phi = 0.37$. 4.23% gap.

Simple Chiral Cubic, $\varepsilon = 16$, Bands 4 - 5.

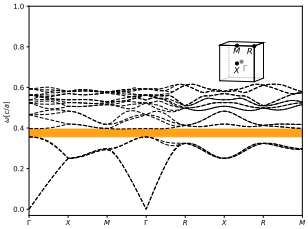

$I = 1$, $\phi = 0.32$. 10.6% gap.

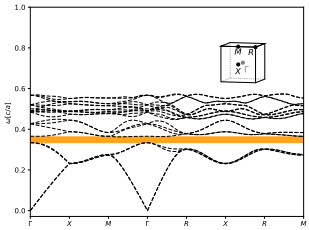

$I = 2$, $\phi = 0.35$. 8.74% gap.

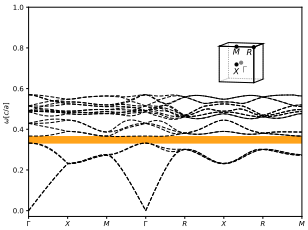

$I = 3$, $\phi = 0.33$. 9.65% gap.

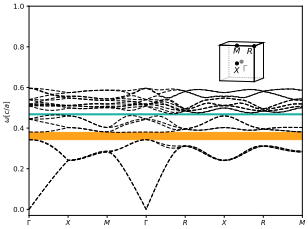

$I = 4$, $\phi = 0.3$. (1) 9.94% gap between bands 4-5, and (2) 1.62% gap between bands 8-9.

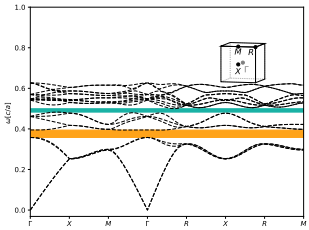

$I = 5$, $\phi = 0.27$. (1) 9.63% gap between bands 4-5, and (2) 3.95% gap between bands 8-9.

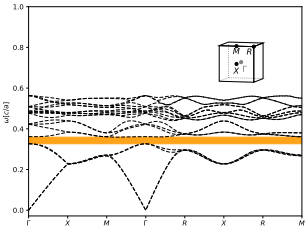

$I = 6$, $\phi = 0.35$. 9.67% gap.

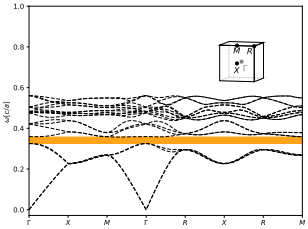

$I = 7$, $\phi = 0.35$. 9.63% gap.

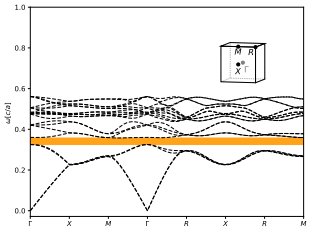

$I = 8$, $\phi = 0.35$. 9.71% gap.

Simple Chiral Cubic, $\varepsilon = 16$, Bands 8 - 9.

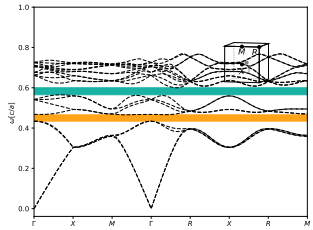

$I = 2$, $\phi = 0.19$. (1) 7.08% gap between bands 4-5, and (2) 6.08% gap between bands 8-9.

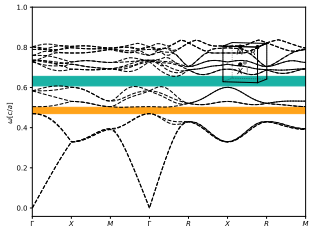

$I = 3$, $\phi = 0.15$. (1) 6.7% gap between bands 4-5, and (2) 7.44% gap between bands 8-9.

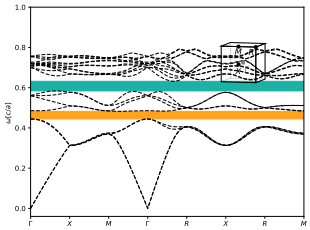

$I = 4$, $\phi = 0.16$. (1) 8.46% gap between bands 4-5, and (2) 8.91% gap between bands 8-9.

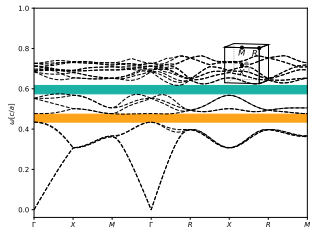

$I = 5$, $\phi = 0.17$. (1) 9.22% gap between bands 4-5, and (2) 8.82% gap between bands 8-9.

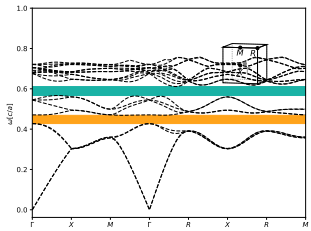

$I = 6$, $\phi = 0.17$. (1) 9.15% gap between bands 4-5, and (2) 8.91% gap between bands 8-9.

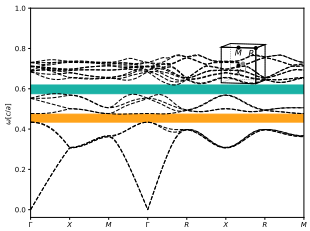

$I = 7$, $\phi = 0.17$. (1) 9.03% gap between bands 4-5, and (2) 9.14% gap between bands 8-9.

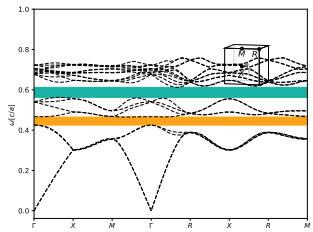

$I = 8$, $\phi = 0.18$. (1) 8.97% gap between bands 4-5, and (2) 9.29% gap between bands 8-9.

Simple Chiral Cubic, $I = 9$, Bands 4 - 5.

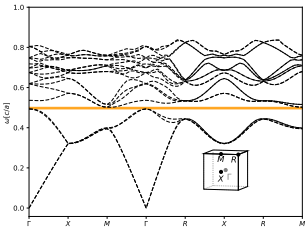

$\varepsilon = 7$, $\phi = 0.31$. 2.0% gap.

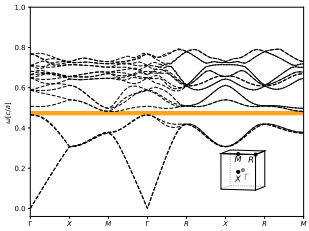

$\varepsilon = 8$, $\phi = 0.31$. 3.9% gap.

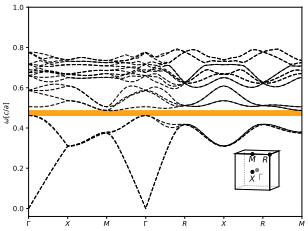

$\varepsilon = 9$, $\phi = 0.28$. 5.4% gap.

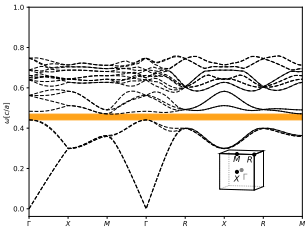

$\varepsilon = 10$, $\phi = 0.28$. 6.65% gap.

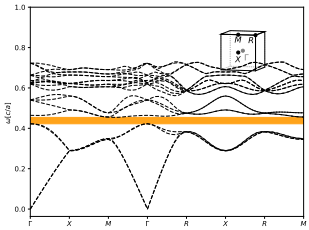

$\varepsilon = 11$, $\phi = 0.28$. 7.67% gap.

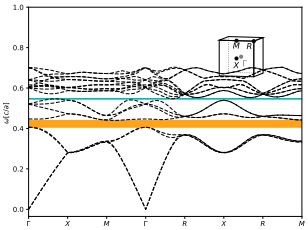

$\varepsilon = 12$, $\phi = 0.28$. 8.5% gap.

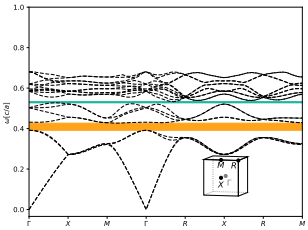

$\varepsilon = 13$, $\phi = 0.28$. (1) 9.05% gap between bands 4-5, and (2) 1.44% gap between bands 8-9.

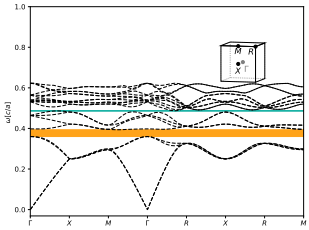

$\varepsilon = 14$, $\phi = 0.31$. 9.31% gap.

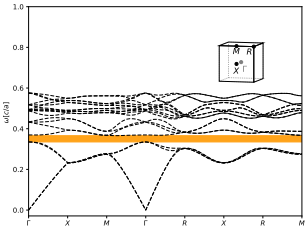

$\varepsilon = 15$, $\phi = 0.35$. 9.5% gap.

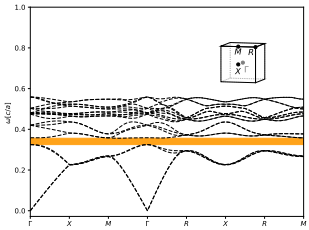

$\varepsilon = 16$, $\phi = 0.35$. 9.65% gap.

Simple Chiral Cubic, $I = 9$, Bands 8-9.

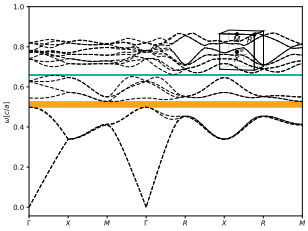

$\varepsilon = 11$, $\phi = 0.18$. (1) 6.08% gap between bands 4-5, and (2) 1.55% gap between bands 8-9.

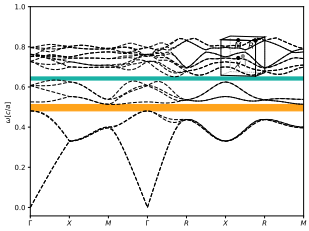

$\varepsilon = 12$, $\phi = 0.18$. (1) 7.14% gap between bands 4-5, and (2) 3.42% gap between bands 8-9.

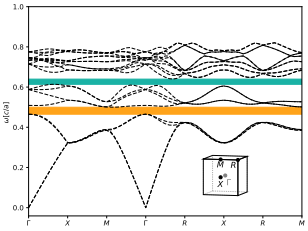

$\varepsilon = 13$, $\phi = 0.18$. (1) 8.01% gap between bands 4-5, and (2) 5.13% gap between bands 8-9.

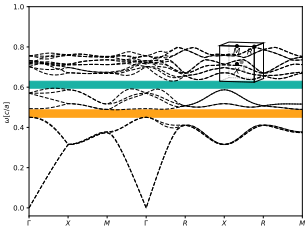

$\varepsilon = 14$, $\phi = 0.18$. (1) 8.53% gap between bands 4-5, and (2) 6.69% gap between bands 8-9.

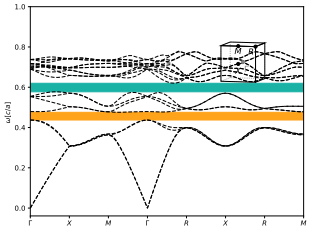

$\varepsilon = 15$, $\phi = 0.18$. (1) 8.77% gap between bands 4-5, and (2) 8.11% gap between bands 8-9.

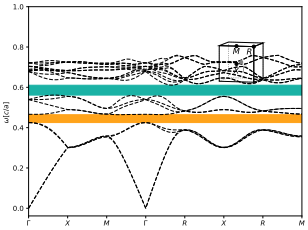

$\varepsilon = 16$, $\phi = 0.18$. (1) 8.9% gap between bands 4-5, and (2) 9.4% gap between bands 8-9.

Diamond, $I = 0$, Bands 2 - 3.

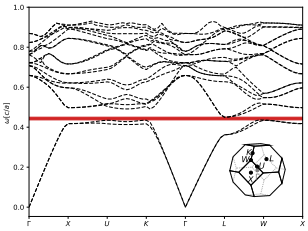

$\varepsilon = 5$, $\phi = 0.42$. 2.88% gap.

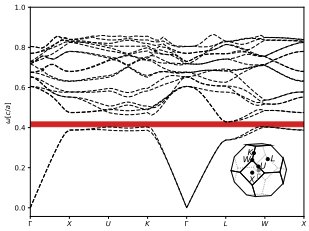

$\varepsilon = 6$, $\phi = 0.42$. 5.52% gap.

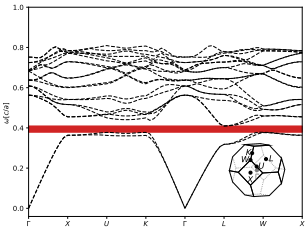

$\varepsilon = 7$, $\phi = 0.42$. 7.55% gap.

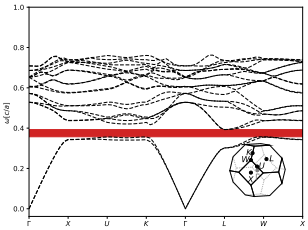

$\varepsilon = 8$, $\phi = 0.42$. 9.16% gap.

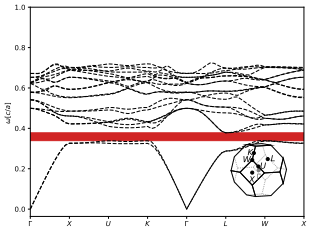

$\varepsilon = 9$, $\phi = 0.42$. 10.45% gap.

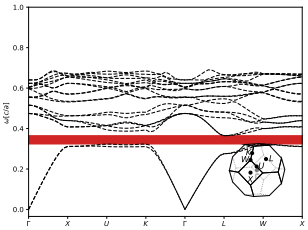

$\varepsilon = 10$, $\phi = 0.42$. 11.5% gap.

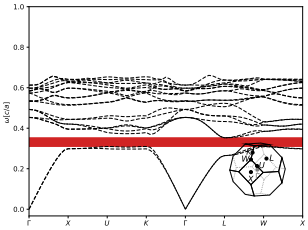

$\varepsilon = 11$, $\phi = 0.42$. 12.36% gap.

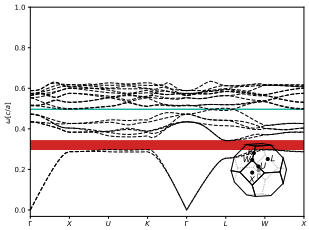

$\varepsilon = 12$, $\phi = 0.42$. (1) 13.09% gap between bands 2-3, and (2) 1.38% gap between bands 8-9.

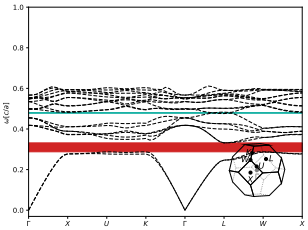

$\varepsilon = 13$, $\phi = 0.42$. (1) 13.71% gap between bands 2-3, and (2) 1.32% gap between bands 8-9.

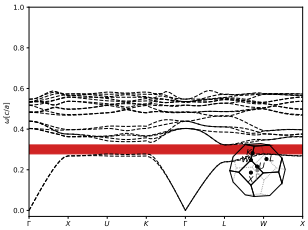

$\varepsilon = 14$, $\phi = 0.42$. 14.24% gap.

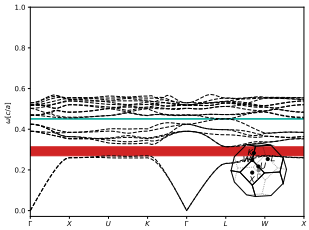

$\varepsilon = 15$, $\phi = 0.42$. 14.69% gap.

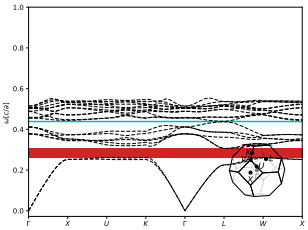

$\varepsilon = 16$, $\phi = 0.42$. 15.09% gap.

Diamond, $I = 0$, Bands 8-9.

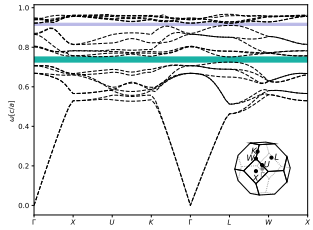

$\varepsilon = 9$, $\phi = 0.16$. 3.21% gap.

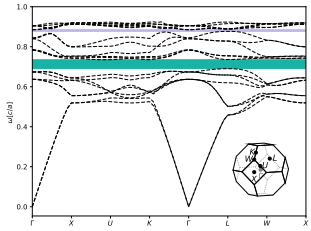

$\varepsilon = 10$, $\phi = 0.16$. 5.98% gap.

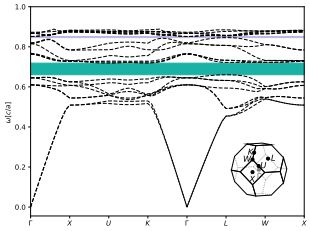

$\varepsilon = 11$, $\phi = 0.16$. 8.24% gap.

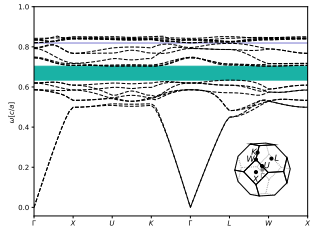

$\varepsilon = 12$, $\phi = 0.16$. 10.22% gap.

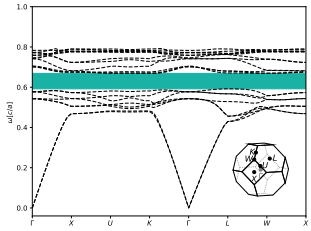

$\varepsilon = 13$, $\phi = 0.19$. 11.9% gap.

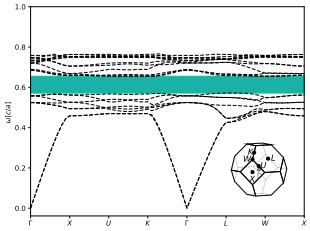

$\varepsilon = 14$, $\phi = 0.19$. 13.38% gap.

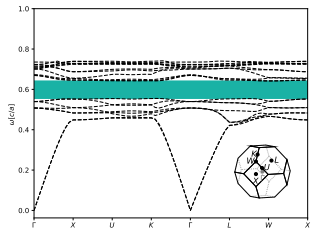

$\varepsilon = 15$, $\phi = 0.19$. 14.4% gap.

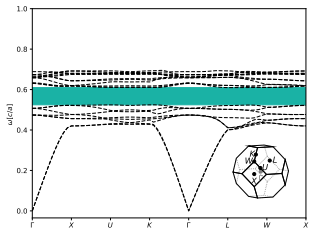

$\varepsilon = 16$, $\phi = 0.21$. 14.54% gap.

Diamond, $I = 0$, Bands 14 - 15.

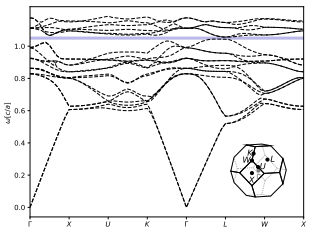

$\varepsilon = 8$, $\phi = 0.09$. 1.12% gap.

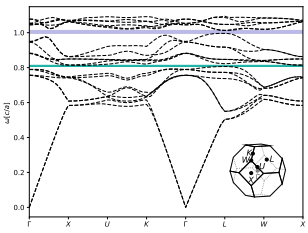

$\varepsilon = 9$, $\phi = 0.11$. 1.42% gap.

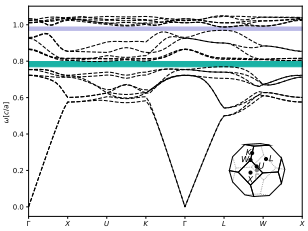

$\varepsilon = 10$, $\phi = 0.11$. (1) 3.82% gap between bands 8-9, and (2) 1.54% gap between bands 14-15.

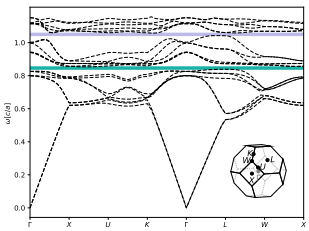

$\varepsilon = 11$, $\phi = 0.07$. (1) 2.09% gap between bands 8-9, and (2) 1.61% gap between bands 14-15.

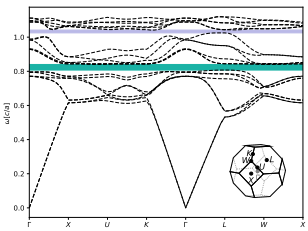

$\varepsilon = 12$, $\phi = 0.07$. (1) 4.06% gap between bands 8-9, and (2) 1.57% gap between bands 14-15.

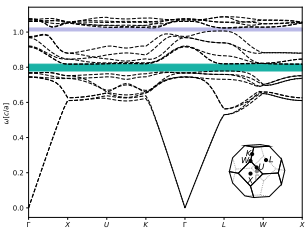

$\varepsilon = 13$, $\phi = 0.07$. (1) 4.84% gap between bands 8-9, and (2) 1.45% gap between bands 14-15.

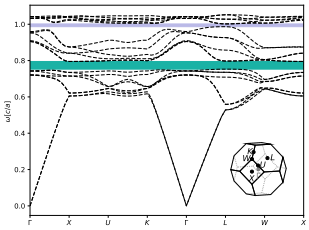

$\varepsilon = 14$, $\phi = 0.07$. (1) 5.41% gap between bands 8-9, and (2) 1.28% gap between bands 14-15.

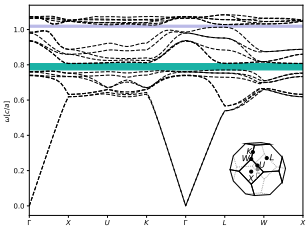

$\varepsilon = 15$, $\phi = 0.06$. (1) 4.58% gap between bands 8-9, and (2) 1.22% gap between bands 14-15.

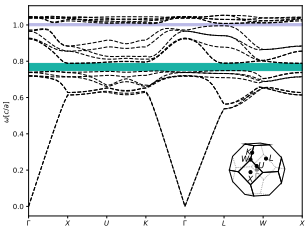

$\varepsilon = 16$, $\phi = 0.06$. 5.14% gap.

Diamond, $\varepsilon = 16$, Bands 2-3.

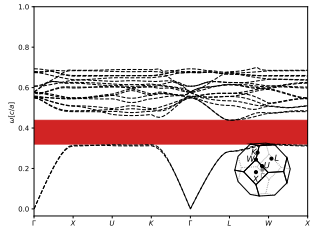

$I = 1$, $\phi = 0.23$. 30.8% gap.

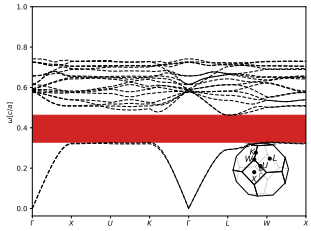

$I = 2$, $\phi = 0.19$. 33.77% gap.

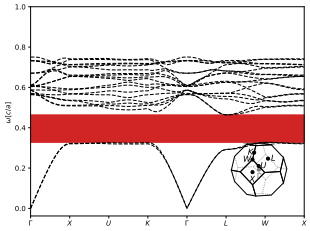

$I = 3$, $\phi = 0.18$. 34.4% gap.

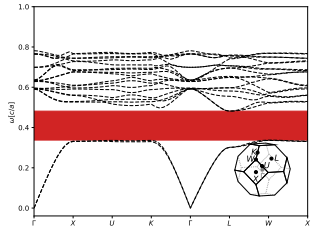

$I = 4$, $\phi = 0.17$. 34.97% gap.

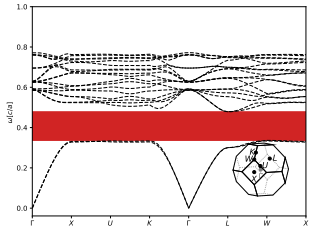

$I = 5$, $\phi = 0.17$. 34.85% gap.

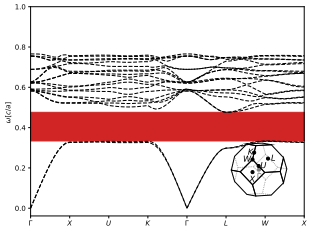

$I = 6$, $\phi = 0.17$. 35.07% gap.

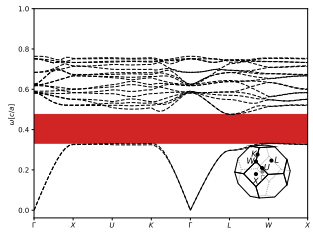

$I = 7$, $\phi = 0.17$. 35.28% gap.

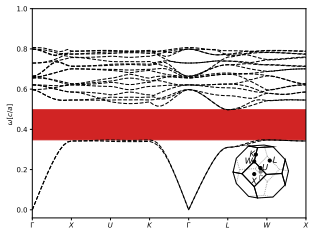

$I = 8$, $\phi = 0.15$. 35.28% gap.

Diamond, $I = 9$, Bands 2 - 3.

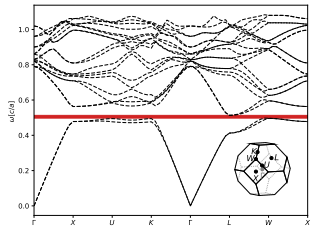

$\varepsilon = 4$, $\phi = 0.32$. 3.12% gap.

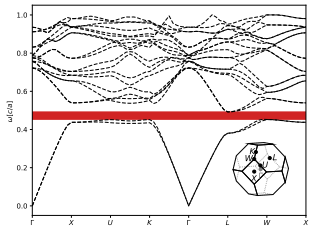

$\varepsilon = 5$, $\phi = 0.32$. 8.12% gap.

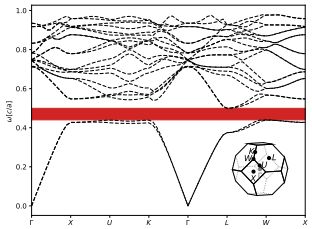

$\varepsilon = 6$, $\phi = 0.27$. 12.44% gap.

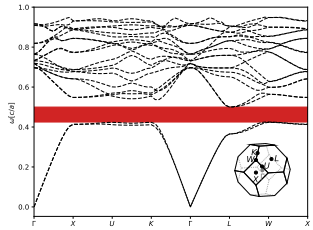

$\varepsilon = 7$, $\phi = 0.24$. 16.03% gap.

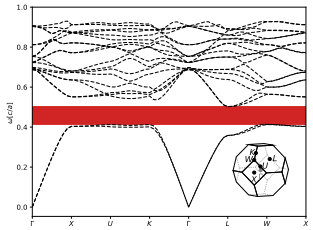

$\varepsilon = 8$, $\phi = 0.22$. 19.28% gap.

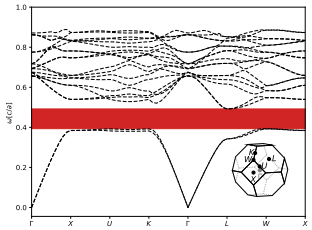

$\varepsilon = 9$, $\phi = 0.22$. 22.14% gap.

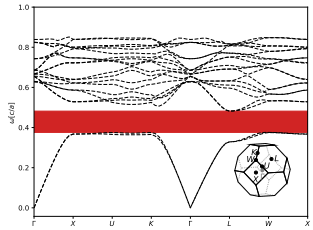

$\varepsilon = 10$, $\phi = 0.22$. 24.52% gap.

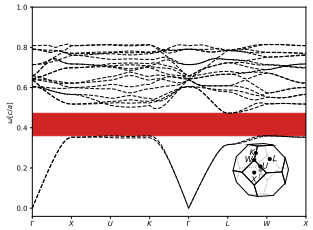

$\varepsilon = 11$, $\phi = 0.22$. 26.63% gap.

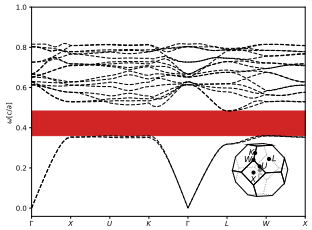

$\varepsilon = 12$, $\phi = 0.19$. 28.64% gap.

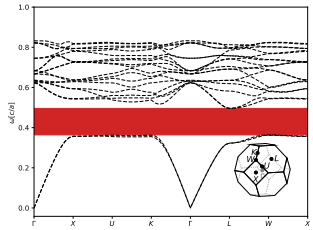

$\varepsilon = 13$, $\phi = 0.17$. 30.55% gap.

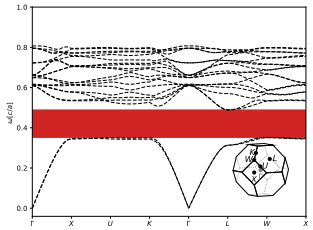

$\varepsilon = 14$, $\phi = 0.17$. 32.31% gap.

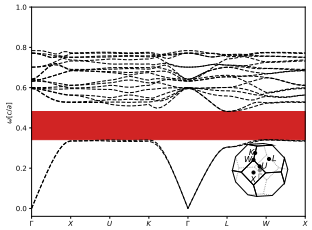

$\varepsilon = 15$, $\phi = 0.17$. 33.88% gap.

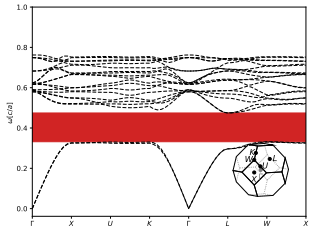

$\varepsilon = 16$, $\phi = 0.17$. 35.34% gap.

Face-Centered Cubic, $\varepsilon = 16$, Bands 8 - 9.

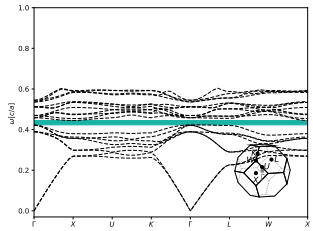

$I = 3$, $\phi = 0.43$. 4.97% gap.

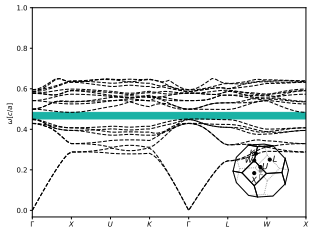

$I = 4$, $\phi = 0.36$. 6.97% gap.

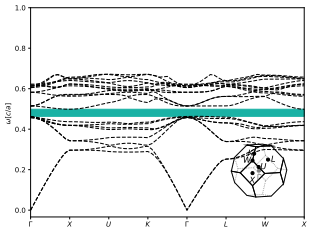

$I = 5$, $\phi = 0.33$. 7.27% gap.

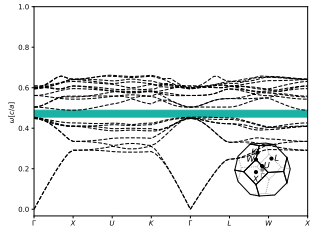

$I = 6$, $\phi = 0.35$. 7.32% gap.

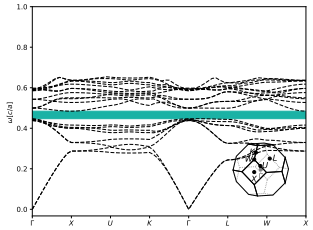

$I = 7$, $\phi = 0.35$. 8.07% gap.

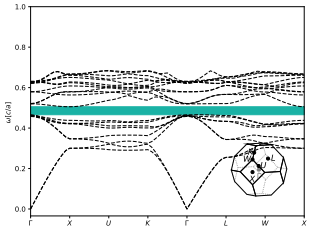

$I = 8$, $\phi = 0.31$. 8.17% gap.

Face-Centered Cubic, $I = 9$, Bands 8-9.

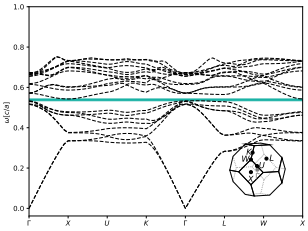

$\varepsilon = 10$, $\phi = 0.4$. 2.29% gap.

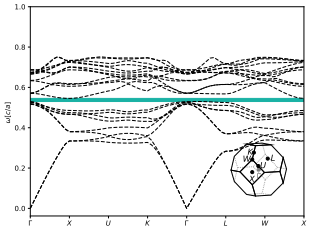

$\varepsilon = 11$, $\phi = 0.36$. 3.52% gap.

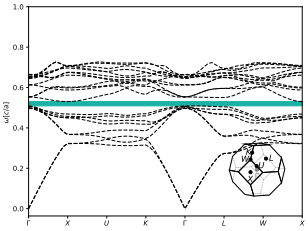

$\varepsilon = 12$, $\phi = 0.36$. 4.73% gap.

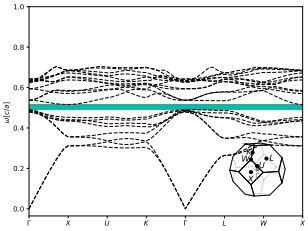

$\varepsilon = 13$, $\phi = 0.36$. 5.82% gap.

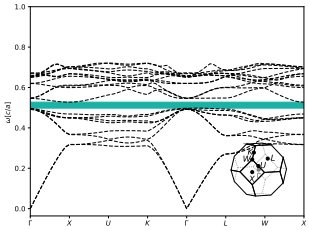

$\varepsilon = 14$, $\phi = 0.32$. 6.86% gap.

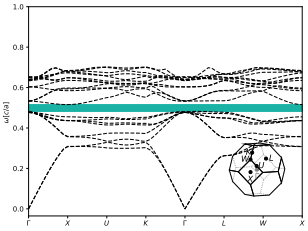

$\varepsilon = 15$, $\phi = 0.32$. 7.84% gap.

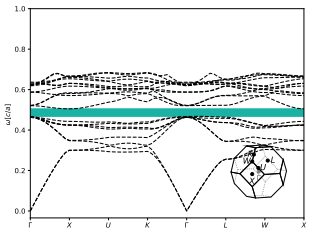

$\varepsilon = 16$, $\phi = 0.32$. 8.85% gap.

Face-Centered Cubic (Modified), $\varepsilon = 16$, Bands 11 - 12.

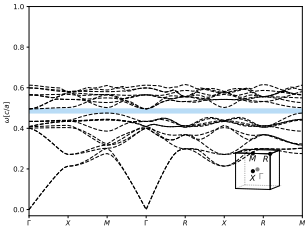

$I = 3$, $\phi = 0.33$. 4.17% gap.

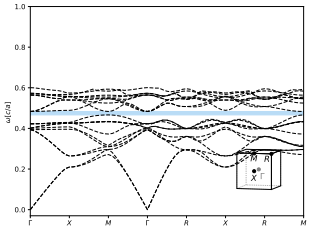

$I = 4$, $\phi = 0.35$. 3.94% gap.

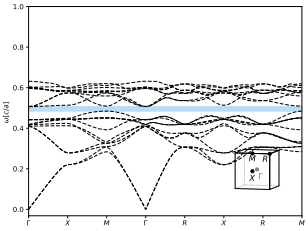

$I = 5$, $\phi = 0.31$. 4.19% gap.

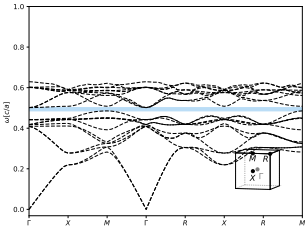

$I = 6$, $\phi = 0.32$. 4.22% gap.

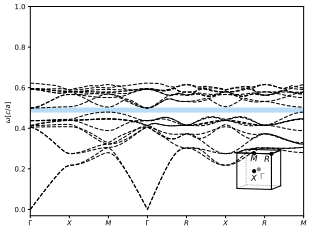

$I = 7$, $\phi = 0.32$. 4.12% gap.

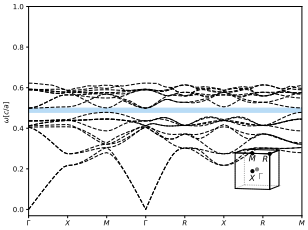

$I = 8$, $\phi = 0.32$. 4.23% gap.

Face-Centered Cubic (Modified), $I = 9$, Bands 11 - 12.

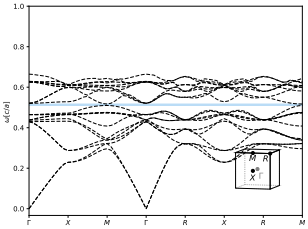

$\varepsilon = 14$, $\phi = 0.32$. 2.36% gap.

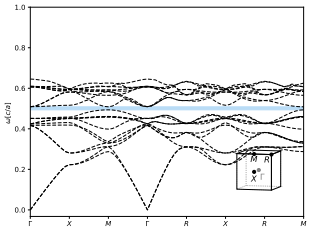

$\varepsilon = 15$, $\phi = 0.32$. 3.38% gap.

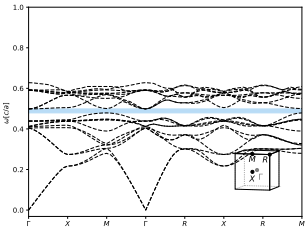

$\varepsilon = 16$, $\phi = 0.32$. 4.31% gap.

Lonsdaleite (Hexagonal Diamond), $\varepsilon = 16$, Bands 16 - 17.

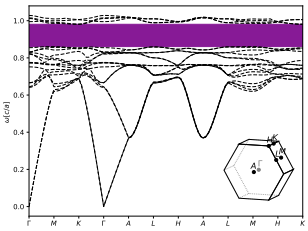

$I = 0$, $\varepsilon = 16$, $\phi = 0.22$. 12.54% gap.

Lonsdaleite (Hexagonal Diamond), $\varepsilon = 16$, Bands 4 - 5.

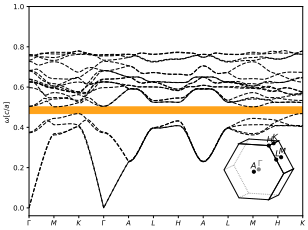

$I = 0$, $\phi = 0.42$. 6.8% gap.

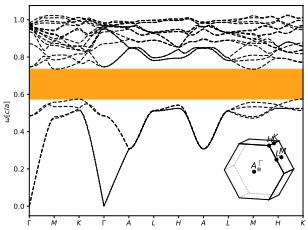

$I = 1$, $\phi = 0.2$. 24.08% gap.

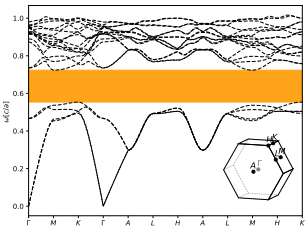

$I = 2$, $\phi = 0.21$. 26.45% gap.

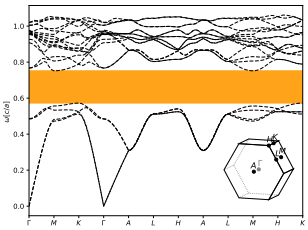

$I = 3$, $\phi = 0.18$. 26.81% gap.

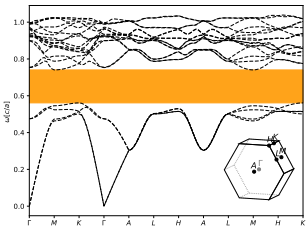

$I = 4$, $\phi = 0.19$. 27.18% gap.

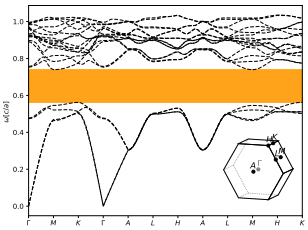

$I = 5$, $\phi = 0.19$. 27.11% gap.

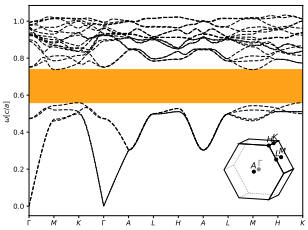

$I = 6$, $\phi = 0.19$. 28.5% gap.

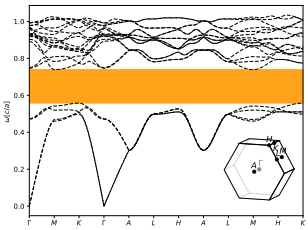

$I = 7$, $\phi = 0.19$. 28.55% gap.

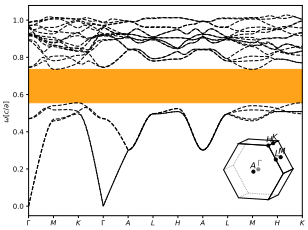

$I = 8$, $\phi = 0.19$. 28.45% gap.

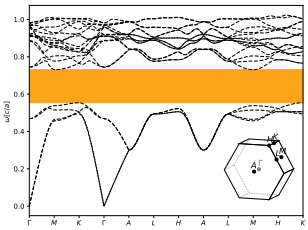

$\varepsilon = 16$, $\phi = 0.19$. 28.49% gap.

Hexagonal Close Packing, $\varepsilon = 16$, Bands 4 - 5.

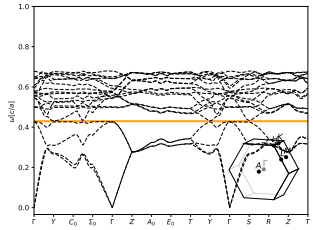

$I = 2$, $\phi = 0.26$. 1.18% gap.

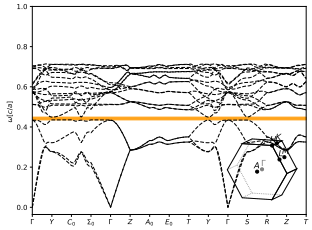

$I = 3$, $\phi = 0.22$. 3.02% gap.

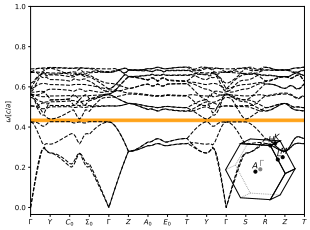

$I = 4$, $\phi = 0.23$. 3.07% gap.

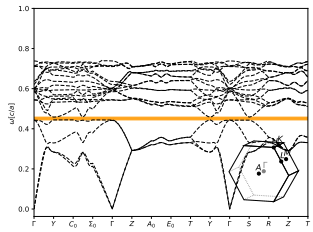

$I = 5$, $\phi = 0.21$. 3.08% gap.

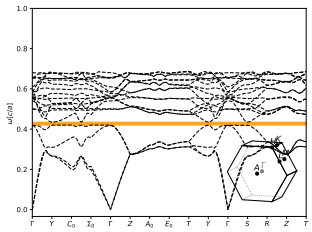

$I = 6$, $\phi = 0.24$. 3.39% gap.

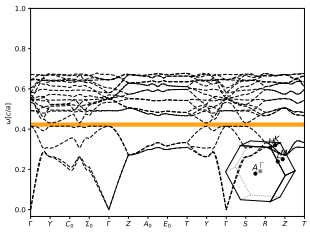

$I = 7$, $\phi = 0.24$. 3.69% gap.

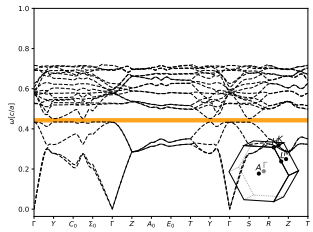

$I = 8$, $\phi = 0.21$. 3.71% gap.

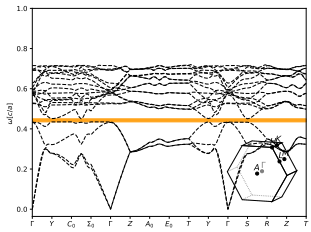

$I = 9$, $\phi = 0.22$. 4.57% gap.

Simple Hexagonal, $\varepsilon = 16$, Bands 16 - 17.

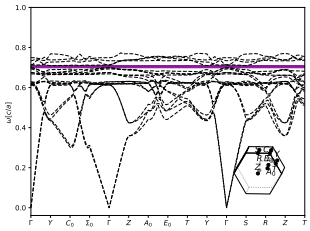

$I = 1$, $\varepsilon = 16$, $\phi = 0.17$. 1.54% gap.

Simple Hexagonal, $\varepsilon = 16$, Bands 6 - 7.

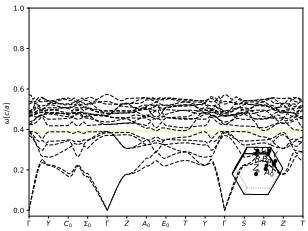

$I = 3$, $\phi = 0.36$. 1.24% gap.

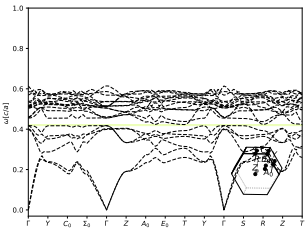

$I = 4$, $\phi = 0.31$. 1.23% gap.

Pyrite, $\varepsilon = 16$, Bands 12 - 13.

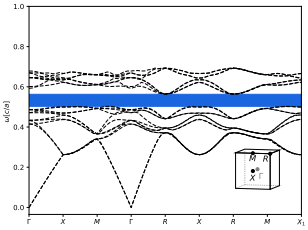

$I = 1$, $\phi = 0.3$. 11.72% gap.

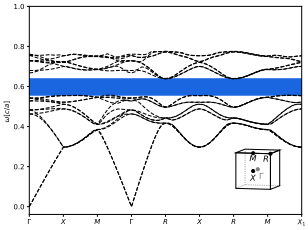

$I = 2$, $\phi = 0.21$. 15.19% gap.

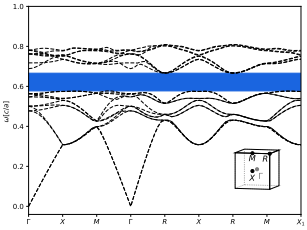

$I = 3$, $\phi = 0.18$. 15.87% gap.

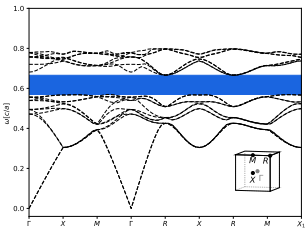

$I = 4$, $\phi = 0.19$. 16.97% gap.

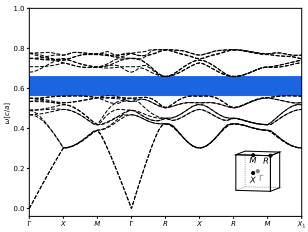

$I = 5$, $\phi = 0.19$. 17.31% gap.

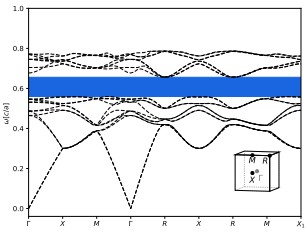

$I = 6$, $\phi = 0.2$. 17.4% gap.

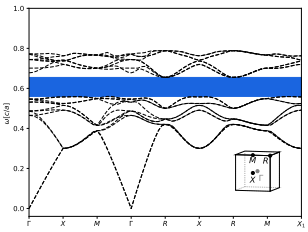

$I = 7$, $\phi = 0.2$. 17.53% gap.

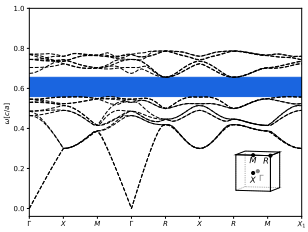

$I = 8$, $\phi = 0.2$. 17.37% gap.

Pyrite, $I = 9$, Bands 12 - 13.

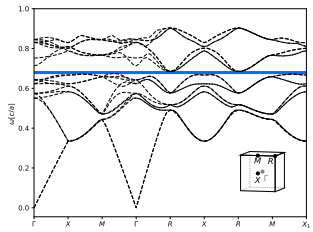

$\varepsilon = 9$, $\phi = 0.24$. 3.29% gap.

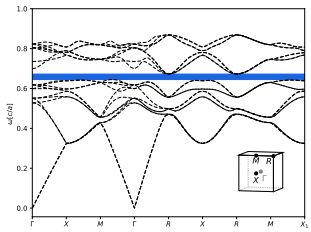

$\varepsilon = 10$, $\phi = 0.24$. 5.9% gap.

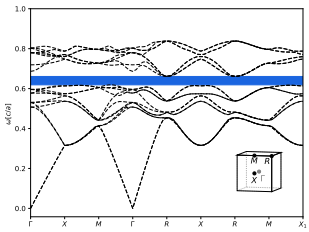

$\varepsilon = 11$, $\phi = 0.24$. 8.2% gap.

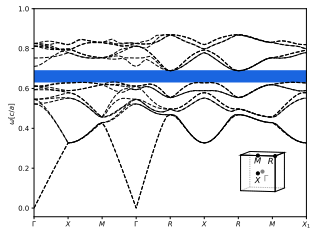

$\varepsilon = 12$, $\phi = 0.2$. 10.27% gap.

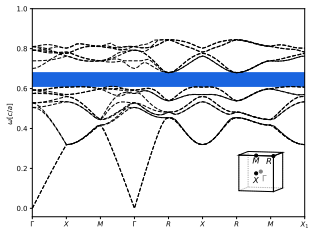

$\varepsilon = 13$, $\phi = 0.2$. 12.36% gap.

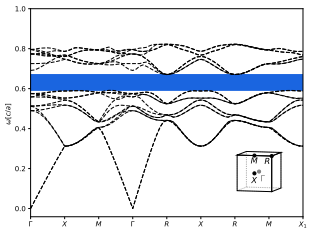

$\varepsilon = 14$, $\phi = 0.2$. 14.25% gap.

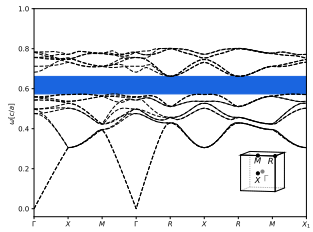

$\varepsilon = 15$, $\phi = 0.2$. 15.94% gap.

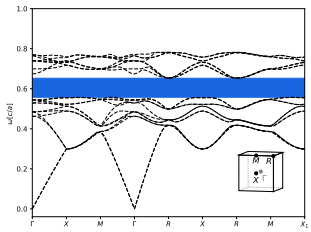

$\varepsilon = 16$, $\phi = 0.2$. 17.47% gap.

Simple Cubic, $\varepsilon = 16$, Bands 2-3.

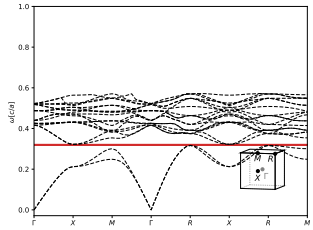

$I = 1$, $\phi = 0.33$. 1.94% gap.

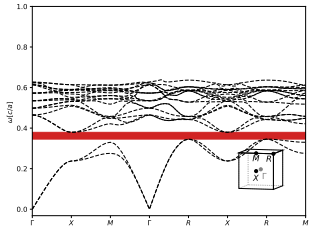

$I = 2$, $\phi = 0.22$. 9.26% gap.

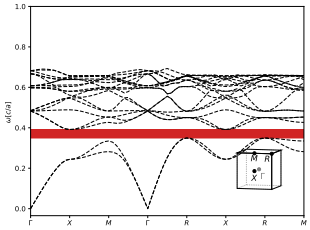

$I = 4$, $\phi = 0.17$. 11.28% gap.

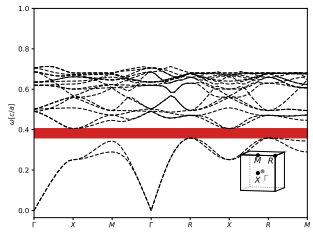

$I = 5$, $\phi = 0.16$. 11.9% gap.

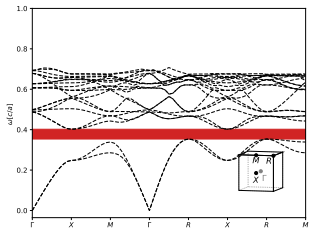

$I = 6$, $\phi = 0.16$. 12.75% gap.

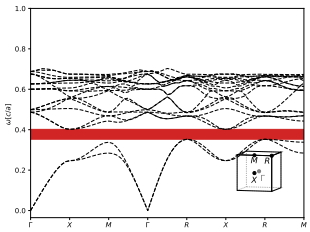

$I = 7$, $\phi = 0.16$. 12.89% gap.

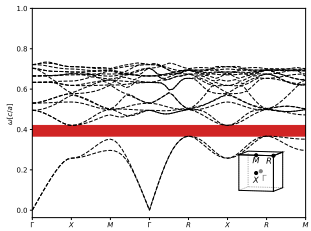

$I = 8$, $\phi = 0.15$. 13.26% gap.

Simple Cubic, $\varepsilon = 16$, Bands 14-15.

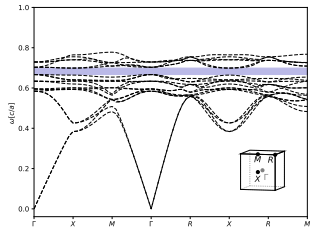

$I = 1$, $\varepsilon = 16$, $\phi = 0.13$. 4.68% gap.

Simple Cubic, $I = 9$, Bands 2 - 3.

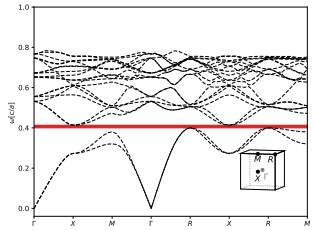

$\varepsilon = 11$, $\phi = 0.19$. 3.2% gap.

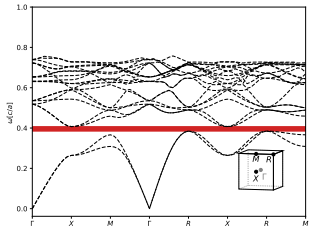

$\varepsilon = 12$, $\phi = 0.19$. 5.54% gap.

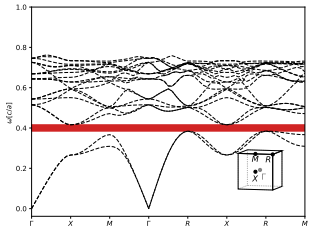

$\varepsilon = 13$, $\phi = 0.17$. 7.75% gap.

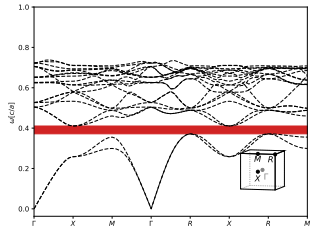

$\varepsilon = 14$, $\phi = 0.17$. 9.76% gap.

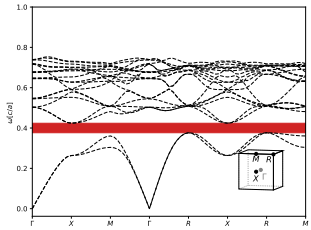

$\varepsilon = 15$, $\phi = 0.15$. 11.69% gap.

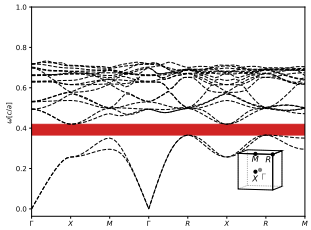

$\varepsilon = 16$, $\phi = 0.15$. 13.53% gap.

CN=10, $\varepsilon = 16$, Bands 7 - 8.

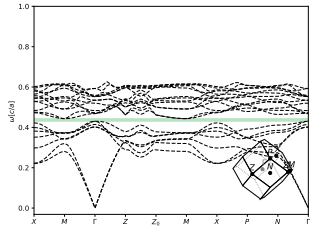

$I = 3$, $\phi = 0.36$. 2.83% gap.

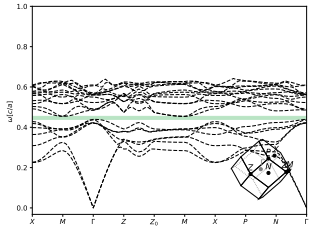

$I = 4$, $\phi = 0.34$. 3.53% gap.

Yttrium Manganese, $\varepsilon = 16$, Bands 2 - 3.

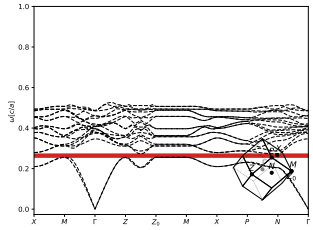

$I = 0$, $\phi = 0.5$. 6.05% gap.

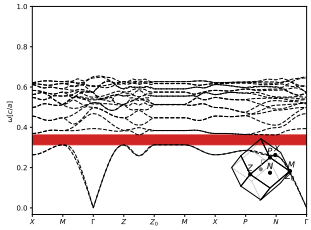

$I = 1$, $\phi = 0.27$. 14.36% gap.

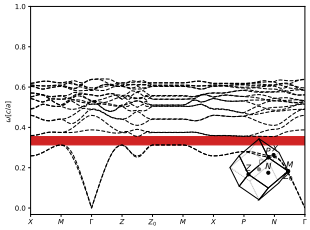

$I = 2$, $\phi = 0.27$. 12.22% gap.

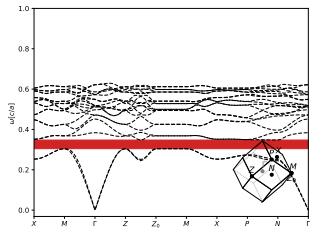

$I = 3$, $\phi = 0.29$. 12.98% gap.

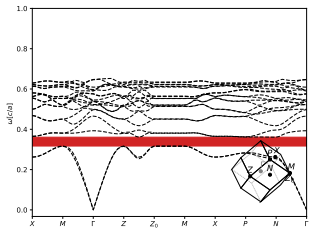

$I = 4$, $\phi = 0.26$. 12.68% gap.

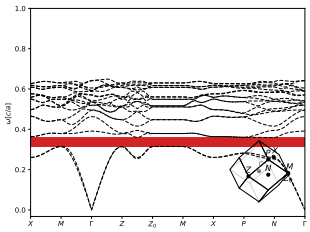

$I = 5$, $\phi = 0.26$. 12.89% gap.

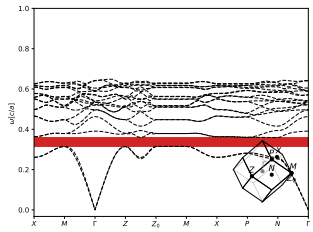

$I = 6$, $\phi = 0.26$. 13.08% gap.

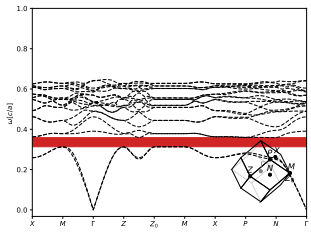

$I = 7$, $\phi = 0.26$. 13.08% gap.

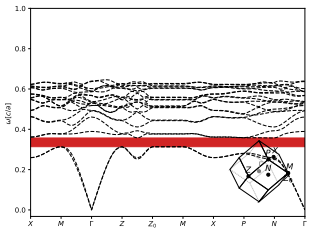

$I = 8$, $\phi = 0.26$. 13.07% gap.

Yttrium Manganese, $\varepsilon = 16$, Bands 14 - 15.

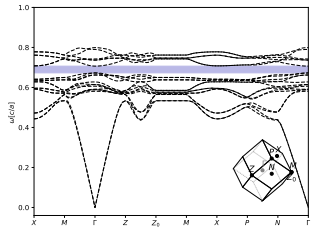

$I = 0$, $\varepsilon = 16$, $\phi = 0.17$. 4.86% gap.

Yttrium Manganese, $I = 9$, Bands 2-3.

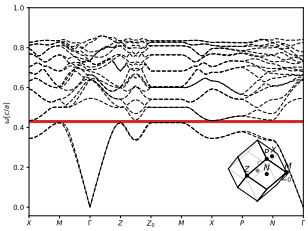

$\varepsilon = 7$, $\phi = 0.32$. 2.46% gap.

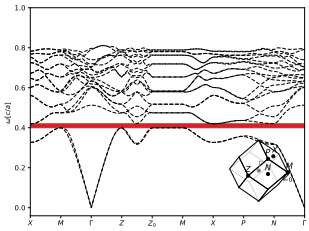

$\varepsilon = 8$, $\phi = 0.32$. 4.91% gap.

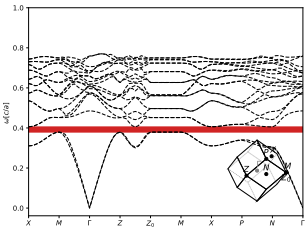

$\varepsilon = 9$, $\phi = 0.32$. 6.69% gap.

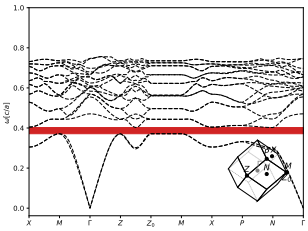

$\varepsilon = 10$, $\phi = 0.29$. 8.05% gap.

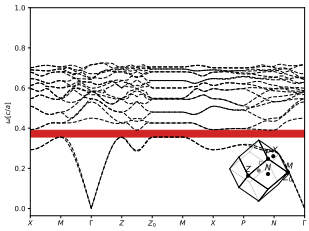

$\varepsilon = 11$, $\phi = 0.29$. 9.22% gap.

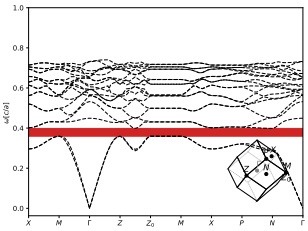

$\varepsilon = 12$, $\phi = 0.26$. 10.25% gap.

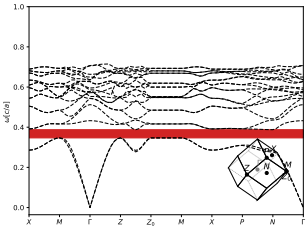

$\varepsilon = 13$, $\phi = 0.26$. 11.15% gap.

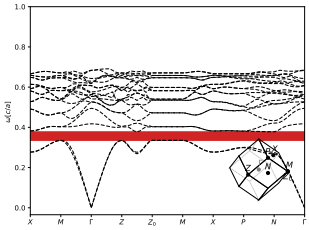

$\varepsilon = 14$, $\phi = 0.26$. 11.92% gap.

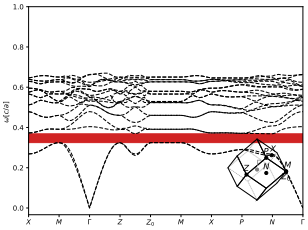

$\varepsilon = 15$, $\phi = 0.26$. 12.57% gap.

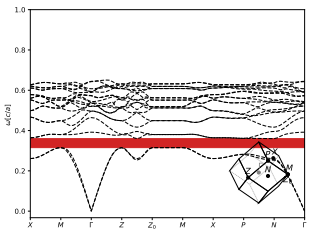

$\varepsilon = 16$, $\phi = 0.26$. 13.1% gap.

Palladium Oxide, $\varepsilon = 16$, Bands 18 - 19.

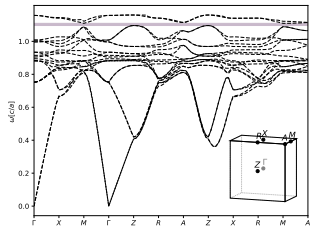

$I = 0$, $\varepsilon = 16$, $\phi = 0.14$. 1.18% gap.

Palladium Oxide, $\varepsilon = 16$, Bands 4 - 5.

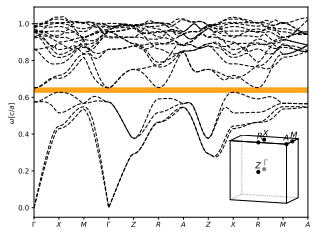

$I = 1$, $\phi = 0.2$. 3.63% gap.

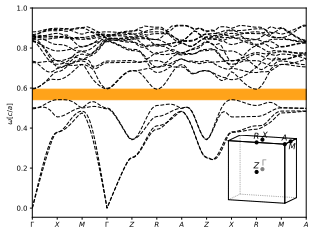

$I = 2$, $\phi = 0.25$. 7.57% gap.

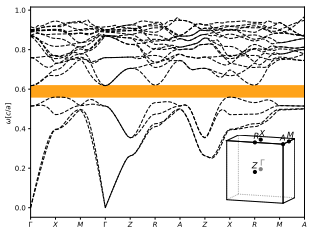

$I = 3$, $\phi = 0.22$. 9.65% gap.

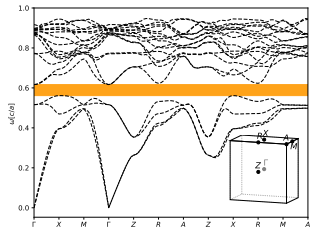

$I = 4$, $\phi = 0.22$. 9.14% gap.

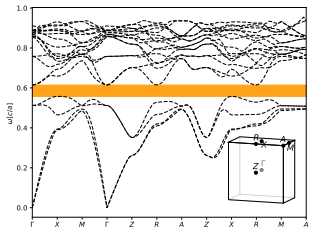

$I = 5$, $\phi = 0.22$. 9.46% gap.

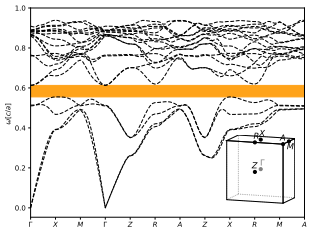

$I = 6$, $\phi = 0.23$. 10.02% gap.

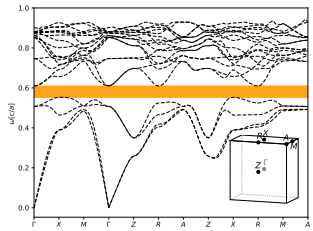

$I = 7$, $\phi = 0.23$. 10.1% gap.

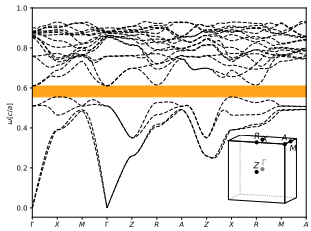

$I = 8$, $\phi = 0.23$. 10.02% gap.

Palladium Oxide, $I = 9$, Bands 4 - 5.

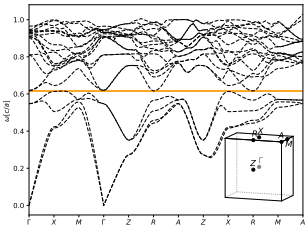

$\varepsilon = 10$, $\phi = 0.31$. 1.01% gap.

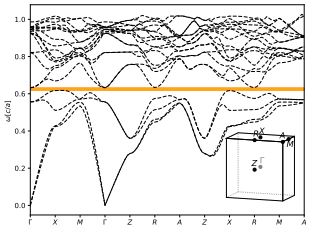

$\varepsilon = 11$, $\phi = 0.27$. 2.74% gap.

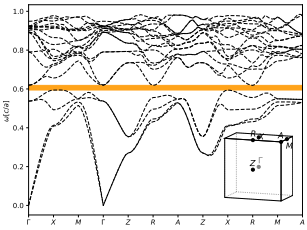

$\varepsilon = 12$, $\phi = 0.27$. 4.49% gap.

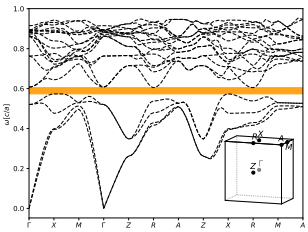

$\varepsilon = 13$, $\phi = 0.27$. 6.06% gap.

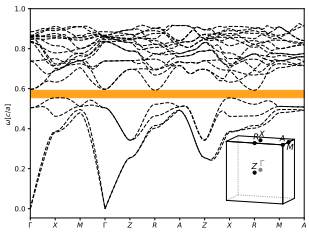

$\varepsilon = 14$, $\phi = 0.27$. 7.27% gap.

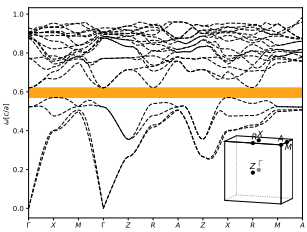

$\varepsilon = 15$, $\phi = 0.23$. 8.65% gap.

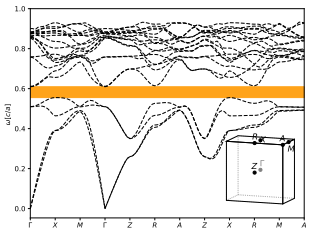

$\varepsilon = 16$, $\phi = 0.23$. 10.1% gap.

APPENDIX E

Glossary of Photonic Band Structures from Section 8.3

Diamond, Bands 2 - 3.

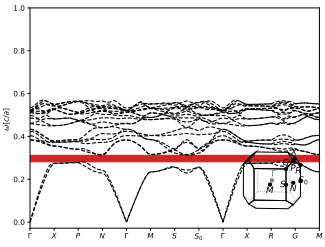

Distorted by $y = 0.75$, $z = 0.75$ **(tI4),** $\phi = 0.47$. 10.14% gap.

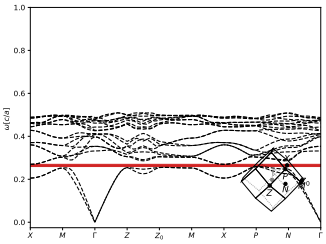

Distorted by $y = 1.0$, $z = 0.5$ **(tI4),** $\phi = 0.54$. 2.27% gap.

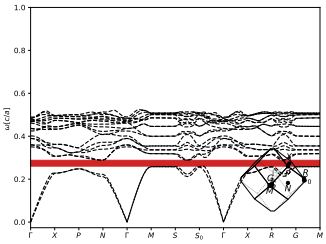

Distorted by $y = 1.0$, $z = 0.75$ **(tI4),** $\phi = 0.46$. 10.06% gap.

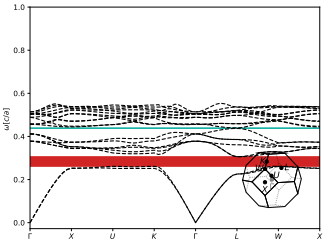

Original Structure (cF8), $\phi = 0.42$. 15.07% gap.

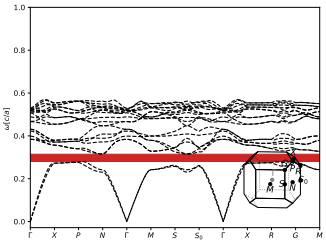

Distorted by $y = 1.0$, $z = 1.25$ **(tI4),** $\phi = 0.44$. 11.28% gap.

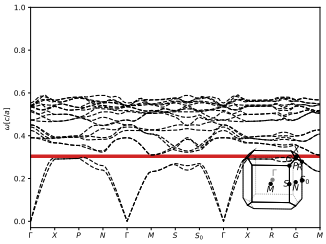

Distorted by $y = 1.0$, $z = 1.5$ **(tI4),** $\phi = 0.48$. 3.77% gap.

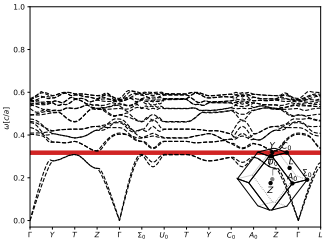

Distorted by $y = 1.25$, $z = 0.75$ **(oF8),** $\phi = 0.49$. 4.99% gap.

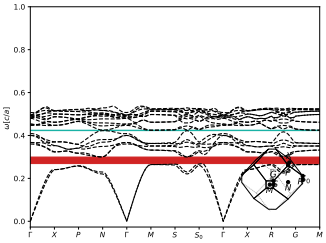

Distorted by $y = 1.25$, $z = 1.25$ **(tI4),** $\phi = 0.43$. 11.22% gap.

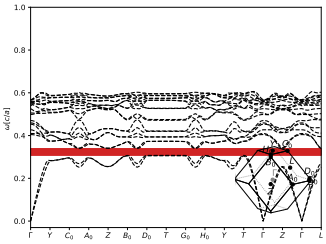

Distorted by $y = 1.5$, $z = 1.25$ **(oF8),** $\phi = 0.44$. 8.64% gap.

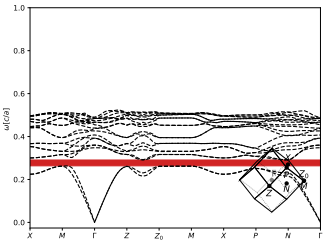

Distorted by $y = 1.5$, $z = 1.5$ **(tI4),** $\phi = 0.46$. 9.91% gap.

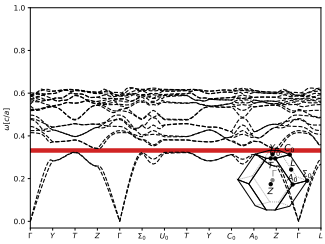

Distorted by $y = 1.75$, $z = 1.5$ **(oF8),** $\phi = 0.47$. 5.06% gap.

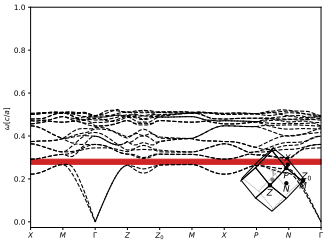

Distorted by $y = 1.75$, $z = 1.75$ **(tI4),** $\phi = 0.48$. 8.34% gap.

Diamond, Bands 2 - 3 (continued).

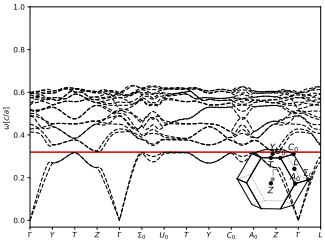

Distorted by $y = 2.0$**,** $z = 1.75$ **(oF8),** $\phi = 0.54$. 1.01% gap.

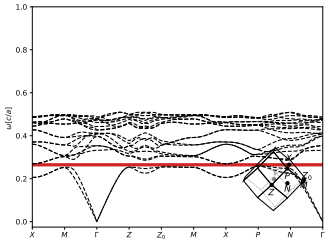

Distorted by $y = 2.0$**,** $z = 2.0$ **(tI4),** $\phi = 0.54$. 2.27% gap.

Diamond, Bands 6 - 7.

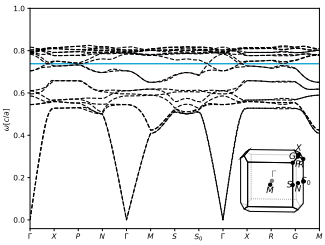

Distorted by $y = 1.0$**,** $z = 1.75$ **(tI4),** $\phi = 0.21$. .

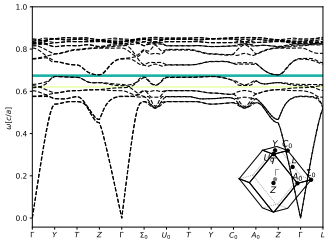

Distorted by $y = 1.75$**,** $z = 1.25$ **(oF8),** $\phi = 0.18$. 1.08% gap.

Diamond, Bands 8 - 9.

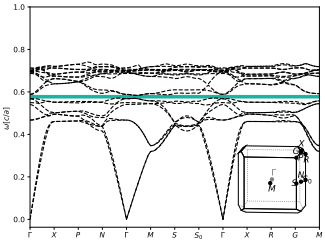

Distorted by $y = 0.5$**,** $z = 0.5$ **(tI4),** $\phi = 0.37$. 2.17% gap.

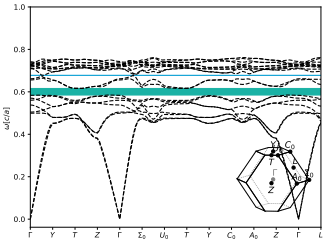

Distorted by $y = 0.75$**,** $z = 0.5$ **(oF8),** $\phi = 0.3$. 4.54% gap.

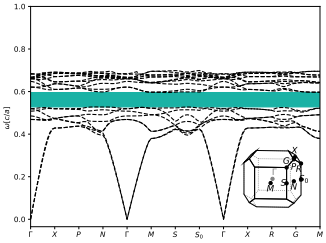

Distorted by $y = 0.75$**,** $z = 0.75$ **(tI4),** $\phi = 0.26$. 12.18% gap.

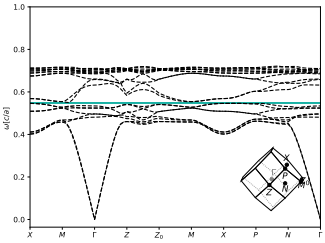

Distorted by $y = 1.0$**,** $z = 0.5$ **(tI4),** $\phi = 0.18$. 1.42% gap.

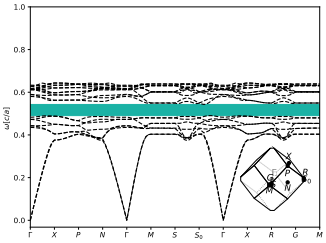

Distorted by $y = 1.0$**,** $z = 0.75$ **(tI4),** $\phi = 0.24$. 10.42% gap.

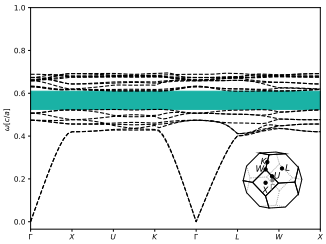

Original Structure (cF8), $\phi = 0.21$. 14.54% gap.

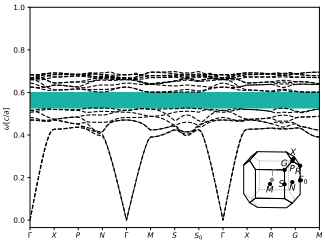

Distorted by $y = 1.0$**,** $z = 1.25$ **(tI4),** $\phi = 0.24$. 13.01% gap.

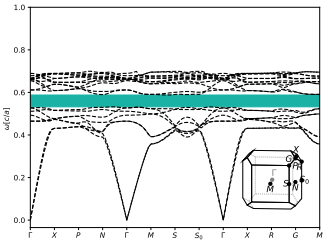

Distorted by $y = 1.0$**,** $z = 1.5$ **(tI4),** $\phi = 0.29$. 9.93% gap.

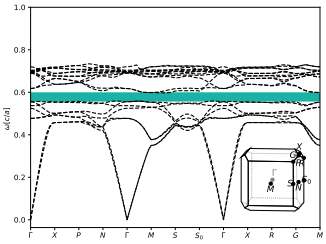

Distorted by $y = 1.0$**,** $z = 1.75$ **(tI4),** $\phi = 0.31$. 6.93% gap.

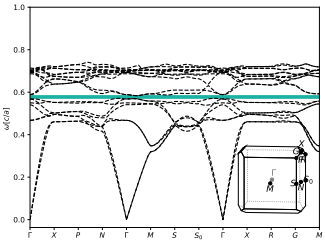

Distorted by $y = 1.0$**,** $z = 2.0$ **(tI4),** $\phi = 0.37$. 2.17% gap.

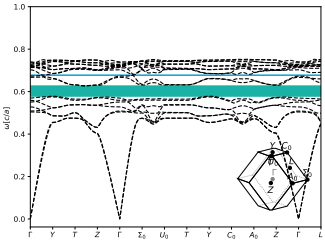

Distorted by $y = 1.25$**,** $z = 0.75$ **(oF8),** $\phi = 0.25$. 7.38% gap.

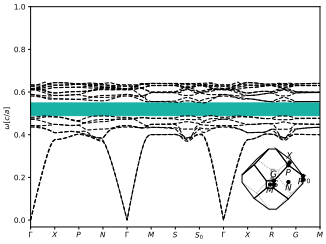

Distorted by $y = 1.25$**,** $z = 1.25$ **(tI4),** $\phi = 0.24$. 11.82% gap.

Diamond, Bands 8 - 9 (continued).

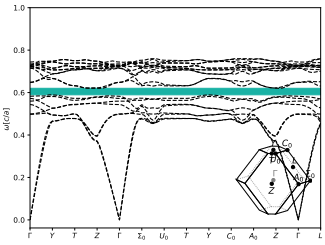

Distorted by $y = 1.5$, $z = 0.75$ **(oF8)**, $\phi = 0.3$. 5.35% gap.

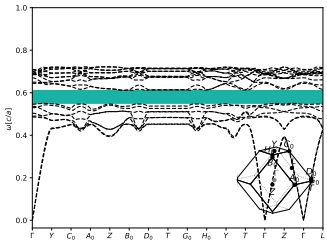

Distorted by $y = 1.5$, $z = 1.25$ **(oF8)**, $\phi = 0.26$. 9.42% gap.

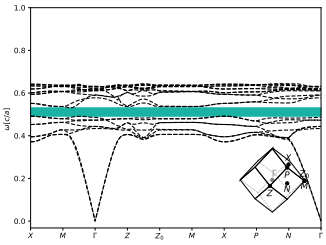

Distorted by $y = 1.5$, $z = 1.5$ **(tI4)**, $\phi = 0.24$. 7.78% gap.

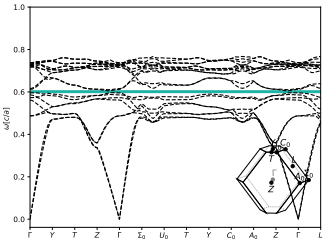

Distorted by $y = 1.75$, $z = 0.75$ **(oF8)**, $\phi = 0.36$. 1.53% gap.

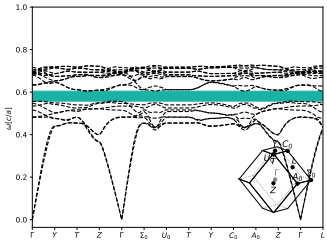

Distorted by $y = 1.75$, $z = 1.25$ **(oF8)**, $\phi = 0.3$. 7.45% gap.

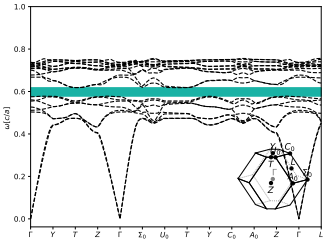

Distorted by $y = 1.75$, $z = 1.5$ **(oF8)**, $\phi = 0.27$. 6.14% gap.

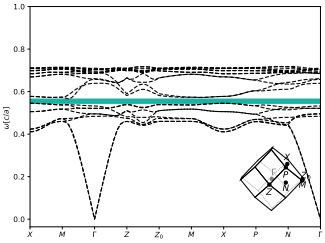

Distorted by $y = 1.75$, $z = 1.75$ **(tI4)**, $\phi = 0.18$. 5.01% gap.

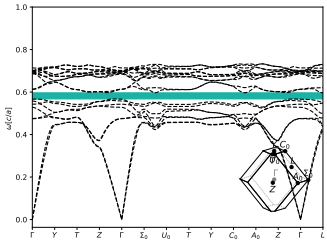

Distorted by $y = 2.0$, $z = 1.25$ **(oF8)**, $\phi = 0.34$. 4.98% gap.

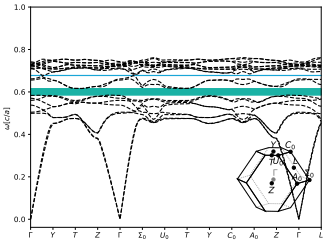

Distorted by $y = 2.0$, $z = 1.5$ **(oF8)**, $\phi = 0.3$. 4.54% gap.

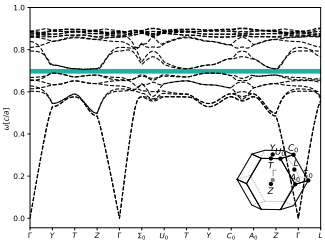

Distorted by $y = 2.0$, $z = 1.75$ **(oF8)**, $\phi = 0.18$. 2.85% gap.

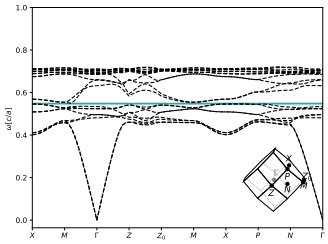

Distorted by $y = 2.0$, $z = 2.0$ **(tI4)**, $\phi = 0.18$. 1.42% gap.

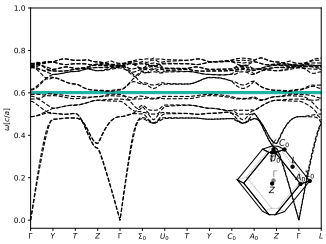

Distorted by $y = 2.25$, $z = 1.25$ **(oF8)**, $\phi = 0.35$. 1.59% gap.

Diamond, Bands 8 - 9 (continued).

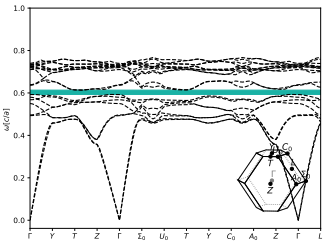

Distorted by $y = 2.25$**,** $z = 1.5$ **(oF8),** $\phi = 0.34$. 3.02% gap.

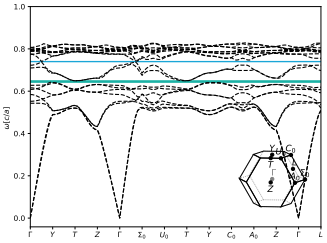

Distorted by $y = 2.25$**,** $z = 1.75$ **(oF8),** $\phi = 0.26$. 1.27% gap.

Diamond, Bands 10 - 11.

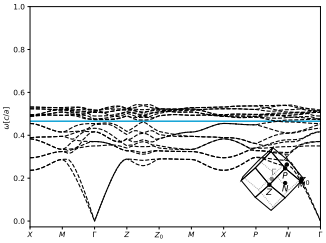

Distorted by $y = 1.0$**,** $z = 0.5$ **(tI4),** $\phi = 0.46$. .

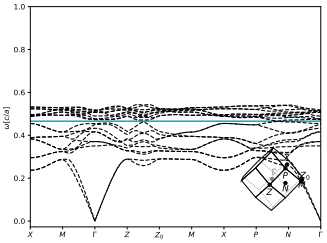

Distorted by $y = 2.0$**,** $z = 2.0$ **(tI4),** $\phi = 0.46$. .

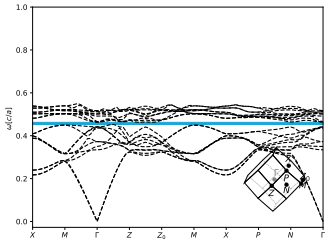

Distorted by $y = 2.75$**,** $z = 2.75$ **(tI4),** $\phi = 0.55$. 2.19% gap.

Diamond, Bands 14 - 15.

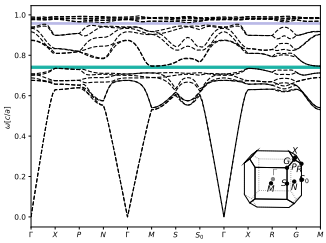

Distorted by $y = 0.75$**,** $z = 0.75$ **(tI4),** $\phi = 0.08$. 1.47% gap.

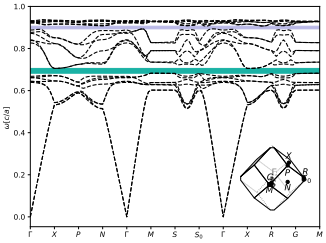

Distorted by $y = 1.0$**,** $z = 0.75$ **(tI4),** $\phi = 0.07$. (1) 3.27% gap between bands 8-9, and (2) 1.36% gap between bands 14-15.

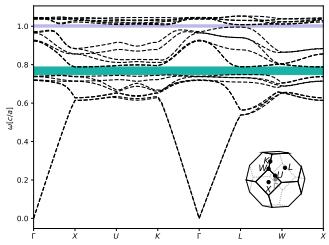

Original Structure (cF8), $\phi = 0.06$. 5.14% gap.

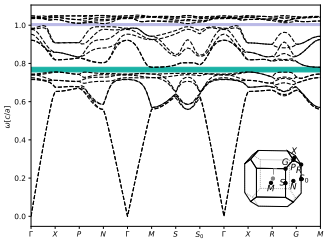

Distorted by $y = 1.0$**,** $z = 1.25$ **(tI4),** $\phi = 0.07$. (1) 3.1% gap between bands 8-9, and (2) 1.06% gap between bands 14-15.

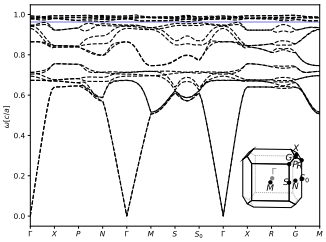

Distorted by $y = 1.0$**,** $z = 1.5$ **(tI4),** $\phi = 0.1$. .

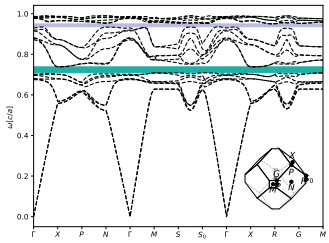

Distorted by $y = 1.25$**,** $z = 1.25$ **(tI4),** $\phi = 0.06$. (1) 4.02% gap between bands 8-9, and (2) 1.51% gap between bands 14-15.

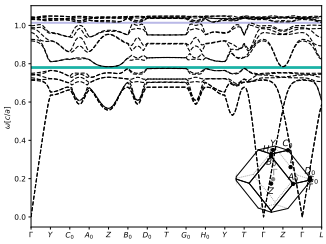

Distorted by $y = 1.5$**,** $z = 1.25$ **(oF8),** $\phi = 0.08$. 1.09% gap.

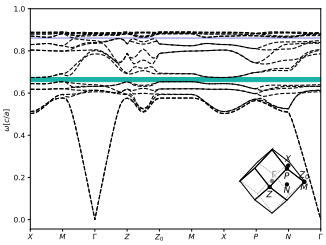

Distorted by $y = 1.5$**,** $z = 1.5$ **(tI4),** $\phi = 0.09$. 2.96% gap.

Lithium Oxide, Bands 8 - 9.

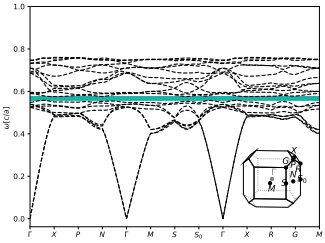

Distorted by $y = 0.75$**,** $z = 0.75$ **(tI6),** $\phi = 0.27$. 3.11% gap.

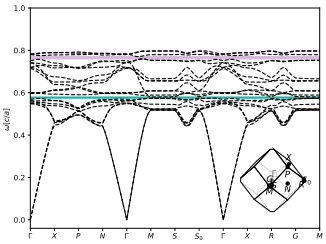

Distorted by $y = 1.0$**,** $z = 0.75$ **(tI6),** $\phi = 0.17$. 1.47% gap.

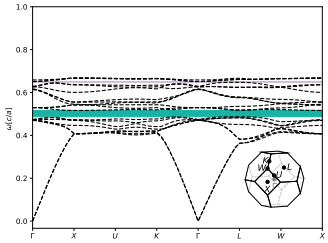

Original Structure (cF12), $\phi = 0.31$. 5.86% gap.

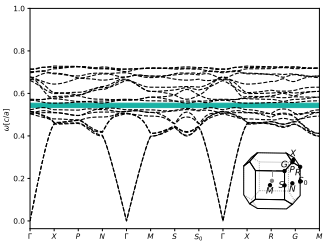

Distorted by $y = 1.0$**,** $z = 1.25$ **(tI6),** $\phi = 0.29$. 3.84% gap.

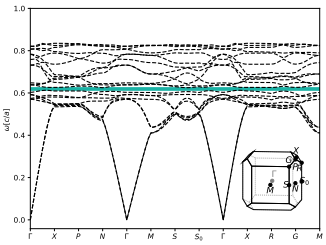

Distorted by $y = 1.0$**,** $z = 1.5$ **(tI6),** $\phi = 0.23$. 1.97% gap.

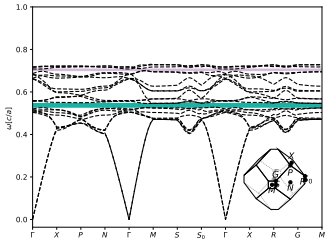

Distorted by $y = 1.25$**,** $z = 1.25$ **(tI6),** $\phi = 0.23$. (1) 3.28% gap between bands 8-9, and (2) 1.09% gap between bands 17-18.

Lithium Oxide, Bands 11 - 12.

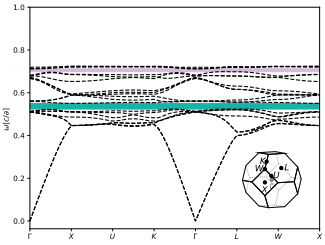

Original Structure (cF12), $\phi = 0.25$. (1) 4.92% gap between bands 8-9, and (3) 1.89% gap between bands 17-18.

Lithium Oxide, Bands 14 - 15.

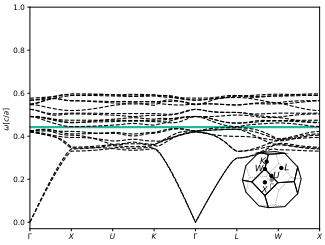

Original Structure (cF12), $\phi = 0.43$. 1.88% gap.

Lithium Oxide, Bands 17 - 18.

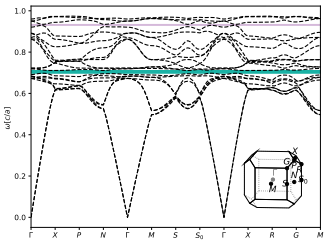

Distorted by $y = 0.75$, $z = 0.75$ **(tI6),** $\phi = 0.13$. 1.86% gap.

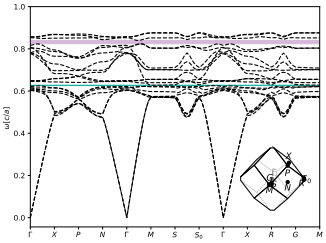

Distorted by $y = 1.0$, $z = 0.75$ **(tI6),** $\phi = 0.13$. 1.87% gap.

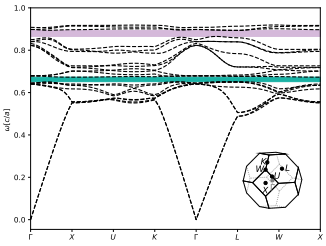

Original Structure (cF12), $\phi = 0.12$. (1) 3.15% gap between bands 8-9, and (2) 3.1% gap between bands 17-18.

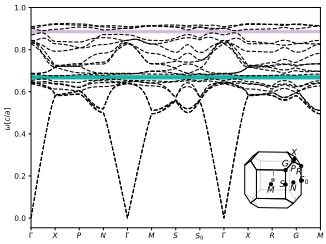

Distorted by $y = 1.0$, $z = 1.25$ **(tI6),** $\phi = 0.14$. (1) 2.29% gap between bands 8-9, and (2) 1.12% gap between bands 17-18.

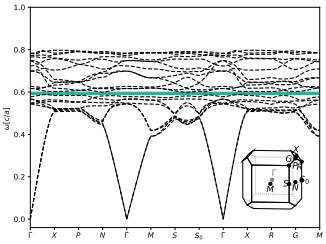

Distorted by $y = 1.0$, $z = 1.5$ **(tI6),** $\phi = 0.26$. 1.92% gap.

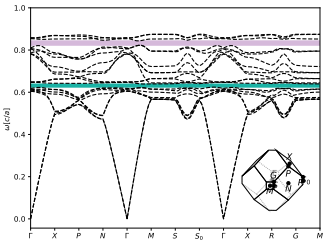

Distorted by $y = 1.25$, $z = 1.25$ **(tI6),** $\phi = 0.13$. (1) 2.39% gap between bands 8-9, and (2) 2.45% gap between bands 17-18.

SCC, Bands 4 - 5.

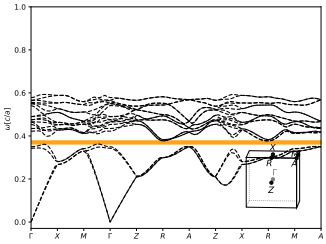

Distorted by $y = 0.75$, $z = 0.75$ **(tP4),** $\phi = 0.52$. 4.57% gap.

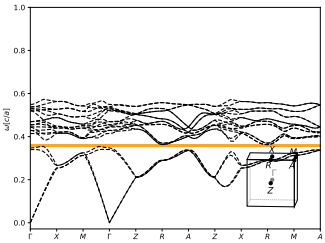

Distorted by $y = 1.25$, $z = 1.0$ **(tP4),** $\phi = 0.51$. 2.33% gap.

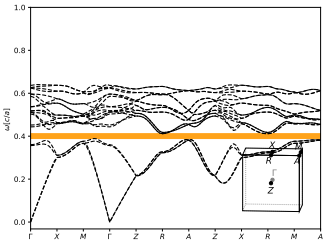

Distorted by $y = 1.5$, $z = 1.0$ **(tP4),** $\phi = 0.51$. 6.84% gap.

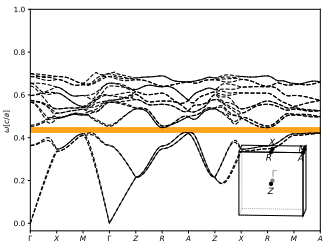

Distorted by $y = 1.75$, $z = 1.0$ **(tP4),** $\phi = 0.54$. 4.83% gap.

SCC, Bands 8 - 9.

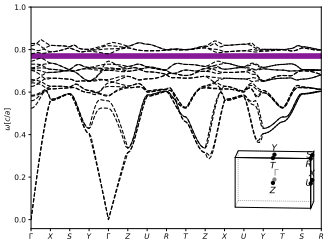

Distorted by $y = 0.75$**,** $z = 0.5$ **(oP4),** $\phi = 0.31$. 2.8% gap.

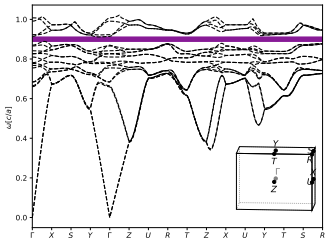

Distorted by $y = 1.5$**,** $z = 0.75$ **(oP4),** $\phi = 0.21$. 2.54% gap.

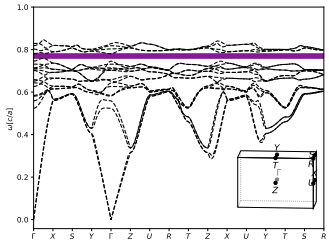

Distorted by $y = 2.0$**,** $z = 1.5$ **(oP4),** $\phi = 0.31$. 2.8% gap.

SCC, Bands 16 - 17.

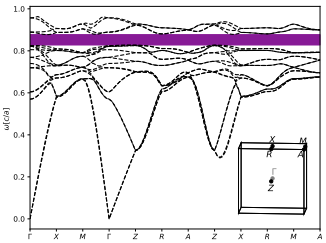

Distorted by $y = 0.5$, $z = 0.5$ **(tP4),** $\phi = 0.33$. 5.86% gap.

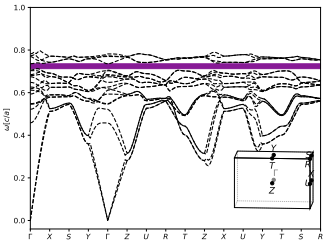

Distorted by $y = 0.75$, $z = 0.5$ **(oP4),** $\phi = 0.36$. 3.21% gap.

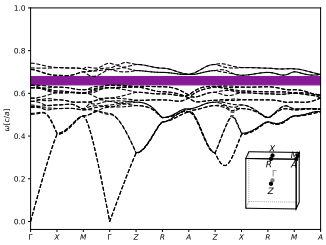

Distorted by $y = 0.75$, $z = 0.75$ **(tP4),** $\phi = 0.32$. 6.97% gap.

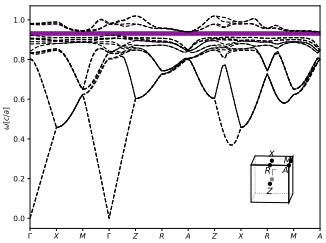

Distorted by $y = 1.0$, $z = 0.75$ **(tP4),** $\phi = 0.06$. 1.86% gap.

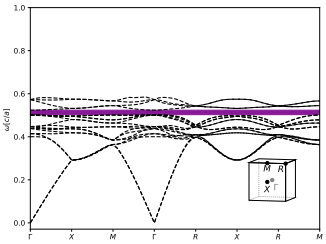

Original Structure (cP4), $\phi = 0.37$. 4.23% gap.

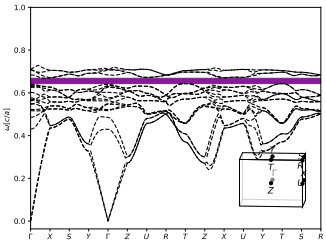

Distorted by $y = 1.25$, $z = 0.75$ **(oP4),** $\phi = 0.37$. 3.78% gap.

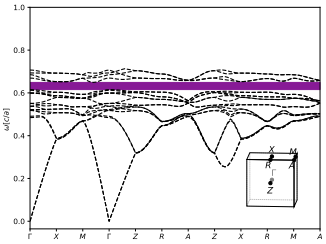

Distorted by $y = 1.25$, $z = 1.0$ **(tP4),** $\phi = 0.32$. 5.91% gap.

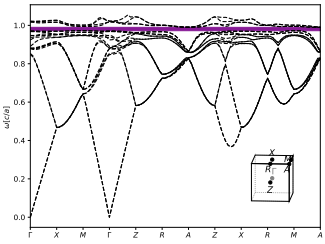

Distorted by $y = 1.25$, $z = 1.25$ **(tP4),** $\phi = 0.05$. 1.52% gap.

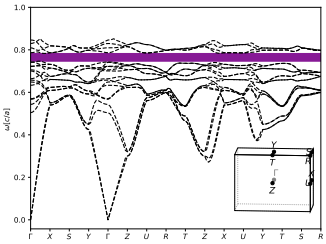

Distorted by $y = 1.5$, $z = 0.75$ **(oP4),** $\phi = 0.34$. 4.88% gap.

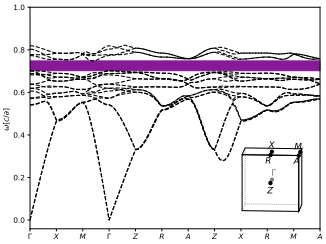

Distorted by $y = 1.5$, $z = 1.0$ **(tP4),** $\phi = 0.3$. 7.27% gap.

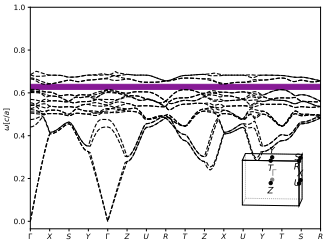

Distorted by $y = 1.5$, $z = 1.25$ **(oP4),** $\phi = 0.37$. 3.68% gap.

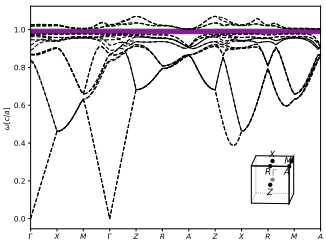

Distorted by $y = 1.5$, $z = 1.5$ **(tP4),** $\phi = 0.06$. 2.29% gap.

SCC, Bands 16 - 17 (continued).

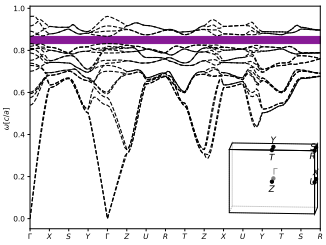

Distorted by $y = 1.75$, $z = 0.75$ **(oP4),** $\phi = 0.34$. 4.01% gap.

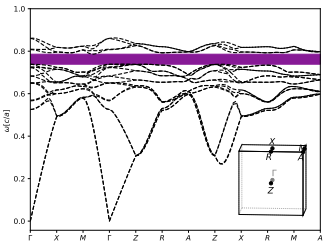

Distorted by $y = 1.75$, $z = 1.0$ **(tP4),** $\phi = 0.35$. 6.86% gap.

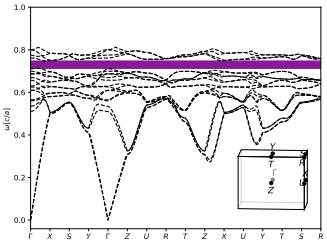

Distorted by $y = 1.75$, $z = 1.25$ **(oP4),** $\phi = 0.33$. 5.0% gap.

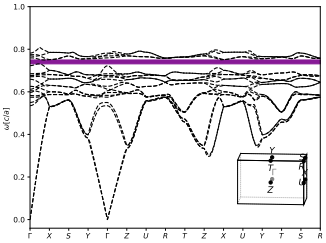

Distorted by $y = 1.75$, $z = 1.5$ **(oP4),** $\phi = 0.27$. 2.43% gap.

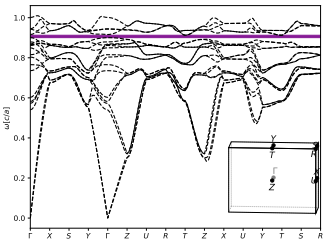

Distorted by $y = 2.0$, $z = 0.75$ **(oP4),** $\phi = 0.37$. 1.36% gap.

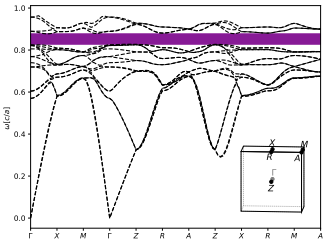

Distorted by $y = 2.0$, $z = 1.0$ **(tP4),** $\phi = 0.33$. 5.86% gap.

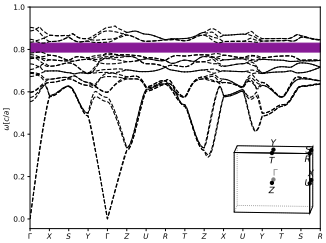

Distorted by $y = 2.0$, $z = 1.25$ **(oP4),** $\phi = 0.31$. 5.28% gap.

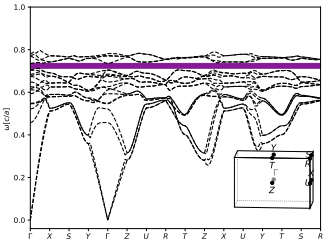

Distorted by $y = 2.0$, $z = 1.5$ **(oP4),** $\phi = 0.36$. 3.21% gap.

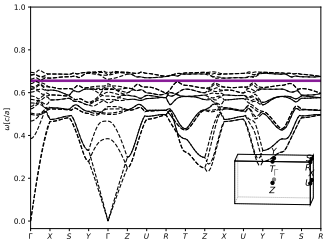

Distorted by $y = 2.0$, $z = 1.75$ **(oP4),** $\phi = 0.41$. 1.44% gap.

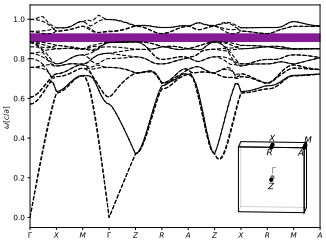

Distorted by $y = 2.25$, $z = 1.0$ **(tP4),** $\phi = 0.35$. 4.28% gap.

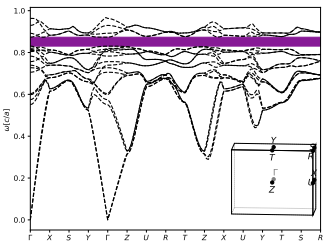

Distorted by $y = 2.25$, $z = 1.25$ **(oP4),** $\phi = 0.33$. 5.01% gap.

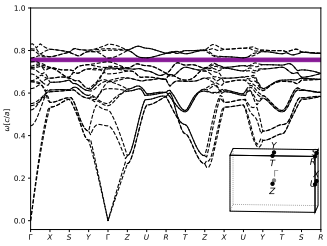

Distorted by $y = 2.25$, $z = 1.5$ **(oP4),** $\phi = 0.39$. 2.26% gap.

SCC, Bands 16 - 17 (continued).

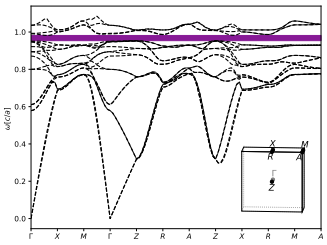

Distorted by $y = 2.5$**,** $z = 1.0$ **(tP4),** $\phi = 0.35$. 2.89% gap.

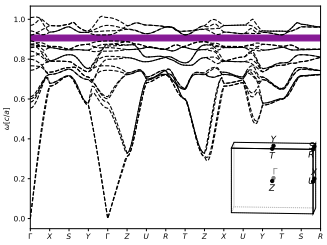

Distorted by $y = 2.5$**,** $z = 1.25$ **(oP4),** $\phi = 0.34$. 3.3% gap.

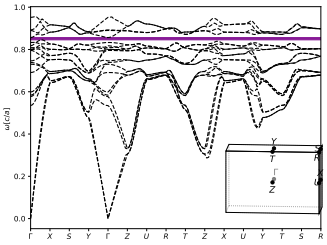

Distorted by $y = 2.5$**,** $z = 1.5$ **(oP4),** $\phi = 0.34$. 1.22% gap.

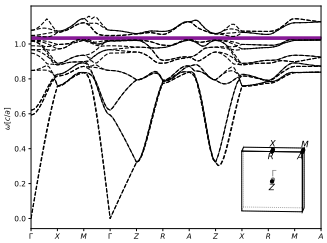

Distorted by $y = 2.75$**,** $z = 1.0$ **(tP4),** $\phi = 0.35$. 1.75% gap.

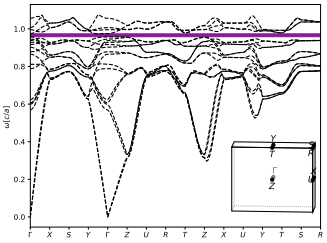

Distorted by $y = 2.75$**,** $z = 1.25$ **(oP4),** $\phi = 0.34$. 1.61% gap.